High Green Density Metal Parts by Vibrational Compaction of Dry Powder in the Three Dimensional Printing Process

by

Steven Joseph Gregorski

B.S., Mechanical Engineering
Massachusetts Institute of Technology, 1989

M.S., Mechanical Engineering
Massachusetts Institute of Technology, 1994

Submitted to the Department of Mechanical Engineering
in Partial Fulfillment of the Requirements for the Degree of

Doctor of Philosophy

at the

Massachusetts Institute of Technology

July 1996
[September 1996]

Signature of Author . . . . . .
Department of Mechanical Engineering
uly 31, 1996

Certified by . . . . . .
Emanuel M. Sachs
Professor of Mechanical Engineering
Laboratory for Manufacturing and Productivity
Thesis Supervisor

Accepted by . .
Ain A. Sonin
Chairman of Graduate Committee

High Green Density Metal Parts by Vibrational Compaction of Dry Powder in the Three Dimensional Printing Process

by

Steven J. Gregorski

Submitted to the Department of Mechanical Engineering on July 31, 1996 in Partial Fulfillment of the Requirements for the Degree of Doctor of Philosophy in Mechanical Engineering

ABSTRACT

The material properties and dimensional accuracy of metal tooling produced by the Three Dimensional Printing process can be enhanced by increasing the green density of the 3D printed part. Green density is the ratio of metal powder volume to the external volume of the printed part, and is a measure of how tightly packed the powder particles in the printed part are. The central goal of this thesis was to increase the green density of metal parts from the current level of 58% to levels greater than 75%.

Two approaches were taken for increasing green density. The first was to utilize bimodal mixtures of metal powders which could be packed to significantly higher densities than the monomodal powders which had been previously used. Three bimodal powder mixtures, with tap densities near 80%, were studied. The second approach was to develop a new powder layering device which could pack these bimodal powders to the tap density during layer creation. New understandings about the relationship between the stresses applied to the powder layer and the resulting packing density changes were required to design this device.

Shear cell and unconfined compression tests were performed to characterize the metal powder stress / strain behavior. Particulate stress / strain models, such as the Mohr-Coulomb failure law and the Jenike yield locus theory, were used to interpret the packing behavior of the metal powders under various stress conditions. A simple frictional model of powder behavior was proposed for the low stress levels permissible in the 3DP process. The application of a small static normal stress, in combination with an oscillatory horizontal shear stress, was found to be the most effective means of reducing particle interlocking and provided the best layer densification results.

A new layer densification mechanism was constructed and successfully used to generate printed parts with green densities in excess of 75%. Photographic analysis techniques used to analyze part microstructures indicated significant improvements in packing homogeneity. Packing defects between the printed layers were reduced or eliminated. Compositional analysis indicated no significant segregation of the bimodal components during layer spreading.

Thesis Committee

Prof. Emanuel M. Sachs, Chairman
Prof. Michael J. Cima
Prof. Samuel M. Allen

Acknowledgments

This thesis is dedicated to my mother, Joan Michaels, and my wife, Joan Gregorski. They provided the foundation of inspiration, encouragement and love upon which all my efforts rested.

To David Brancazio, for being the true friend who acted as my safety net, emergency exit, and sounding board in good times and in bad.

To Ely Sachs, for standing by me through it all.

To my thesis committee, Profs. Ely Sachs, Michael Cima and Sam Allen, for providing me with guidance and insight during my research.

To Jim Serdy, who acted as my example of how unstoppable determination can overcome any obstacle.

To Steve and Charlene Hinton, for providing an endless variety of distractions, diversions and extremely unhealthy comfort food.

Finally, to all the students of the Three Dimensional Printing Project beside whom I have had the pleasure of working for these last six years. Best wishes to you all.

Table of Contents

List of Figures

Chapter 1. Introduction

Chapter 2. Literature Review

Chapter 3. Development of a Bimodal Printing Process

Chapter 4. Analysis of the Baseline Bimodal Printing Process

Chapter 5. Investigation of Layer Densification Mechanisms

Chapter 6. Evaluation of the New Printing Techniques

Appendix C: Measuring Packing and Compositional Homogeneity Using Photographic Analysis Techniques

Appendix E: A Preliminary Investigation of Metal Slurry Spreading

List of Tables

Chapter 1. Introduction

Chapter 2. Literature Review

Chapter 3. Development of a Bimodal Printing Process

Chapter 4. Analysis of the Baseline Bimodal Printing Process

Chapter 5. Investigation of Layer Densification Mechanisms

Chapter 6. Evaluation of the New Printing Techniques

Appendix C: Measuring Packing and Compositional Homogeneity Using Photographic Analysis Techniques

Executive Summary

Metal parts produced by the Three Dimensional Printing process must meet specified material property and dimensional accuracy requirements. These requirements become exceptionally stringent when producing metal tooling for use in industrial applications such as plastic injection molding. The green density of the printed part has a significant impact on both these requirement areas. Green density is the ratio of metal powder volume to the external volume of the printed part, and is a measure of how tightly packed the powder particles in the printed part are. The original 3DP metals printing green density levels of 52 to 58% were unacceptably low, and resulted in finished parts with poor overall properties. The central goal of this thesis was to increase the green density of metal parts to levels greater than 75%.

Motivation for Producing 3D Printed Metal Parts with High Green Densities

The original 3DP process for producing green metal parts utilized monomodal powders with sizes which ranges between 20 and 70μm. In addition to the previously mentioned low green densities of these printed parts, the parts also contained significant packing defects, which would become incorporated into the fully densified parts after furnace post-processing operations. Figure 1 is a cross-sectional micrograph taken from a part printed with 20μm 316L stainless steel powder. Packing defects which exist between the printed layers are clearly visible.

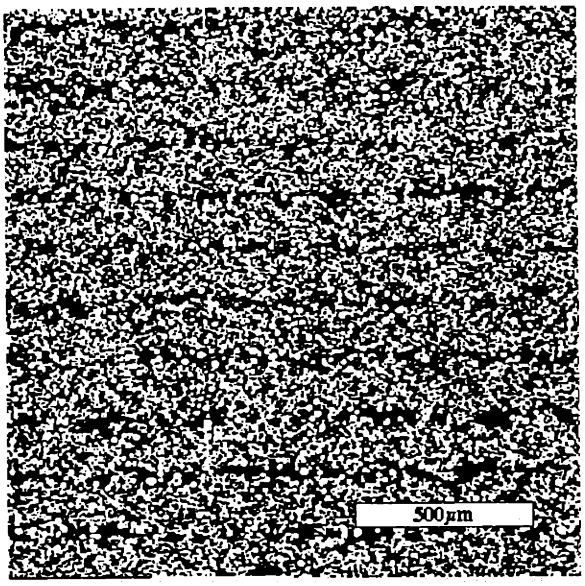

Figure 1: A cross-sectional image taken from a bar printed with 20μm 316L powder.

Increasing the green density of the printed parts was identified as a means of improving the material properties of the fully post-processed parts. This would occur for two reasons. The first was related to the reduction in the amount of infiltrant incorporated into the final, all-metal tool. The major constituent of the finished tool was the steel powder used to produce the green part. Increasing the green density would result in elevated levels of steel alloy in the finished tool, with a subsequent reduction in the amount of copper-alloy infiltrant. Since the steel powder had superior hardness and stiffness properties compared to the copper infiltrant, these properties would be enhanced in a tool which contained a greater proportion of steel. Material properties would also be improved because increased green density would result in improved homogeneity throughout the finished part by removing defects such as those shown in figure 1.

Dimensional accuracy in the finished parts would also be improved by increasing green density. Prior to infiltration, the metal skeleton must be sintered to strengthen it enough to resist distortions caused by capillary pressures. The amount of sintering required prior to infiltration is related to the green density. Parts with higher green densities require less sintering and hence less overall shrinkage.

Two approaches were taken for increasing green density. The first was to utilize bimodal mixtures of metal powders which could be packed to significantly higher densities than the monomodal powders which had been previously used. Three bimodal powder mixtures, blended from different sizes of powders and alloys, were studied. Tap densities near 80% were obtained with these powders. Figure 2 is photograph of a bimodal powder mixture.

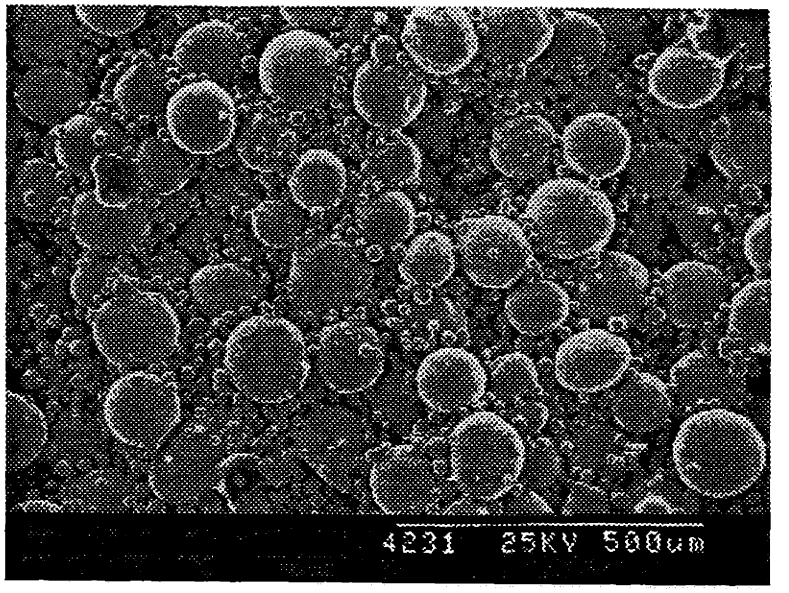

Figure 2: A bimodal powder mixture.

The properties of the three bimodal mixtures which were investigated in this research are given in table 1.

Table 1: Properties of the Bimodal Powder Mixtures

Attribute	120/20μm Mixture	71/9μm Mixture	66/9μm Mixture
Stainless Alloy	316L	316L	420
Shapes	spherical	spherical	spherical
Large Powder Sieve Cut	-100 / +170 mesh	-170 / +270 mesh	-170 / +325 mesh
Small Powder Sieve Cut	-30μm / +15μm	-16μm / +4μm	-16μm / +4μm
Apparent Density	60.5%	58.0%	64.4%
Tap Density	76.2%	78.5%	75.6%

The second avenue for increasing green density was to develop a new powder layering device which packed these bimodal powders to their maximum density during the 3DP process, thereby fully utilizing their packing capabilities. This latter approach required an understanding of the relationship between the stresses applied to the powder during the layering process and the packing density changes in the powder itself.

Overview of this Research Effort

This research effort can be chronologically divided into five stages, as illustrated in figure 3. A detailed description of each of these stages is given in the sections below.

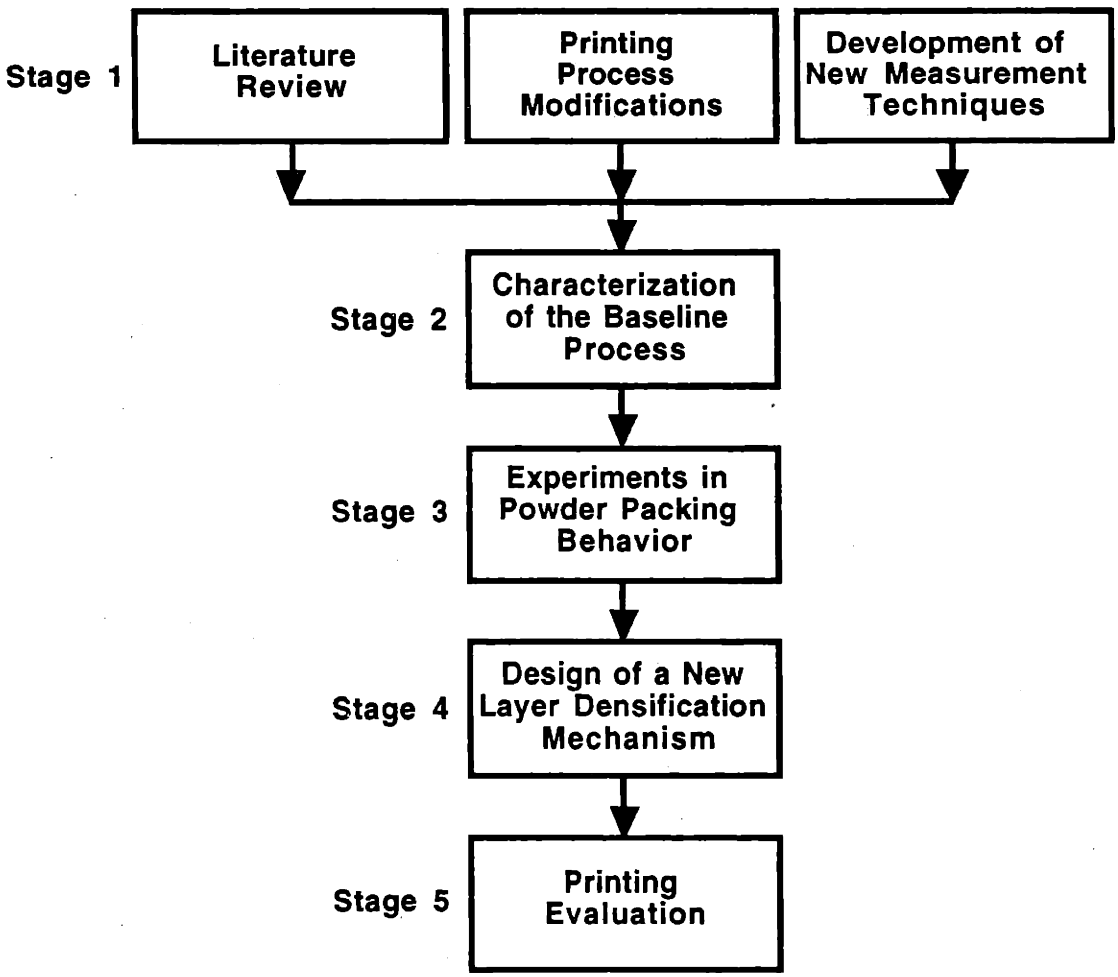

Figure 3: Research summary flowchart showing chronologically the five stages of investigation.

New Printing and Measurement Techniques

The first stage in this research involved work in three distinct areas, and laid the foundation for later investigation. Two of these areas were printing process modifications and the development of new part measurement techniques.

The original metals printing process was modified and improved so that bimodal test parts could be reliably produced using all the bimodal powder mixtures listed in table 1. The goal was not to create an optimized process, but rather to locate a single operating condition with which could be used to produce test bars produced using different layer densification mechanisms. Process improvements were made to the layer drying, powder coating activation, powder preparation and recycling procedures. Some processes were partially automated in order to produce more consistent results. Because of the additional steps in the new printing process, however, the overall printing rate was lowered.

New photographic analysis techniques were developed which could quantitatively measure local packing variation in the 3D printed parts. Local compositional variation could also be measured in parts printed with the bimodal powder mixtures. These techniques allowed for a more rigorous comparison of the printed part microstructures than was previously possible, and also acted as an indicator for which printing process variations were indeed producing better parts.

The new measurement techniques involved analysis of multiple cross-sectional images which were obtained from test bars, as illustrated in figure 4. Computer algorithms were written which processed these images and generated descriptive packing and composition parameters.

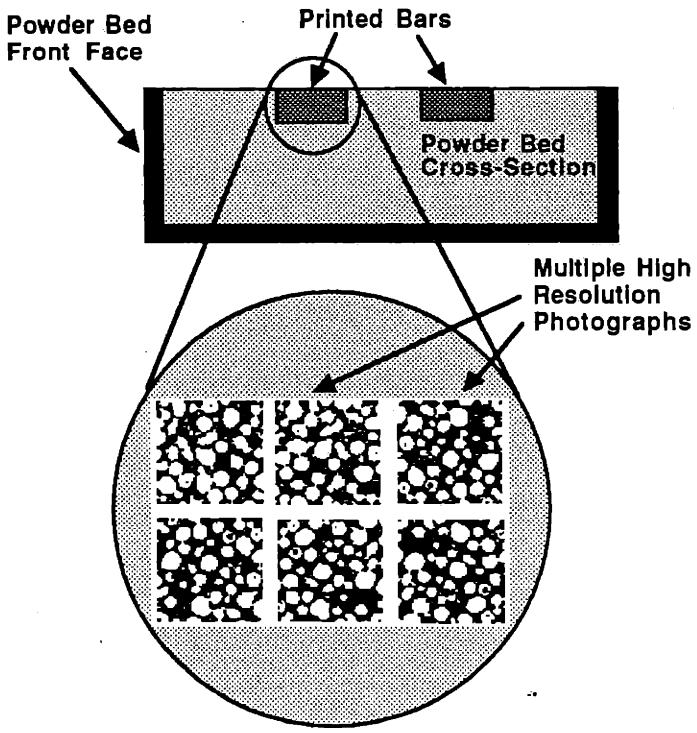

Figure 4: An illustration of how multiple cross-sectional images were obtained from printed bars.

Theoretical Considerations

The literature related to powder packing theory was reviewed in order to guide this research effort. The goal of the literature review was first to identify those aspects of particulate materials which inhibited them from packing to high densities, and second to understand how a stress distribution applied to a powder mass might be used to overcome these inhibiting factors and produce a tightly packed body.

For the size range of powders being tested, frictional resistance between the individual surfaces of the sliding and rolling particles, and mechanical interlocking forces created by the engagement of geometric features on these surfaces, were identified as the primary inhibitors of particle mobility. Other factors such as capillary bonds, chemical bridges and van der Waals forces were judged to be less important. Both the frictional and interlocking forces in a powder mass increase with packing density, since both are related to the number of interparticle contacts per unit volume. Thus, increasing the packing density of a powder mass becomes continually more difficult.

The fields of soil and powder mechanics were studied to understand the relationship between an applied stress field and the changes in packing (i.e. strains) of a particulate body. This information would be useful in the later design of a new powder densification device. Two powder stress / strain models were studied. These were the Mohr-Coulomb failure law, and the Jenike yield locus theory.

In the realm of soil mechanics, the earliest and most basic stress / strain relationship proposed is the Mohr - Coulomb failure law. It is not really a law at all, but is simply based on a collection of observations about when a powder mass will begin to deform, or "fail", under an applied load. The failure law places a *Mohr envelope* on a graph of shear stress versus normal stress. The envelope is defined by the relation

$$\tau = c + \sigma(\tan\theta), \qquad \text{(eq. 1)}$$

where c is called the cohesion or cohesion intercept, and θ is called the angle of internal friction or angle of shearing resistance. Figure 5 is an illustration of the Mohr - Coulomb failure law. The Mohr envelope is drawn as a straight line.

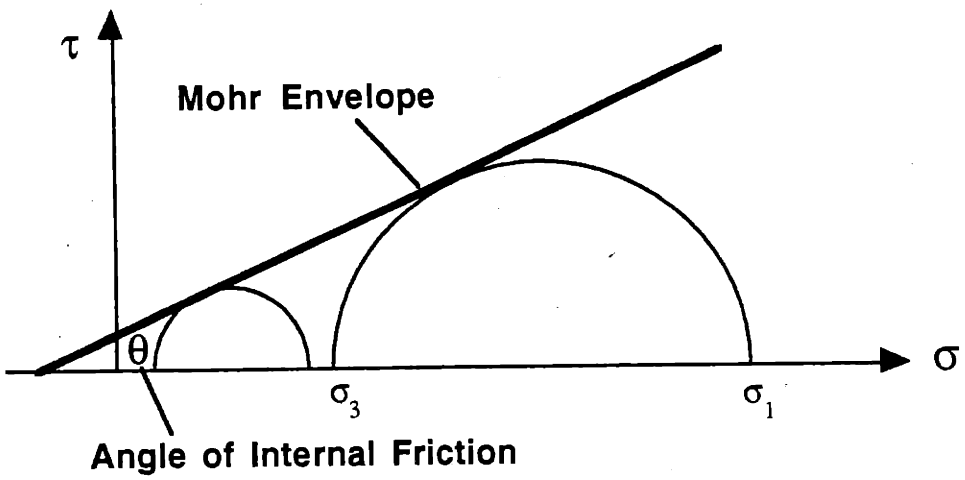

Figure 5: An illustration of the Mohr - Coulomb failure law.

The Mohr - Coulomb failure law may be understood from the following statements:

1. If the Mohr circle for a given state of stress lies entirely below the Mohr envelope for a soil, then the soil will be stable (i.e. not deform) for that state of stress.

2. If the Mohr circle is just tangent to the Mohr envelope, the full strength of the soil has been reached on some plane through the soil. This plane is called the *failure plane*.

3. It is not possible to have a soil in a state of stress whose Mohr circle intersects the Mohr envelope for that soil. Any attempt to impose such a state of stress would result in unlimited strains (i.e. the soil would flow freely).

The Mohr envelope for a given soil can be measured by locating the point of failure for two different stress conditions, such as those illustrated in figure 5. A line tangent to the Mohr circles which describe these two states of stress defines the Mohr envelope for that soil.

The Mohr - Coulomb failure law is significantly different from the stress / strain models used in solid body mechanics, such as the Tresca and von Mises yield criteria. The most important difference is that for solid bodies, only the deviatoric component of the total stress can cause plastic strains, whereas in particulate bodies, both the deviatoric and hydrostatic components can cause deformation of the overall body by rearrangement of the individual particles.

Although a useful first step towards understanding the stress / strain behavior of particulate materials, a primary deficiency of the Mohr - Coulomb failure law is that it can only be used to predict at what stress levels a particulate mass will fail, and ignores the subsequent effects of failure on the packing density of the soil or powder. A modified version of the Mohr - Coulomb failure law is presented as the Jenike yield locus theory. Similar to the Mohr envelope, a Jenike yield locus is constructed on a plot of shear stress versus normal stress, as shown in figure 6. The yield locus is curved, as this was stated to be a more accurate representation of the yield criterion over a large range of normal stresses. Similar to the Mohr envelope, failure is predicted to occur in the powder mass when the Mohr circle representing the state of stress crosses the yield locus. In the Jenike theory, however, the yield locus drawn in figure 6 is stated to apply only to powder with an initial packing density of $\emptyset = \emptyset_1$. Multiple yield loci which correspond to different values of initial packing density exist for single powder. An illustration of multiple yield loci is given in figure 7.

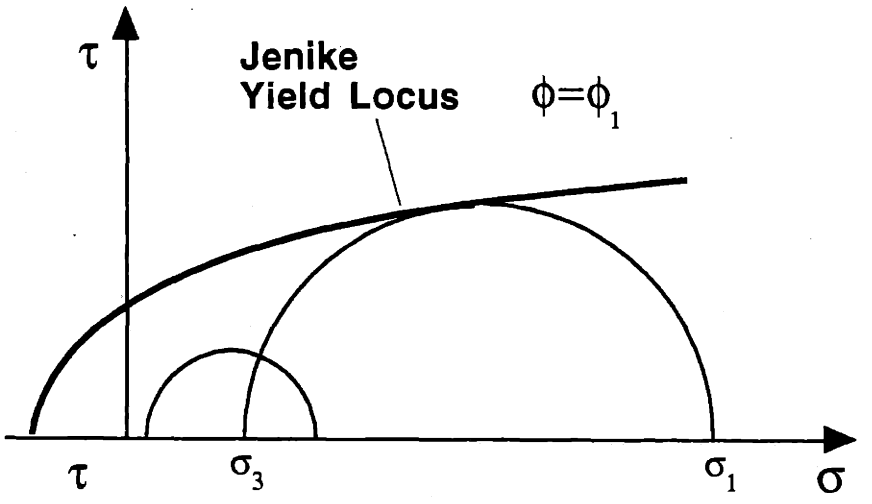

Figure 6: Illustration of a Jenike yield locus for a powder with an initial packing density of $\emptyset = \emptyset_1$.

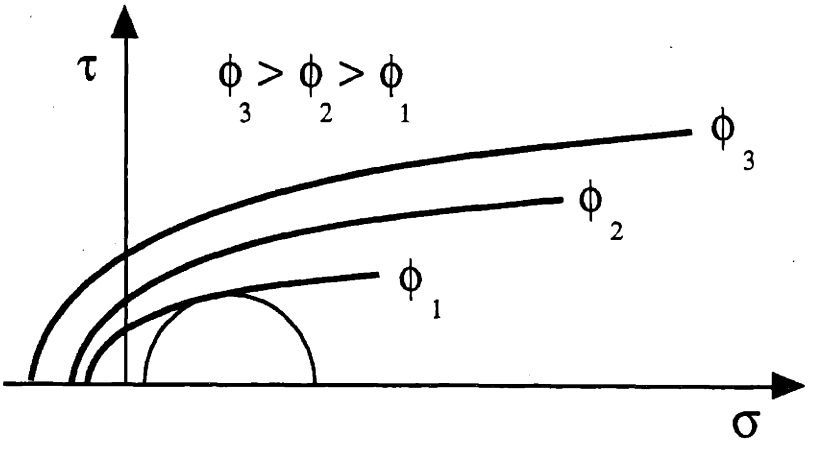

Figure 7: Illustration of three yield loci, each representing the yield condition for different values of initial packing density in a power mass.

A further modification of the Jenike yield locus theory over the Mohr - Coulomb failure law is its ability to predict how the packing density of a powder will change at the moment of failure. An extension of the yield locus, called the consolidation locus, is shown in figure 8. The Jenike theory predicts that if the Mohr circle representing the state of stress in the powder mass crosses the yield locus, then the powder will dilate (i.e. its packing density will drop) at the moment of failure. Furthermore, if the state of stress crosses the consolidation locus, then powder packing density will increase at the moment of failure.

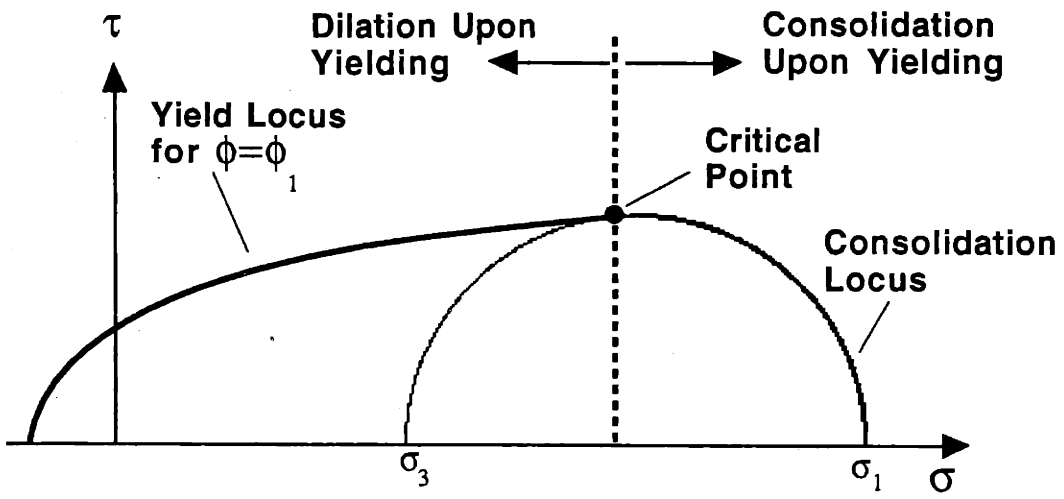

Figure 8: The Jenike yield and consolidation loci for a single powder packing density.

The Mohr - Coulomb and Jenike theories are powerful tools for predicting how a powder mass will behave when loaded. Both provide a conceptual understanding about how the combination of shear and normal stresses which act on any plane through a powder mass directly determine when powder along that plane will begin to flow. For any given powder, however, the actual Mohr envelope or the many Jenike yield and consolidation loci must be determine experimentally.

The above theoretical discussion has been limited to the area of *powder statics*, or how powders respond to non-oscillatory loadings. It is well known, however, that the presence of an oscillatory component in the stress distribution applied to a powder mass can significantly affect the packing behavior. Studies of these vibratory response phenomena are described in the field of *powder dynamics*, and are considerably more complex than powder statics. A list of those variables which have been identified as being influential during the vibratory compaction of a particulate material is given in table 2.

Table 2: Variables Involved in Vibratory Compacting

1. Characteristics of the Powder Density of Powdered Material Average Particle Size Particle Size Distribution Particle Shape Particle Surface Conditions Adhesion Forces Between Particles Total Weight of Powder	**2. Characteristics of the Vibrations** Frequency of Vibration Amplitude of Vibration Duration Of Vibration Direction of Applied Vibration Number of Vibrators Applied
3. Characteristics of the Container Shape, Size and Wall Thickness Container Material	**4. Characterization of Processing** Humidity Temperature Pressure Applied

After completion of the literature review, effort was directed towards measuring the performance of the then-current printing process. This characterization is described below.

Characterization of the Baseline Printing Capabilities

Using a baseline printing process in which the original spreader rod was used to strike each powder layer, monomodal and bimodal printed parts were produced to serve as a benchmark for future comparison. These parts were found to have green densities far below the tap densities of the powders used, indicating that the spreader rod was far from an ideal layer densification mechanism. Green density results for two bimodal powders, printed both with and without spreader rod vibration, are given in table 3.

Table 3: Green Density Results for Printed Bimodal Samples

Measurement Parameter	120/20μm no vibration	120/20μm vibration	71/9μm no vibration	71/9μm vibration
Average Packing Density	62.7%	64.0%	62.3%	65.0%

Representative microstructures from the 120/20μm and 71/9μm bimodal test bars are shown in figures 9 and 10 below. Significant layer packing defects are visible in the 71/9μm sample.

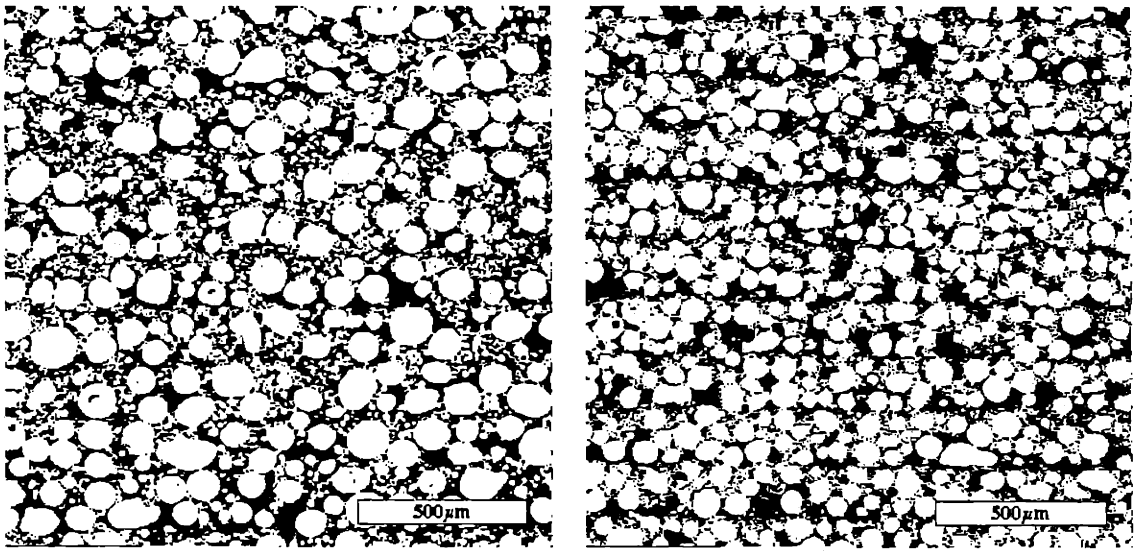

Figures 9 and 10: Microstructures of the 120/20μm (left) and 71/9μm printed bimodal baseline samples. Magnification 50x. No vibration.

The baseline spreading process was also analyzed to determine if it was causing segregation of the bimodal components during layer generation. Segregation was to be avoided, since it would cause anisotropic sintering behavior in the printed parts. Tests were conducted in which the local bimodal composition was measured at 5mm intervals in the direction of spreading. Tests were performed on the 120/20μm and 71/9μm bimodal mixtures, both with and without spreader rod vibration. Other than the expected statistical variation in composition data, no indication of bimodal segregation was found over 15cm of spreading distance. Figure 11 is a plot of composition versus spread distance for the 120/20μm powder.

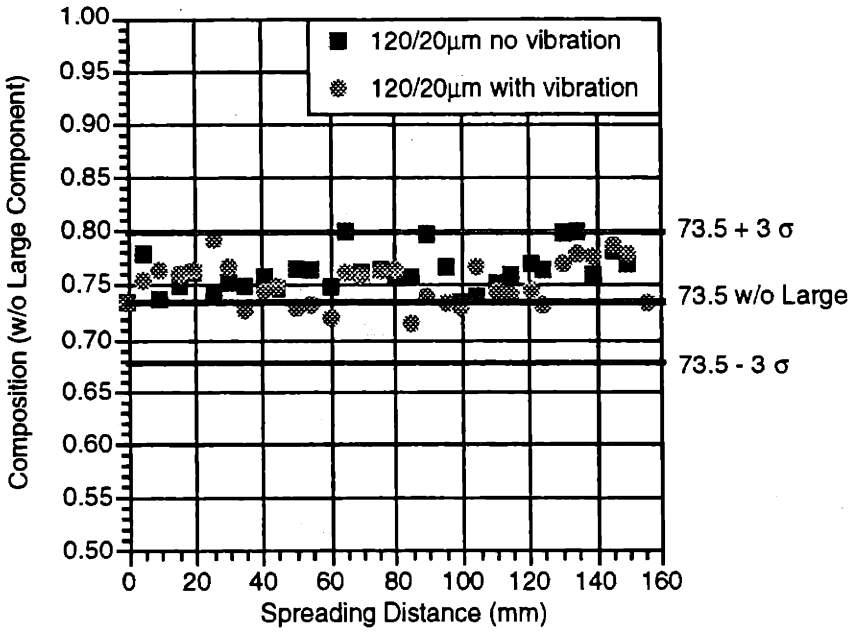

Figure 11: Localized composition vs. spread distance for the 120/20μm bimodal powder mixture.

Experimental Investigation of Powder Densification Behavior

Shear Cell Tests

A variety of tests were performed on the metal powders to study their response to different stress input conditions. The goal of these tests was to determine the optimal stress condition for the densification of a metal powder layer, so that this information could later be used in the design of a new layer densification device.

The first set of powder densification tests utilized a specially constructed shear cell. A schematic illustration of a shear cell is shown in figure 12. The shear cell apparatus consists of a shallow cylindrical cell split horizontally. A sample of powdered material under examination is placed in the cell prior to the test. The lower half of the cell is fixed and a constant low shear displacement rate is applied to the movable upper half. The resultant shear force is continuously recorded during each run. A number of normal loads are applied so that the relationship between shear stress and normal stress can be determined.

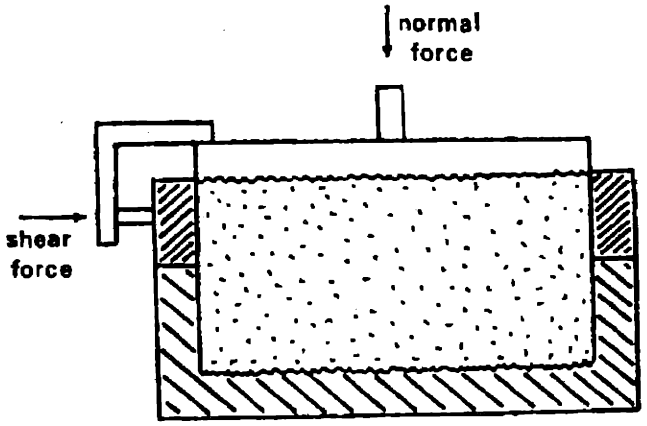

Figure 12: A shear cell.

Many shear cell tests were performed with different powders and stress conditions. For all the tests performed, the shear cell was initially filled to the tap density prior to the beginning of shearing. In addition to performing "standard" tests in which both the applied normal and shear stresses were non-oscillatory, two other categories of shear cell tests were performed. In the first category, an oscillatory stress component was superimposed over the applied normal stress, while in the second category, an oscillatory stress component was superimposed over the applied shear stress. These vibratory tests were performed to observe the effect vibratory excitation on the shearing behavior of the metal powders.

All the individual shear cell test run results had a distinctive shape which is illustrated in figure 13. The measured shear stress went through a peak value at the moment that failure occurred along the shear plane, and then decreased to a near-constant value once continuous sliding had begun. The peak and sliding shear stress values are labels as points *A* and *B* below.

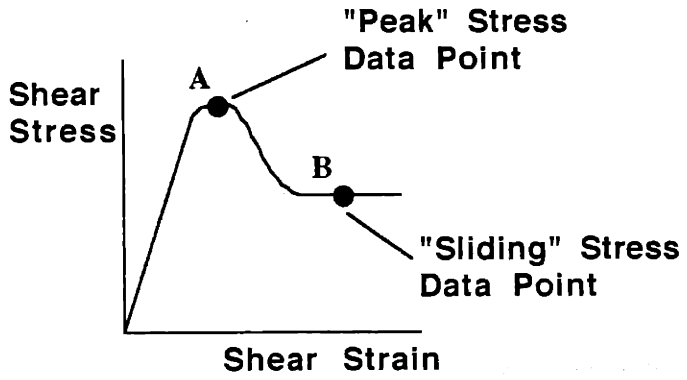

Figure 13: Shear stress vs. shear strain for a single shear cell run.

Results from the non-oscillatory shear cell tests are shown in figure 14. Five different powders were tested. The peak stress data points are plotted in the left-hand graph, and the sliding stress data points are plotted in the right-hand graph.

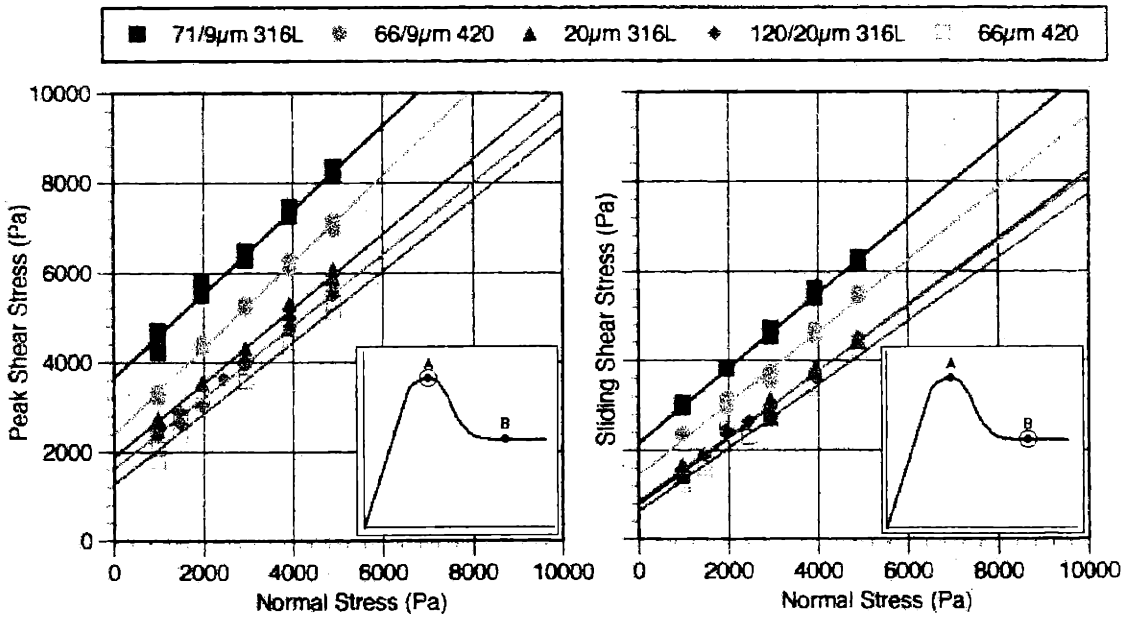

Figure 14: Peak shear stress (left) and sliding shear stress (right) vs. normal stress for five different powders.

The highly linear relationship between the applied normal stress and both peak and sliding shear stresses shown in figure 14 suggested a possible interpretation of these shear cell results. The most basic model of frictional resistance between two solid, flat surfaces

relates the normal and shear forces applied to the surfaces with the static and kinetic coefficients of friction. These coefficients are μ_s and μ_k, respectively. Referring to figure 15, the shear force τ_s required to initiate sliding between two solid surfaces is given by the expression

$$\tau_s = \mu_s \sigma, \qquad \text{(eq. 2)}$$

and the shear force τ_k required to maintain sliding between two solid surfaces is given by the expression

$$\tau_k = \mu_k \sigma. \qquad \text{(eq. 3)}$$

In general, it is the case that $\mu_k < \mu_s$, indicating that, for a given normal stress, it is easier to maintain sliding than it is to initiate it.

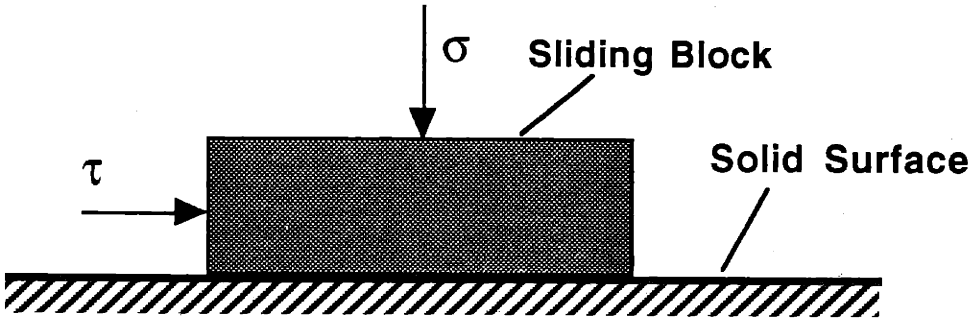

Figure 15: Illustration of a blocking sliding on a solid surface.

The observed shear cell behavior for both the peak and sliding conditions can be described by two relations which are analogous to equations 2 and 3. For the peak results, the relation has the form

$$\tau_p = \sigma \tan(\theta_p) + c_p, \qquad \text{(eq. 4)}$$

where θ_p is the angle of internal friction for the powder at the onset of failure from the tap density, and c_p is the shear axis intercept which defines the powder cohesion at the onset of failure from the tap density. Similarly, for the sliding results, the relation has the form

$$\tau_s = \sigma \tan(\theta_s) + c_s, \qquad \text{(eq. 5)}$$

where θ_s is the angle of internal friction for the powder during continuous sliding, and c_s is the shear axis intercept which defines the powder cohesion during sliding.

If the powder cohesion c is ignored, then the angle of internal friction θ for a given powder can be expressed in the same "terms" as the coefficient of friction μ for sliding solid surfaces by using the relationship

$$\tan(\theta) = \mu. \qquad \text{(eq. 6)}$$

Figure 16 is an illustration of how the observed failure and sliding behavior along the shear plane is analogous to the sliding behavior of solid surfaces.

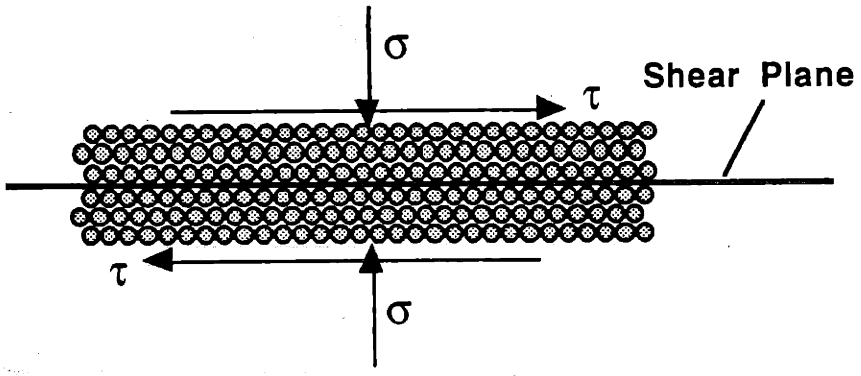

Figure 16: Illustration of how the observed failure and sliding behavior along the shear plane is analogous to the sliding behavior of solid surfaces.

Figure 17 is a graph of the peak and sliding angles of internal friction for the non-oscillatory shear cell tests, which were obtained by measuring the slopes of the data in figure 14. In all cases, θ_p was greater that θ_s.

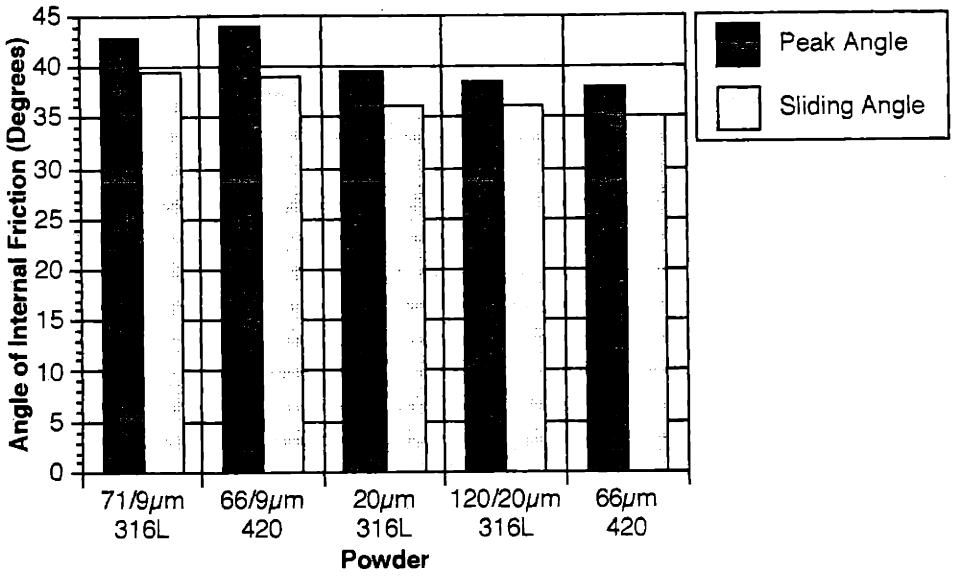

Figure 17: Peak and sliding angles of internal friction for the non-oscillatory shear cell tests. Data shown for five different powders.

Figure 18 is a graph of the peak and sliding angles of internal friction for the 120/20μm bimodal powder with an oscillatory normal stress of +/- 500Pa superimposed. Excitation frequencies between 47 and 520Hz were used. As the excitation frequency was increased, the values of θ_p and θ_s decreased, indicating that it became progressively easier to both initiate and maintain sliding along the failure plane. Similar results were obtained for the other powders tested.

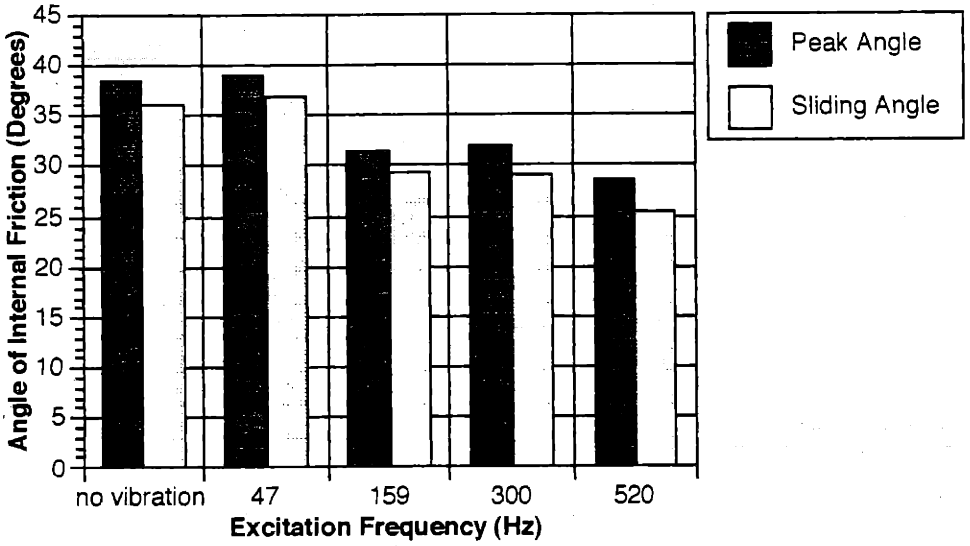

Figure 18: Peak and sliding angles of internal friction for 120/20μm bimodal powder with an oscillatory normal stress of +/- 500Pa superimposed.

Figure 19 is a graph of the peak and sliding angles of internal friction for the 120/20μm bimodal powder with an oscillatory shear stress of +/- 200Pa superimposed. Excitation frequencies between 189 and 560Hz were used. Again, as the excitation frequency was increased, the values of θ_p and θ_s decreased, but even more dramatically than in the previous case of the superimposed oscillatory normal stress.

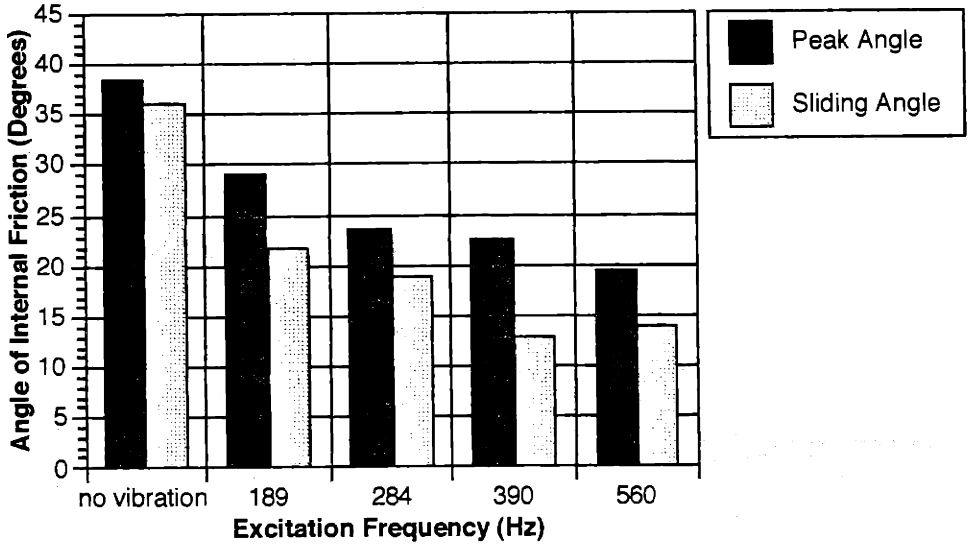

Figure 19: Peak and sliding angles of internal friction for the 120/20μm Bimodal Powder with an oscillatory shear stress of +/- 200Pa superimposed.

The results from the shear cell tests indicated that the shearing behavior for the metal powders was similar to the frictional sliding behavior of solid surfaces. Addition of an oscillatory stress component during shearing lowered both the peak and sliding shear stress values. Oscillation along the shearing plane was found to be the most effective means of lowering shear stress levels, both at failure and during sliding. Also, higher oscillatory frequencies and amplitudes were more effective at reducing shear stress levels. The proposed explanation for why vibration was effective in lowering the shear stress levels was that the vibration of the particles along the shear plane reduced the effects of particle interlocking, making it easier for particles to roll and slide past one another.

Layer Densification Tests

The shear cell tests produced important insights into powder behavior, but did not provide any data about how powder packing density along the shear plane changed over time. To obtain more information about the relationship between applied stresses and changes in packing density, a second set of tests was performed. In these tests, a single layer of powder, 3.1mm in thickness, was compressed with a rectangular pressure plate. This pressure plate could apply static and oscillatory vertical loads, and could also be vibrated horizontally to induce shear loads on the top surface of the powder layer. Measurement of the vertical displacement of the pressure plate into the powder layer directly correlated to changes in packing density for the powder under the plate, as long as significant amounts of powder were not ejected from underneath. The testing concept is illustrated in figure 20.

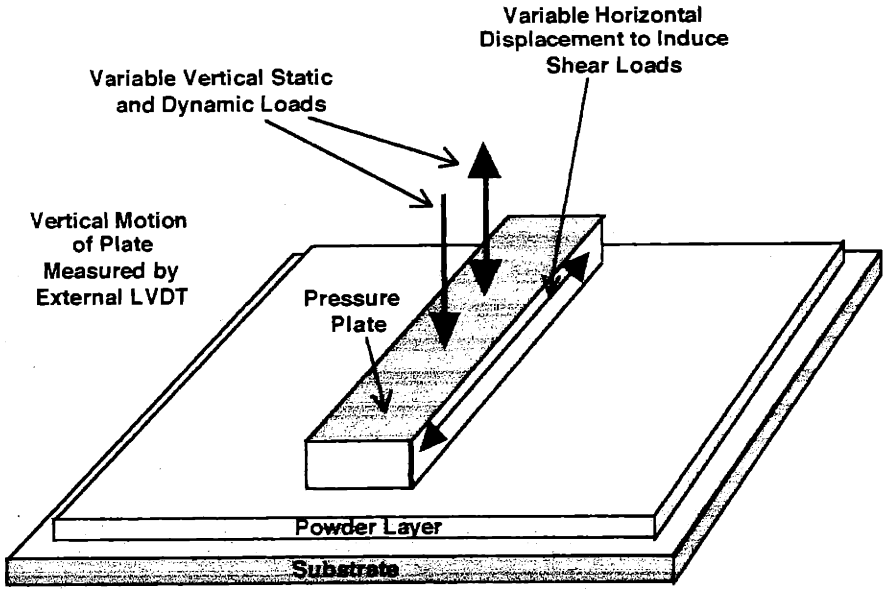

Figure 20: A schematic drawing of the layer densification tests.

Figure 21 shows the results from tests using a combination of static and oscillatory vertical stresses. The applied vertical stress condition was 2000 +/- 2000Pa, and excitation frequencies between 52 and 300Hz were tested. The results are for the 71/9μm powder .

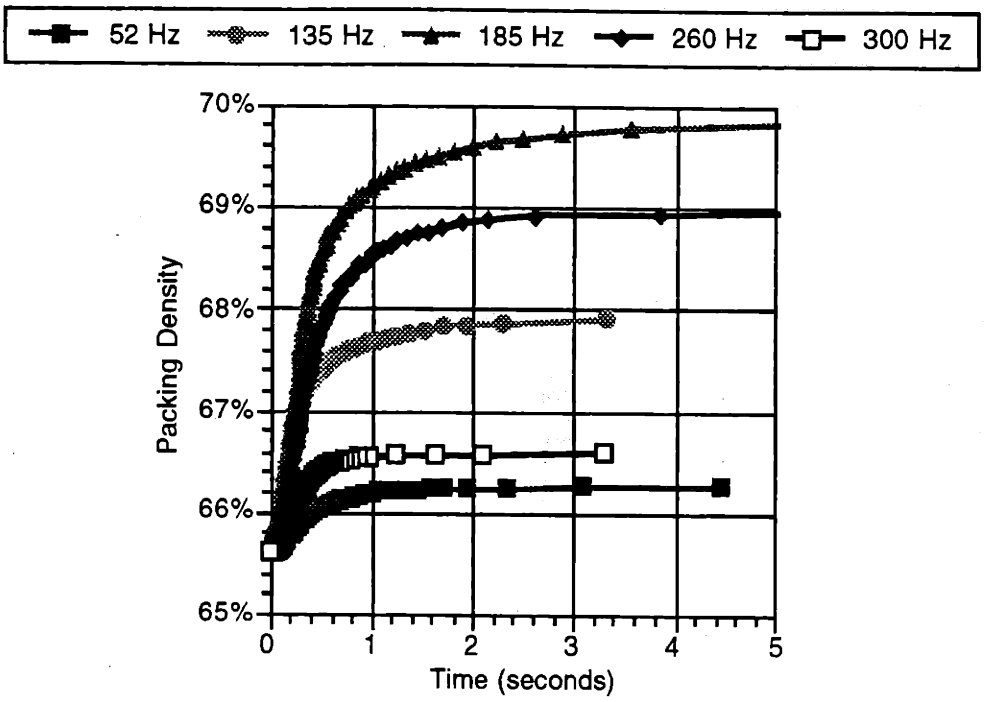

Figure 21: Effect of frequency on densification behavior. 71/9μm powder. Vertical stress condition of 2000 +/- 2000Pa.

Figure 22 shows the results from tests using a combination of a static vertical stress and a oscillatory horizontal shearing stress. Again, the results are for the 71/9μm powder. Gray regions of the graph are areas in which packing density measurement error occurred due to ejection of powder from underneath the plate. The applied vertical stress was fixed at 1000Pa. The horizontal peak-to-peak displacement was fixed at 100μm, except at the higher frequencies. The excitation frequency was varied between 86 and 400Hz.

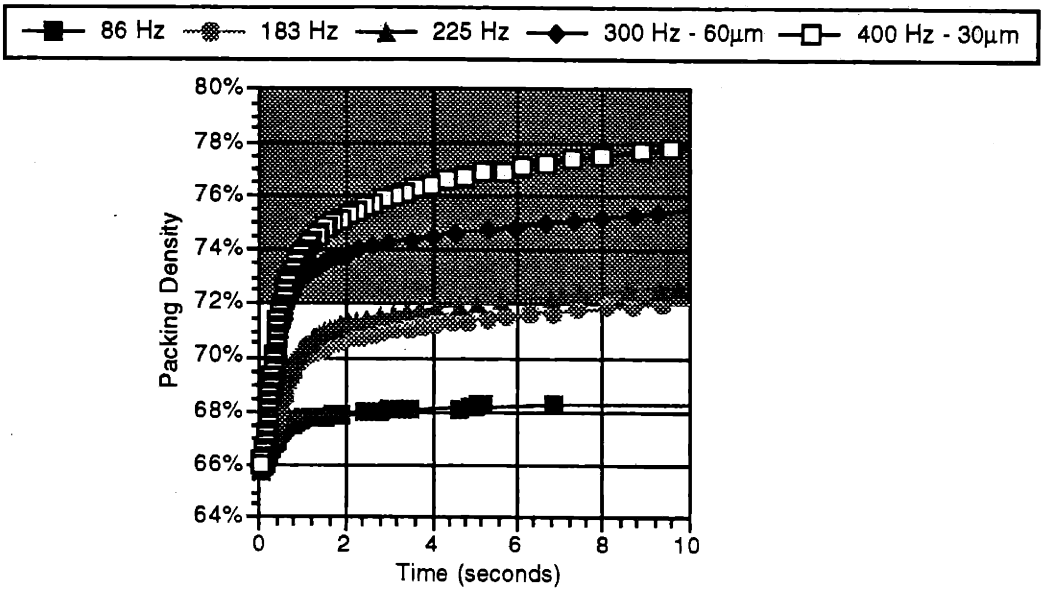

Figure 22: Effect of horizontal shear frequency on densification behavior. 71/9µm powder. 100µm peak-to-peak horizontal displacement (unless otherwise noted). 1000Pa static vertical stress.

From the earlier shear cell tests, it was expected that higher excitation frequencies would result in higher ultimate packing densities, due to reduced particle interlocking and enhanced particle mobility. This frequency dependency was indeed observed in the horizontal oscillation tests, but not in the vertical oscillation tests.

The results from the layer densification tests indicated that an oscillatory shear stress, combined with a small confining normal stress, generated the best densification results. The higher shear excitation frequencies were more effective at destabilizing the pore structures within the powder layer, thereby resulting in greater densification. Also, it was observed that most densification occurred in the first two seconds of excitation

Packing Propagation Tests

A final set of powder packing experiments was performed with the goal of determining how changes in packing density propagated from powder regions immediately adjacent to the pressure plate to regions further away. For each of these tests, a ceramic boat with internal dimensions of 1.5cm x 5cm x 10cm was filled with the 71/9µm powder. After filling, the average packing density in the boat was approximately 66%. Using the pressure plate apparatus from the previous layer densification tests, a strip of powder in the

top center of the boat was densified. Vibration was applied for 30 seconds to ensure that the packing limit had been reached in each case. Different variations of vertical stress and horizontal shear displacement were tried. Figure 23 is an illustration of the densification technique.

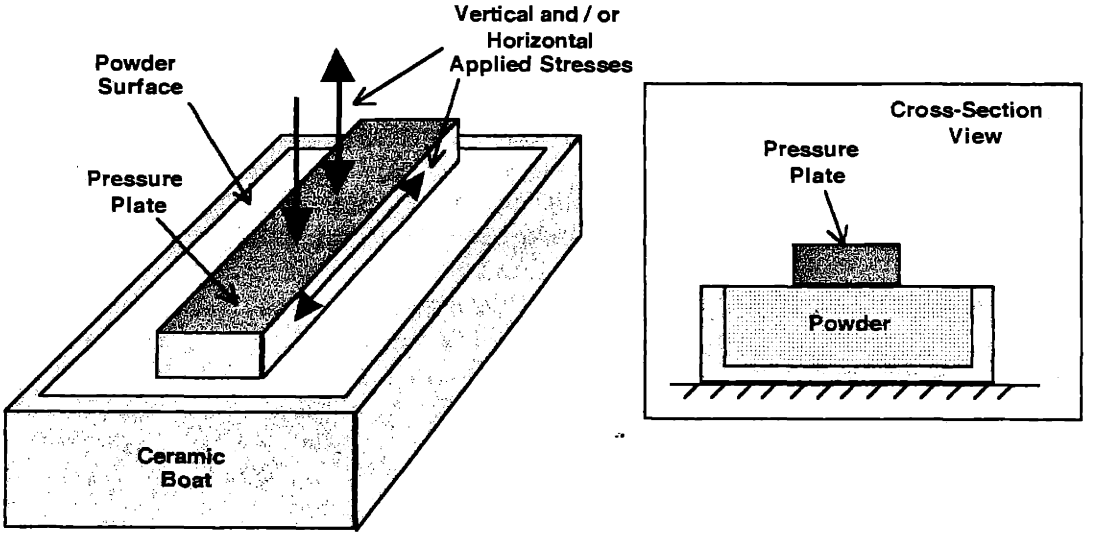

Figure 23: An illustration of how the packing density propagation samples were produced.

Figure 24 is a packing density map for the region of powder below the pressure plate. This map was generated for an applied stress condition of 500Pa vertical static stress and 300Hz, 60μm horizontal shearing oscillation. The bottom of the pressure plate was roughened to increase the level of transmitted shear forces.

Highest packing was concentrated to a region directly beneath the plate, and attained values near the tap density of the powder. The attenuation of shear stress with increasing distance from the pressure plate was believed to be the cause of the stratified packing density values near the bottom of the plate.

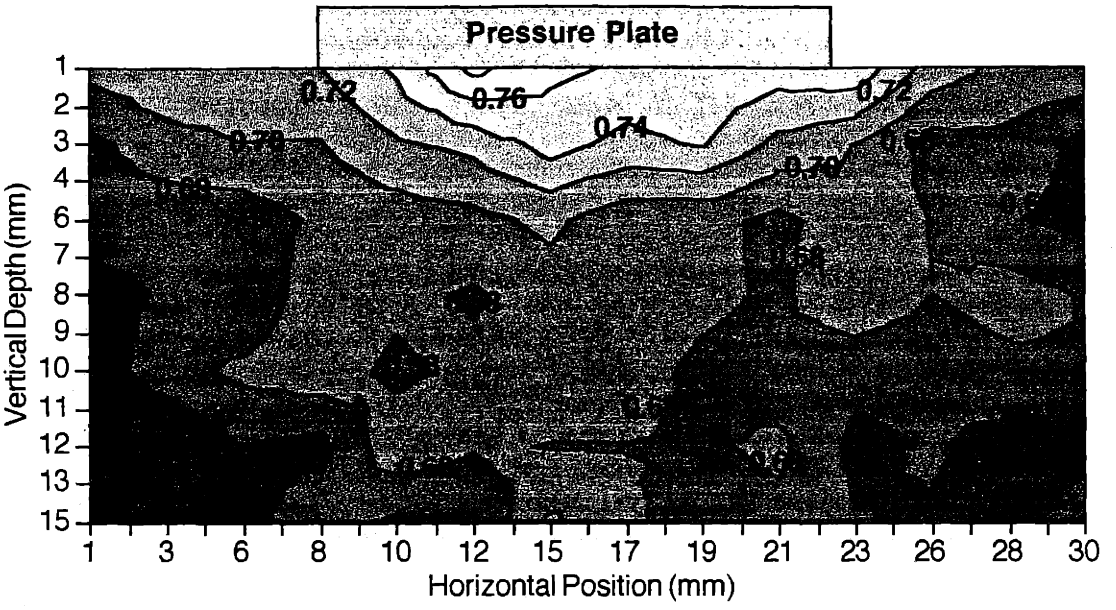

Figure 24: Packing density map for the condition of 500Pa vertical static stress and 300Hz, 60μm horizontal shearing oscillation. Rough surface pressure plate. 71/9μm powder. Vibration was applied for 30 seconds.

The conclusions drawn from the packing propagation tests were as follows:

1. For vibrational densification conditions similar to those used in the earlier layer densification tests, significant densification occurs at distances of 4 to 6mm from the pressure plate. Since a typical layer thickness in 3DP is 175μm, complete layer densification should not be an issue.

2. Horizontal shearing vibration, in the presence of a small static vertical stress, was again observed to be the preferred method for powder layer densification.

Design of a New Layer Densification Mechanism

Based on the results from the shear cell and layer densification tests, a preliminary design for a new layer densification mechanism was proposed. This design is illustrated in figure 25. The design consisted of a counter-rotating spreader rod used in tandem with a horizontally oscillating wedge. The non-vibrating spreader rod was used to strike an extra-thick prelayer, which the horizontally oscillating metal wedge would then densify. The wedge would also apply a controlled normal stress to the powder layer during

densification. The velocity of the wedge across the powder surface was chosen so that any strip of powder would receive a minimum of 2 seconds of vibrational excitation.

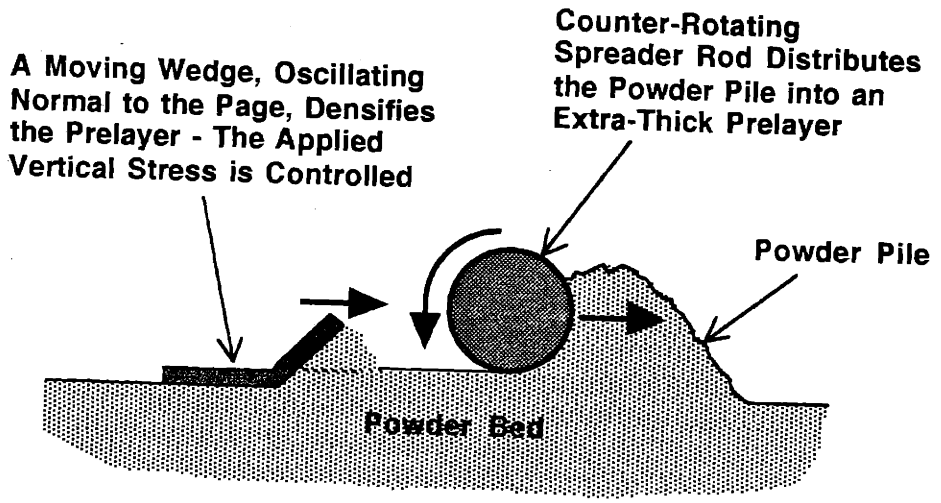

Figure 25: Illustration of the proposed layer densification mechanism.

Printing Evaluation

Initial printing attempts with the new layer densification device were unsuccessful because the oscillating wedge could not strike a uniform final layer thickness. As the wedge was swept across the prelayer surface, it would slowly dig in, pushing excess powder out in front of it. This effect occurred for all values of normal stress and horizontal excitation frequency which were tried, and prevented the printed of test bars. This digging effect is illustrated in figure 26.

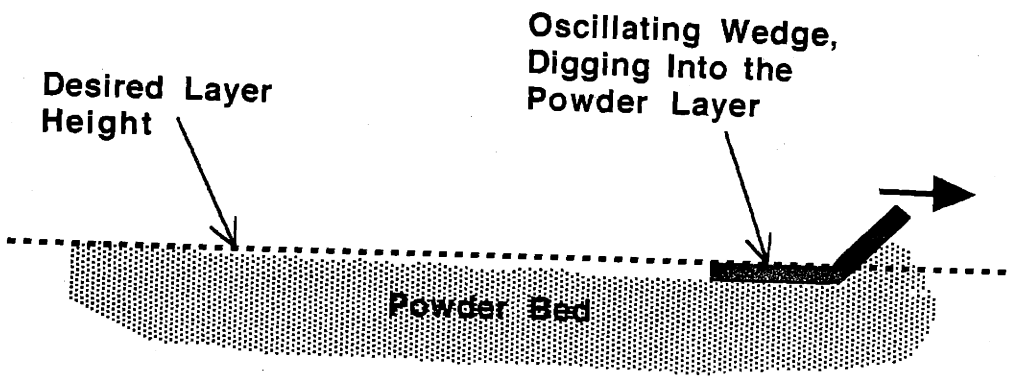

Figure 26: Illustration of how the oscillating wedge created a non-uniform layer.

A modified printing sequence was developed which allowed the use of a controlled normal stress in combination with an oscillatory shearing motion in order to densify the powder layer. This modified printing sequence is illustrated in figure 27. An extra-thick prelayer was again spread using the spreader rod. A single region of the prelayer was then densified by lowering the pressure plate into it and activating the vibrational excitation for two seconds. The plate was removed, and a single test bar was printed into the densified region.

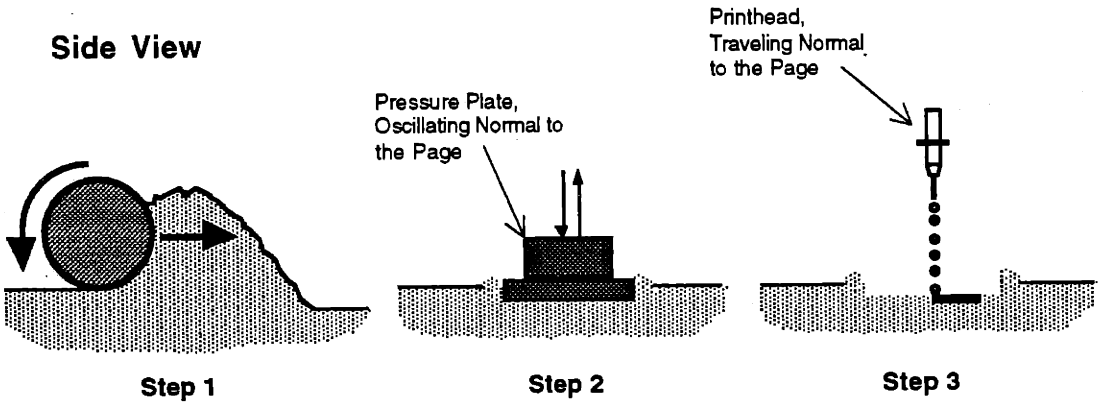

Figure 27: The modified printing sequence.

Using the modified printing sequence, printed densities near the tap density were obtained for all powders except the 120/20μm bimodal mixture. Printing results are given in table 4. In the case of the 120/20μm powder, it was believed that the low packing densities resulted from dilation of the densified layer during removal of the pressure plate. This dilation occurred due to a slight adhesion between the powder layer and plate surfaces.

Table 4: Printing Results Using the Modified Pressure Plate Layer Densification Approach.

Powder	Vibrational Frequency (Hz)	Vibrational Amplitude (μm)	Static Stress (Pa)	Packing Density
71/9μm 316L	120	200	500	74.7%
	320	20	500	73.4%
	320	20	2500	75.8%
66/9μm 420	120	200	500	73.0%
	320	20	500	75.8%
	320	20	2500	73.8%
120/20μm 316L	120	200	500	64.3%
	320	20	500	66.2%
20μm 316L	320	20	500	60.6%

Microstructures of 71/9μm bimodal test bars printed with the conventional spreader rod and the pressure plate apparatus are shown in figures 28 and 29. Although the bimodal bar printed with the pressure was near the tap density of the powder, obvious layer defects still occurred. The layer defects were a result of the exclusion of large particles from the inter-layer regions.

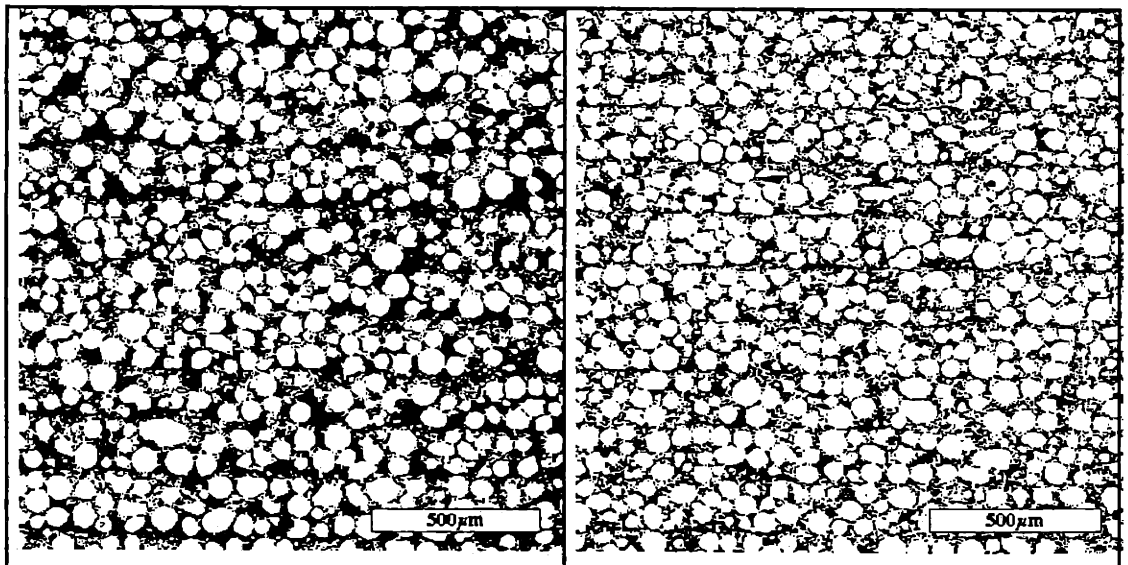

Densified with the Conventional Spreader Rod

Densified with Pressure Plate 320Hz Excitation / 20μm Amplitude and 2500Pa Normal Stress.

Figures 28 and 29: Microstructures of test bars printed with the conventional spreader rod (left) and the pressure plate apparatus (right). 71/9μm powder.

The initial design of the oscillating wedge concept failed to perform adequately because it could not strike a uniform layer thickness. By fixing the vertical height of the wedge, the generation of a uniform layer would be guaranteed. In fixing the height, however, the resultant vertical stress would then become uncontrolled, making this approach fundamentally different from all previous densification concepts. Many new unknowns enter into a fixed-height design, such as how the specific shape of the powder wedge affected the resultant vertical stress levels.

A preliminary evaluation of a fixed-height, horizontally oscillating wedge design (renamed below as the shear sled concept) was performed as the final set of testing in this thesis. It was believed that, based on the previous layer densification results, the shear sled would densify the powder layer in a similar fashion to the pressure plate. In both cases, the powder particles in the layer would be subjected to an oscillatory horizontal shearing motion which should encourage densification. Also in both cases, a confining vertical stress would be present, except that in the case of the shear sled the magnitude of this vertical stress would not be known.

A single shear sled geometry was evaluated, and only the horizontal shear frequency and amplitude were measured. As a further simplification of the layer generation apparatus, the spreader rod was no longer used to strike the extra-thick prelayer prior to densification. Instead, the shear sled was used to both distribute the powder pile and densify the powder layer simultaneously. This testing was intended to be a "proof of concept" for the shear sled design. The shear sled design is illustrated in figure 30.

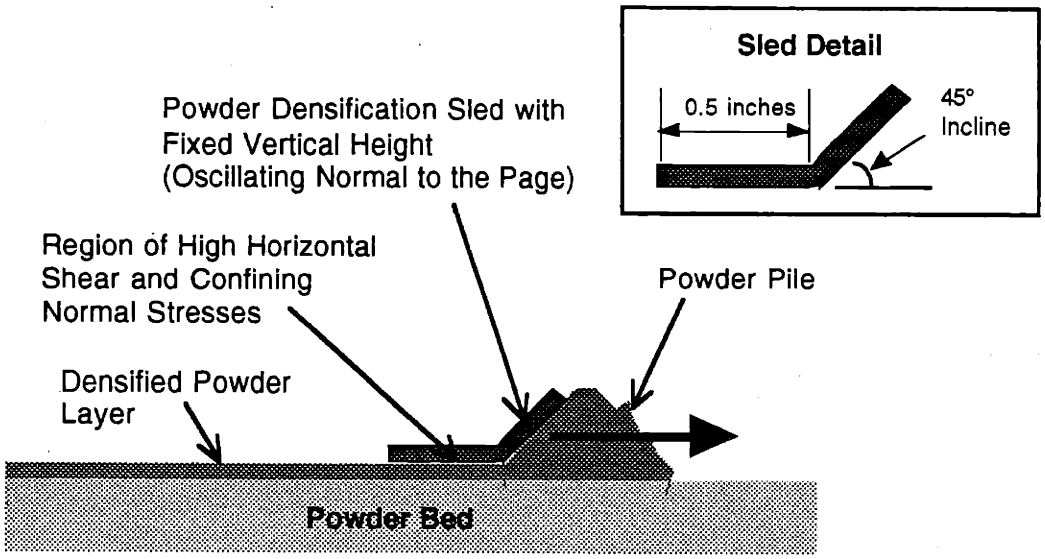

Figure 30: A prototype shear sled.

Printing results using the shear sled design are given in table 5. Even using non-optimized vibrational parameters, packing densities near the tap densities of the powder tested were obtained. Also, bars printed with 30μm platelet alumina show increased green density compared to those printed with the conventional spreader rod apparatus. This demonstrated the applicability of the shear sled mechanism to non-spherical powders.

Table 5: Printing Results Using the Prototype Shear Sled Layer Densification Mechanism.

Powder	Vibrational Frequency (Hz)	Vibrational Amplitude (μm)	Packing Density
71/9μm 316L	120	200	76.8%
66/9μm 420	320	20	73.4%
120/20μm 316L	320	20	70.8%
20μm 316L	320	20	60.6%
30μm alumina	320	20	38.9%

Conclusions

The central goal of this research, which was to produce a printed metal part with a green density between 75 - 80%, was reached. The use of bimodal powder mixtures was

critical in reaching this goal. Improvements in part packing uniformity and homogeneity were obtained, in both monomodal and bimodal parts. The large layer defects present in parts printed with fine, monomodal powders were eliminated in both the metal and ceramic material systems. The increased green density should have a profound effect on the properties of the fully post-processed parts, moving them that much closer to those required by the industrial users of injection molding tooling.

Powder testing equipment and procedures were developed to evaluate densification phenomena. Shear cell tests revealed that powder flow along the failure plane was analogous to the frictional behavior of solid sliding surfaces. It was observed that the addition of a vibratory stress component had a significant effect on enhancing particle mobility and reducing the overall stress levels required for particle rearrangement.

A new layer densification mechanism was developed which improved part green density and packing uniformity not only in metal, but also ceramic parts. This mechanism provided a horizontal oscillatory shear stress in combination with a confining normal stress in order to achieve layer packing levels near the tap density. The mechanism also supplied vibrational energy for a sufficient time to ensure that the maximum packing level was reached.

Chapter 1. Introduction

1.0 The 3DP Process

Three Dimensional Printing (3DP) is a manufacturing process used for the rapid fabrication of three-dimensional parts directly from computer models. [53] 3DP is one of several rapid prototyping techniques which fall under the more general heading of Solid Freeform Fabrication (SFF). A unique feature of all SFF process is that they are additive, with part geometries being generated by the selective addition of material throughout a 3D workspace. [31] This is in contrast to other manufacturing process such as machining and turning, which are subtractive processes.

In the 3DP process, a solid object is created by printing a sequence of two-dimensional layers. The creation of each layer involves the spreading of a thin layer of powdered material followed by the selective joining of powder in the layer by ink-jet printing of a binder material. A continuous-jet printhead is raster scanned over each layer of powder using a computer controlled x-y table. Individual lines are stitched together to form 2D layers, and the layers are stitched together to form a 3D part. The powder bed is lowered at the completion of each layer by lowering the bottom of the rectangular cylinder which contains the bed. Unbound powder temporarily supports unconnected portions of the component, allowing overhangs, undercuts and internal cavities to be created. The unbound powder is removed upon process completion, leaving the finished part. Commands to modulate the binder stream are derived from CAD data. The 3D Printing process sequence is shown in figure 1.1. The architecture of the 3D Printing machine is optimized for high build rate, high part quality and flexibility. The continuous-jet printhead can deliver a variety of binder materials at high flowrates and with very high precision. Multiple nozzle printheads provide for high build rate and the option of printing multiple materials. The raster scan design provides high printing speeds, accuracy, and is easily scaleable.

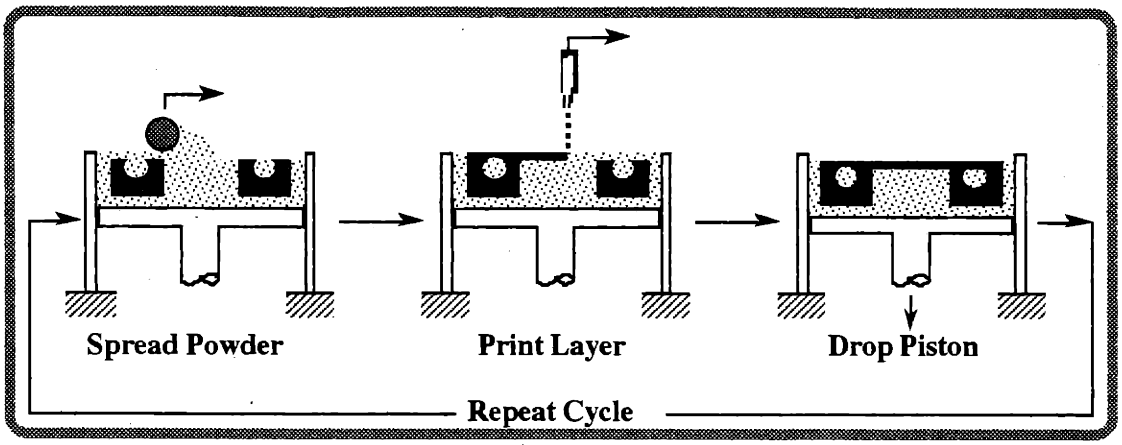

Figure 1.1: The 3D Printing sequence.

1.0.1 Material System Flexibility

An important aspect of the 3D Printing process is its inherent flexibility with respect to material systems. The 3DP machine is a processing engine which takes the raw material inputs of powder and binder and transforms them into a three dimensional printed part. The printed part is a composite of the powder and binder used during printing. All printed parts typically require a post-processing operation in order to transform them into a usable final condition. This usually entails a furnace processing step, in which then powder particles are fused or sintered together. Figure 1.2 is an illustration of the 3DP transformation process.

3D Printing was initially developed for the production of ceramic shells and cores to be later used for the casting of metal parts. In this embodiment of the process, alumina powder is spread into the powder piston and selectively bound using colloidal silica as a binder. After completion of printing, the part is fired in a furnace to further bond the silica to the alumina and strengthen the part sufficiently so that it can be used as a ceramic mold. Although initially developed around alumina powder and silica binder, there were no fundamental restrictions to the type of powder and binder which could be used in the 3DP process. Any material which can be attained in powdered form - which is almost every material - should, in principle, be usable in the process. Binder selection for a given powder is determined by the specific method of post-processing which is utilized to finish the part.

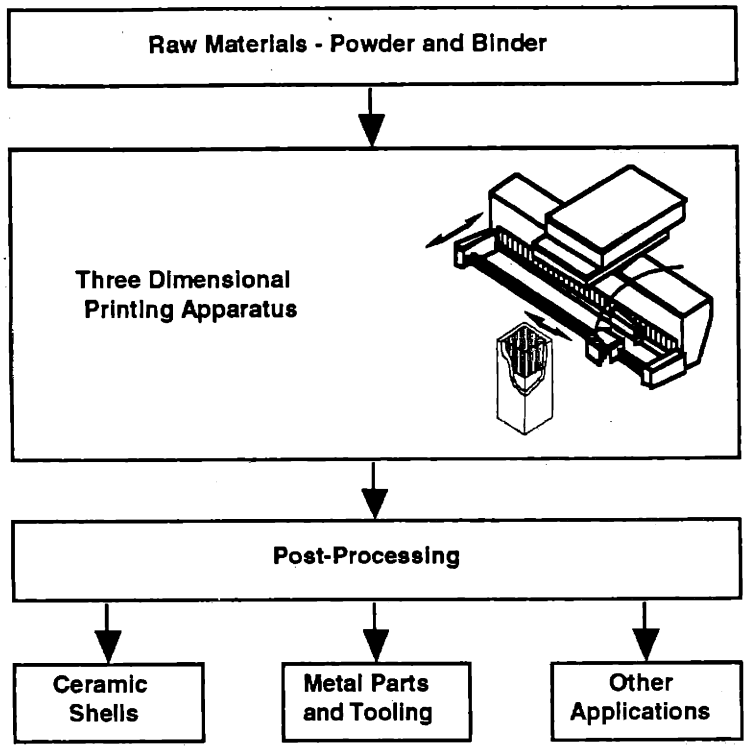

Figure 1.2: The 3DP transformation process.

The second major material system which was adapted to the 3DP process used metal powder and polymeric binder as the raw material inputs. The printed part was a metal powder / polymer composite with properties similar to those of parts produced by the powder injection molding (PIM) process used in the powder metallurgy (P/M) industry. [36, 37] An example of a 316L stainless steel powder used in the initial metal printing process is shown in figure 1.3. Interparticle polymer bonds which were formed during the printing process are shown in figure 1.4.

After printing, the metal / polymer "green" part is removed from the powder bed. The part is then fired in an inert atmosphere furnace. During the first stage of furnace processing, the polymer binder is removed by thermal decomposition at temperatures around 500°C. Furnace temperature is then further increased to between 1200 - 1400°C in order to sinter the powder particles together.

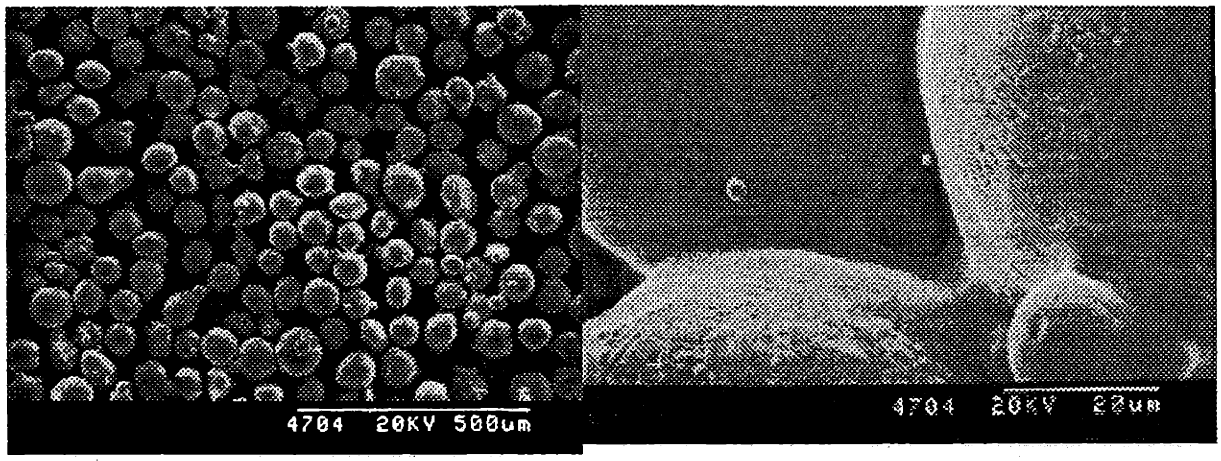

Figure 1.3 and 1.4: A 316L stainless steel powder used in early metal part printing (left) and the polymer bonds which formed between particles during printing (right).

Post-processing of metal and ceramic parts differs in two fundamental ways. First, the alumina / silica parts are fired while they were still in the powder bed, while the metal / polymer parts are removed from the bed prior to firing. In the alumina / silica system, maximum furnace temperatures of approximately 900°C are used to reflow the silica and strengthen the printed regions of the bed. This firing temperature is far below the sintering temperature of the alumina powder, so the silica-free regions of the bed remain unbonded. After firing, the can therefore be removed from the bed, since unprinted regions still consist of loose powder. In contrast, metal parts need to be removed from the powder bed prior to firing. Otherwise, the entire bed will become sintered together, thereby "trapping" the printed part inside.

The second post-processing difference related to the presence of binder in the finished part. The colloidal silica binder used in the alumina / silica system is a "permanent" binder, since it remained inside the printed part throughout post-processing. In contrast, the polymer binder in the metal powder / polymer parts is a "temporary" binder, since it is removed during post-processing. Final part strength in metal parts is determined by the metallurgical bonds formed between particles during sintering.

1.0.2 Full Density Processing Options

In order to have material properties comparable with those of metal parts produced with conventional manufacturing processes, post-processing of the green metal parts needs

to remove all the internal porosity, transforming the parts into a fully dense microstructure. Two separate post-processing routes were identified for accomplishing this task. Parts could either sintered directly to full density, or partially sintered and then infiltrated with a copper-based alloy to remove the residual porosity. [22] Figure 1.5 is an illustration of the two post-processing options.

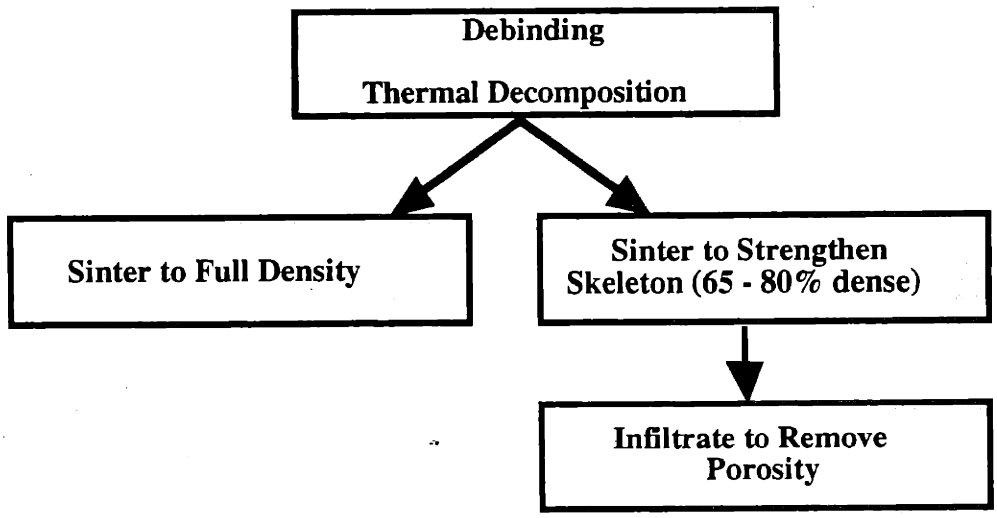

Figure 1.5: Post-processing options.

Although both post-processing approaches produce shrinkage of the printed part during sintering, the method involving sintering followed by infiltration results in substantially less dimensional change. Reduced dimensional change during firing translates into more accurate final part dimensions with less part distortion. Also, the metal powders used during the initial development of the metals printing process, which ranged in size from 50 to 80μm, were not well suited for sintering directly to full density due to their large size. (Typically, powders need to be below approximately 20μm in diameter before there is enough thermodynamic driving force to fully sinter the part.)

1.0.3 State of the Art at the Beginning of this Research

Using the previously described procedures for metal part printing and post-processing, a variety of parts were produced. Some of these parts were quite large, as in the case of the injection molding tooling inserts shown in figures 1.6-7.

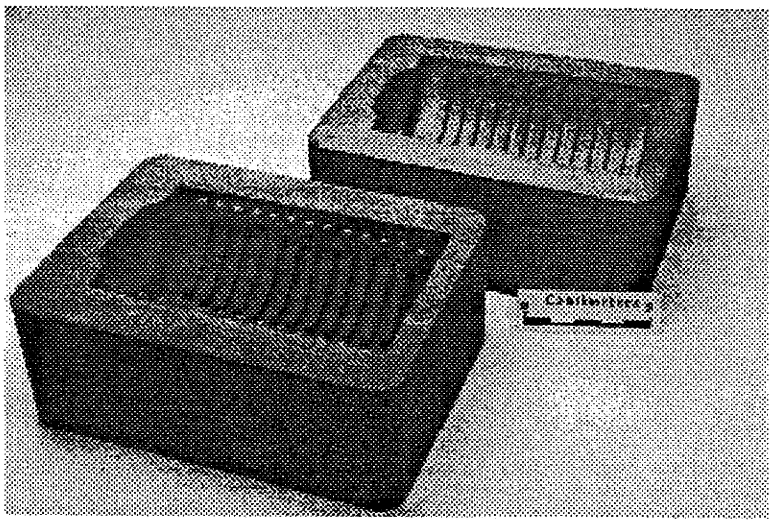

Figure 1.6: Green (foreground) and post-processed injection molding tool made with the 3D Printing process.

These metal tools had a composite metal microstructure which was approximately 65% 316L stainless steel and 35% copper-tin bronze infiltrant.

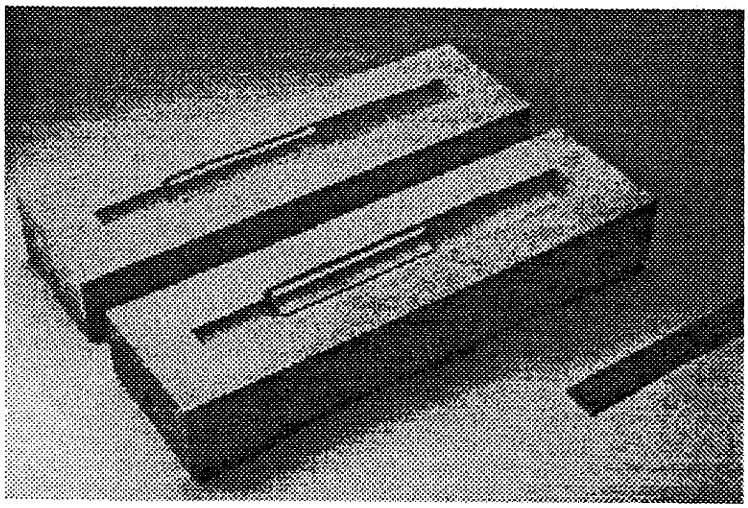

Figure 1.7: Another example of injection molding tooling made with the 3DP process.

1.1 Desired Properties for 3D Printed Metal Parts

With a basic process for metal parts production in place, application areas in which the metal printing technology could have the greatest impact were next identified. These industrial areas of use would help define the required properties for the finished tools.

1.1.1 Industrial Customers

The application of the 3DP metal printing process for the direct production of injection molding cavities and cores was identified as an ideal use of the technology. Injection molding tools are typically one-of-a-kind, with geometries which can be extremely complex. Both the manufacturing lead time and cost for injection molding tools is extremely large, with moderate-to-large size tools ranging in cost from $100,000 to $1,000,000, and taking in excess of three months to complete. Tools are typically produced using a complex series of manufacturing processes, in which a block of tool steel is rough machined, finish machined, hardened and then brought to final dimension by a combination of grinding and EDM processes. The very nature of this diverse set of processing steps requires a great deal of human involvement, both in process planning and execution. The use of the 3D printing process for the direct production of injection molding tools, whether in the near-net-shape or finished condition, was an ideal opportunity to reduce tooling lead time and cost.

The unique additive approach of the 3DP process would furthermore enable the generation of unique tool features which were not attainable using conventional manufacturing techniques. An example of such a feature is a conformal mold cooling channel. [62] In a typical injection molding tool, the cavity and core are cooled during the molding process by circulating fluid through a series of coolant channels in the back of the mold. These channels are produced by drilling holes across the tool bottom, and are therefore limited to straight passages. Since the surface contours of the cavity and core are typically complex, the straight cooling lines are less than ideal for the uniform and rapid removal of heat from the tool surface during molding. In contrast, a conformal cooling channel, which lies directly below the tool surfaces and follows the surface contours, could provide much more effective heat removal. The conformal cooling passage concept is illustrated in figure 1.8.

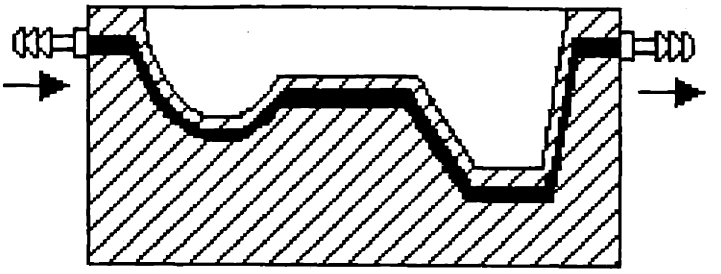

Figure 1.8: An illustration of a tool cavity cross-section, showing the conformal cooling concept.

The generation of injection molding tooling was made the primary focus of the 3DP metal printing effort. It was understood, however, that if the requirements of injection molding tooling users could be satisfied, then it was certainly the case that tooling for other less demanding manufacturing processes, such as vacuum forming or blow molding, could also be produced.

1.1.2 Tool Property Focus Areas

The unique property requirements of injection molding tools which separate them from other tooling applications include material properties, dimensional accuracy, and surface finish. Exceptionally demanding specifications in each of these property areas is the norm for injection molds.

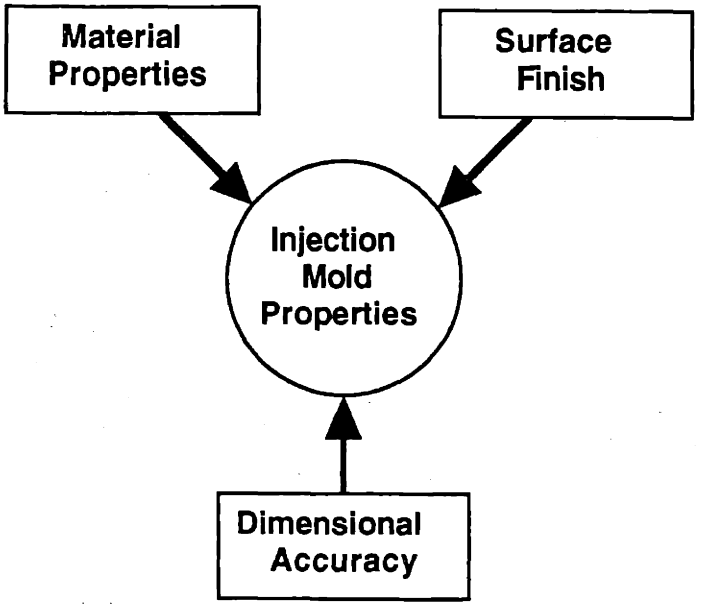

Figure 1.9: The three requirement groups which define the properties of an injection mold.

For 3D printing to succeed in producing usable injection molding tools which required little or no post-machining prior to use, similarly rigorous specifications would have be set and achieved for each of these three requirement areas. Table 1.1 lists typical values of tool specifications as defined by the injection molding tooling industry, along with the same values for tools produced by the 3DP process at the start of this research.

Table 1.1: Comparison of Industry Requirements and 3DP Capabilities For Injection Molding Tools.

Mold Property	Industry Requirements	3DP Capabilities
Material Properties Hardness: UTS: Porosity:	 30 - 60HRC 150 - 250ksi none	 60 - 80HRB 60 - 80ksi 1 - 2%
Dimensional Accuracy	most dimensions better than +/- 0.005", with some better than +/- 0.001"	+/-(0.005"+ 0.0025*L) where L=part dimension in inches e.g. for a 4 inch part, accuracy = +/- 0.015"
Surface Finish	better than 50 µin. R_a	between 200 and 2000 µin. R_a, depending on the printed surface measured

From the results in table 1.1, it was clear at the start of this research that substantial improvements in all three property areas were necessary in order to even approach the industry requirements.

The various printing parameters which affected each of the tool property areas are given in table 1.2. A small change in any one of these printing parameters might have a profound effect on the final part properties. For instance, since the thermodynamic sintering driving force was a exponential function of the average particle size, a small change in this parameter would strongly influence the amount of sintering shrinkage which a tool experiences during firing. The variation in total shrinkage would also be influenced, and this would in turn affect dimensional accuracy. [6]

Table 1.2: Printing Parameters Which Influence the Properties of 3D Printed Molds.

3D Printed Mold Property	Influencing Parameters
Material Properties	Alloy composition of the components Volume percent of each alloy component Amount and location of porosity Metallurgical changes during post-processing
Dimensional Accuracy	Binder placement accuracy of the printhead Capillary transport effects Powder particle size Shrinkage and distortion during post-processing
Surface Finish	Layer thickness and line spacing Use of proportional deflection Capillary transport effects Powder particle size

1.2 Improving Tool Properties by Increasing Green Density

The printed part characteristic which has the single greatest influence over the final properties of a fully post-processed 3D printed tool was the packing, or "green", density. Green density is the ratio of the total volume of metal in a printed to total part volume. Parts with high green density have low internal porosity. Parts printed with the previously described metal printing process had green densities between 56 and 58%. Over 40 volume % (written 40v/o) of porosity therefore had to be removed during post-processing, either by sintering, infiltration, or some combination of both.

Increases in printed part green density had the potential to significantly improve finished part properties in two of the three tool property groups defined above. Specifically, both finished part material properties and dimensional accuracy could be improved by increasing the green density of the as-printed part. The reasons for these improvements are explained below. Developing printing process improvements which increased the green density of printed parts was identified as the most expedient way to raise 3D printed tool properties to those required in industry. The work done to increase the green density of 3D printed metal parts is the focus of this thesis.

1.2.1 Effects of Green Density on Finished Part Dimensional Accuracy

A high green density part leads to improved dimensional accuracy in the finished tool because a high green density part will require less dimensional change during post-

processing. After printing, the two post-processing options for the green part are either to sinter the part to full density, or to partially sinter the part and the infiltrate with a low melting point alloy. Both of these options require some amount of shrinkage from the green part dimensions. The larger the amount of sintering densification required during post-processing, the larger the resulting shrinkage. When a part sinters, the powdered particles are drawn closer together as interparticle necks form. From conservation of mass it must be the case that as a part sinters and its density increases, its size decreases. The change in part dimensions is related to the initial and final packing densities by the expression

$$\frac{\phi}{\phi_o} = \frac{X_o Y_o Z_o}{XYZ}, \qquad 1.1$$

where $\emptyset_o$ is the initial packing density, $\emptyset$ is the final packing density, X_o, Y_o, and Z_o are the initial part dimensions, and X, Y, and Z are the final part dimensions.

If a part sinters isotropically, meaning that it shrinks a proportionally equal amount in all directions, then the change in packing density can be related to the dimensional change by the expression

$$\frac{\phi}{\phi_o} = \left(\frac{L_o}{L}\right)^3, \qquad 1.2$$

where L_o is an initial part dimension and L is a final part dimension.

Normally, the percentage linear shrinkage is referred to when discussing dimensional change, i.e.

$$\% \text{ linear shrinkage} = \left[1 - \left(\frac{L}{L_o}\right)\right](100), \qquad 1.3$$

or

$$\% \text{ linear shrinkage} = \left[1 - \left(\frac{\phi_o}{\phi}\right)^{1/3}\right](100). \qquad 1.4$$

As an example, if a green part was 60% dense after printing and was sintered to 80% density prior to infiltration, then its linear shrinkage was 9.1%. Sintering the same part to full density would require each dimension to be reduced by 15.7%. Powder injection molded (PIM) parts, which have green densities of around 62%, and which are usually sintered to densities greater that 96%, experience linear shrinkages of greater than 15%.

Shrinkage can, in theory, be compensated for by oversizing the green part. The scaling factor for part dimensions to give the correct amount of oversize is given by the expression

$$\text{scaling factor} = \left[\left(\frac{\phi}{\phi_o}\right)^{1/3}\right](100). \qquad 1.5$$

As an example, consider the case of a printed cube for which the density changed from 60% to 80% during post-processing. If the desired final dimensions for the cube were 1.0 inches on a side, then the CAD file of the cube would be scaled using a factor of 1.10 prior to printing.

Part tolerances are adversely affected by shrinkage, especially if the shrinkage is anisotropic. Parts made using standard P/M compaction techniques can experience anisotropic shrinkage during sintering due to green density variations in the part. [1] The very nature of 3D printed parts, where lines are stitched into layers and layers are joined to form parts, almost ensures some degree of anisotropy. Variations in shrinkage along the different axis of the part, particularly along the Z-axis, have been observed in the sintering of printed parts. Also, in addition to shrinkage, part distortion is common and is related to the amount of sintering performed. The effects of gravitational slumping, friction, non-uniform temperature distribution and variations in the initial part density all combine to alter the part shape during sintering, with a subsequent loss in dimensional control. PIM parts, which are sintered from about 62% to near full density, often receive a post-sinter forging operation to return critical dimensions to tolerance. The tooling used to compact P/M green parts can receive several design iterations before it can produce a part which will be in-tolerance after sintering.

3D printed metal parts are difficult to sinter to full density because of the large diameter powders used. Therefore, the usual means of attaining full density is to partially sinter, or presinter, the green part and then infiltrate will a low melting point alloy. Presintered part densities in the range of 65 to 75% are usually required in order for the skeleton to be rigid enough during infiltration to resist deformation due to capillary pressure. The amount of presintering dimensional change required to reach the 65 to 75% density range is determined by the initial green density of the part. A part with a green density which exceeded 65% would require very little presintering, and therefore little dimensional change, prior to infiltration. Maximizing green density, therefore, is an ideal means of minimizing part shrinkage and distortion, and should lead to improved dimensional accuracy in the finished part.

1.2.2 Effects of Green Density on Finished Part Material Properties

The material properties of the fully dense part were also improved by increasing the packing density of the initial green part. There are few restrictions on the alloy composition of the powder(s) used in the printing of the green part. Hardenable steels, stainless steels, tool steels and/or hard materials such as tungsten carbide and titanium carbide can all potentially be printed. The greater the green density of the part, the greater the percentage of the part will be composed of "true" tool materials upon completion of post-processing. In contrast, the alloys used to fill the remaining porosity during infiltration are restricted to those which can successfully penetrate the skeleton at a suitably low temperature. These infiltrant materials are usually copper or silver based alloys, and have inferior properties to the matrix alloy. Increasing the green density would therefore minimize the amount of infiltrant needed to fill the void space, and improve the final part material properties.

1.3 Different Approaches to High Green Density

A variety of methods to increase the green density of the printed metal part were considered prior to the start of this research. These are described below.

1.3.1 Increasing the Packing Density of the Spread Layer

The most intuitive approach to increasing green density in the printed part was to increase the packing density of each layer as it was created. Denser layers implied a denser printed part. Increased layer density could originate from a variety of sources. First, the

device used to create each layer could be optimized so that it packed the powder to its maximum, or tap, density during layer spreading. It had been previously observed that the spreader rod mechanism which was the "standard" layer generation device was not able to produce layers which attained the maximum packing density of a given powder. For example, the powders used to create the tools in figures 1.6-7 had a maximum packing density of 62 - 64%, but the printed green densities were much lower at 56 - 58%.

The application of vibratory energy to a powder mass is a frequently used technique for increasing packing density. [54] The spreader rod mechanism utilized in the early development of metals printing also employed vibratory excitation, but its use was not well understood. The design of a new spreader mechanism, which more effectively used vibrational energy to densify the powder layer, was one route to increasing printed part green density. The specifics of how vibrational energy should be applied in order to attain the maximum packing density, however, were not known. The effect of vibrational parameters such as the frequency, amplitude, direction and duration of vibratory application on powder densification were known to depend on the characteristics of the densification environment. [23] To effectively utilize vibratory compaction techniques in the 3DP process would therefore require a detailed understanding of the effects of each of these parameters.

The second approach for increasing the density of the spread layer was to utilize metal powders which had higher maximum packing density values than those currently being used. Bimodal powder mixtures, in which large and small powder particles were blended together in specific proportions, had the ability to reach packing densities in excess of 80%. For these powders, the smaller particles fit into the interstices between the larger particles, filling up unused space and increasing overall packing. Figure 1.10 is a photograph of a bimodal powder blend. If bimodal powders could be successfully spread and fully densified during layer generation, then the green density of the printed parts could be substantially increased.

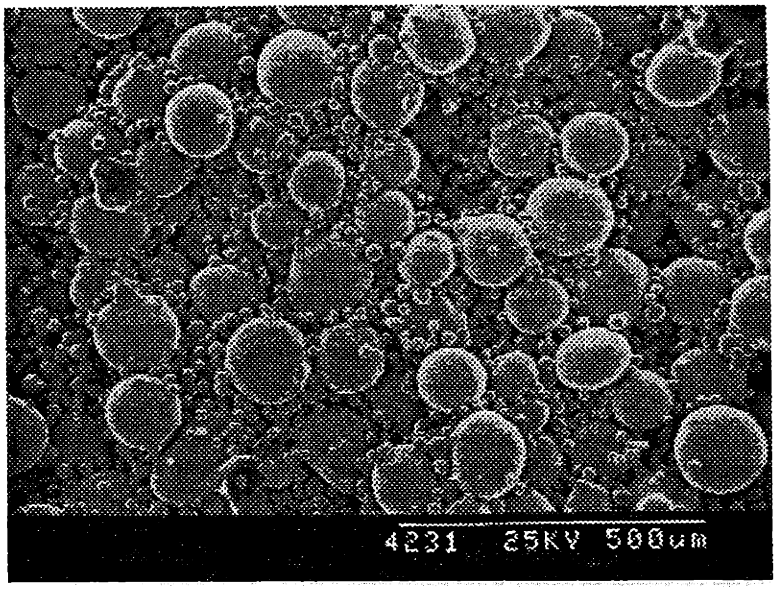

Figure 1.10: A bimodal powder mixture.

A final approach which had potential for increasing packing density was to alter the fluidity of the powder. In the PIM process, it was known that the polymeric binder present in the feedstock acted as a lubricant during the injection process, reducing interparticle friction and increasing green density. [21] In all prior 3DP layer generation techniques, the powder was in a dry state during the spreading operation. If instead the powder was spread in a wet, or slurried, form, a similar reduction in interparticle friction might be obtained. Methods of generating thin, high green density layers of powdered material from a slurry feedstock had already been developed in the field of tape casting. [38] Such methods might be adapted to 3D printing. Spreading powder in a wet form had other advantages over dry. Metal powders finer than 10μm have extremely poor fluidity in the dry state, making them difficult to work with. In slurried form, however, the fluidity is greatly enhanced. Also, extremely fine powders are safer to work with in slurried form because they are prevented from becoming airborne.

1.3.2 Printing Solids or Solid Precursors Through the Nozzle

A second approach for increasing the green density of the printed part was to utilize the binder stream as a delivery vehicle for additional solid material. The concept was similar to that of a bimodal powder, in that the pore space between the powder particles in the newly spread layer could be partially or completely filled by a material which would

become a permanent component of the microstructure. (Recall that the polymeric binder used for metals printing was temporary, and was burned away during debinding.)

Dispensing highly loaded ceramic slurries through the printhead had been previously investigated by [28]. In this application, the goal was to increase the alumina content of 3D printed ceramic parts. Slurries of up to 40v/o alumina were successfully dispensed from a 1.8mil diameter orifice. Particle sizes in the slurry were sub-micron. Precise control of both the chemical stability and filtering of the slurry suspension were necessary to prevent nozzle clogging. The more concentrated the slurry, the more difficult it became to obtain consistent results.

Adaptation of the slurry printing concept to metal powders was possible, but would present new challenges. Metal powders were not available in sub-micron sizes, with the smallest iron and nickel carbonyl powders having diameters in the 2 - 4 micron range. Stabilizing a metal slurry of these larger particles, and preventing them from clogging the printhead orifice, would therefore be more difficult. Also, stabilization of the alumina slurry was provided by electrostatic repulsion between the particles, and was possible because the alumina was an insulator. For the conductive metal powders, a different type of stabilization would need to be developed.

An alternative to printing a metal slurry was to instead dispense a metal precursor solution from the nozzle. For example, highly concentrated, aqueous-based metal salt solutions could be printed into each layer. At the completion of printing of an individual layer, the water vehicle would be evaporated, leaving behind a substantial amount of metal salt. If during later furnace post-processing, a strongly reducing atmosphere such as hydrogen was used, then the salt would be reduced to the base metal. In the process, a gaseous byproduct would be expelled. Metal salts such as silver nitrate, copper nitrate and copper chloride could all potentially be used to form highly concentrated solutions, thereby maximizing the amount of actual metal which was delivered through the nozzle. These salts could also be reduced to their base metals at fairly low furnace temperatures, which might be important if the printed part could not be removed from the powder bed prior to firing. Binder filtering and nozzle clogging would not be a problem, since the salt solutions would contain no solid particles. These solutions would require new handling and delivery procedures, however, since in a concentrated form they would be highly corrosive.

A final approach for delivering metal solids through the printhead involved extruding wax-based metal powder feedstocks, similar to those used in the PIM process. Galla [19] performed an initial investigation of this concept. Substantial modifications to the printhead assembly were required to heat the powder feedstock to a semi-fluid condition and then extrude a fine line of material onto the powder layer surface. The powder bed was also heated, so that after deposition, the feedstock would remain fluid and wick into the powder layer. Since the powder feedstock used in this approach was solid immediately prior to extrusion onto the layer surface, the stabilization and settling problems associated with printing liquid-based slurries was avoided. Galla's work indicated, however, that precise control of an extrusion printhead was rather difficult. Also, the overall printing rate was substantially reduced.

1.3.3 Post-Processing Approaches

The remaining approaches for increasing the green density of the printed part all employed techniques which acted on the part *after* it had been printed. In any of these approaches, the metal / polymer green part would be removed from the powder bed and debound using standard techniques. The part would then be presintered, but by an extremely small amount which only gave the part sufficient strength to be delicately handled. Dimensional change during presintering would therefore be negligible. At this point, the part would be an all-metal porous skeleton, ready for additional processing.

The first post-processing approach involved the use of flow-through metal plating to remove porosity in the part. Using a technology similar to electroless nickel plating, the plating solution would be pumped through the metal skeleton, with the particle surfaces acting as substrates for the deposition of additional material. Once a suitable amount of metal had been deposited, the part would again be furnace processed, using a final infiltration step to eliminate any residual porosity. Difficulties would likely arise in controlling the rate of deposition throughout the part. Also, how the part would be fixtured during the plating process was unclear.

A second approach involved immersing the metal skeleton in a concentrated salt bath in order to fill the pores with a metal precursor. Similar to the metal salt printing idea, after immersion, the part would be dried and fired in a reducing atmosphere to convert the salt into solid metal and a gaseous byproduct. In order to avoid mass transport of the salt to the surface of the part during evaporation of the water carrier, a freeze-drying approach

would need to be used. The entire immersion / reduction procedure might be repeated several times in order to maximize the amount of metal deposited. A final infiltration step would again be used to remove the remaining porosity.

A final post-processing method involved the vacuum infiltration of the metal skeleton with a low viscosity metal slurry composed of near-micron sized particles in a fluid carrier. Similar to a potting process, the metal skeleton would be placed in a vacuum chamber to remove gases from within the pores. A high solids loading slurry would be used to fully cover the part, and pressure would then be restored, forcing the slurry into the pores. Applied pressures higher than atmospheric could be used to accelerate the slurry infiltration. The slurry infiltrated part could then be freeze dried and fired to form metallurgical bonds between the skeleton and slurry particles. Slurry dispersion and stability would be less critical compared with the above approach in which slurry was printed through a nozzle. More of a concern would be the prevention of slurry particle buildup on the surface of the metal skeleton. If any buildup did occur, it would then act as a filter, straining the remaining particles before they could enter the internal pores. For this approach to be successful, the slurry particles would have to be substantially smaller than the dimensions of the skeleton porosity.

1.3.4 The Approach Taken for this Work

A full investigation of any of the above approaches for increasing part green density would be a substantial undertaking. In order to perform a full and thorough investigation, only one approach area could realistically by studied. After careful consideration of the potential benefits and difficulties of each approach, it was decided that increasing the packing density of the spread layer had the greatest potential for success. This approach area was the only one which did not place restrictions on the specific materials which could be used to increase part density. If desired, the entire green part could be composed of tool steels or other hard materials. The other approach areas required the use of micron-sized particles or metal solutions, both of which were available in a limited number of metallurgical compositions.

To further focus this investigation, the research would be limited to the study of vibratory compaction of dry powder layers. Both monomodal and bimodal powders would be investigated. This decision was made after a preliminary investigation of the issues involved in the spreading of wet metal slurries. Many difficulties associated with the slurry

approach were discovered in this brief study, the results of which are presented in appendix E.

1.4 The Goals of this Research

The central goal of this research was to understand the vibratory compaction of dry powders in the spread layer to obtain the highest possible green density. Ideally, predictive models would be developed which would help determine the best densification approach for any given powder. Green part densities between 75 - 80% were desired, since this level of packing would greatly improve both final part material properties and dimensional accuracy. Secondary goals of this research were as follows:

- Construct and evaluate all equipment necessary to perform the vibratory compaction process.

- Modify as necessary the entire metals printing process to accommodate the new densification equipment.

- Develop measurement techniques to quantitatively describe the unique microstructures of 3D printed metal parts, so that parts produced by different printing techniques could be more readily compared.

1.5 Organization of this Work

A brief overview of the research presented in this thesis is as follows:

Chapter 2. Literature Review - The work of other researchers in the areas of bimodal powder packing theory and powder mechanics and dynamics were considered prior to the start of this investigation. Although most of the information presented in chapter 2 is not referenced again until chapter 5, the literature review is presented early on to ensure that the reader is familiar with all related terms and concepts before continuing.

Chapter 3. Development of a Bimodal Printing Process - The modifications and improvements which were made to the existing metals printing process so that bimodal powders could be printed are described. This chapter also provides a

review of the entire printing process, and concepts defined here will be of use throughout this thesis.

Chapter 4. Analysis of the Baseline Bimodal Printing Process - Parts made with the baseline printing process, in which the original spreader rod is used to generate the powder layers, are analyzed to serve as a basis for future comparison.

Chapter 5. Investigation of Layer Densification Mechanisms - Using modified versions of powder tests initially developed in the fields of powder and soil mechanics, the densification behavior of monomodal and bimodal metal powder mixtures are studied. A conceptual model describing the parameters which are critical for the successful use of vibrational compaction techniques is presented. Different designs for a new layer densification mechanism which would replace the current spreader rod are proposed, and a final selection is made based on the results from the powder tests.

Chapter 6. Evaluation of the New Printing Techniques - The new layer densification mechanism is constructed and evaluated in actual printing conditions. Modifications to the initial mechanism concept are made after initial printing problems were discovered. Using a modified densification approach, packing densities near the tap density of the powders tested are obtained.

Chapter 7. Conclusions and Recommendations for Future Work - The overall conclusions from this research effort are summarized. Appropriate starting points for the continuation of this work are listed.

Appendices. The appendices contain related background material. Appendix A is a database containing all relevant information about the powders used during this research. Appendix B describes the development of a piezo-driven resonant force source which was used to provide vibrational inputs to the various pieces of experimental equipment used throughout this thesis. Appendix C describes the development of a photographic analysis techniques for quantitatively measuring packing defects and compositional variation throughout the printed parts. This material is critical for interpretation of the analysis results presented in the main text. Appendix D outlines the steps taken to prepare the chemically coated metal powders

used during printing. Finally, appendix E presents results from a preliminary investigation on the use of wet metal slurries during layer spreading.

Chapter 2. Literature Review

2.0 Introduction

The three questions central to this investigation of dry powder packing in the 3DP process are:

1) What is the maximum packing density which a given powder can attain ?

2) What densification actions are required to attain this packing density ?

3) How can these densification actions be effectively used in the 3D printing process ?

The answer to the first question has to do with the geometrical packing of the individual powder particles. An understanding of the maximum packing which a given powder mixture can attain will guide powder selection in the development of a high green density 3DP process. These packing concepts are reviewed in section 2.1. The answer to the second question is much more complex. The diverse fields of soil engineering and powder mechanics will serve as the sources of information for approaching the problem of powder densification. This topic is reviewed in sections 2.2 through 2.4. Finally, the pertinent information gathered from the literature review will be used to analyze the specific problem of spreading densely packed layers in the 3DP process. This discussion is presented in section 2.5.

2.1 Packing Theory

This section discusses those factors which determine the maximum packing density of a given powder mixture. We begin with a review of several basic definitions from powder packing theory, which will be useful throughout this thesis. An excellent review of terms related to powder packing can be found in Gray. [23]

2.1.1 Key Concepts and Definitions Related to the Packing of Powders

Listed below are the definitions of terms used in the characterization of particulate materials.

Theoretical Density - The density of a solid, non-porous block of a material. Table 2.1 lists the theoretical densities for several materials of interest.

Table 2.1: Theoretical Densities for Several Materials

Material	Density (g/cm^3)
316L Stainless	7.91
420, 440 Stainless	7.8
Copper, Copper Alloys	8.9

Packing Density - The ratio of the density of a volume of particulate material to the theoretical density for that material. The more tightly packed a material, the higher the packing density. In order to be statistically significant, the volume of particulate material over which the packing density is measured must have dimensions many times larger than that of the largest powder particle.

Green Density - The packing density of a printed, or "green", part. Green density typically refers to the average packing density of a part, with the assumption that the density does not vary significantly throughout the part. To measure packing variation throughout a part, the green density must be measured locally at multiple locations. Measurement techniques for local and average green density are presented in Chapter 4.

Apparent Density - The lowest packing density which a particulate material can exhibit.

Tap Density - The packing density of a particulate material after it has been vibrated or tapped. The tap density is obtained by vertically tapping a cylindrical volume of powder for 1000 to 3000 cycles at 284 cycles per minute using a 3.2 mm throw from an eccentric cam. For steel powders, a 25cc graduated cylinder is filled with 100g of powder prior to tapping. [20]

Hausner Ratio - The ratio of tap density to apparent density. The Hausner ratio in an indication of the compressibility of a given powder. [24]

Random Packing - A theoretical packing in which the positions of the particles are randomly distributed. During deposition, particles form a bed under the influence of several constraining forces, including gravity. They take up positions of minimum potential energy related to the packing formed at that stage and to the behavior of the other depositing particles.

Angle of Repose - The angle to the horizontal assumed by the free surface of a pile of powder at rest. The angle of repose is an indication of the degree of interparticle friction. The pile is initially formed be pouring powder from a fixed-height funnel. Figure 2.1 is an illustration of the measurement of the angle of repose.

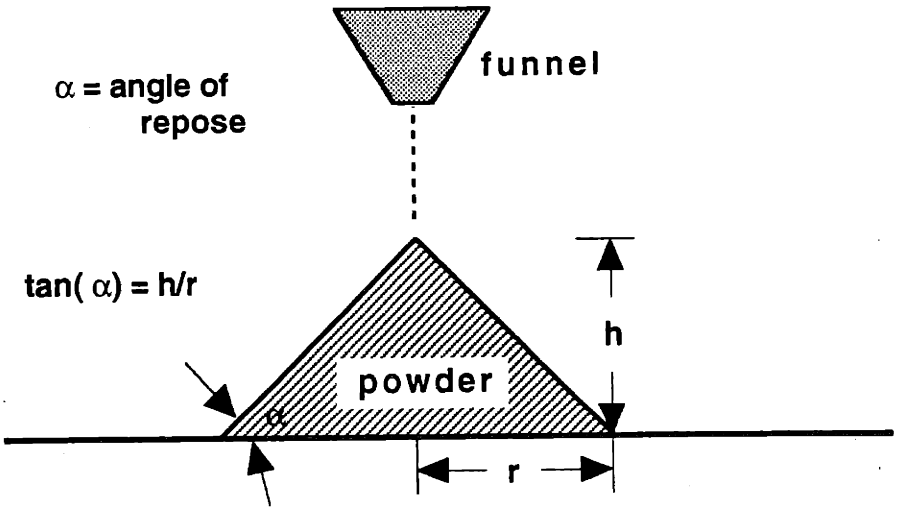

Figure 2.1: Measurement of the angle of repose.

Coordination Number (of a sphere) - The number of other spheres touching a particular sphere. The coordination number increases with increasing packing density. Although there is no exact relation between packing density and coordination number, an accurate and simple model is as follows [21]:

$$\text{Coordination Number} = 2e^{(2.4*\text{Packing Density})} \qquad 2.1$$

(Average) Particle Size - The average particle size in a powder mass.

Size Distribution - The frequency distribution of particle sizes in a powder mixture.

Monomodal Distribution - A powder mixture in which all the particles are approximately the same size. The distribution is characterized be an average particle size and a standard deviation about this mean. Only theoretical monomodal distributions have zero or near-zero size variance. All manufactured powders have some degree of size variance.

Bimodal Distribution - A powder mixture formed by blending two monomodal distributions with different average particle sizes.

Figure 2.2 is an illustration of three typical powder size distributions.

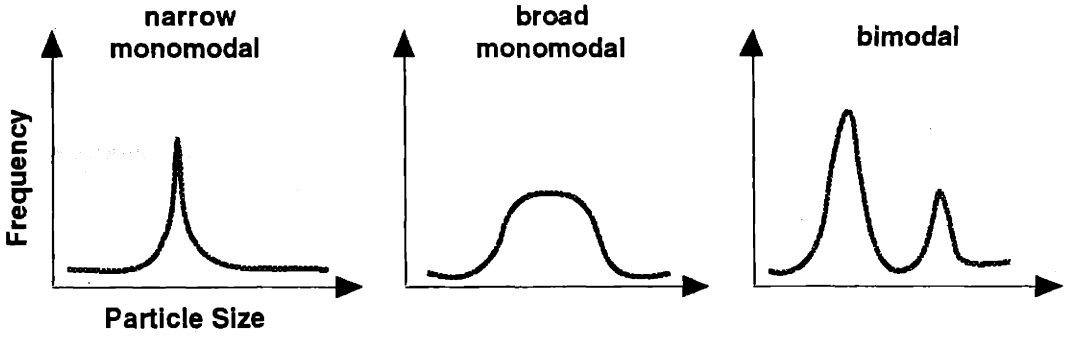

Figure 2.2: Three different types of powder size distributions.

Particle Shape - A qualitative description of the geometry of individual particles. Figure 2.3 is a illustration of the qualitative descriptors frequently used to characterize powder particles. For this thesis, we are primarily interested in spherical powders.

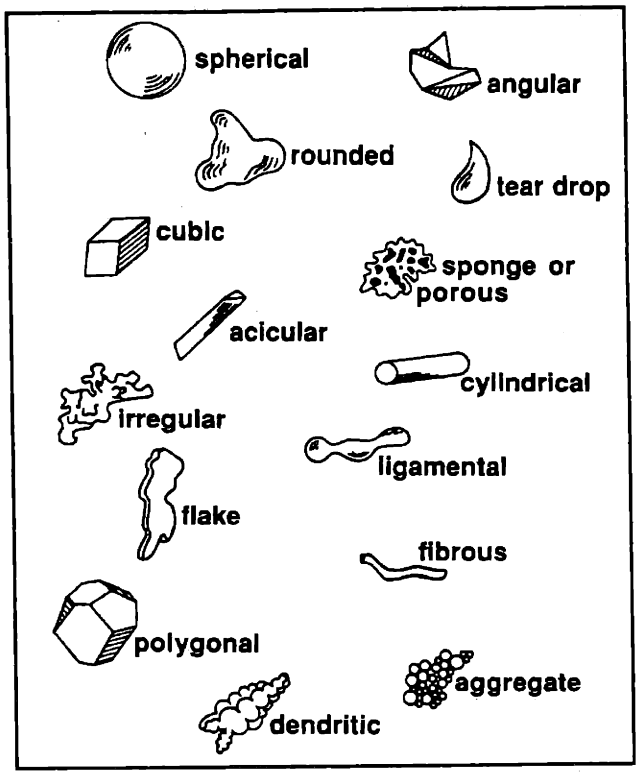

Figure 2.3: The possible shapes for particulate materials. [ref. 20, p.63]

2.1.2 Packing of Monomodal Distributions

We will first consider the packing of monomodal distributions, and review how some of the powder parameters defined above can affect packing density. Studies on the packing of powders have shown that the particles can be arranged in either an ordered or random distribution. Hard sphere models for crystalline atomic structures such as face centered cubic (fcc) or body centered cubic (bcc) exhibit ordered packing. Face centered cubic structures have a packing of 74% and body centered cubic structures pack to 68%. For an actual packing of particulate materials, a random packing distribution is exhibited. Random packing can be either loose or dense. Loose packing corresponds to the apparent density of the powder, which is the packing of the powder in a non-agitated form. Random dense packing corresponds to the tap density of the powder. The random dense packing for monosized spheres is approximately between 60 and 64%. [20] This is the highest packing which can be attained from a monosized spherical powder, regardless of the average particle size.

Powder shape affects packing because rough, non-spherical particles cannot nest as tightly together as smooth, spherical particles. Figure 2.4 shows the effect of relative roundness on the fractional packing density of monosized powders.

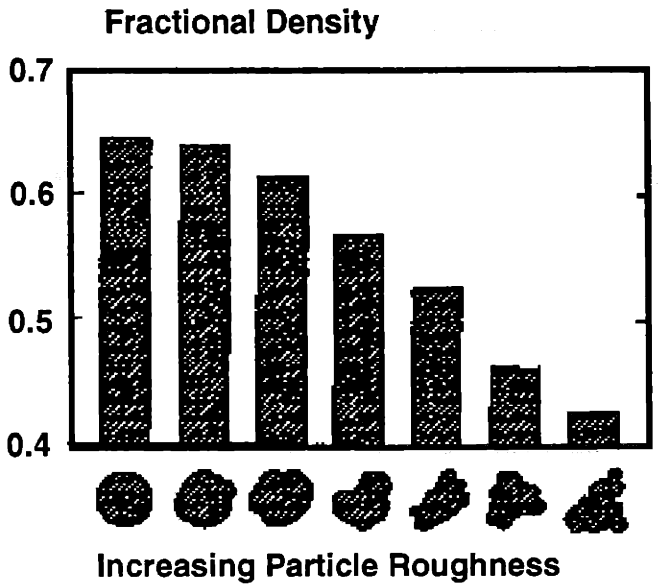

Figure 2.4: Fractional packing density versus relative roundness for randomly packed monosized particles. [ref.20, p.167]

Particle size also affects packing of monomodal distributions. As the particles become smaller, the specific surface area and interparticle friction increase. Particles no longer flow readily and cannot pack tightly. Spherical stainless steel powder below 20μm in size is non-flowing. Adhesion forces between particles increase as particle size decreases. The value of 64% for the random dense packing of monosized spheres has been experimentally verified only for powders greater than about 20μm in size. Below this size, packing drops due to increased interparticle friction. A detailed discussion of interparticle friction is presented later in this chapter.

2.1.3 Packing of Bimodal Distributions

The best possible packing which a monosized powder can attain is about 64%. Since a goal of this research is to attain a green density of 75 - 80%, a simple monosized spherical powder will not suffice. It is only through manipulation of the powder size distribution that the green density goal of 75 - 80% can be approached.

Bimodal distributions are mixtures of two monomodal distributions with differing average sizes. Bimodal mixtures can pack to higher densities than monosized particles. The smaller particles fit into the interstices between the larger particles without forcing them apart, thereby partially filling a previously unused volume with the smaller powder. Figure 2.5 illustrates the concept of bimodal packing. The large pore in the left image can be packed with many smaller particles, as shown in the center image. To be effective, the small particles must be significantly smaller than the large particles, or the large particles will be forced apart. This is shown in the left image. The two parameters which affect bimodal packing are the mass proportions of large and small powders mixed, and the diameter ratio of the powders. By selecting the optimum amount of small particles, the interstice void space between the large particles can just be filled, and packing will be maximized. Too many or too few small particles will adversely affect this maximum packing value. The diameter ratio of the powders will also affect the maximum packing value. Clearly, as the diameter of the small powder approaches that of the large, any packing benefit will be lost. Ideally, therefore, the particle diameter ratio should be made as big as possible. Usually, practical limitations place restrictions on the diameter ratio which can be used.

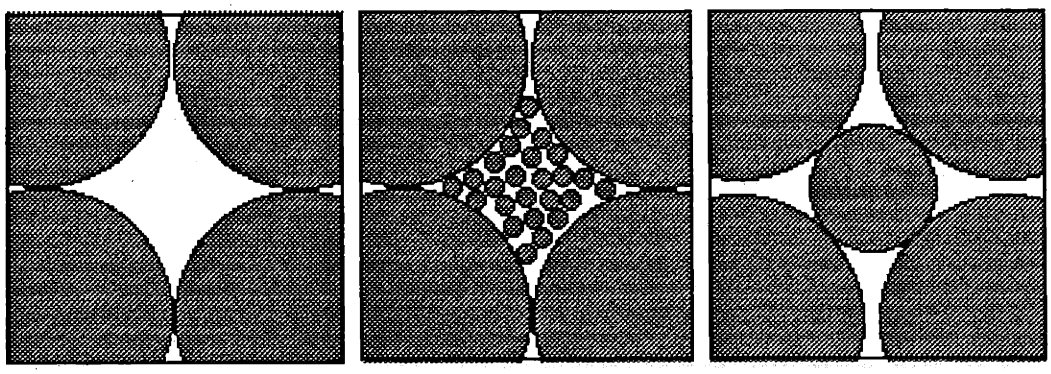

Figure 2.5: The bimodal packing concept.

2.1.4 Mathematics of Bimodal Packing

A mathematical representation of bimodal packing can be attained as follows. For this initial derivation, it assumed that the particles have an infinite diameter ratio. Let $\emptyset_L$ and $\emptyset_S$ be the monomodal tap densities of the large and small powders, respectively. The fractional amount of void space e_L between the interstices of the large powder is given by

$$e_L = 1 - \phi_L. \qquad 2.2$$

For the condition of maximum bimodal packing density, this fractional void space eL will be completely packed with small particles. The packing density of the bimodal mixture, $\emptyset B$, is the summation of the packing contributions from the large and small components,

$$\phi_B = \phi_L + \phi_S(e_L) = \phi_L + \phi_S(1 - \phi_L). \qquad 2.3$$

For a bimodal mixture of idealized spherical powders with infinite size ratio and monomodal packing densities of 0.64, the maximum packing density is 0.87, or 87%. This maximum value assumes a perfectly homogeneous mixture with no interparticle interactions.

For this ideal bimodal mixture, the large particles occupy 64% of the volume, the small particles occupy 23% of the volume, and 13% of the volume is void space. For large and small particles with equal densities, the mass fraction of large particles, M_L, is given by

$$M_L = \frac{\phi_L}{\phi_L + \phi_S(1 - \phi_L)}, \qquad 2.4$$

and the mass fraction of small particles, M_S, is given by

$$M_S = 1 - M_L. \qquad 2.5$$

This latter quantity is also equal to the composition C of the bimodal mixture.

In the above case, the large particles would comprise 73.5% of the mixture's mass. The bimodal composition for the mixture would therefore be 26.5% fines.

For large and small particles of different densities, M_L is given by

$$M_L = \frac{(\phi_L)\rho_L}{(\phi_L)\rho_L + (\phi_S)(1 - \phi_L)\rho_S}, \qquad 2.6$$

where ρ_L and ρ_S are the densities of the large and small powders, respectively.

A composition of 26.5% fine particles will produce the maximum packing density attainable from an ideal bimodal powder mixture. Other bimodal compositions will have packing densities somewhere between this maximum and the tap densities of the monomodal components. For these sub-optimal bimodal compositions, the maximum packing density of the mixture is assumed to be a linear function of composition. For compositions less than 26.5% fines (i.e. $C < 0.265$), the maximum packing density of the mixture is given by

$$\phi_B = \left(\frac{C}{0.265}\right)\left(\phi_{B,26.5\%fines} - \phi_S\right) + \phi_S. \qquad 2.7$$

Again, equation 2.x is simply a linear interpolation between the tap density of the small component, ϕ_S, and the tap density of the optimum bimodal mixture, $\phi_{B,26.5\%fines}$. For compositions greater than 26.5% fines, the bimodal packing density is given by

$$\phi_B = \phi_{B,26.5\%fines} - \left(\frac{C - 0.265}{0.735}\right)\left(\phi_{B,26.5\%fines} - \phi_L\right). \qquad 2.8$$

Figure 2.6 illustrates these relationships in a plot of bimodal packing density vs. composition.

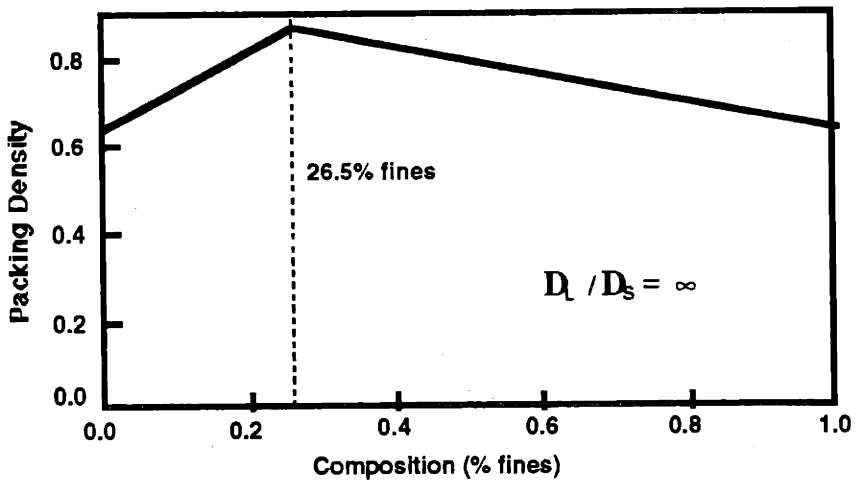

Figure 2.6: Bimodal packing density as a function of composition, assuming an infinite particle size ratio and a monomodal packing density of 64%.

Blending monomodal components with high individual packing densities will result in a bimodal mixture with high packing density. Therefore, the monomodal components should meet all the requirements for tightly packing powders, such as a spherical shape.

2.1.5 The Effect of Particle Diameter Ratio

The above calculations all assume an infinite diameter ratio between the large and small particles. For 3D Printing applications, certain restrictions are placed on the sizes of the powders in a bimodal mixture. The small component of the mixture should be greater than about 10μm to reduce interparticle friction and allow the powder mixture to be spread with the 3DP apparatus. The size of the large powder is also limited. The large powder size will have a direct impact on the minimum feature size attainable in the printed green part, in addition to affecting surface roughness and dimensional accuracy. An upper size limit of 100μm is reasonable, although a much smaller maximum particle size would be preferred in practice. The largest experimental particle size ratio which can be attained is therefore approximately 10:1.

Lee [30] has compiled data on the effects of composition and diameter ratio on the packing of bimodal mixtures. The data were obtained predominately from tests of equi-sized steel spheres ranging in size from 50 to 8000μm. Figures 2.7-8 are graphs which show the effect of particle diameter ratio and mixture composition on bimodal packing. Figure 2.7 plots diameter ratio versus maximum packing density Ø for bimodal mixtures of spherical powders with the ideal proportions of 73.5% large particles and 26.5% small particles. Below a diameter ratio of 7:1 there is a steep drop in maximum packing density. At a size ratio of 5:1, the maximum packing is 75.9%, and at 16:1 the maximum packing is 84.5%.

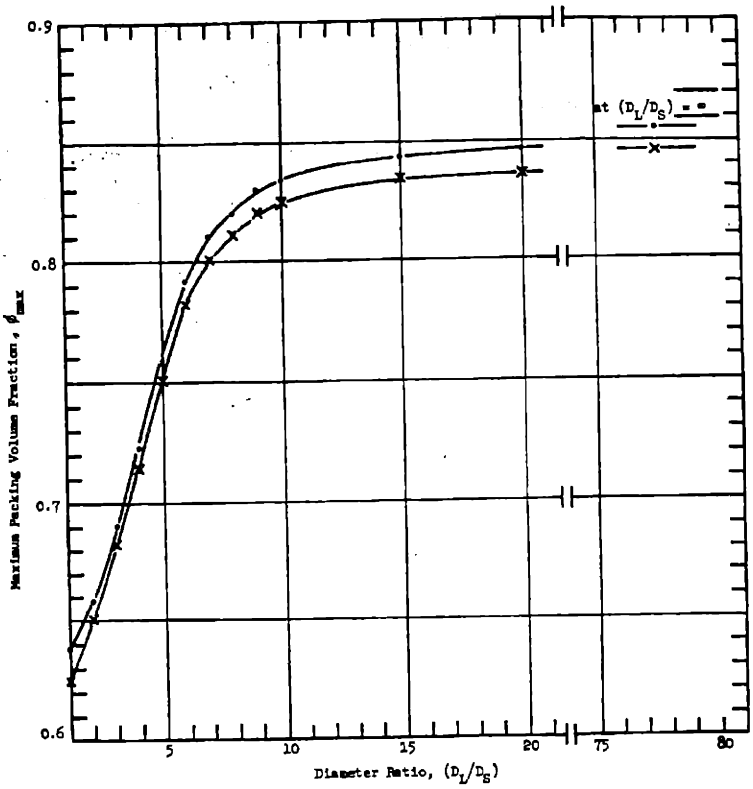

-----X----- ; Experimental data
-----•----- ; Corrected value

Figure 2.7: Maximum packing volume fraction versus diameter ratio for bimodal mixtures of spheres. [ref.30, p.581]

Ayer and Soppet [3] derived an empirical expression for relating the diameter ratio to the packing density for a bimodal mixture with 26.5% fines and monomodal packing densities of 64%. The bimodal packing density, $\emptyset_B$, is given by

$$\phi_B = 0.867 - 0.269e^{-0.201(D_L/D_S)}. \qquad 2.9$$

Figure 2.8 is a graph of fractional packing density Ø versus volume fraction of large spheres for the ideal case of no interparticle interactions and perfect mixture homogeneity. Both the large and small powders are assumed to have a 0.64 fractional monomodal packing density. Plotted are the curves for several diameter ratios varying from 1:1 to infinite. Several items are of note here. First, for all diameter ratios, the maximum packing always occurs at 0.735 volume fraction of large particles. In all cases, an excess of large particles causes the packing to fall off more rapidly than a deficit of large

particles. It is therefore better to error on the side of too few large particles when preparing a bimodal mixture. Finally, as noted above, at ratios of less than 7:1 the maximum packing falls off rapidly.

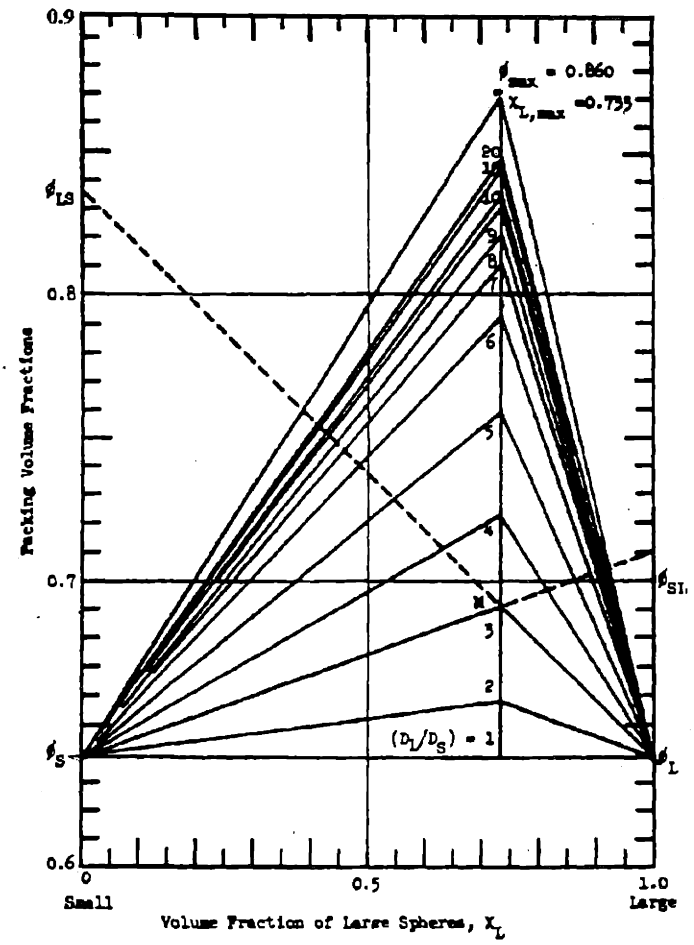

Figure 2.8: Idealized packing of bimodal mixtures of spheres as a function of mixture composition with diameter ratio as a parameter. [ref. 30, p.581]

2.1.6 Trimodal and Continuous Distributions

It is possible to reach even higher packing densities than those possible with a bimodal mixture by using a more complicated distribution, such as trimodal or continuous. [30] Table 2.2 illustrates the packing densities for various optimized trimodal mixtures. For a trimodal mixture with infinite size ratios, a maximum packing density of 92.6% is possible.

Table 2.2: Maximum Packing for Trimodal Mixtures [ref. 30, p.584]

Size Ratio	% Small	% Medium	% Large	Packing Density
1:5:25	0.216	0.092	0.692	0.850
1:7:49	0.132	0.207	0.661	0.878
1:9:81	0.114	0.224	0.662	0.888
1:10:100	0.112	0.225	0.663	0.892
1:100:10000	0.100	0.234	0.666	0.916
infinite	0.087	0.242	0.671	0.926

Distributions more complex than trimodal, from quarternary to continuous, are also possible. The required particle size ratio becomes the dominant issue in using these distributions. Furnas calculated, based on the particle size ratio, whether optimal packing would occur with bimodal, trimodal, or higher-order systems. The results of his model are shown in figure 2.9. For a given particle size ratio and a 0.6 monomodal packing density for each component, this plot indicates the number of components corresponding to optimal packing. For a particle size ratio less than 100:1, a bimodal mixture offers the best packing density. A size ratio of 100:1 is already exceeding the practical limits of the 3DP operation. It is difficult to obtain and handle metal powder less than 10μm in size, and powders with diameters much greater than 100μm would provide poor minimum feature size in printed parts. A maximum particle size ratio of 10:1 is therefore imposed, making a bimodal distribution the only workable approach.

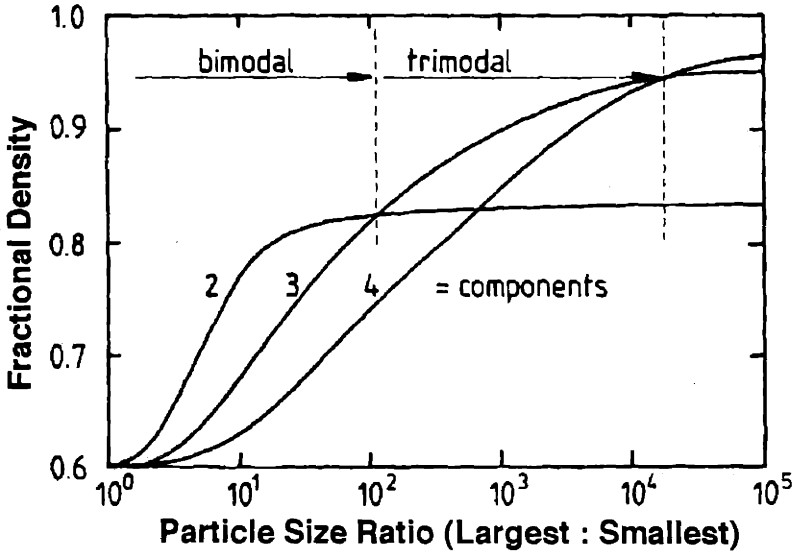

Figure 2.9: The effect of particle size ratio on the optimal packing density, showing the number of components for optimization assuming a monomodal packing density of 0.6. [ref. 18, p.1052]

2.1.7 Inhomogeneity / Segregation Effects

All the above calculations assume a bimodal mixture which is perfectly mixed and homogeneous. No bimodal mixture will be perfectly mixed. There will always be some degree of segregation, however small. Packing density will increase with the homogeneity of the mixture.

Onoda and Messing [43] defined the mixture homogeneity M as

$$M = 1 - (\sigma/\sigma_0), \qquad 2.10$$

where σ is the standard deviation in the composition between random samples taken from the mixture, and σ_0 is the standard deviation in composition for the unmixed system, which they defined as

$$\sigma_0 = (C(1-C))^{1/2}. \qquad 2.11$$

Figure 2.10 shows how composition and the degree of homogeneity will affect the packing density. The figure plots the fractional packing density versus composition for

several levels of mixture homogeneity for an infinite particle size ratio. In this case, the packing density of the monomodal components is taken to be 50%. The density improves with the degree of mixing. The upper limit is based on perfect mixing, while the lower limit assumes a totally segregated structure. Randomly mixed systems will range between the unmixed and fully mixed limits.

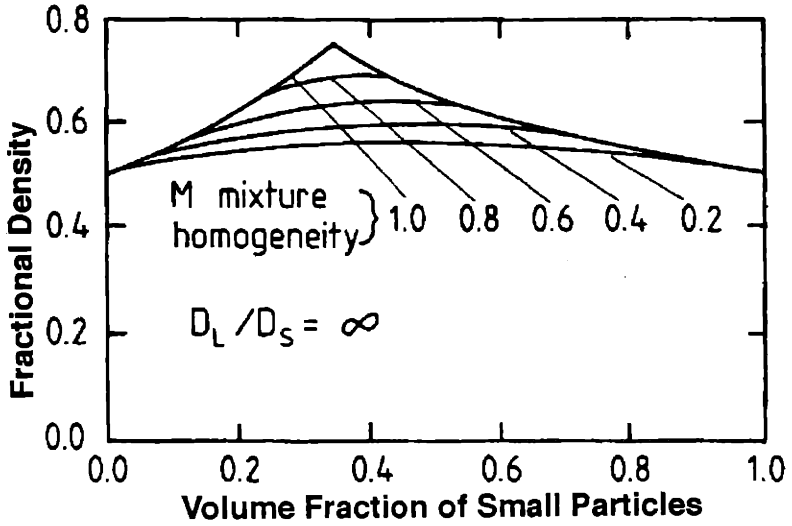

Figure 2.10: A plot of the homogeneity effect on the fractional packing density for binary mixtures with an infinite particle size ratio and a 50% monomodal packing density. [ref. 43, p.104]

Most random mixtures exhibit a homogeneity value for *M* near 0.7. [21] PIM bimodal feedstocks typically exhibit a higher degree of homogeneity than dry random bimodal mixtures, primarily due to the presence of a binder material. The binder in PIM feedstock allows for better mixing and greatly reduces powder segregation.

2.1.8 Causes of Segregation

Meakin and Skjeltorp [34] state that processes such as pouring, shaking, vibration, shear, freeze-thaw cycling and fluidization can all cause particle segregation. Williams [61] states that the four factors which influence segregation are differences in particle size, density, shape and resilience. In most cases, particle size is by far the most important property involved in segregation. Segregation can occur even in processes developed for particle mixing. Rosato *et al.* [49] performed Monte Carlo simulations of bimodal powders being shaken in containers. They concluded that as shaking occurs, a large particle will

rise due to simple, geometrical effects. As the particles fall during a "shake", small particles easily move beneath a large particle whenever a gap opens up. A large particle may move back down only if many small particles simultaneously move from beneath it, which is an unlikely event. The speed with which large particles rose increased with the size ratio of large to small particles.

In considering the 3DP process, powder segregation is most likely to occur during the dispensing of the powder pile before spreading, and during the distribution of the powder pile in the layer formation process. During dispensing operations, the powder is allowed to free-fall anywhere from 1cm, in the case of hand dispensing, to about 2 meters, during automating dispensing from an overhead hopper. The large particles will settle faster than the small due to viscous drag caused by the surrounding air. The larger the free-fall distance and the greater the particle size ratio, the more likely it is that segregation will occur.

When the powder pile is spread to form the new layer, the powder in the pile tends to tumble in front of the spreading device. Work performed by Ristow [48] and Baumann *et al.* [4] on the segregation of particles in a two-dimensional rotating drum considers particle motions which are very similar to those in the powder pile during spreading. In both studies, computer simulations were used to track the paths of individual particles as the drum was rotated multiple revolutions. The studies found that differences in particle size and mass can cause segregation, with one component tending to move to the center of the powder mass. Whether or not a similar segregation effect occurs within the powder pile to any significant extent during powder spreading remains to be seen.

2.2 Densification Theory

The packing and densification of granular or powdered materials is a topic which has been studied extensively, and there is an abundance of literature on the subject. The two primary sources of information are from the fields of powder metallurgy, and soil mechanics and dynamics (the later falling under the more general field of civil engineering). In the field of powder metallurgy, the goal of these studies is usually to determine methods to obtain maximum densification of a powdered metal part, while minimizing negative aspects such as density gradients, distortions and residual stresses. Literature from the fields of soil mechanics and dynamics is concerned with predicting the motion and densification of soils and other granular materials under a variety of loading conditions,

ranging from foundations subjected to machinery oscillations to earthen slopes which experience earthquake forces. This literature review can be viewed as a distillation process, in which useful information and insights on compaction and densification processes were obtained from a broad spectrum of previous work. The goal of this literature review was to extract from these very diverse fields information which could be applied to the densification of metal powder in the 3D printing process.

The contents of sections 2.2 through 2.4 is as follows. In section 2.2, the interparticle forces which act inside a particulate body are reviewed. It is these forces which will tend to impede any densification approach. Material from the field of powder mechanics (or statics) is presented next in section 2.3. This section discusses the stress / strain / packing behavior of particulate materials under monotonic (non-oscillatory) loading conditions. Finally, the effects of vibration on the compaction process are reviewed in section 2.4.

2.2.1 Factors Which Inhibit the Densification of Particulate Materials

Before examining the different methods for compaction and densification of particulate materials, it is helpful to examine those aspects of powdered bodies which tend to inhibit densification. The concept of "interparticle friction" was introduced earlier as the cause of poor packing in sub-20μm powders. Interparticle friction is a catch-all term which describes the cumulative effect of several independent mechanisms which inhibit particle motion and densification. [54] states that resistance to rearrangement and deformation exhibited by particulate bodies is explained by the interaction of the particles, caused by three groups of factors. The first group represents mechanical factors: mechanical engagement and wedging of the non-uniformities of the particle surfaces. The second group consists of physical factors: forces of cohesion (adhesion) and sliding friction, oscillating friction and magnetic forces. The third group consists of physiochemical factors, including chemical interactions of the particles in the presence of oxide or absorbed films, and capillary forces in the presence of liquids.

An understanding of the various interparticle forces which may be present during the 3DP process is essential to predicting the consolidation behavior of powders. These forces are described below.

Externally Applied Forces - These are the forces applied by external loads to the powder surfaces. Pressure applied to the top surface of a powder mass by a weighted plate, or the walls of the container in which a powder is stored, are both external force sources.

Hertz Contact Forces - The repulsive elastic force which is developed at the point of contact between two spheres [60]. When two spheres of equal diameter *d* are pushed into contact by an external force acting along a line joining their centers, a plane circular area of contact is developed. If the radius *a* of the circle of contact is much less than the diameters *d*, it can be expressed as

$$a = \frac{1}{2}\left[d^2 - \left[\mathbf{r}_i - \mathbf{r}_j\right]^2\right]^{1/2}, \qquad 2.12$$

where $\mathbf{r}_i$ and $\mathbf{r}_j$ are the position vectors for the two particles. The contact force on the *i*th particle due to all contacts is given by

$$\mathbf{F}^i_{Hertz} = \sum_j^{contacts} \frac{8Ea_{ij}^3}{3(1-\nu^2)d} \frac{\mathbf{r}_i - \mathbf{r}_j}{\left|\mathbf{r}_i - \mathbf{r}_j\right|}. \qquad 2.13$$

Gravitational Forces - This force is affected by the volume and density of the individual particles. The gravitational force is given by the expression

$$\mathbf{F}_{Grav} = m\mathbf{g}, \qquad 2.14$$

where m is the mass of the particle and $\mathbf{g}$ is the gravitational acceleration.

Interlocking Forces - These are not really forces at all, but refer to the mechanical interlocking and wedging between particles which can significantly impede particle motion and rearrangement. Interlocking is largely a function of packing density and particle shape. [29] The interlocking effect is distinctly different from the frictional forces, which are described next.

Friction Forces - Particles which slide against each other experience a shear resistance at their points of contact. In order to quantify the magnitude of this shear resistance, an understanding of the complex factors which influence the interaction between the two surfaces at their points of contact is necessary. These factors can include the deformation

of the sub-micron asperities on the surfaces of the powder, and the localized chemical bonding of the particles to one another. Such a discussion is beyond the scope of this thesis. However, the interaction effects can be summarized by saying that the total shear resistance between two particles is proportional to the normal force which is pushing the two particles together. Hence interparticle shear resistance is frictional in nature. [29] This friction force can be described by the relation

$$\mathbf{F}^{i}_{\text{Friction}} = -\mu \sum_{j}^{\text{contacts}} \mathbf{n}_{ij} \,, \qquad 2.15$$

where μ is the coefficient of friction and $\mathbf{n}$ is the normal force between the *i*th and *j*th particles.

The shear force required to initiate sliding between two particles is often greater than the force required to maintain motion. Hence, the concepts of static and kinetic friction also apply to the contacts between particles. This may explain why a small oscillatory stress applied to a particulate system can, over time, produce more particle rearrangement than a large monotonic stress, since in the former case the particles are continuously experiencing small motions which reduce the friction force between them.

Capillary Bridge Forces - If small amounts of a liquid phase are present in the powder, liquid bridges form at interparticle contact points and produce a capillary pressure which holds the particles together. Very small quantities of moisture are necessary to have a noticeable effect on powder fluidity and spreading behavior. Previous studies in the 3DP process have shown that trace amounts of water delivered from an ultrasonic humidifier can provide significant cohesion force to the powder bed. [36] The attraction force between two spherical particles separated by a variable distance and connected by a liquid bridge of variable volume is attainable by solving the corresponding differential equation. A graphical representation of the results generated by Rumpf and Schubert is reproduced in figure 2.11. [52] Here, a dimensionless adhesion force $F/(\gamma \cdot x)$ is plotted as a function of a/x, where a is the distance between the two spheres and x is the sphere diameter. The other variables are:

F = adhesion force
γ = surface tension
δ = contact angle (assumed to be zero)

V_l = volume of liquid

V_S = volume of both spheres.

The results are plotted with V_l/V_S as a parameter. When particles are touching, as is the case during spreading and in the powder bed, the ratio a/x approaches zero and significant adhesion forces can be generated with a very small volume of liquid. Clearly, to maximize powder fluidity and packing density, the powder must be kept very dry.

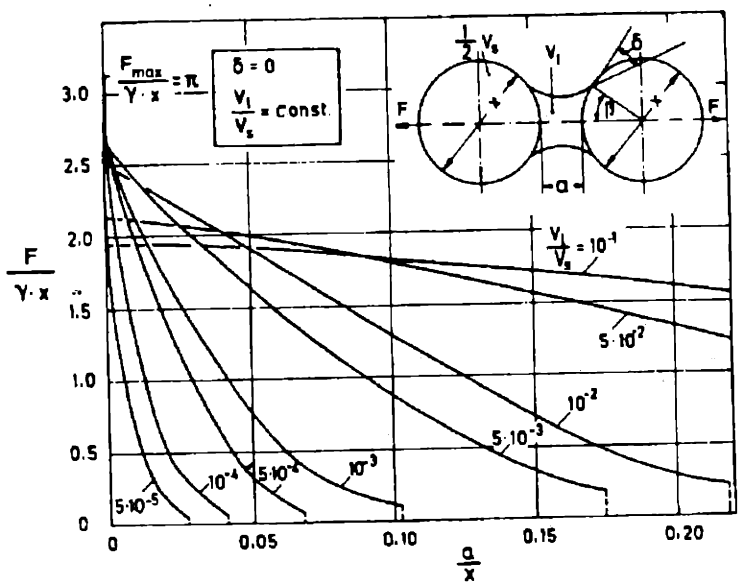

Figure 2.11: Dimensionless adhesion force $F/(\gamma \cdot x)$ of a liquid bridge between two spheres as a function of a/x. [ref. 52, pp.362]

Chemical Bonds - Chemical bonds which form between powder particles can strongly agglomerate powders. An example of a chemical bond is the formation of inter-connected oxide layers which often occur when iron powder suffers prolonged exposure to a moist atmosphere. Also, chemical bridges between particles are sometimes intentionally formed during the 3DP process by crystallizing salts. [36] These salt bonds provide cohesive strength to the powder layer in order to resist printing effects such as ballistic ejection.

van der Waals Forces - When particles are in close proximity, they feel considerable attractive force due to van der Waals interaction. [63] The attractive force increases as particles come closer, but attains a constant value as the separation between the two

approaching surfaces is less than a certain value h_0, typically in the range 0.4 - 1 nm. [47] For spherical particles of diameter d, the van der Waals interaction force F on the ith particle is given by

$$\mathbf{F}^{i}_{VDWI} = -\sum_{j} \frac{Ad}{(|\mathbf{r}_i - \mathbf{r}_j| - d)^2} \frac{\mathbf{r}_i - \mathbf{r}_j}{|\mathbf{r}_i - \mathbf{r}_j|} \qquad 2.16$$

if $|\mathbf{r}_i - \mathbf{r}_j| > r_0$, and

$$\mathbf{F}^{i}_{VDWI} = -\sum_{j} \frac{Ad}{(r_0 - d)^2} \frac{\mathbf{r}_i - \mathbf{r}_j}{|\mathbf{r}_i - \mathbf{r}_j|} \qquad 2.17$$

if $|\mathbf{r}_i - \mathbf{r}_j| \leq r_0$, where A is the Hamaker constant and r_0 - d is the minimal surface separation h_0, below which the van der Waals force attains a saturation value given by the second expression. For iron, A can be taken as 21.1E-20 J. The summation over j includes only the nearest neighbors, because the van der Waals force is too weak for second neighbors. Note that for small particles, the van der Waals force can be many times larger than the force of gravity on the particle and can play a significant role in particle rearrangement. In the figure 2.12 below, the ratio of the saturation of the van der Waals force to gravitational force between two equal steel spheres has been plotted against sphere diameter. Three different values of the minimum saturation distance h_0, namely 0.5, 1.0 and 1.5, have been plotted.

Micro-asperities on the surfaces of particles can greatly influence the effect of the van der Waals interaction by separating the particles and lowering the attractive force. These asperities are common on P/M powders. German states that for P/M applications, van der Waals forces are only important for particles below 0.05μm in size. [20]

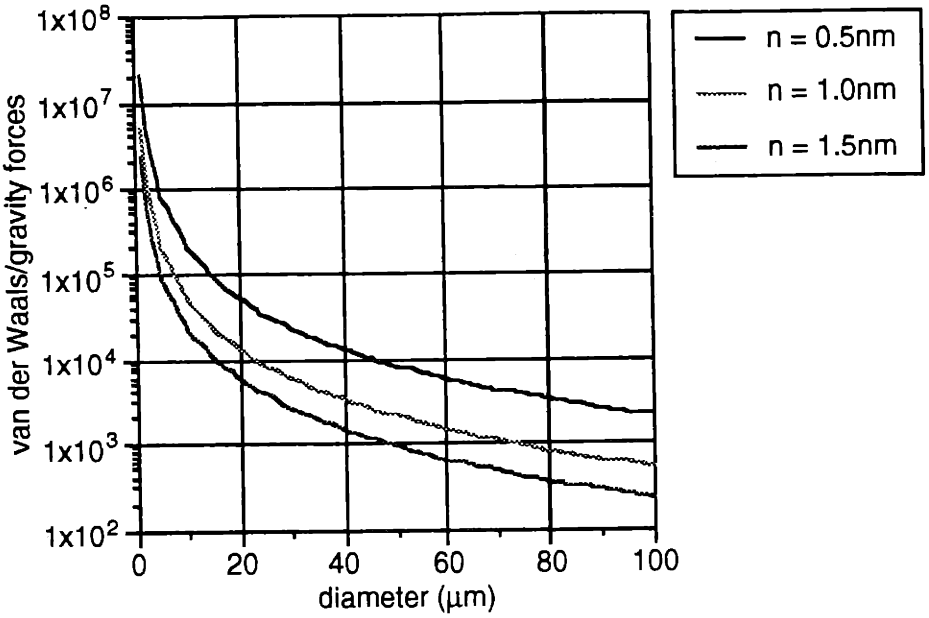

Figure 2.12: The ratio of van der Waals to gravity forces plotted against particle diameter.

Yen and Chaki developed a computer simulation to study the effect of some of the forces described above on the packing of monomodal, spherical particles. [63] Particles with 100μm and 50μm diameters were allowed to settle in a container from an initial free-fall condition. In each case, 948 particles were considered. Particle motion was determined by numerically solving Newton's equations of motion for a multi-particle system. The interaction forces considered were gravity, Hertz contact force, frictional force and van der Waals interaction (VDWI). Two values for the friction coefficient, 0.3 and 0.7, were tested. Without friction and VDWI, the packing density reached 0.633, which is comparable to the random close-packed density for random structures of steel ball bearings. Both friction and VDWI were found to reduce packing. For small particles, the effect of VDWI was to reduce packing by agglomeration of particles into local clusters. Note that no external force was applied for the purpose of enhancing densification.

The forces described above all combine to produce the normal and tangential contact forces between particles, and, in more general terms, the shear deformation resistance of the powder mass. For this study of the 3DP process, the interparticle forces resulting from interlocking, friction, capillary bridges and chemical bonds are the most critical. These four forces will determine how a particulate body reacts to a given set of externally applied forces.

2.3 Powder Mechanics (Statics)

For both monomodal and bimodal powder distributions, a high degree of fluidity is important to attaining maximum packing. Opposing the densification process are the interparticle forces described above, which reduce fluidity and make densification more difficult. These interparticle forces impede particle motion, and can cause the formation of agglomerates which negate any beneficial packing effects which might have been obtained from a specific powder size distribution. Lambe and Whitman [29] provide an excellent review of the forces which act throughout particulate systems, and a large portion of this section is based on their work. When an external force is applied to a particulate system, as might be the case in a building foundation resting on soil, or a roller spreading powder in the 3DP system, the force is divided up between the many interparticle contacts bearing the load. The force at each interparticle contact can be resolved into normal and tangential components. This is illustrated in figure 2.13. Individual particles experience elastic and plastic strains in the immediate vicinity of the contact points, bringing the particles closer together. When shear forces in the bed become larger than the shear resistance at the points of contact, there will be relative sliding between the particles. The overall strain in a powder mass is therefore a combination of the deformation of the individual particles, and the sliding between particles. Even at large applied forces, it has been observed that interparticle sliding and the overall motion of individual particles contributes the majority of the total strain. For the low stresses which will be applied during densification of metal powders in the 3DP process, it is safe to conclude that all bulk strain will be accomplished by the sliding and rolling of individual particles over each other.

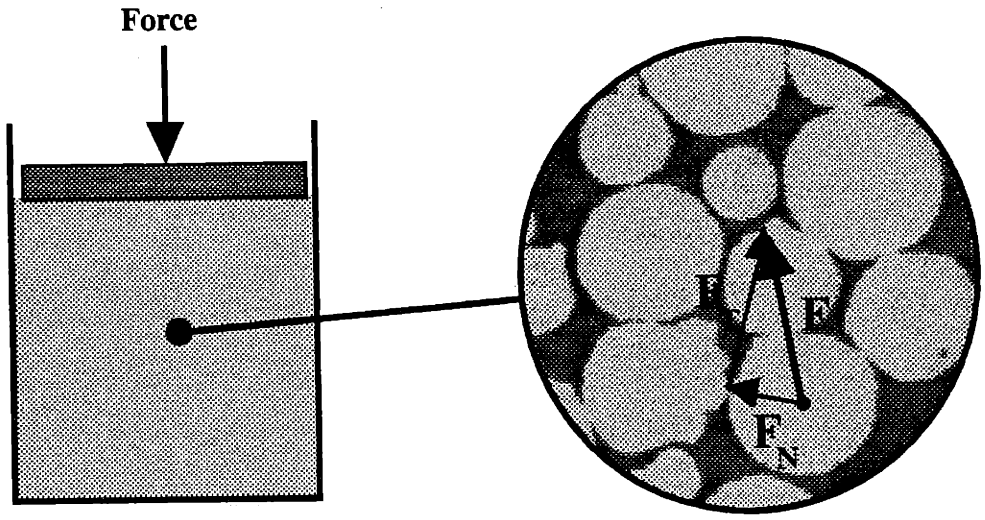

Figure 2.13: A schematic representation of force transmission in a particulate system. An externally applied force can be resolved into normal and tangential forces at the points of contact.

An important consequence of the deformation mechanism for particulate materials is that, since sliding and rolling are nonlinear and irreversible, it is to be expected that the stress / strain behavior of a particulate system will be strongly nonlinear and irreversible.

Although an understanding of the interactions between particles at their points of contact provides valuable insights into the behavior of particulate systems, it is clearly impossible to keep track of the forces and displacements at each individual contact. Rather, the study of particulate systems usually involves the measurement of more macroscopic properties, with the goal of obtaining an understanding of the stress / strain relationships for an entire particulate system. Before embarking on a review of these relationships for particulate materials, we will first briefly review the stress / strain / failure laws for solid materials. These will provide an important basis for later comparison.

2.3.1 The Stress / Strain / Failure Laws for Solid Materials

There are three principle steps in the analysis of how a solid body will respond to an arbitrary stress condition. First, the external loading condition on the body is precisely defined, typically by vector quantities representing the force inputs. Next, the stress condition at every internal point throughout the body is calculated, using the laws of

continuum mechanics. Finally, the deformations of the entire body are determined, based on the individual distortions of the internal points. These deformations are classified as elastic and recoverable if the stress levels are below the yield condition for the material, or plastic if permanent deformation occurs as a result of the loading condition. It is the permanent deformations of solids which are of relevance to this discussion, since these permanent deformations are analogous to those which occur in particulate bodies during changes in packing density.

In solid mechanics, two different yield criterion exist for determining when the onset of plastic deformation will occur. These are the Tresca and von Mises criterion. [32] Tresca's maximum shear theory of 1864 is the simplest yield criterion, which states that yielding occurs when the maximum shear stress along any plane exceeds a critical value. If we define the principal stresses at a point to be σ_1, σ_2, and σ_3, subject to the condition that $\sigma_1 > \sigma_2 > \sigma_3$, then the Tresca criterion can be expressed mathematically as

$$\tau = \frac{\sigma_1 - \sigma_3}{2} \geq k, \qquad 2.18$$

where τ is the shear stress value and k is the critical value or maximum shear stress for yield to occur. The von Mises criterion can be expressed as

$$\sqrt{\frac{(\sigma_2 - \sigma_3)^2 + (\sigma_3 - \sigma_1)^2 + (\sigma_1 - \sigma_2)^2}{2}} \geq Y, \qquad 2.19$$

where Y is the von Mises yield stress obtained in an axial tension test.

Yield surfaces for the Tresca and von Mises criterion can be plotted in three dimensions with the principal stresses σ_1, σ_2, and σ_3 as the coordinate axes. Figure 2.14 is an illustration of the two yield surfaces. The Tresca yield surface is a hexagonal prism, and the von Mises yield surface is a cylinder, both of which have the line $\sigma_1 = \sigma_2 = \sigma_3$ as their central axis.

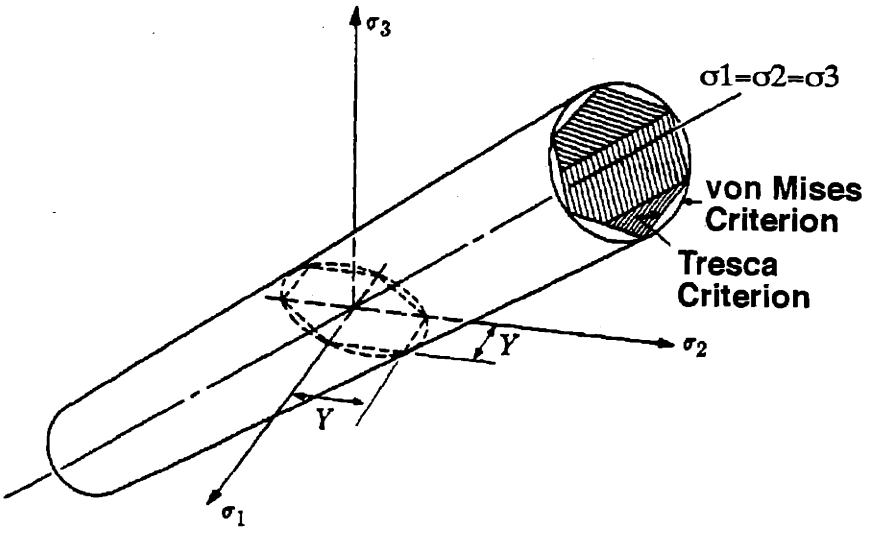

Figure 2.14: Geometrical representation in principal stress space of the Tresca and von Mises yield criterion. [ref. 32, p.278]

The yield surfaces are shown from along the line $\sigma_1 = \sigma_2 = \sigma_3$ in figure 2.15. The Tresca hexagon is completely contained by the von Mises circle, and is therefore the more conservative criterion.

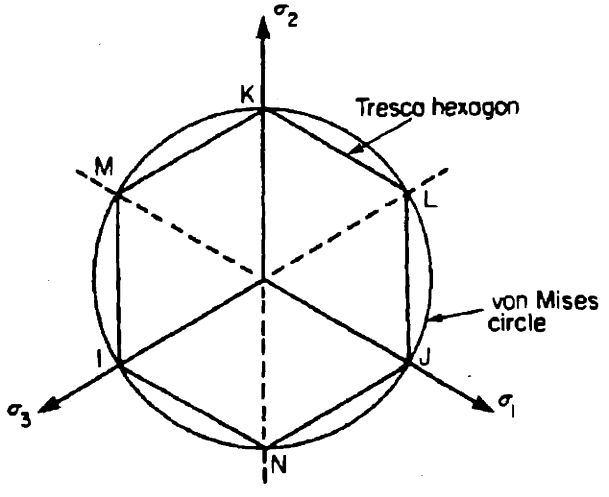

Figure 2.15: A view of the Tresca and von Mises yield surfaces from along the line $\sigma_1 = \sigma_2 = \sigma_3$. [ref. 55, p.197]

Plastic yielding occurs when a point within the loaded body reaches a principal stress condition which crosses a yield surface. Note that both surfaces are open-ended along the line $\sigma_1 = \sigma_2 = \sigma_3$, which represents the condition of hydrostatic stress. No plastic deformation can occur if only a hydrostatic stress condition is applied, regardless of the magnitude of the stress level. Only the deviatoric stress component (the component not included in the hydrostatic stress) can cause plastic yielding.

2.3.2 A Stress Distribution Approximation for Particulate Systems

We will now turn our attention back to the stress / strain behavior of particulate materials. First, an important distinction must be made in what is meant by plastic deformation in both solid and particulate bodies. In solid bodies, plastic deformation refers to the motion of dislocations along the slip planes in the solid, and takes place on an atomic scale. For particulate bodies, plastic deformation refers to the *rearrangement* of the individual particles in the powder mass such that the overall shape of the body changes. For all of the discussions which follow, it is assumed that no shape changes occur in the *individual particles* which form the particulate body. (Note that in standard P/M practice, where high pressures are used to increase the density of a particulate body, the individual particles do deform.)

Similar to the case of a homogeneous solid, before we can predict the plastic deformations of a particulate body, we must know the stress distribution throughout the body. The stress distribution can reveal at what distance from the applied load the resulting stresses in the powder mass drop below a certain value. In soil mechanics, the stress distribution from an applied load can be estimated using theories of elasticity, if the soil is assumed to be homogeneous and isotropic. [29] This assumption is never completely true, and in some cases is seriously violated. In the case of 3DP, where it has been previously demonstrated that printed parts often have anisotropic microstructures, this assumption will also be partially incorrect. Nevertheless, an approximate picture of the stress distributions which may be produced during densification will likely be useful in explaining densification behavior.

Figures 2.16 and 2.17 present graphical solutions to the elastic stress distributions which occur in semi-infinite solid bodies under uniform loads applied to either circular or strip areas, respectively. The stress distributions which would exist in a comparably loaded semi-infinite particulate body are assumed to be approximately equal to these solid

body distributions. This assumption is valid only for static conditions, and is violated if the stresses in the particulate body are large enough that the particles begin to flow. For the strip load solution shown in figure 2.17, the strip width is the narrow dimension of the rectangular loading surface. The strip load is of particular relevance to 3DP, since powder spreading devices such as the roller tend to act over a single strip of powder bed at any given time. For the calculation of the stress distribution beneath a strip load, it is assumed that the loading surface is infinitely long in the direction normal to the paper. In the figures, σ_1 is the applied vertical stress, and the resultant vertical and horizontal stress isobars are shown. The zone under the loaded area wherein the vertical stresses are significant is frequently termed the "bulb" of stresses. For a strip load, it can be seen that the vertical stresses are still significant at a depth three times the width of the strip (note that the strip width is equal to $2a$ in the figure), but horizontal stresses are essentially zero below two strip widths in depth.

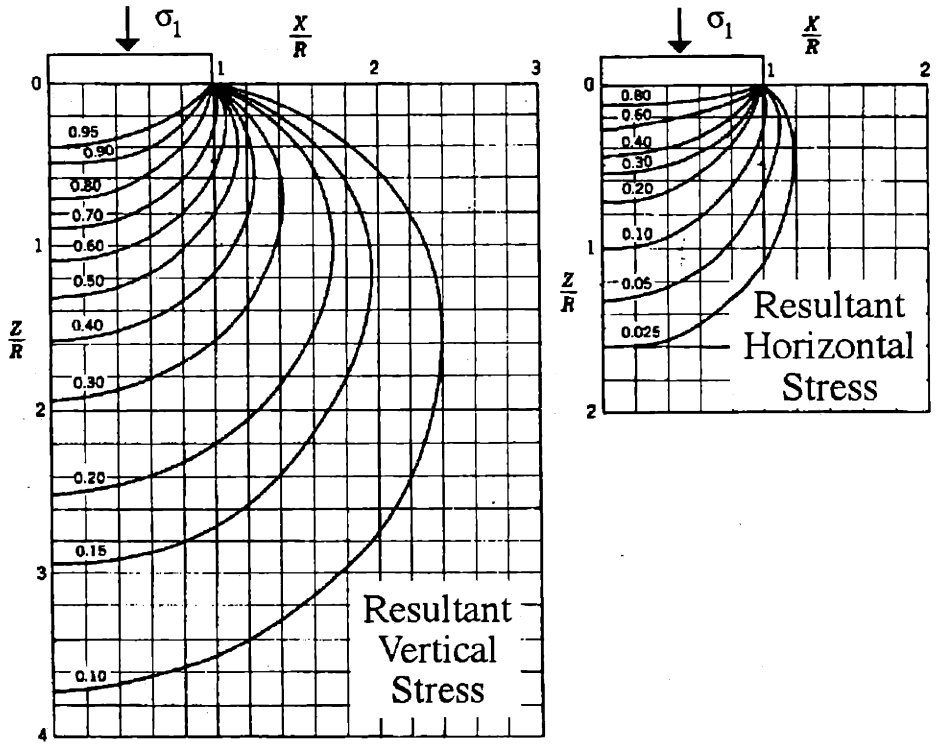

Figure 2.16: Stress from uniform load under a circular area. [ref. 29, p.102]

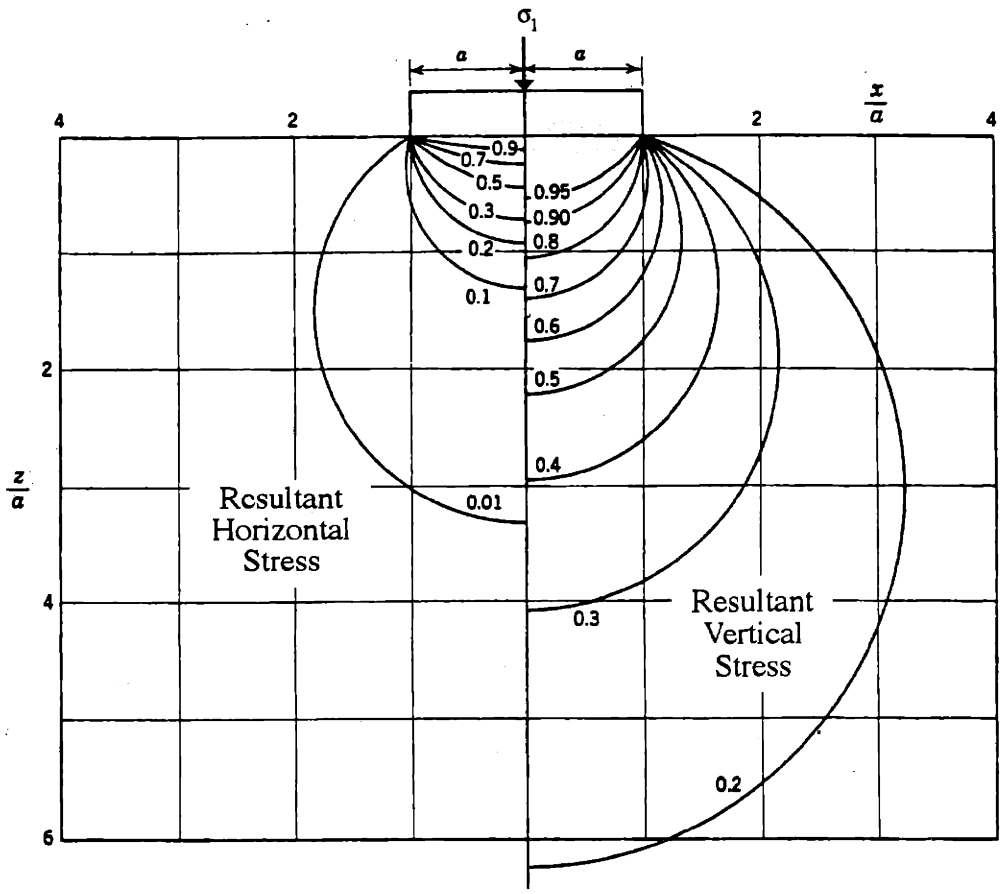

Figure 2.17: Principal stresses under a strip load. [ref. 29, p.105]

The mathematical relations used to derive the elastic stress distribution in a solid body when loaded by a strip load are taken from [58]. Figure 2.18 illustrates the variables used.

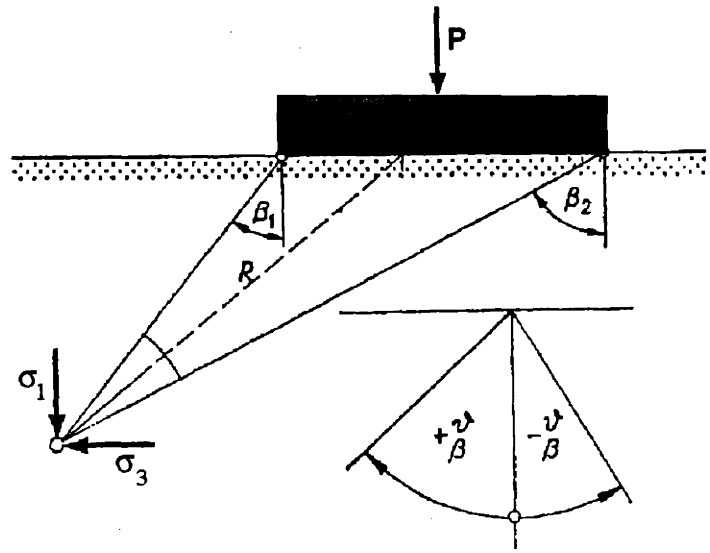

Figure 2.18: Uniformly distributed strip load acting on a surface of a semi-space. [ref. 58, p.228]

The vertical stress, σ_1, is given by

$$\sigma_1=\frac{P}{\pi}\left[\sin(\beta_2-\beta_1)\cdot\cos(\beta_2+\beta_1)+(\beta_2-\beta_1)\right], \qquad 2.20$$

and the horizontal stress, σ_3, is given by

$$\sigma_3=\frac{P}{\pi}\left[-\sin(\beta_2-\beta_1)\cdot\cos(\beta_2+\beta_1)+(\beta_2-\beta_1)\right]. \qquad 2.21$$

The tangential stress, t_{13}, is given by

$$t_{13}=\frac{P}{\pi}\left[\sin^2\beta_2-\sin^2\beta_1\right]. \qquad 2.22$$

P in the above expressions is the load applied to the strip.

2.3.3 A Mohr Circle Description of Local Stress in a Powder Mass

In solid body mechanics, a Mohr circle graphical representation is often used to depict the state of stress at a given point in a body, and to determine the stress values

associated with any plane through that point. A similar representation is used in soil mechanics, with the primary difference being that compressive stresses are defined as being positive in value. This is strictly for convenience, since most stresses encountered in soils engineering are compressive. The Mohr circle representation will be briefly reviewed here. It will be an extremely valuable tool in the sections which follow.

Given the magnitude and direction of the major and minor principal stresses acting on a powder element, σ_1 and σ_3, it is possible to compute normal and shear stresses in any other direction. Referring to figure 2.19, we se that

$$\sigma_\theta = \sigma_1 \cos^2\theta + \sigma_3 \sin^2\theta = \frac{\sigma_1 + \sigma_3}{2} + \frac{\sigma_1 - \sigma_3}{2}\cos 2\theta, \qquad 2.23$$

and that

$$t_{\theta} = (\sigma_1 - \sigma_3)\sin\theta\cos\theta = \frac{\sigma_1 - \sigma_3}{2}\sin 2\theta. \qquad 2.24$$

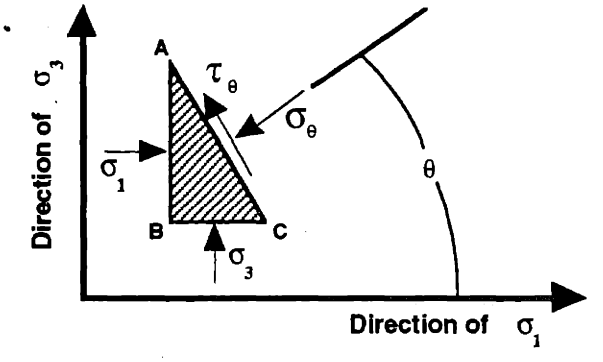

Figure 2.19: Stress condition along different planes in a powder element.

Given σ_1 and σ_3, it is possible to find the stress in any other direction by graphical construction using the Mohr circle. Or, given the σ_θ and t_q that act on any *two* planes, the magnitude and direction of the principal stresses can be found. A Mohr circle diagram for the powder element in figure 2.19 is shown in figure 2.20.

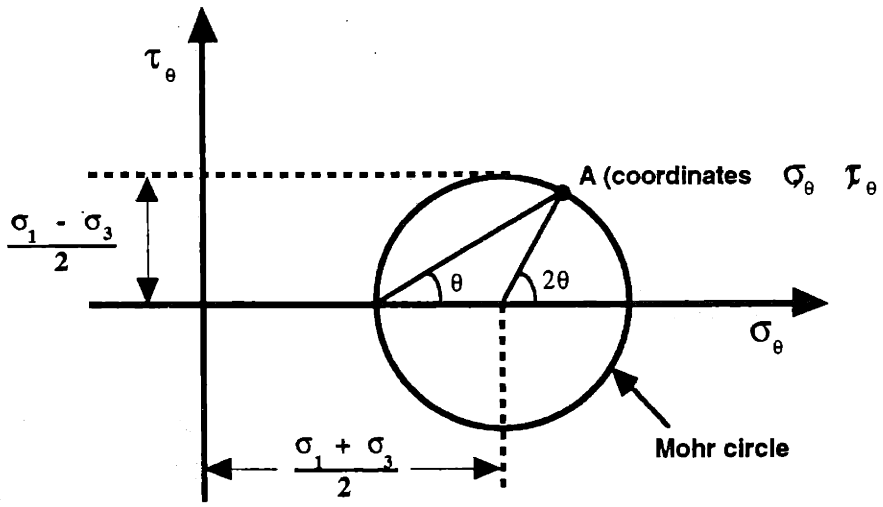

Figure 2.20: Mohr diagram for the state of stress at the point in figure 2.19. θ is measured counter-clockwise from the direction of σ_1.

The maximum shear stress at a point, t_{max}, is always equal to $(\sigma_1 - \sigma_3) / 2$. The maximum shear stress, therefore, also equals the radius of the Mohr circle. This maximum shear stress occurs on planes which lie at +/- 45° to the major principal stress direction.

2.3.4 Stress / Strain / Packing Relationships for Particulate Materials

Strains experienced by a particulate mass result from two effects: the elastic-plastic deformations within each particle, and the relative sliding and rolling of particles past one another. For the purposes of 3DP, strains resulting from the elastic-plastic deformations of particles are negligible, since the permissible level of stress which can be applied to the powder bed is far below the level where these effects are important. The densification mechanisms of interest will occur when the level of applied stress is sufficient to cause rolling and sliding of the particles. Stated another way, particle rearrangement begins when the shear stress applied to a given plane in the powder bed exceeds the shear strength of the particles in that plane. Using the background material presented above as an aid, we can now consider the yielding criterion for particulate materials given by various authors. As we will see, the critical difference in yielding behavior between solid and particulate materials is that particulate materials can undergo volume (i.e. packing density) changes.

Roscoe proposed a relationship between porosity and isostatic pressure. [50] For a powder mass with porosity e, he found that

$$e - e_0 = -\frac{1}{B}\ln\left(\frac{\sigma}{\sigma_0}\right), \qquad 2.25$$

where σ is the applied isostatic pressure, and e_0, B and σ_0 are constants. The logarithmic form of this relationship reflects experience that low forces are sufficient to produce visible changes in volume for loosely compacted powder, but very large forces produce only small volume changes when the powder is closely packed. [9]

In the realm of soil mechanics, the earliest and most basic yield criterion proposed was the Mohr - Coulomb failure law. It is not really a law at all, but is simply based on a collection of observations about when a powder mass will begin to deform, or "fail", under an applied load. The failure law places a Mohr envelope on a graph of shear stress versus normal stress. The envelope is defined by the relation

$$\tau = c + \sigma(\tan\theta), \qquad 2.26$$

where c is called the cohesion or cohesion intercept, and θ is called the friction angle or angle of shearing resistance. [29] Figure 2.21 is an illustration of the Mohr - Coulomb failure law. The Mohr envelope is drawn as a straight line.

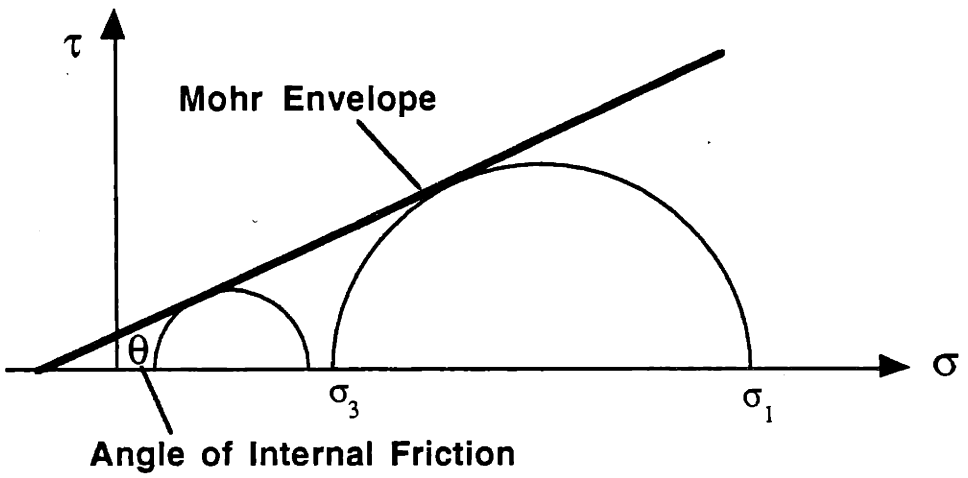

Figure 2.21: An illustration of the Mohr - Coulomb failure law.

The Mohr - Coulomb failure law may be understood from the following statements:

1. If the Mohr circle for a given state of stress lies entirely below the Mohr envelope for a soil, then the soil will be stable (i.e. not deform) for that state of stress.

2. If the Mohr circle is just tangent to the Mohr envelope, the full strength of the soil has been reached on some plane through the soil. This plane is called the *failure plane*.

3. It is not possible to have a soil in a state of stress whose Mohr circle intersects the Mohr envelope for that soil. Any attempt to impose such a state of stress would result in unlimited strains (i.e. the soil would flow freely).

The Mohr envelope for a given soil can be measured by locating the point of failure for two different stress conditions, such as those illustrated in figure 2.21. A line tangent to the Mohr circles which describe these two states of stress defines the Mohr envelope for that soil. The test equipment used to locate the failure envelope is described later in this section.

The Mohr - Coulomb failure law is significantly different from the previously described Tresca and von Mises solid body yield criteria. In figure 2.22, the Tresca yield criterion for solid bodies has been redrawn on a Mohr circle diagram so that it can be directly compared with the Mohr - Coulomb failure law illustrated above. The analogous Tresca criterion "envelope" is drawn as a horizontal line in the figure.

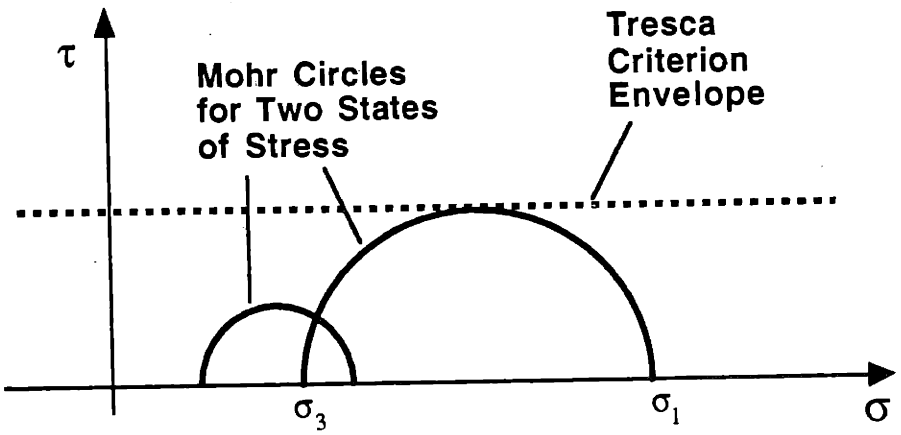

Figure 2.22: An illustration of the Tresca yield criterion redrawn on a Mohr circle diagram.

For solid bodies, the Tresca criterion states that failure will occur when the shear stress along any plane in the body reaches a critical value. The stress which is normal to this failure plane is irrelevant in determining the failure condition. Although this critical shear stress is a function of the major and minor principal stresses, σ_1 and σ_3, it is independent of the hydrostatic stress. For particulate bodies, the Mohr - Coulomb failure law predicts that failure will occur along the plane in which the *ratio* of the shear to normal stresses exceeds a critical value. Therefore, both the shear and normal stresses along the failure plane are of relevance when determining the failure condition. As the stress component normal to any given plane in the powder mass increases, the shear stress necessary to induce failure along that plane also increases.

In the simplifying case for which the powder cohesion c is taken to be zero, the Mohr - Coulomb failure law can be expressed in terms of the major and minor principal stresses and the friction angle θ. This expression is given in table 2.3, along with the analogous Tresca criterion. The Tresca yield criterion is a function of the *difference* between σ_1 and σ_3, while the Mohr - Coulomb criterion is a function of the *ratio* between σ_1 and σ_3.

Table 2.3: A Comparison of the Tresca and Mohr-Coulomb Yield Criterion Written in Terms of the Major and Minor Principal Stresses.

Tresca for Solids	Mohr-Coulomb for Powders (c=0)
$\frac{\sigma_1 - \sigma_3}{2} \geq k$	$\frac{\sigma_1}{\sigma_3} \geq \frac{1+\sin\theta}{1-\sin\theta}$

Although the Mohr - Coulomb failure law is widely cited in the soil mechanics literature, it is stated to be an over-simplification of the stress / strain response of particulate materials. [27] Furthermore, the packing density of the powder in question is not considered. Jenike described a modified version of the Mohr - Coulomb failure law which incorporated several changes and additions which better described the behavior of the powder located in the plane of failure. In the Jenike yield locus theory, a curved yield locus replaced the straight line of the Mohr envelope. This curved yield locus was stated to more closely predict the actual yielding behavior of powdered materials. An illustration of a Jenike yield locus is given in figure 2.23.

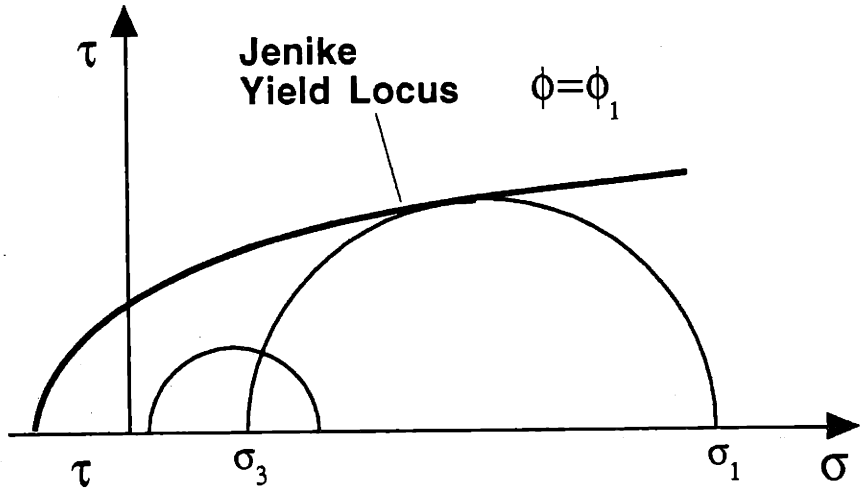

Figure 2.23: Illustration of the curved shape of the Jenike yield locus.

The interpretation and usage of the Jenike yield locus is similar to that of the Mohr - Coulomb failure law. Failure in the powder mass will occur when Mohr circle describing the state of stress within the powder crosses the yield locus. Powder will again begin to

flow along the failure plane within the powder mass for which the ratio shear to normal stress exceeds some critical value defined by the yield locus.

In the yield locus theory, the initial packing density of the powder mass is a key parameter. The location of the yield locus on the Mohr circle diagram is stated by Jenike to be a function of the initial packing density Ø of the powder mass. The applicability of the curve drawn in figure 2.23 is limited to a powder mass with an initial packing density equal to $Ø_1$. Separate and distinct yield loci exist for all possible initial packing density values. An illustration of three different yield loci is given in figure 2.24. As packing density increases, the corresponding yield locus expands outward.

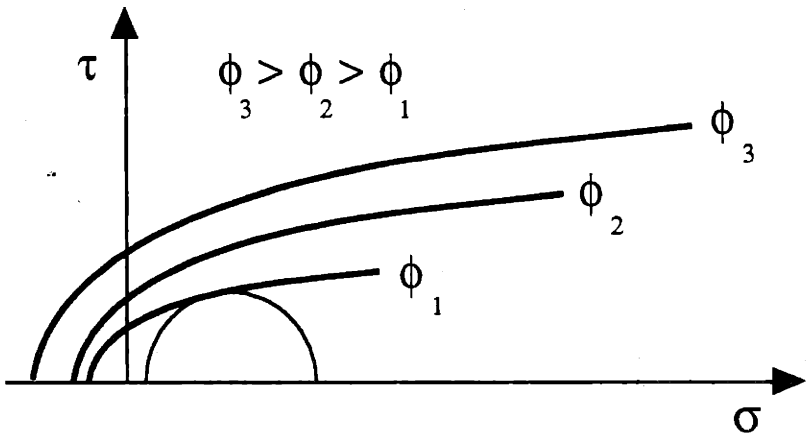

Figure 2.24: Illustration of three yield loci, each representing the yield condition for different values of initial packing density.

Unlike the Mohr - Coulomb failure law, which simply makes a prediction for the stress levels necessary for yielding to occur, the Jenike yield locus theory can also be used to predict how the packing density of the powder along the failure plane will change once failure begins. At the onset of failure, the flowing powder along the failure plane will either have its packing density increase, decrease or remain the same. The Jenike yield locus theory can be used to predict the stress conditions for which any of these three outcomes will occur. Since in this thesis we are trying to determine how to appropriately apply stresses to a powder mass in order to densify or compact the powder, the value of the additional capabilities of the Jenike yield locus theory is evident.

Figure 2.25 is another illustration of a yield locus for a single packing density, but also contains additional constructions which will be needed for the following discussion. Let us first consider only the portion of figure 2.25 which we are already familiar with, the yield locus for an initial packing density of $\emptyset_1$.

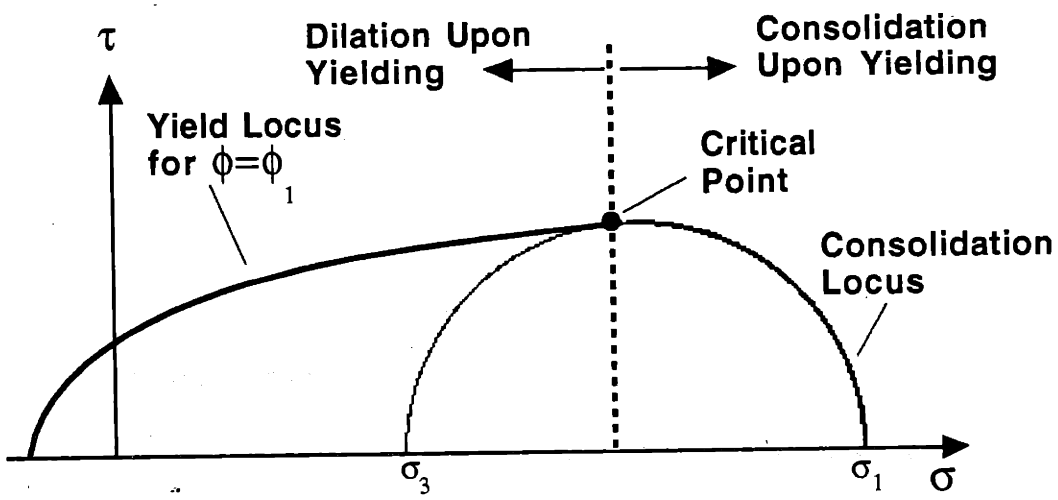

Figure 2.25: The Jenike yield and consolidation loci for a single powder packing density.

As before, when a state of stress exists in the powder mass for which the corresponding Mohr circle crosses the yield locus at any point, then the powder fails and begins to flow along the failure plane. Furthermore, the theory predicts that at the moment of failure, the powder along failure plane will *dilate* (i.e. its packing density will drop). Figure 2.26 is a conceptual illustration of why dilation occurs. In this illustration, two plates with firmly attached particles are experiencing both shear and normal forces. In order to slide past each other, the gap between the plates must increase. This gap increase represents dilation, or a reduction in local packing.

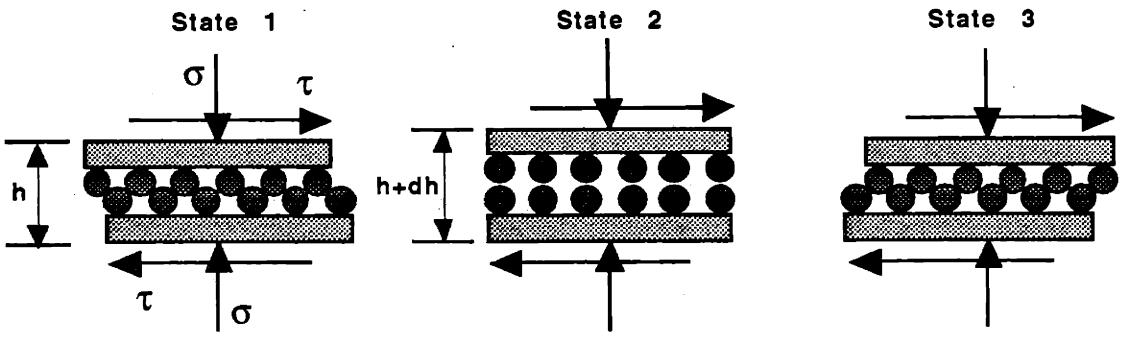

Figure 2.26: An illustration of how dilatancy is required during shearing of an over-consolidated system.

Dilation will occur in those instances where the normal stress applied to the failure plane is below a critical value. This critical value is identified on the yield locus in figure 2.25 as the *critical point.* The critical point is unique on the yield locus because it defines the one combination of normal and shear stress levels for which the powder will begin to flow *without changing in packing density.*

Jenike defined the critical point to be the end of the yield locus. He then considered the unique state of stress which was represented by a Mohr circle which both *passed through the critical point* and was *tangent to the yield locus at that point.* The portion of this Mohr circle which is to the right of the critical point is defined as the consolidation locus, and is also illustrated in figure 2.25. (Note - Since the yield locus is still sloped when it ends at the critical point, the critical point is not located at the top of the Mohr circle which defines the consolidation locus. Instead, it is always located to the left of the top.) Similar to the yield locus, if a state of stress is applied to the powder mass which is represented by a Mohr circle which crosses the consolidation locus, then the powder will fail along some plane. In this case, however, the packing density of the powder along the failure plane will *increase* as the powder begins to flow.

Figure 2.27 is an illustration of three individual yield and consolidation loci, each pertaining to a different level of packing density. [51] As the packing density Ø increases, both the yield and consolidation loci expand outward. The line drawn through the critical points of the different loci is defined as the *effective yield locus.*

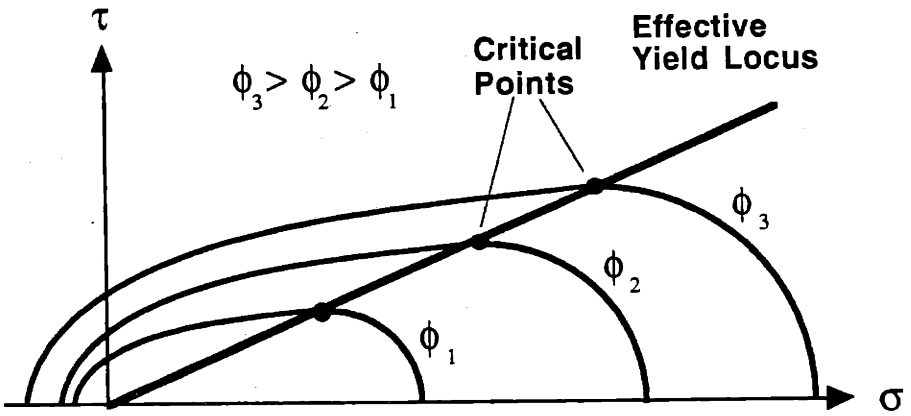

Figure 2.27: Yield / consolidation loci for three levels of packing, and the effective yield locus.

The use of the Jenike yield and consolidation loci can be illustrated by several examples. In figure 2.28, the three yield loci have been reproduced, and various loading paths have been added. For each example which follows, we will always start with a powder bed which has a packing density equal to $\emptyset_2$, represented by the middle curve. Somewhere within this hypothetical powder bed is a plane along which we can independently control the applied normal and shear stresses. (How we would do this is not important for these examples.) In the first example, we begin at point A in figure 2.28. At point A, the plane of interest is experiencing a small normal stress and no shear stress. The packing is stable, since we are far from the yield or consolidation loci for $\emptyset_2$. We now slowly apply an increasing shear stress, moving along the line A - B, until we reach point B, which lies on the yield locus for $\emptyset_2$. If the shear stress is increased infinitesimally beyond point B, then the powder bed fails along the shear plane. At failure, the powder along the shear plane dilates (i.e. the packing density drops). The shear resistance along the plane drops, and powder begins to flow freely. This is represented by a move from point B to point C in the diagram. At point C the packing density is $\emptyset_1$. (Note - We can no longer independently control the shear stress once the powder begins to flow.) At point C the powder continues to flow indefinitely along the shear plane. Point C is a *critical point* which lies on the *effective yield locus.* At point C the powder is freely flowing along the shear plane and has a packing density of $\emptyset_1$ along that plane.

Now consider the alternate stress path A' - B' - C'. The behavior is identical to the previous case, except that, after failure, the freely flowing powder along the shear plane

has a packing density less than $\emptyset_1$. The point C' is a critical point which lies on a yield locus (not shown in the figure) corresponding to a packing density less than $\emptyset_1$.

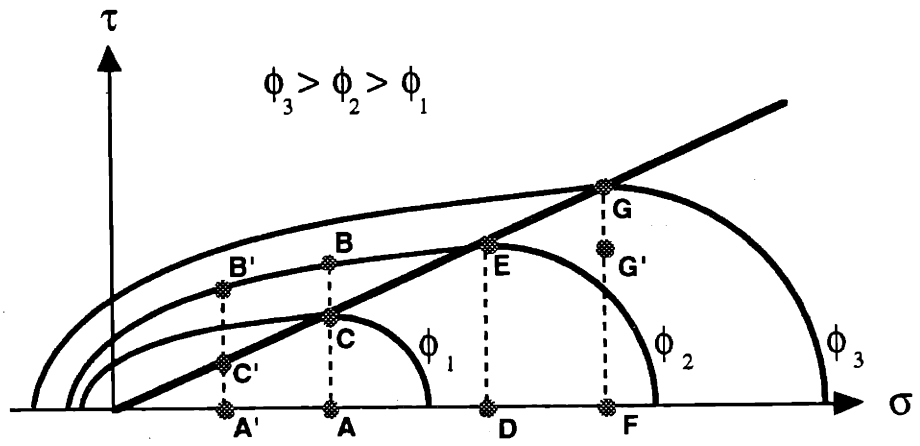

Figure 2.28: Illustration of how different stress paths result in different levels of packing.

In the above two examples, the powder was said to dilate when a critical shear stress was reached. In these cases, the powder was "over-consolidated" for the state of stress which it was experiencing. Returning again to figure 2.28, we now consider the stress path which starts at point D. As the shear stress increases, the powder mass remains stable until point E is reached. At point E, the powder along the shear plane begins to flow freely *without a change in packing density*. This is because point E, which is also a critical point, lies on the yield locus representing the packing density $\emptyset_2$, which is the packing density the powder mass started out at.

As a final example, we can consider the stress path which starts a point F. As the shear stress increases, the consolidation locus for $\emptyset_2$ is crossed. With further increases in shear stress, the packing density along the shear plane will begin to increase. Note that the powder is not freely flowing. Instead, these packing density increases are caused by minuscule rolling and sliding motions of the individual particles. For each incremental increase in shear stress above the consolidation locus, there is a corresponding incremental increase in packing density along the failure plane. If the shear stress increase was stopped at point G', then a stable, non-flowing powder packing would exist with a packing density somewhere between $\emptyset_2$ and $\emptyset_3$. If the shear stress is increased past point G' to point G, the packing density will continue to increase. At point G, the powder along the shear plane will have a packing density of $\emptyset_3$. Point G also lies on the effective yield locus and is

therefore a critical point. This implies the powder will begin to flow freely, at a packing density of $\emptyset_3$, once point G is reached.

As was defined earlier, the packing density for a given volume of powder can have any value between the apparent and tap densities for that powder. Therefore, in theory there exists a continuous range of yield and consolidation loci associated with packing density values between the apparent and tap density. No loci exist for packing values above the tap density. For stress conditions which cross the tap density yield locus, the predicted behavior of the powder mass is the same as before, with dilation and powder flow occurring along the shear plane. For stress conditions which cross the tap density consolidation locus, the behavior of the powder mass is not defined by the Jenike theory. This region is illustrated in figure 2.29. For stress levels in this range, only plastic deformation of the individual particles can cause further densification of the powder mass.

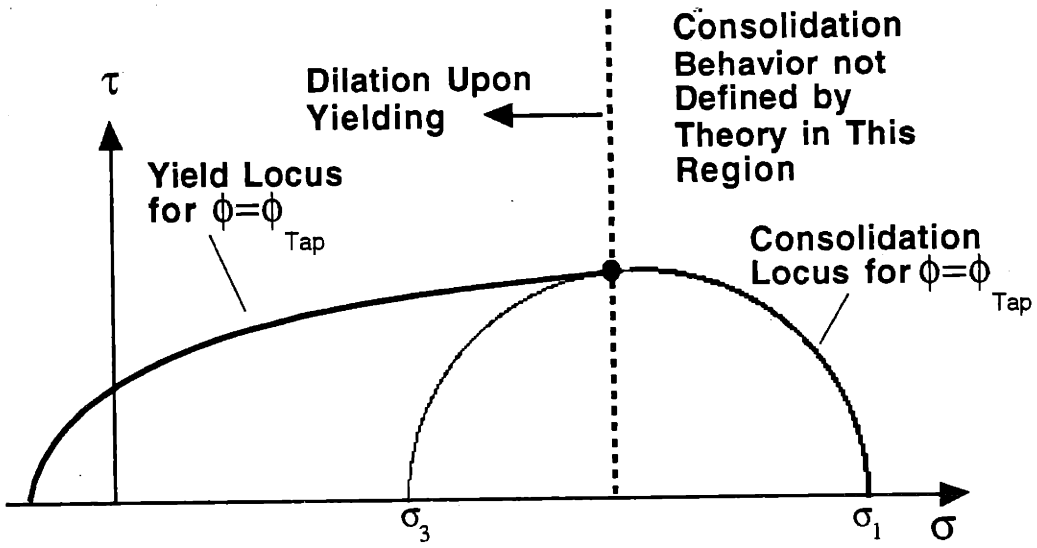

Figure 2.29: Yield and consolidation loci for the tap density of a powder.

The Jenike yield and consolidation loci are powerful conceptual tools for predicting how a powder mass might respond to an arbitrary stress input. To accurately predict packing, however, the shapes and locations of several yield and consolidation loci, in addition to the loading condition, must be known a priori.

2.3.5 Possible Shapes of the Consolidation Loci

As a final point concerning the Jenike yield and consolidation loci, we refer back to figure 2.25. The consolidation locus in this figure is represented by a portion of the Mohr circle which passes through the critical point for the $\emptyset = \emptyset_1$ yield loci, and which is tangent to the yield locus at this point. Other authors have proposed different shapes for the consolidation loci. Figures 2.30 is a sketch of a three dimensional yield surface presented by Suh. [56] The orthogonal axes in this image are the three principal stresses σ_1, σ_2, and σ_3, making the failure surface comparable to the Tresca and von Mises failure surfaces shown in figure 2.14. The surface includes both the yield and consolidation surfaces for a single packing density. The surface proposed by Suh closely resembles the 2D Jenike consolidation locus, although the bulb end deviates slightly from spherical.

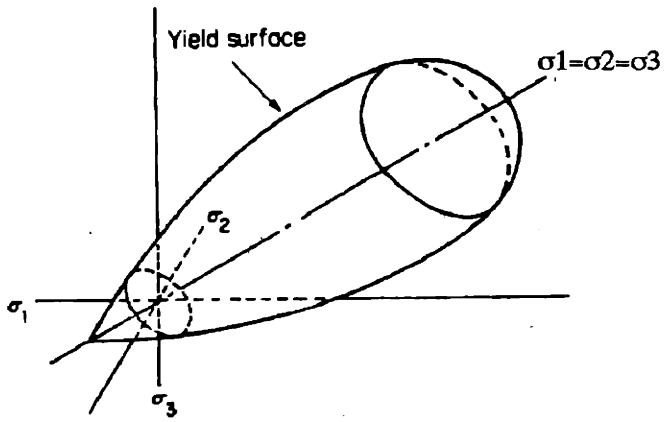

Figure 2.30: A 3D failure surface for particulate materials as presented by Suh. [ref. 55, p.204]

2.3.6 Comparison of Failure Laws for Solid and Particulate Materials

A comparison of the yield surfaces illustrated in figures 2.14 and 2.30 reveals significant differences in the yielding behavior of solid and particulate materials. The most obvious difference is that the particulate yield surface is close-ended, and only applies to a single packing density. In contrast, both the Tresca and von Mises yield surfaces are open-ended, and the material volume is assumed constant. These differences demonstrate that the isostatic component of an applied stress field can have a significant influence on the

plastic yielding of a particulate material, compared to a solid material where it causes not plastic deformation at all.

Another difference between the failure characteristics of solid and particulate materials is the location of the shear failure plane. In an earlier description of the Mohr circle, it was shown how the maximum shear stress occurs on planes which lie at +/- 45° to the major principal stress direction. According to the Tresca yielding criterion, shear failure will occur along this plane of maximum shear stress. In contrast, the definitions of both the Mohr - Coulomb failure envelope and the Jenike yield loci state that shear failure (and subsequent dilation) will occur along the plane where the *ratio of shear to normal stress* has a specified value, and not along the plane of maximum shear stress.

2.3.7 Tests Used to Characterize the Behavior of Particulate Materials

We will conclude this section on powder statics with a description of the standard tests used in soil and powder mechanics to evaluate the deformation behavior of particulate materials. These include the triaxial, shear cell, and oedometer (confined compression) tests. All these tests involve the application of an increasing stress distribution to a powder mass and observations of how and when the powder mass plastically deforms.

The triaxial compression test from soil mechanics is the most sophisticated of the three tests, and allows the most precisely controlled stress distribution. Figure 2.31 shows a schematic diagram of a triaxial test apparatus. In this test, the sample of soil, a cylindrical core of length at least twice that of the diameter, is enclosed in a rubber sleeve and placed inside a cylinder so that a hydrostatic fluid pressure may be applied as the minor principal stress on the soil. The major principal stress is applied in the axial direction by a vertical ram. The axial load is increased until failure occurs. The Mohr circle corresponding to the stress distribution at the time of failure is recorded on a graph of shear stress versus normal stress. By varying the initial hydrostatic pressure, different stress distributions at the time of failure can be recorded, and the Mohr - Coulomb failure envelope or the Jenike yield locus can be drawn.

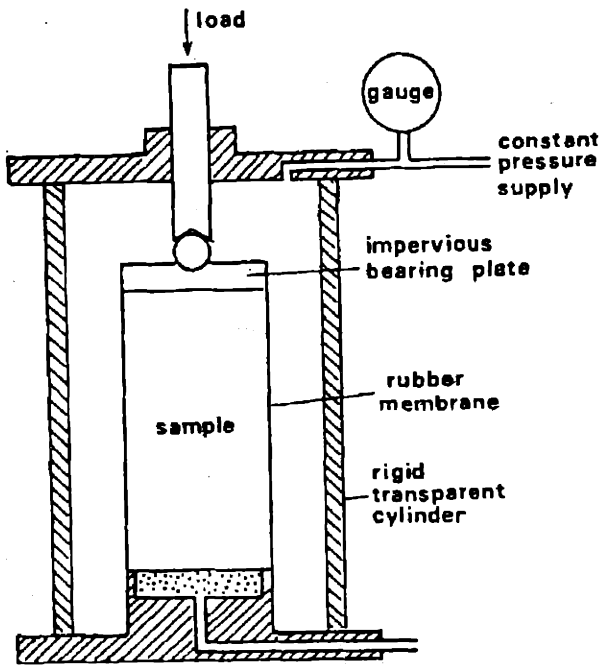

Figure 2.31: A triaxial compression cell. [ref. 61, p.25]

There are several shortcomings to the triaxial test. During failure, the actual shear planes within the sample cannot be observed. Although the average packing density of the sample can be measured volumetrically both before and during the test, it is not possible to measure the local packing density along the shear planes. Multiple Jenike yield loci for different packing values can only be obtained if it is possible to alter the initial packing density of the sample at the beginning of the test. It practice, this is usually not possible. There is no convenient method for uniformly loading a container to a specified packing density value somewhere between the apparent and tap density for a given powder. This limitation is not relevant to soil mechanics, where there is usually only one packing density of interest for a given soil sample, specifically the packing density in the region of earth from which the sample was obtained.

The shear cell apparatus consists of a shallow cylindrical cell split horizontally. A sample of powdered material under examination is placed in the cell prior to the test. The lower half of the cell is fixed and a constant low shear strain rate is applied to the movable upper half. The resultant shear force is continuously recorded during each run. A number of normal loads are applied so that the relationship between shear stress and normal stress can be determined. A illustration of a shear cell is shown in figure 2.32.

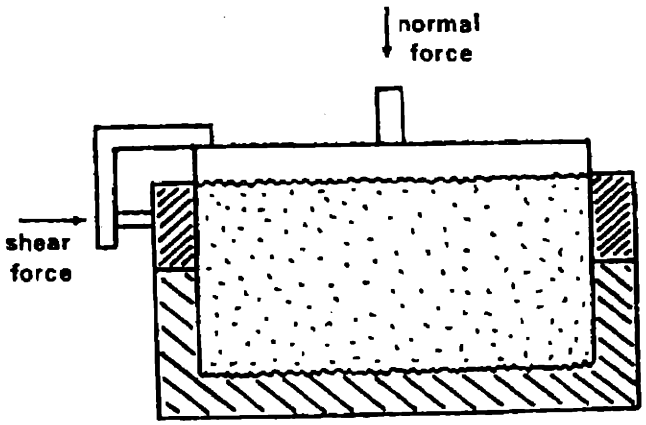

Figure 2.32: A shear cell. [ref. 61, p.27]

Depending on the applied normal load and the initial state of powder packing in the shear cell, there is one of three possible characteristic response modes which can occur during shearing. These response modes are illustrated in plots of shear stress versus shear strain in figure 2.33. If the powder is over-consolidated, then it is too tightly packed for the applied normal load. During shearing, the powder will dilate along the shear plane. The shear stress will go through a peak value at the instant prior to failure, and then drop off to a constant value after the powder along the shear plane has dilated and is flowing freely. If the powder is critically consolidated prior to shearing, then no dilation will occur during shearing. Once a certain value of shear stress is reached, the powder will fail along the shear plane with no change in packing. The asymptotic shear stress value for the over and critically consolidated cases is identical, as is the final packing density along the shear plane.

If the powder is under-consolidated, failure will begin as soon as any shear stress is developed along the shear plane. During shearing, the powder will consolidate, and the shear resistance will increase. Shear cells are limited in the amount of travel which the upper portion can experience before the shearing area has been significantly altered. If it were possible to shear the powder indefinitely, then in the under-consolidated case the asymptotic shear stress value and the final packing density along the shear plane would again reach the same value of the other two modes.

For all three modes it is the case that if the test were continued until the asymptotic behavior was reached, and the shearing was momentarily stopped and then started again,

the latter response curve would always be that of the critically consolidated case. These three response modes correspond to the previous examples given to describe the Jenike yield loci.

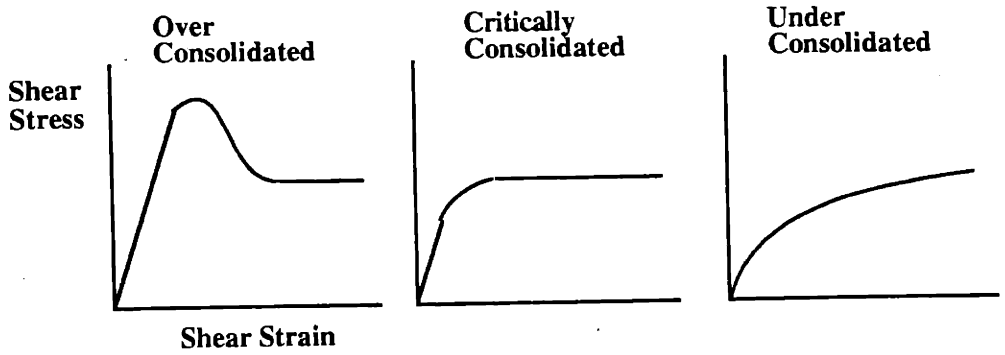

Figure 2.33. Three possible response modes for a shear cell run. The mode obtained depends on the applied normal load and the initial packing density.

The shear cell test can be used to locate the yield locus for a given initial packing density, as well as the effective yield locus of the powder as defined in the Jenike theory. The process for obtaining these loci can be best explained by considering several runs of a shear cell test, all of which start with the powder in the cell loaded to the tap density. The applied normal load for the first test is near zero, with subsequent runs having incremental increases in the normal load. (Recall that the normal load remains constant during each test.) Since the powder being tested is at the tap density and the initial tests are to be performed at low normal loads, the powder in the cell is in a over-consolidated condition. The shear stress versus shear strain response for these tests will resemble the plot shown in figure 2.34. During each test, the shear stress will go through some peak value, at which point the powder along the shear plane fails. As the powder dilates the resulting shear stress will eventually reach a constant value at which point the powder along the shear plane is sliding while remaining at some new, lower packing density. A single peak and sliding shear stress data point can therefore be obtained from each shear cell run. These are labeled as points *A* and *B*, respectively, in figure 2.34.

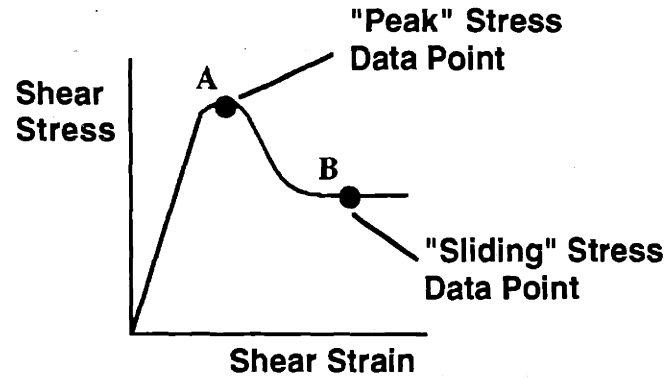

Figure 2.34: Shear stress vs. shear strain for a single shear cell run. For the normal stress applied, the powder is in an over-consolidated condition.

After several runs have been performed at different values of applied normal stress, the collected data can be used to construct the yield locus for the tap density, and effective yield locus. This is illustrated in figure 2.35.

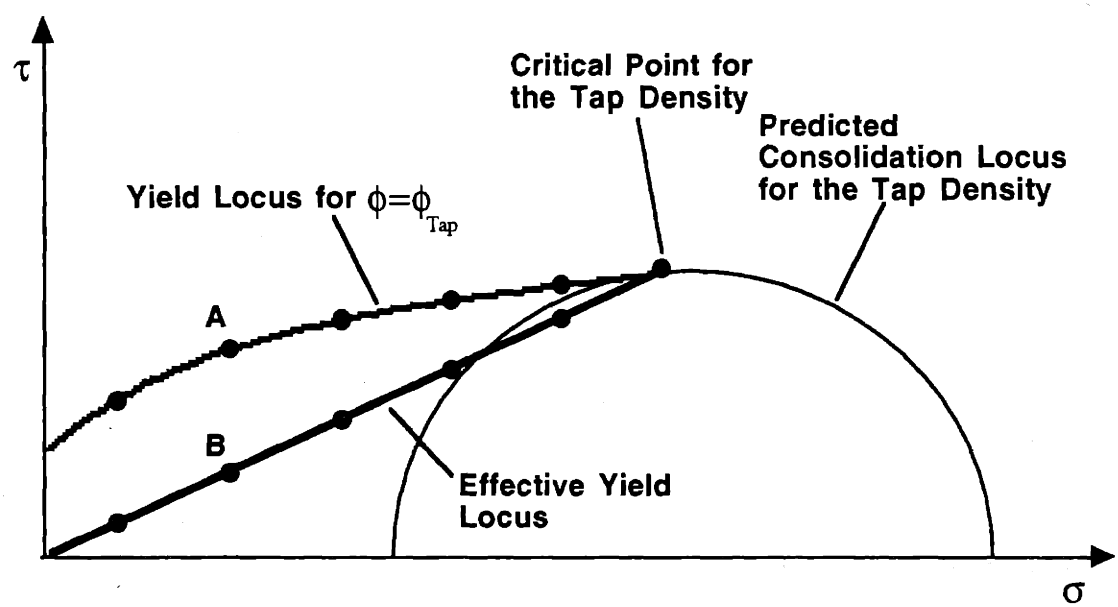

Figure 2.35: Construction of the yield locus for the tap density, and effective yield locus, based on the peak and sliding shear stress data from several shear cell runs.

All the *B* data points in figure 2.35 are critical points which lie upon the curved yield loci for packing densities less than the tap density. Unfortunately, the packing density corresponding to each *B* data point is not known. A drawback of the shear cell test is that it is not possible to measure the packing density of the powder along the shear plane

during and after failure. Although it is possible to measure the vertical rise of the plate used to apply the normal stress, and therefore the change in volume of the shear cell, the packing along the failure plane cannot be deduced from this measurement. This is because there are regions of powder above and below the failure plane which do not change in packing during the test.

As the normal stress applied in each shear cell run is increased, the difference between the measured peak and sliding shear stress values decreases. At some high normal stress value, the difference becomes zero, and the powder was therefore critically consolidated at the start of this shear cell run. The value of normal and shear stress at this point locate the critical point on the tap density yield locus. The Mohr circle which both contains this point and is tangent to the tap density yield locus locates the consolidation locus for the tap density.

The shear cell test has drawbacks similar to the triaxial test. It is usually not possible to uniformly load the cell to a specified packing density. Powder is typically tamped into the cell to attain at or near the tap density of the powder sample, since this is the only density which can be consistently reproduced.

The third test used to measure the stress / strain properties of soils is the oedometer test. This is a one-dimensional, confined compression test. In an oedometer test, a vertical stress is applied to a powdered mass while the powder is constrained horizontally by rigid walls. Vertical strain is recorded during the test. The applied load can be monotonic or varied over time. The oedometer test is the simplest of the three tests to perform.

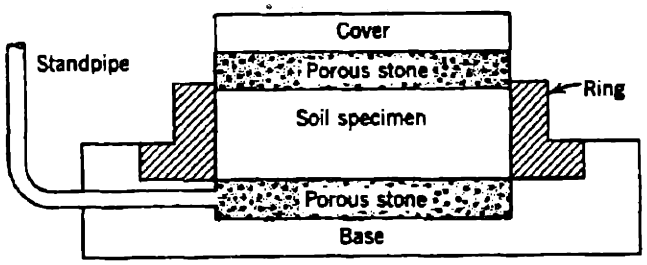

Figure 2.36: An oedometer (confined compression) test apparatus.
[ref. 29, p.118]

The principle drawback of the oedometer test is that the complete state of stress in the powder is not known. Although it is possible to measure the resultant horizontal stress generated by the retaining walls in order to have a more complete picture of the powder stress condition, this additional complexity is usually avoided. The oedometer is the only test, however, in which it is possible to estimate packing based on the vertical position of the pressure plate. This is true only if the powder mass has at least a 4:1 width to height ratio. The oedometer test is often used for its simplicity and because it approximately represents field loading conditions often encountered in soil mechanics.

Figure 2.37 shows two oedometer stress / strain curves for a medium to coarse quartz sand. The curves show the stress / strain behavior before plastic deformation of the individual particles, and are very characteristic of particulate systems. Note that positive strains are plotted downward, which is a common practice in soil mechanics. The stress / strain curves are concave upward, indicating the sand gets stiffer and stiffer as the stress is increased. This stiffening behavior is called *locking*. The strains result from the collapse of pores, with loose arrays of particles collapsing first, followed by denser arrays.

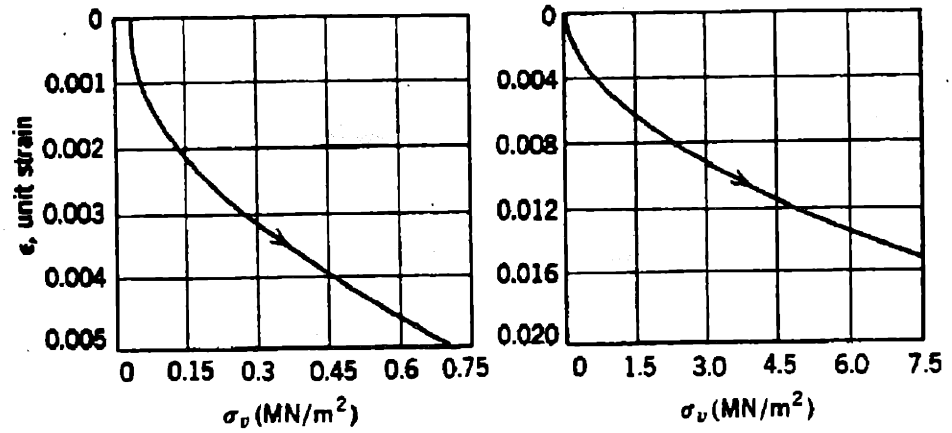

Figure 2.37: Stress-strain curves for confined compression. [ref. 29, p.123]

The strains which result for the sliding of particles are largely irreversible. Rebound which occurs during unloading is caused by the release of elastic energy from the particles, and also from some reverse sliding. [29] The stress / strain behavior of course, uniform sand to repeated loading cycles in an oedometer is shown in figure 2.38. Note that the majority of the permanent strain occurs during the first several cycles. Eventually, a stable hysteresis loop is obtained in which there is no further permanent strain.

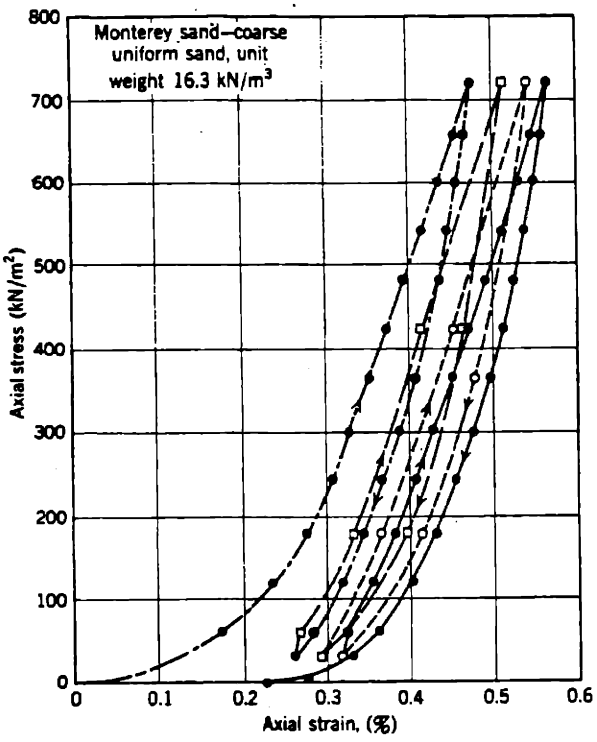

Figure 2.38: Stress-strain curves during several cycles of loading.
[ref. 29, p.125]

2.4 Powder Dynamics

A powder body can support extremely large monotonic loads without most points in the body ever reaching the tap density of the powder. The culprit in this instance is particle interlocking - the mechanical wedging of powder particles. Once a powder body is extensively locked, further increases in monotonic loading only serve to enhance the locking effect. Densification by particle sliding and rolling becomes less effective, and only plastic deformation of the individual particles can result in significant increases in packing density. The magnitude of stresses required for individual particle deformation are far beyond those allowable in the 3DP process. A method of reaching the tap density of the powder, other than by brute force, is required.

Figure 2.38 from the previous section showed how several loading cycles in an oedometer compression test could result in significantly higher packing than a single loading, even though the initial stress level was never exceeded. A conceptual model of

why this is the case is that during each unloading, there is a small amount of particle rearrangement which subtly alters the geometric arrangement of the individual particles. During the subsequent loading cycle, some fraction of the pore structure which was previously mechanically interlocked and stable has now become unstable and will collapse. Over the course of several loading cycles, the rearrangement and densification process continues.

The use of oscillating stress fields to improve powder densification over those levels which could be attained with a monotonic stress field of similar magnitude is the topic of this section.

2.4.1 Conceptual Models of How Dynamic Compaction Proceeds

Modeling of the permanent or plastic deformation response of a particulate mass to cyclic loading has been approached by many researchers, and is considerably more complex than the modeling of the static response. Gray summarized the work of several authors and found that, in addition to the time for which particles were vibrated, there were five parameters of vibration, one or more of which may be instrumental in causing the particulate material to adopt a closer packing. [23] These included frequency, amplitude, acceleration, energy input and power input. Only two of these parameters can be defined independently, but each one had been named, in various circumstances, as being the critical factor in ensuring the closest packing. Gray concluded that

> ... in spite of the considerable amount of empirical investigation of the effect of vibration on the compaction of particulate material and the widespread industrial usage of vibration for this purpose, it remains difficult to predict the characteristics of the most appropriate vibration equipment for material and situations which have not already been examined experimentally. [ref. 23, p.92]

Because of the many variables which can affect the densification process, a given model is usually limited to a specific set of initial conditions, such as size and direction of applied load, and the type of particulate material which is being loaded. Although the densification response for any particulate system is usually unique, some common characteristics exist across systems. In general, the majority of the permanent strain occurs during the initial period in which stress reversals are applied. This is the primary consolidation period. The particulate mass exhibits increasing stiffness with each stress

cycle. Eventually, for a given loading condition, a steady-state response will be reached at which point there is little or no further densification. This is referred to as the secondary consolidation period. A characteristic soil response to dynamic loadings is illustrated in figure 2.39. Note that the horizontal axis is log(time).

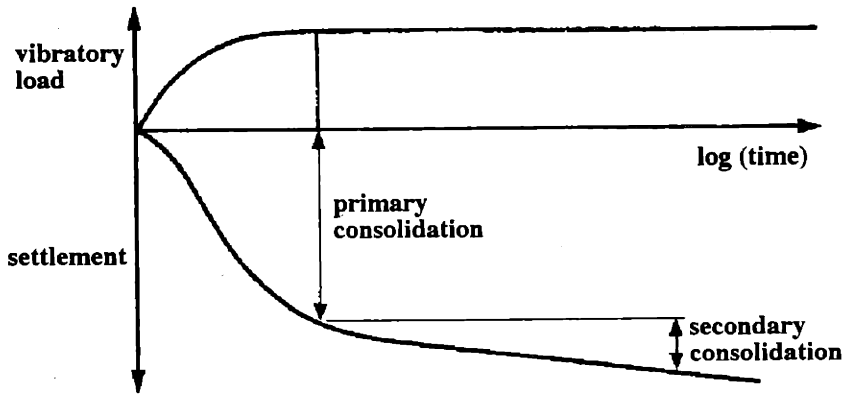

Figure 2.39: The effect of cyclic loading on the settlement of soils. [ref. 46, p.412]

Das stated that the study of the vibrational compaction of soils could be divided into two different vibratory conditions: applied stress and applied acceleration. [12] These conditions are explained by considering the container full of soil illustrated in figure 2.40 In the applied stress condition, the container remains stationary and a stress distribution is applied to one or more of the exposed soil surfaces. Applied stress is representative of vibratory conditions such as steam-rolling of earthen surfaces. In the applied acceleration condition, the entire container of soil oscillates through a pre-defined motion. This condition is representative of an earthen slope undergoing motions imposed by an earthquake. For either condition, the oscillatory input can be smoothly sinusoidal, or can have a regular but abrupt impulse pattern.

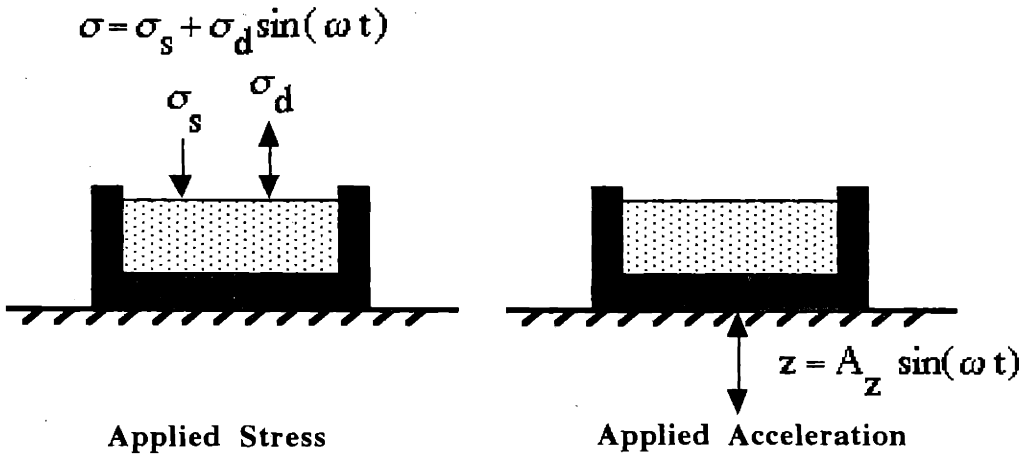

Figure 2.40: Two modes of vibrational densification.

O'Reilly and Brown proposed a simple spring and sliding block model to explain the highly non-linear behavior of soils to cyclic loading. [45] The model is shown in figure 2.41. In the model, sliding blocks represent interparticulate sliding, and the springs between the blocks represent the compliance between particles and groups of particles. The changes in the internal geometry of the soil as particle contacts are made, broken, and re-established are represented by the variable direction and magnitudes of the normal forces N. These variations in direction and magnitude are essentially random about mean values which represent the inherent interparticle geometry of the soil, but are weighted to account for recent changes in geometry. The plane of sliding slopes slightly, representing the propensity of granular materials to reduce their potential energy by densification.

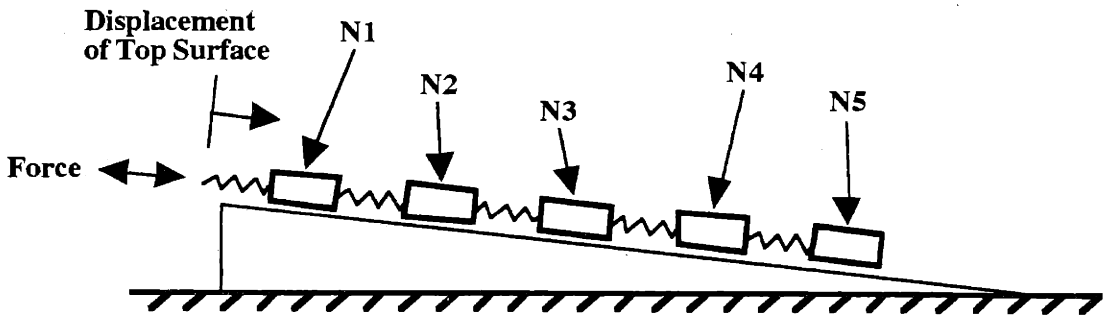

Figure 2.41: A simple spring and block model of soil behavior under cyclic loading. [ref. 45, p.9]

Figure 2.42 shows a typical smoothed response for the above system. During the initial few stress reversals, a significant amount of permanent strain is developed. Over time, only elastic strains remain, and are completely recoverable.

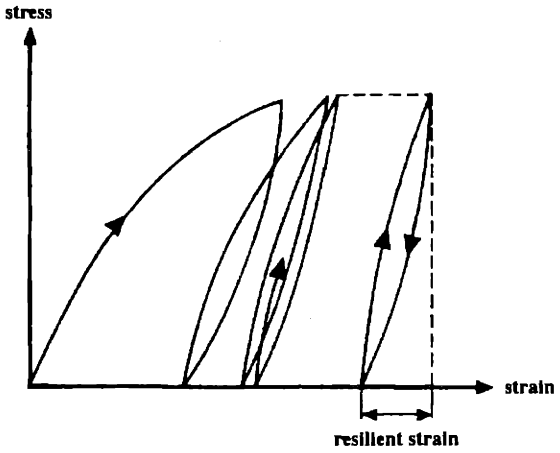

Figure 2.42: Smoothed response of the spring and block model shown in figure 2.41. [ref. 45, p.9]

Takahashi and Suzuki conducted a numerical analysis on the tap densification behavior of ceramic powders, and proposed a general relation between the tapping number N and the fractional volume change of the powder bed. [59] The tapping number is the cumulative number of impacts which the sample has experienced during densification. (Note that tap densification is an example of applied *acceleration* to a powder mass.) The authors viewed the tapping process as one in which holes in the porous bed are filled in. An initial assumption is that the elementary filling process is a first order reaction rate of the reciprocal tapping number. The proposed equation, in differential form, is given as:

$$\frac{dV^*}{dn} = -kV^*, \qquad 2.27$$

where

$$V^* = \frac{(V_o - V)}{(V_o - V_\infty)}, \qquad 2.28$$

and $n = 1/N$. V_o is the initial volume of the powder bed, V_∞ is the apparent final volume, and V is the volume at the tapping number, N. The solution to this expression is given as:

$$V^* = \exp(-k/N). \qquad 2.29$$

Thus, the smaller the constant k, the faster the holes in the bed are filled during tapping. The constant k is viewed by the authors as a type of energy barrier against filling under certain test conditions, although they note that their fundamental equation is only a mathematical model and is not derived from any basic principles about the interactions of powder particles during densification. The authors expand on their initially simple model by further assuming that in a typical powder bed there would be several types of holes, the key difference being predominately the size of the hole, and that each type of hole would have a unique filling rate constant k_i. The overall change in V^* can then be obtained from the summing of the rate equations for the different types of holes. An additional assumption is that the different types of holes are independently filled without interaction. The solution to the initial differential equation can be given in modified form as

$$V^* = \sum_{i=1}^{J} a_i \exp(-k_1/N) \left(\sum_{i=1}^{J} a_i = 1 \right), \qquad 2.30$$

where a_i is a dimensionless coefficient which corresponds to the relative volume occupied by each type of hole.

Although the number of coefficients a_i can be arbitrarily large, the above model can be used to gain insight into the tapping process by considering the case of only two coefficients, a_1 and a_2. In physical terms, this would represent a bed in which there were large macro-voids, in addition to the smaller holes whose size is on the order of that of the powder. During the very initial stages of densification, the large macro-voids are rapidly collapsed. Subsequent densification occurs from the slow process of particle rearrangement in the filling of the small holes.

2.4.2 Lumped Parameter Models of Foundations

The response of a building foundation to cyclic loads from operating machinery is a common area in which lumped parameter models are used. Although much larger in scale than the 3DP system, the response of foundations to vibration has many similarities to the densification of a powder layer on the 3DP apparatus. In both cases, a load is being applied to the top surface of a particulate mass. The load is transmitted through a solid object (a concrete foundation or a spreading device, as the case may be) into the particulate

mass, and the load can be in the vertical or horizontal direction. Although the elastic response of a particulate system is often non-linear, a model which is often applied is a simple, second-order lumped-parameter model with a single degree of freedom. This model is illustrated in figure 2.43. In this model, the mass is taken to be the mass of the foundation, and the mass of the underlying soil is often neglected for simplicity. The spring and damper represent the elastic and dissipation properties of the soil. For a loading of the form $F = F_0 \sin \omega t$, the response of the mass is given by the expression $m\ddot{x} + b\dot{x} + kx = F_0 \sin \omega t$.

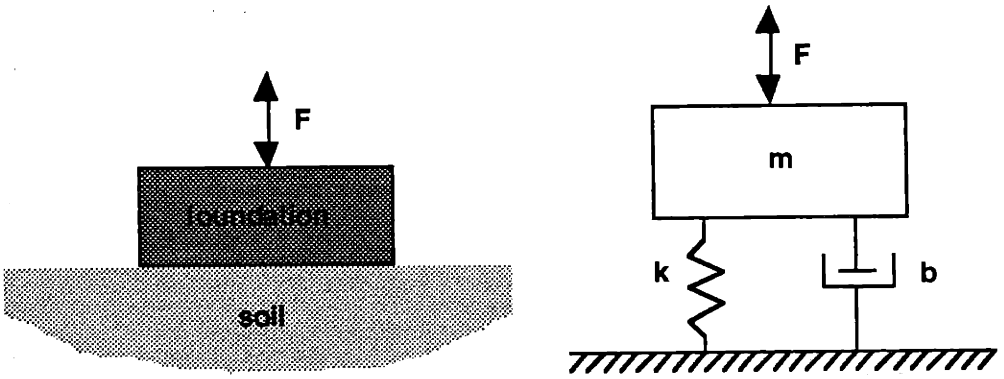

Figure 2.43: A simple second-order model for the elastic response of a particulate mass to a cyclic force input.

Although very simple in nature, this model often does an excellent job of explaining the dynamic response of a variety of systems. Figure 2.44 depicts the frequency response to vertical loading of a surface foundation for a range of load amplitudes. Although the response is clearly non-linear, there is a definite resonant peak for a given load amplitude. The decrease in resonant frequency and the increase in displacement amplitude are consistent with a decrease in soil stiffness over the indicated load range.

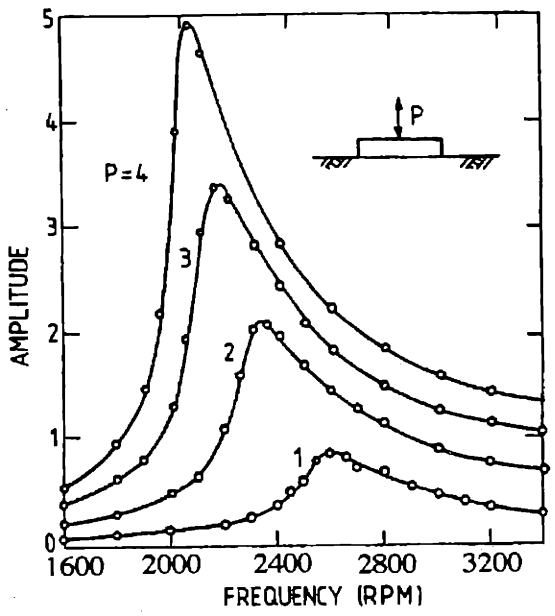

Figure 2.44: Experimental frequency-response curves for vertical vibration of a shallow foundation. [ref. 13, pp.385]

An elastic characterization of a particulate system is useful in vibrational compaction theory because many authors have found that the *plastic deformation* response (i.e. powder densification) proceeds most rapidly at the resonant frequency of powder mass in combination with the vibrational apparatus. [41]

The values of the spring and damping constants used in the above model are generally described by complex functions, not only of the particulate material but also the loading condition. As such, these values can be difficult to measure. As a first approximation, the spring constant can be obtained as follows. The velocity V_c of a compressive wave through particulate material is given by

$$V_c = \sqrt{E/\rho}, \qquad 2.31$$

where E is the Young's modulus and ρ is the bulk density of the material. By measuring V_c and ρ, E can be obtained. The vertical spring constant K_v for a rigid rectangular base of width B and length L resting on an elastic surface is then given by

$$K_{vertical} = \frac{G}{1-\nu}\beta_z (BL)^{1/2}, \quad 2.32$$

where $G = E/2(1+\nu)$ is the shear modulus and ν is the Poisson's ratio, which can be estimated as 0.35 for dry powders. β_z varies between the values of 2.2 and 2.8 as the ratio of *L/B* varies between 1 and 10. [ref. 29, p.231]

The damping in particulate systems results from loss of energy through propagation of waves away from the immediate vicinity of the applied load, and the internal energy loss within the particulate material owing to frictional dissipation. The damping ratio for various applied stresses can be obtained from tables in soil mechanics texts. [ref. 29, p.230] Typical values for the damping ratio range between 0.2 and 0.6.

2.4.3 Additional Experimental Results

Dobry and Whitman performed studies on the compaction of sand on a vertically vibrating table. [14, 15] These studies fall into the category of applied acceleration to a container. In these tests, a container was rigidly attached to a vertically vibrating table and filled with sand. Vibration at a specified frequency and acceleration was applied, and then the packing density of the sand was measured. The variables considered were the frequency and amplitude of vibration, and size and shape of the container. No deadweight was applied to the top of the powder. Peak-to-peak amplitudes of up to 0.15" and frequencies 10 - 60 Hz were used. All samples vibrated for 10 minutes. Quartz sand with particle sizes between 0.25 and 2 mm was used.

Results showed that frequency and acceleration were the key variables, with container size and shape having little importance. Very little densification occurred at accelerations below 0.9 g, and most densification occurred between 0.9 and 1.1 g's. There appeared to be a loosening process between 1.3 and 2g. The theoretical model which was developed replaces the sand by an elastic solid body placed on the table. For table accelerations below 1g, the solid body moves with the table at all times. For accelerations above 1g, the solid body experiences a period of *free fall* followed by an impact with each oscillation. Densification in the actual sand is produced because, during free fall, the intergranular forces are zero. At the point of impact, the grains are free to move to more stable positions. Density increases with larger impacts, until the point where the reflected impact stress wave through the body causes tensile stresses to appear in the sand mass. From this point on, larger impacts loosen the sand. The magnitude of the reflected impact

stress wave is proportional to the impact velocity, which is a function of both table acceleration and frequency.

Note that the method of vibrational application in Dobry and Whitman's work - applied acceleration to the powder container - is not really an option for the 3DP process, since this would correspond to the shaking of the entire powder bed. For 3DP, the bed will have to remain stationary and the vibrational energy will have to be delivered through the top surface. The powder particles in the powder bed will not have an opportunity to experience free fall. Probably the most important point to be taken from this work is that vibrational densification mechanisms can produce both compressive and tensile stress waves in the powder bed. Misapplication of vibrational energy can therefore loosen, instead of densify, the powder layer.

D'Appolonia conducted oedometer tests on a dune sand for a controlled vertical stress condition. [11] This study falls into the category of applied stress to a powder surface. These results are shown in figure 2.45: A superposition of static and dynamic stresses were applied over a frequency range of 1.8 - 6 Hz. A static stress of 20 lb/in^2 was applied, and the dynamic stress was varied such that the ratio of dynamic to static stress, σ_d/σ_s, was between 0.2 - 0.7. It was seen that, for a given value of σ_d/σ_s, the vertical strain ε_z was proportional to log(N), where N is the number of load cycles. Also, for a given number of load cycles, the vertical strain increased with increasing values of σ_d/σ_s.

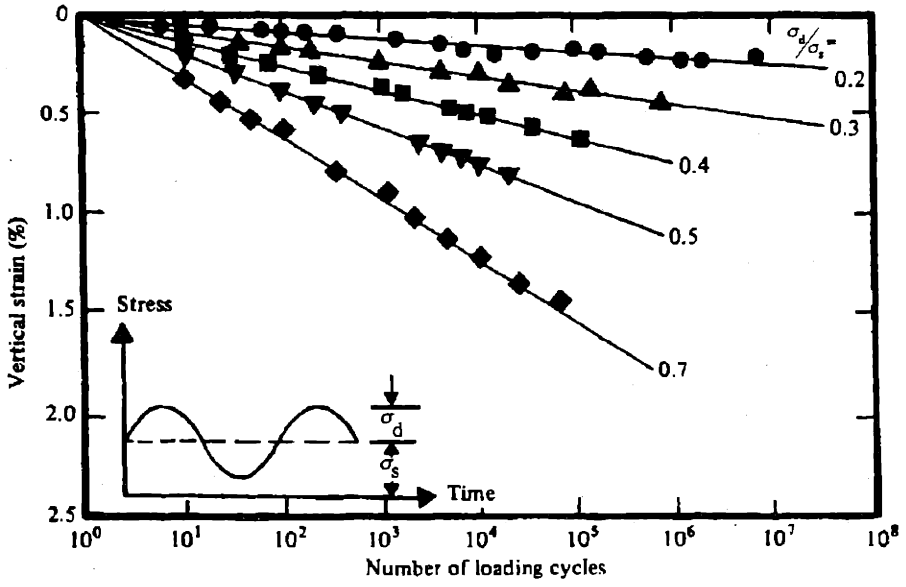

Figure 2.45: Compression of a dune sand under a controlled vertical stress condition. [ref. 11, p.59]

2.5 Discussion

The packing and compaction of powdered or granular materials can be achieved by **many** different methods. For example, in standard P/M practice, large stresses are applied to powdered metal which is constrained by a die. Stresses are large enough such that the individual powder particles are plastically deformed. The applied stress is non-oscillatory in nature. In contrast, densification of soil in construction practice is several orders of magnitude lower in stress. Static and dynamic stresses are applied by a large roller. Densification occurs primarily by particle rearrangement, with almost no plastic deformation of the individual soil particles.

Identifying and studying the variables affecting vibratory compaction is a difficult task, in part because of the large number of variables. Hausner described the variables which are involved in vibratory compacting. [25] These are listed in table 2.4.

Table 2.4: Variables Involved in Vibratory Compacting [25]

1. Characteristics of the Powder Density of Powdered Material Average Particle Size Particle Size Distribution Particle Shape Particle Surface Conditions Adhesion Forces Between Particles Total Weight of Powder	**2. Characteristics of the Vibrations** Frequency of Vibration Amplitude of Vibration Duration Of Vibration Direction of Applied Vibration Number of Vibrators Applied
3. Characteristics of the Container Shape, Size and Wall Thickness Container Material	**4. Characterization of Processing** Humidity Temperature Pressure Applied

We will not attempt to consider here how each of these variables might affect the densification of spread layers in the 3DP process. Such a discussion would not be possible, given our current understanding of the layering event. (Indeed, a complete consideration of the variables in Table 2.4 may not be possible at all.) It is possible, however, to discriminate between those broad areas of densification theory which will or

will not be of interest to us. Figure 2.46 is a flowchart which describes the variables associated with the different methods of powder compaction. The flowchart focuses on those methods which are most likely to be applicable to 3DP. Variables at the top of the chart are the most global in nature, and become more specific to a given densification process towards the bottom of the chart. The variables described in the flowchart are:

Ultimate Level of the Applied Stress - The stresses required to plastically deform metal particles are extremely high, usually exceeding 100MPa. This level of stress far exceeds the permissible level for 3DP. Therefore, compaction processes which plastically deform the particles are ignored. Compaction must therefore be accomplished by particle rearrangement in the powder bed.

Nature of the Applied Stress - The stresses applied during densification processes can be static, oscillatory, or a superposition of both. In general, non-oscillatory stresses are usually associated with high stress, plastic deformation processes as described above. Of interest to 3DP are those processes which use low level vibrational stresses to achieve densification.

Time Frame in which the Stress is Applied - Any compaction process should be as rapid as possible. Processes which affect the packing of material over large time frames are not useful to 3DP.

Method in which the Stress is Applied - It is likely that a new 3DP compaction process will use a mode involving applied stresses instead of applied accelerations. Applied accelerations would probably entail shaking the powder piston during the printing process, which would likely have many undesirable side-effects and would not be easily implemented.

Another distinction in the application of stress is whether stresses are applied continuously or by "tamping". With continuous application, the stresses which the powder experiences oscillate smoothly over time. Tamping, however, is a form of impact loading, in which spikes in stress levels are produced for short durations. Both techniques may be of value for 3DP.

Direction in which the Stress is Applied - Finally, the direction in which stresses are applied to the layer surface - either vertically, horizontally, or a combination of both - can significantly affect the densification process.

At the bottom of the flowchart are listed the most specific parameters associated with any given compaction process. These parameters pertain to the device applying the densification stresses to the powder surfaces. As stated earlier, only two of these parameters can be defined independently, but each one has been named in other research to be the critical factor in attaining maximum densification.

Finally, in our future investigations of powder densification in the 3DP process, it may be helpful to consider those aspects of the process which may help to simplify our analysis. These include:

1. The powder which will need to be densified at any one time is a very thin layer, with a thickness typically between two and twenty times the particle diameters

2. The strains which occur during densification are one dimensional (in the vertical direction).

3. Densification stresses can only be applied to the top surface of the powder layer.

4. The powders to be densified will contain spherical, metal particles with well defined size distributions.

This concludes our investigation of powder densification concepts for the time being. We will return to the study of powder compaction in chapter 5.

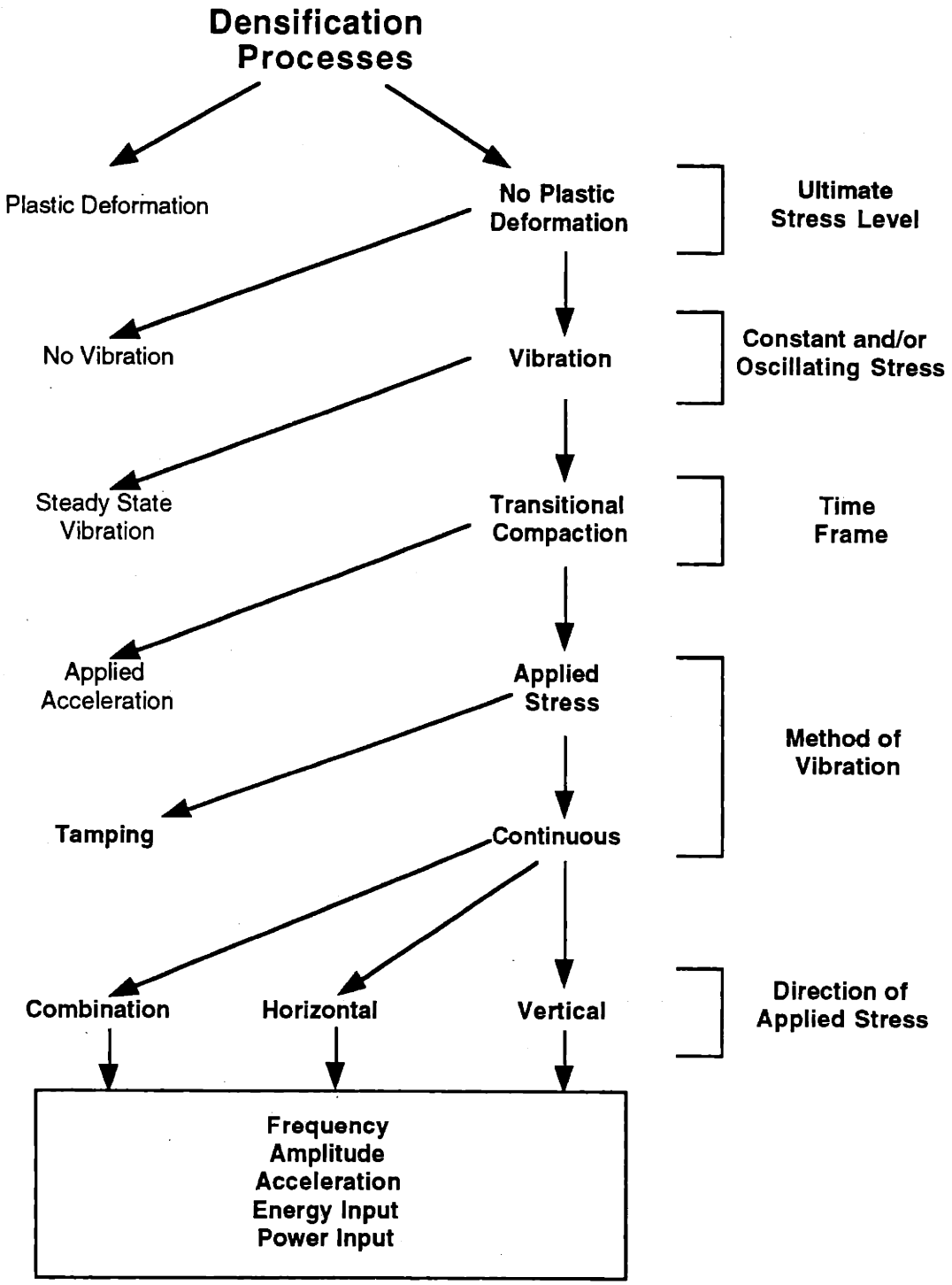

Figure 2.46: Variables associated with the different methods of powder densification. Highlighted variables are most applicable to the 3DP process. The more global variables are at the top of the chart, while the more process specific variables are at the bottom.

Chapter 3. Development of a Bimodal Printing Process

3.0 Introduction

The focus of this thesis is the design and implementation of spreading processes which will result in high green density parts. However, the spreading process is only one portion of the entire 3D printing process, and the *entire* printing process must be viable before green parts can be produced and studied. This chapter focuses on the improvements and modifications which were made to the printing procedures in use at the beginning of this research. The goal of these improvements and modifications was to create a metals printing process which could successfully produce printed bimodal parts. This process would be non-optimized, meaning that once a technique had been identified which could produce what might be considered a "reasonable" part, the development effort would be concluded. This new bimodal printing process would only be a means to an end, a tool to be used in the study of layer densification techniques.

An outline of this chapter is as follows. Background material in the printing of metal parts with monomodal powders is presented in section 3.1. This early work is predominantly that of Michaels, and will prove to be valuable background material for this development effort. [36, 37] A critique of this monomodal printing process is given in section 3.2, describing the process limitations and unknowns. Those areas of the process which were modified or improved are presented in section 3.3, along with a description of new printing process parameters.

3.1 Previous Work in the Printing of Metal Parts

The issues addressed in the development of the initial metals printing process are reviewed in this section. A familiarity with these early issues is critical to an understanding of this research. The majority of this section is based on the Masters thesis of Michaels. [36]

3.1.1 Materials System Selection

The powdered metal which is layered into the powder bed will become the major constituent in the finished 3D Printed part. Powder selection was therefore critical, as most of the final part properties would be directly affected by this choice. A variety of metal

powders which differed in alloy composition, size and shape were tested for their packing properties in the powder bed to determine the best candidate(s) for printing metal parts. Powder packing tests were performed in the 9 x 9 x 9 cm powder piston on the 3D Printing apparatus. 100 layers of powder, each 175μm thick, were spread into the piston, removed and weighed to determine their packing density. Table 3.1 lists the average packing density results for five powders tested. The standard deviation in packing for any given powder was less than 1% of the mean packing value. The two powders which were spherical in shape gave the highest packing.

Table 3.1: Spread Packing Density Results for Several Powders

Material	Size (μm)	Shape	Packing Density (%)
316L Stainless	75	spherical	62
316L Stainless	20	spherical	58
iron	110	equiaxed	49
316L Stainless	60	equiaxed	49
iron	60	equiaxed	45

Based on the powder packing results, the two spherical 316L stainless steel powders were chosen for printing tests. SEM photographs of these powders are shown in figures 3.1-2. It was expected that the dissimilar sizes of the 20 and 75μm powder would reveal any particle size dependencies which were related to the printing process. Also, 316L stainless steel is extremely chemically inert, which was expected to prevent any complicating interactions between powder and binder which might have otherwise occurred.

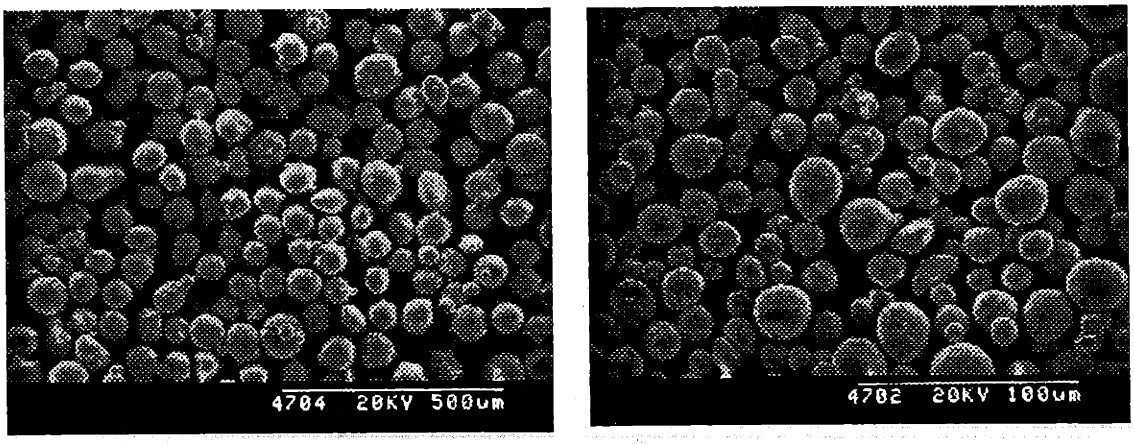

Figures 3.1-2: Spherical 75μm (left) and 20μm (right) 316L stainless steel powders.

A suitable binder for the 3D printing of metal parts needed to meet a double set of requirements. First, the binder needed to be compatible with the 3DP printhead. This set of requirements included:

- can be sufficiently filtered to prevent nozzle clogging
- can be dispensed through 1.8 mil nozzles
- low toxicity
- stable in reservoirs over long periods of time
- compatible with existing printhead electrostatic deflection technology

The second set of requirements which the binder had to meet were those which were unique to metal parts. The green part had to be removable from the powder bed prior to post-processing, therefore the binder had to have sufficient strength to allow the part to be removed from the bed and handled. The binder needed to be easily removable during post-processing, and contain a volatile component which would leave open porosity in the printed part to assist in removal. A wax based binder similar to that used in PIM was not an option, since it could not meet these requirements. The most likely choice to meet these requirements was a polymeric binder which could be removed using thermal decomposition techniques similar to those used in PIM. The new binder requirements added to the above list included:

- high green strength to allow removal from powder bed and handling
- easily removable polymeric binder
- volatile component

After an extensive evaluation process, the binder which was selected was Acrysol WS-24 acrylic sol, a water based acrylic polymer. Acrysol WS-24 was supplied from the manufacturer as a translucent milky white fluid with 36% polymer solids content and could be diluted with water. The average polymer particle size was 150 nanometers. Acrysol WS-24 was part of a family of acrylic sols used as vehicles for clear and pigmented films, and as dip coatings for metal parts.

3.1.2 Printing Process Parameters

The 3D printing process has associated with it numerous parameters which define the printing conditions for any given part. These parameters can be divided into three groups: layer generation parameters, printhead parameters and miscellaneous parameters. The values of these parameters for the initial process development are given below. Many of these initial parameter values were taken from the original alumina / silica ceramic shell printing process.

Layer Generation Parameters - These parameters describe the spreader mechanism and the specifics of the layer generation process. Figure 3.3 is an illustration of the spreading process used in the initial process development. During spreading, a pile of powdered material was leveled into a smooth layer by a metal rod. The rod rotated in a direction opposite of its linear motion across the surface, such that the face of the rod in contact with the powder pile was moving in an upwards direction. The counter-rotating surface of the rod helped to tumble the powder in the pile instead of dragging it, and was intended to reduce shear forces which occurred between the moving powder pile and the previous layer. Reduced shear was desired so that the previously printed regions were not disturbed or offset in the powder bed, which would have caused a loss of part registration. The rod was vibrated during spreading to assist in packing the powder particles tightly.

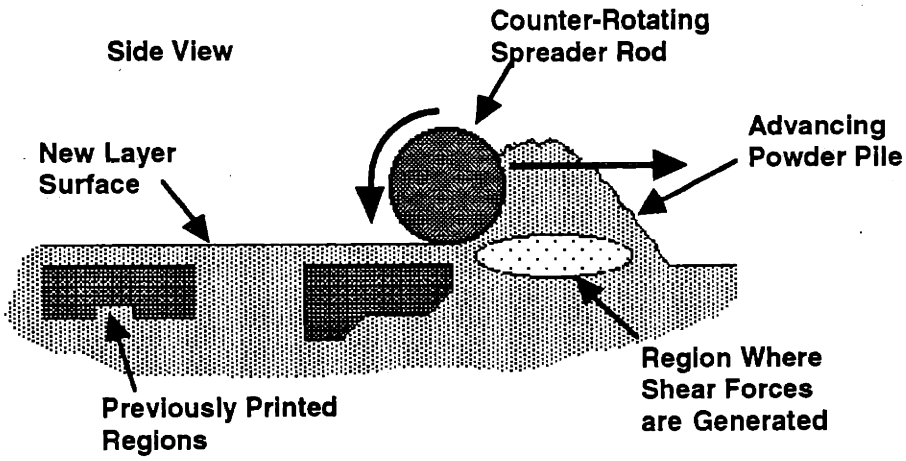

Figure 3.3: Illustration of the spreading process.

The vibratory motion of the spreader rod is illustrated in figure 3.4. The rod moved along a diagonal to the powder surface, thereby providing both a horizontal shearing and vertical tamping oscillatory component for powder densification.

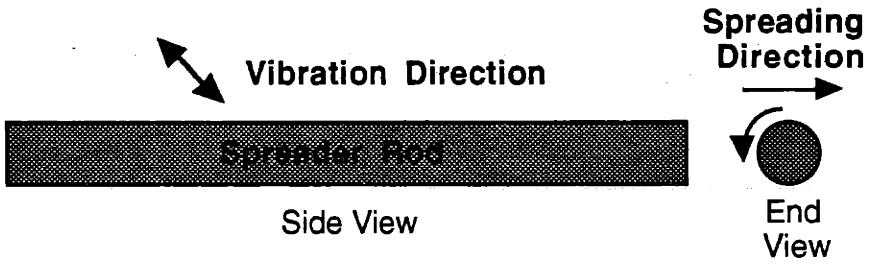

Figure 3.4: Direction of vibratory motion for the spreader rod.

The layer generation parameters were as follows:

Layer Generation Parameter	Value
direction of spreader rod rotation	counter-rotating
method of powder pile dispensing	hand dispensed
mass of powder in the initial pile	approximately 300% of what was required to strike the layer height
single or distributed powder piles	single pile placed on the front lip of the powder piston
number of spreading passes	one
piston motion sequence	drop 175μm between spreading and printing
horizontal spreading speed	0.5 inches / sec
vibration condition	200Hz diagonal motion and 2 mil peak-to-peak displacement
final layer thickness	175μm

Printhead Parameters - These parameters describe the operating characteristics of the electrostatically deflected, continuous jet printhead. Figure 3.5 is an illustration of the printing process. As the printhead moves above the new powder surface, a stream of binder droplets is selectively dispensed.

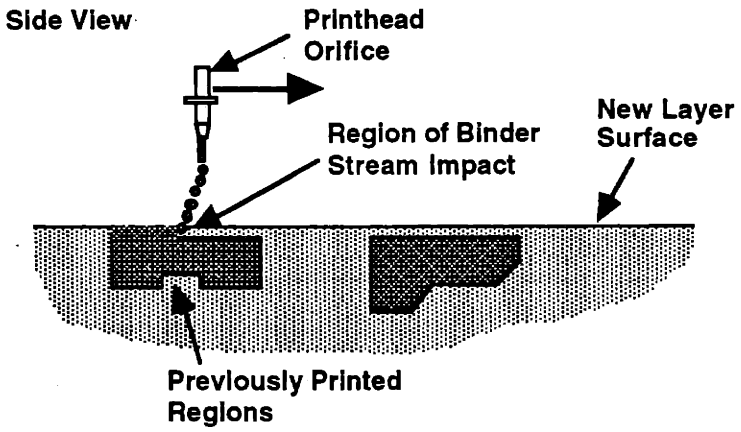

Figure 3.5: Illustration of the printing process.

The printhead parameters were as follows:

Printhead Parameter	Value
nozzle type	wire bonding tool
nozzle orifice diameter	1.8 mils
piezo simulation frequency	50 to 60 KHz
binder flowrate	1.1 to 1.3cc/minute
printhead rastering speed	60 inches / sec
binder concentration	24 weight % polymer

Miscellaneous Parameters - These were parameters not included in the above two groups. The miscellaneous parameters are as follows:

Miscellaneous Parameter	Value
spacing between printed lines	175μm
number of prelayers spread before printing of the first part layer	minimum of 4

3.1.3 New Printing Problems

After selection of the material systems to be evaluated and determination of the printing process parameter values to be used, the next step in the development process was to use the printing techniques previously established in the alumina / silica materials system and observe new printing phenomena, if any. First, a single layer would be printed with either powder. If this step was successful, then a second layer would be spread and

another layer printed. Several new printing phenomena were observed during these initial printing and spreading tests which prevented further advancement. These are described below.

Ballistic ejection

When a binder stream traveling at about 10 m/s impacts the powder surface, a certain amount of powder rearrangement is expected. When powder is thrown from the impact zone along the printed line it is called ballistic ejection. This ballistic ejection effect was observed when printing into the 20μm powder. Figure 3.6 is a high speed strobe photograph of the ballistic ejection phenomena. The binder flowrate was 1.2 cc/minute. The binder stream can be seen as the vertical line of droplets which ends at the powder impact zone. The binder stream was moving from right to left, cutting a dramatic trench through the powder surface. Powder was thrown distances of over one centimeter from the printed line area. This type of ballistic ejection behavior was unacceptable, since the powder surface was highly disrupted.

Printing into the 75μm powder produced very different results. Although there was a slight amount of visually observable powder rearrangement, the effect did not prevent the completion of a single layer. In this case, it was presumed that the greater mass of an individual 75μm powder particle, as compared to a 20μm particle, prevented the ejection effect from occurring.

Balling

A second effect which occurred with the 20μm powder after ballistic ejection was balling. Figure 3.7 is a strobe photograph taken 15 milliseconds after the binder stream had passed. Observable in this photo is the trench cut by the binder stream and several large ball-shaped powder agglomerates, up to a millimeter in diameter, sitting in the trench. These agglomerates were composed of binder and powder. No balling was observed with the 75μm powder.

The balling effect resulted from failure of the binder to soak into the powder bed fast enough, instead curling up into a binder \ powder ball on the printed surface. [8] The combination of ballistic ejection and balling in the 20μm powder made successful printing of a single layer impossible. Tests involving the printing of two or more layers were

therefore carried out with only the 75μm powder. Two additional printing effects were observed during these multiple layer tests.

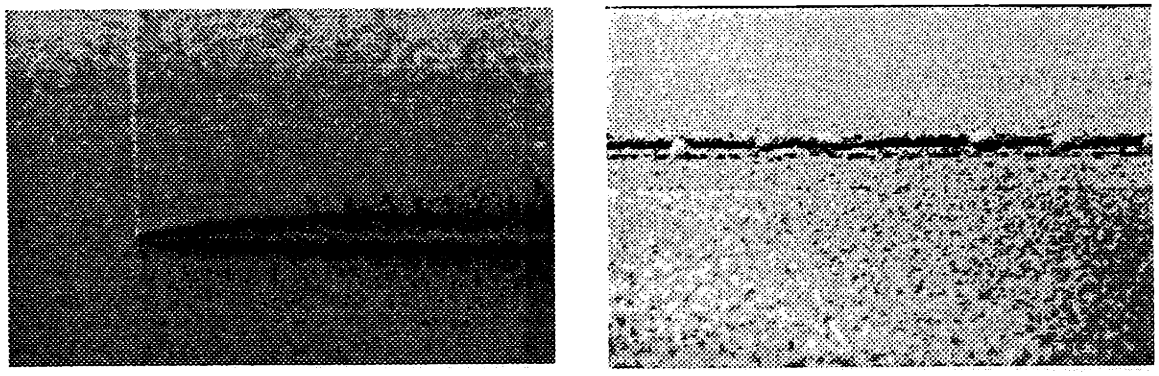

Figures 3.6-7: Ballistic ejection (left) and balling (right) in the 20μm 316L stainless steel powder.

Tearing

The first new multiple layer printing effect occurred during the layering of 75μm powder over previously printed regions. This effect was called "tearing". Observations showed that when the advancing powder pile of 75μm powder was spread over previously printed regions, deformation occurred in the new layer surface. This effect is illustrated in figure 3.8.

The cause of the tearing effect was linked to residual moisture in the previously printed regions. This moisture was wicking up into the powder pile during spreading, causing agglomeration of the powder in the pile and adhesion of the pile to the printed surface, thereby preventing a smooth surface from being spread. Although detrimental to the spreading of a smooth layer, it was possible to print multiple layers with the 75μm powder. Attempting to print a complete multi-layered part revealed the final new printing phenomenon, shifting.

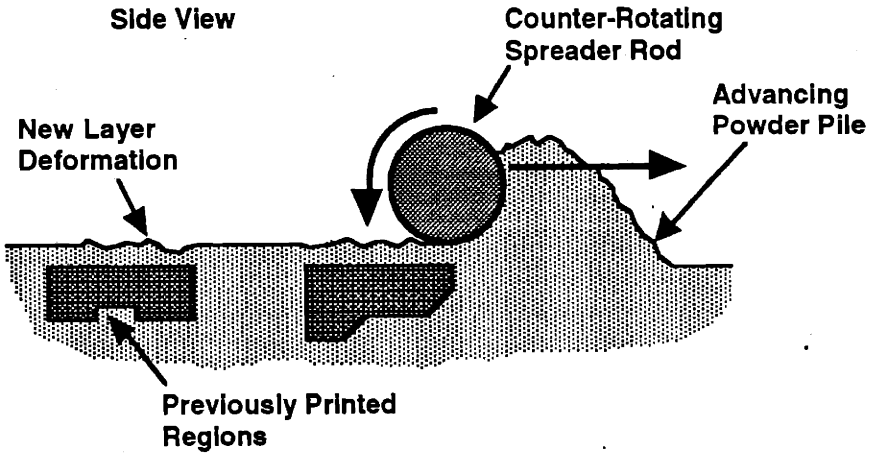

Figure 3.8: Tearing of the new powder surface during spreading of 75μm powder.

Shifting

Shifting was typically observed after the printing of rectangular bars approximately 0.32 x 0.64 x 6.0 cm in dimension. The bars were 18 layers thick, with the standard 175μm layer thickness. Instead of having a rectangular cross section, the actual cross section was diamond shaped. The only explanation for this effect was that the bars were being shifted in the powder bed during spreading, such that the layer registration was being slightly altered with each layer. The shifting effect is shown in figure 3.9.

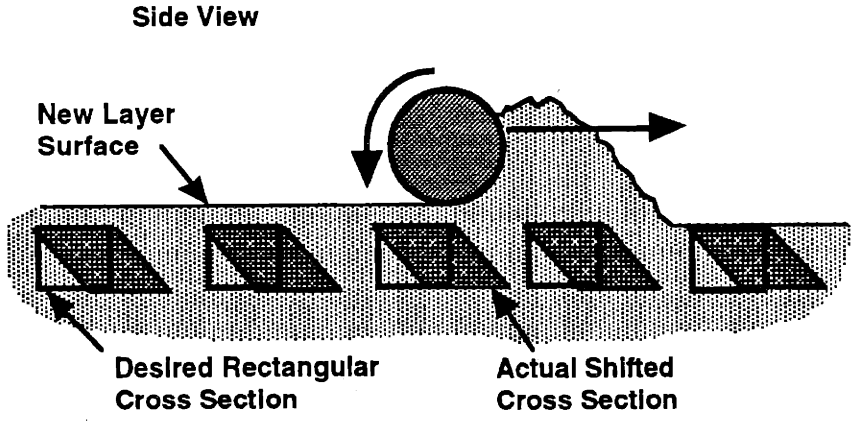

Figure 3.9: Shifting of printed regions during the spreading of 75μm powder

Two combined effects were thought to have caused shifting. First, the spherical 75μm powder in the unprinted regions of the powder bed is extremely flowable, providing little resistance to motion for the printed regions. Second, although the 75μm powder did not experience substantial amounts of tearing, it is likely that higher that normal shear forces were generated when the powder pile moved over the moist printed regions, slightly adhering to them. This adhesion of the powder pile to the printed regions would incrementally move the printed regions in the direction of spreading. Although each new layer would be printed in the correct bed location, that layer and the printed regions below it would then be shifted during the spreading of the new layer.

Table 3.2 summarizes the new printing effects observed during these initial trials.

Table 3.2: Summary of Printing and Spreading Effects

Printing	75μm powder	slight rearrangement
	20μm powder	ballistic ejection / balling
Spreading	75μm powder	tearing / shifting
	20μm powder	N/A

3.1.4 Solutions to the Monomodal Printing Phenomena

The implementation of two new printing techniques which solved the problems of ejection, balling, tearing and shifting are summarized below. A complete description of the methodology used to identify these solutions can be found in [Michaels, 1995].

Layer Drying

Removing the residual moisture from each layer after printing was identified as a method for eliminating tearing and shifting. Each new powder layer would be spread over a dry surface, thereby eliminating the printing problems caused by residual moisture in the previous layer. Moisture was removed by applying forced hot air to the powder surface after the printing of each layer. A hot air gun was used for this purpose. The air gun was manually directed over the printed areas for approximately one minute. The air gun was kept in continuous motion to prevent overheating (or even burning) of the printed areas.

Surface Cohesion Methods

The second new printing technique was used to defeat the ballistic ejection and balling phenomena. The technique involved altering the fluidity of the powder during printing. Powder feedstock for P/M processes is produced so as to minimize any surface contamination, since such contamination may cause adhesion of the powder particles and reduce the fluidity of the powder. It is possible to intentionally coat a powder with a specific "contaminant", however, in order to manipulate this adhesion effect. Coating metal powder with a small quantity of metallic salt allows the powder to be manipulated in a unique way. When the powder is dry, it flows as if it were untreated, since the salt coatings on the individual particles do not interact. If such powder is temporarily exposed to a source of moisture, such as water mist from an ultrasonic humidifier, and then dried, a key reaction occurs. The salt coating partially dissolves during the application of moisture and then recrystalizes at the interparticle contacts during drying, forming weak bonds between the particles. These salt bonds between particles provided a cohesive force among the particles in the powder layer. The term "powder locking" was coined to describe this effect. (Although it should be pointed out that the particles were far from being rigidly locked in place. Indeed, the salt bonds were rather weak, and could be easily broken by simply brushing the powder surface.) When binder droplets impacted into the surface of a locked powder layer, the cohesive salt bonds prevented any visible particle rearrangement, thereby eliminating the ballistic ejection and balling effects.

Figure 3.10 is a strobe photograph of the binder stream impacting into coated and locked 20μm stainless powder. Of note is the complete absence of powder ejection, balling or trench formation.

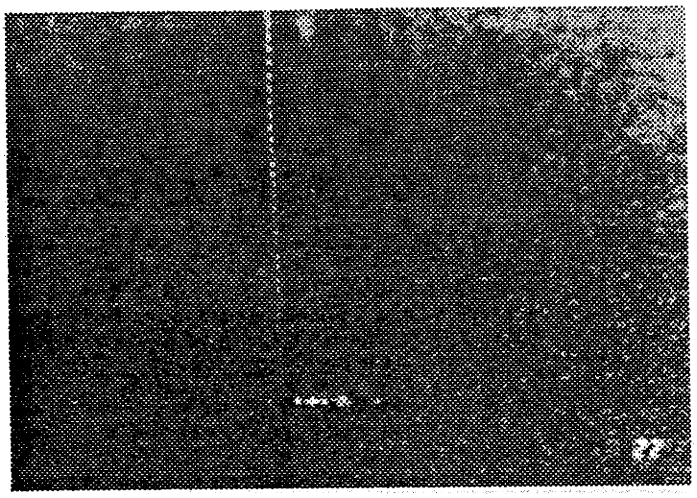

Figure 3.10: Printing into coated and locked 20μm stainless powder.

Sodium carbonate was chosen as the metal salt to provide the locking effect. (This salt was selected because it was expected to have a gelling effect on the Acrysol binder, but this is not relevant to the current discussion.) The minimum amount of salt required to achieve effective locking was found to be 0.025g sodium carbonate per 100g powder. This small quantity of salt would not adversely effect the material properties of the finished part.

3.1.5 Summary of Printing Techniques

At this stage of the initial process development, green parts could be successfully printed with both the chemically treated 20 and 75μm powders. Figure 3.11 is an illustration of the original monomodal printing process. In the first step, coated powder was spread over the previously dried regions of the powder bed. Next, the coating was activated by the application of water mist from an ultrasonic humidifier. The partially dissolved salt bolds were re-crystallized by quickly drying the layer with forced hot air. Binder was then printed into the locked powder. Finally, the printed regions were dried to prevent tearing of the next layer and shifting of the previous layers during spreading.

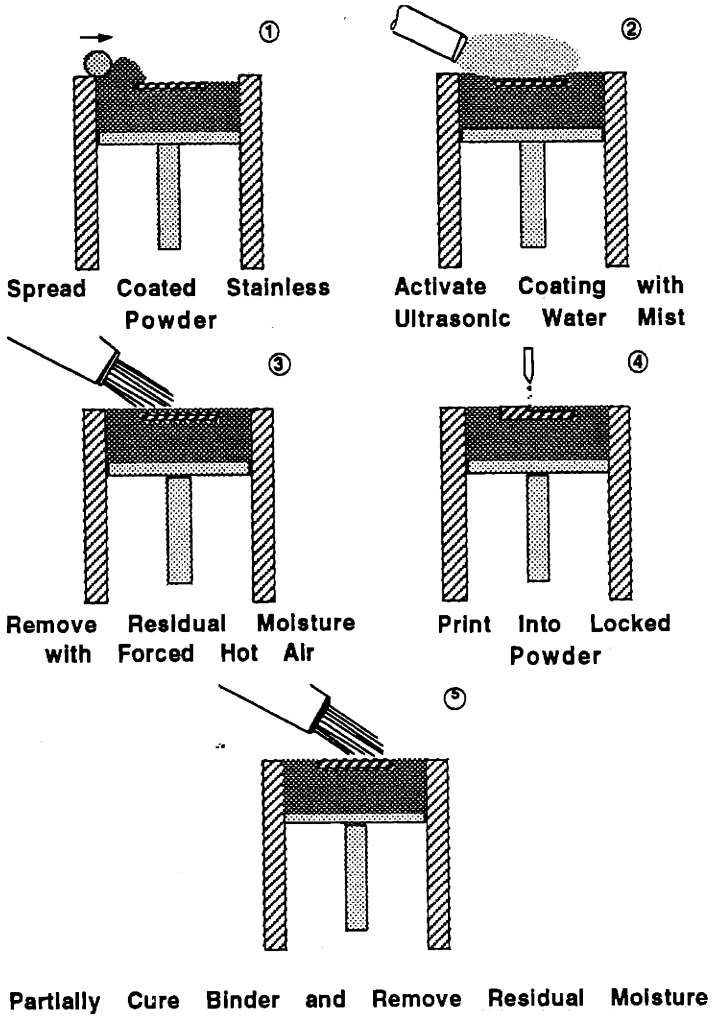

Figure 3.11: The original monomodal printing procedure.

3.1.6 Final Part Properties

Once the part was completed, in was removed from the powder bed. The green strength of the printed parts were sufficient for them to be handled. No problems with layer delamination were observed, as is sometimes the case in the alumina / silica system. Although the packing density of the two powders had been determined previously during spreading tests, green density tests were performed on printed bars measuring 1.0 x 1.0 x 6.0 cm to determine if the printing process affected the powder packing. The green density for bars printed with either powder was 56%. This was lower than the values of 62% and 58% obtained during packing tests with the 75 and 20μm powders, respectively. An

explanation for the lower value was that there was reduced powder particle accommodation over the printed regions during spreading. Since the printed regions were bound by polymer, the particles in these regions were immobile. In order for tight packing to occur, the loose particles in the powder pile must nest into the interstices of these immobile particles. This differs from the situation in the previously described powder spreading experiments, where particles in both the powder pile and the previously spread powder layer were free to move. In this latter case, in was much easier for the particles to nest tightly, since some accommodation could occur in both the powder pile and the previous layer during spreading.

3.2 Process Limitations and Unknowns

The monomodal printing process described above proved adequate for producing green parts with packing densities in the 56 to 58% range. The process was not without its shortcomings, however. Areas which needed improvement or were poorly understood are outlined below. Modifications and improvements to some of these areas will be addressed in this chapter, while others - specifically those that indicate a poor understanding of the spreading and layer densification processes - will be addressed in later chapters.

The problem areas which will be addressed in this chapter are as follows:

1. The printhead nozzle would occasionally clog when dispensing the 24 wt.% Acrysol WS-24.

2. The manual application of forced hot air from a heat was poorly controlled. Also, the forced air had a tendency to blow powder around, which both disrupted the powder layer and created a breathing hazard in the case of fine powders.

3. There was inconsistency in the fluidity of coated powder which was recycled after having been previously locked. The recycling procedure of sieving the powder through a coarse sieve was not breaking up all of the salt bonds.

4. The coated powder was weakly hygroscopic. The fluidity of the coated powder was observed to be less than uncoated powder, especially during humid conditions.

5. Powder locking activation with the ultrasonic humidifier was too inconsistent - it varied with room humidity and temperature, and the usage history of the powder. Also, hand application of the water mist was too variable.

6. The strength of the powder locking was occasionally insufficient, regardless of how much water mist was applied. Portions of printed regions in the layer would exhibit visible particle rearrangement.

7. The sodium carbonate which was used as the locking agent was selected for reasons (i.e. binder gelling) which were no longer important. It was likely that there was a more appropriate chemical compound which could be used.

The problem areas which will be addressed in later chapters are as follows:

1. The vibration parameters chosen for the spreader rod - 200Hz diagonal motion and 2 mil displacement - were a shot in the dark. The effects of spreader frequency, amplitude and direction were unknown.

2. The effects of spreader rod size and spreading speed were unknown. Also, it was unclear that a cylindrical spreader rod was the best geometry for layer creation and densification.

3. The maximum green density for the monomodal parts - about 58% - was below the tap density for the powders used, indicating there was room for improvement. Even if the tap density of these powders (approximately 63%) could be reached, however, the green density would still be far below the target of 75 - 80% set for this research.

4. No information about the microstructures of the printed parts had been previously obtained.

3.3 Improvements to the Metals Printing Process

This section discusses the modifications and improvements which were made to the monomodal printing process so that bimodal parts could be readily printed. Simply put, the overall goal of this section was to produce a bimodal bar which had sufficient strength to be handled and studied. The speed of the new printing process was not emphasized at this point. Another goal was to eliminate as much hand processing (e.g. water mist and forced hot air application) as possible.

3.3.1 Bimodal Powder Systems Selection

Before printing process modifications could begin, several bimodal powder mixtures had to be chosen. These mixtures would serve to evaluate the process modifications, and would also later be used in the development of new layer densification processes. Three bimodal powder blends were chosen. All three mixtures were blends of spherical particles, with a composition of 26.5% small component. (The optimum bimodal composition for maximum packing density.) All three mixtures also had a particle size ratio near 7.0, which was previously shown to be the size ratio at which significant improvements in packing density could be obtained. Table 3.3 summarizes the properties for these three bimodal mixtures.

Two of the blends were made from 316L alloy powders: a mixture of 120μm and 20μm (average particle size) powders, and a mixture of 71μm and 9μm powders. The 316L alloy was again chosen because it was very chemically inert, and because it was the most readily available alloy of all commercially produced gas-atomized stainless steel powders. The two 316L blends had significant differences in fluidity, as indicated by the angles of repose for these powders, with the 71/9μm mixture being much less flowable than the 120/20μm mixture. This difference would be useful in revealing any new printing phenomena which were strongly influenced by interparticle friction.

A bimodal blend made from hardenable 420 alloy stainless steel powder was also used. This alloy was chosen because, in wrought form, it is used in tooling applications similar to those which are the focus to the 3D printing tooling effort. Also, although the 66/9μm 420 mixture was comparable in size to the 71/9μm 316L mixture, the powders had very different fluidity. The higher fluidity of the 420 blend was attributed to the presence of oxide films on the surface of the 420 particles.

A complete description of all the powders used in this research is given in appendix A. The individual monomodal components from these blends will also be used throughout this thesis to study the impact of new layer densification techniques on monomodal powders.

Table 3.3: Properties of the Bimodal Powder Mixtures.

Attribute	120/20μm Mixture	71/9μm Mixture	66/9μm Mixture
Stainless Alloy	316L	316L	420
Shapes	spherical	spherical	spherical
Large Powder Sieve Cut	-100 / +170 mesh	-170 / +270 mesh	-170 / +325 mesh
Small Powder Sieve Cut	-30μm / +15μm	-16μm / +4μm	-16μm / +4μm
Composition (% fines)	26.5%	26.5%	26.5%
Size Ratio	6.3	7.8	7.3
Apparent Density	60.5%	58.0%	64.4%
Tap Density	76.2%	78.5%	75.6%
Angle of Repose	36°	45°	38°

3.3.2 Process Improvement Areas

We will now focus our attention on those problem areas in the monomodal printing process which were described above. The improvements made ranged from "quick fixes" to substantial process modifications, which required the design and construction of new equipment.

Binder composition

In order to prevent nozzle clogging, the Acrysol WS-24 binder was diluted to 20 wt.%. Although this was a small concentration change from the previous composition of 24 wt.%, it significantly reduced nozzle clogging.

Powder coating

A review of P/M reference literature indicated that boric acid salt is sometimes added to powder feedstocks to act as a sintering aid. During sintering, the boric acid acts

as a flux, dissolving oxide layers on the particle surfaces, thereby improving interparticle diffusion. Boric acid was evaluated as a potential locking agent for 3DP, since in addition to providing the locking function during printing it might also provide a beneficial sintering function later during furnace processing. The 71/9μm bimodal powder mixture was used to evaluate several different amounts of boric acid coating. During these printing tests, the coating was activated using the new steamer bar assembly, and the residual moisture was removed using the new heater bar assembly, both of which are described below. Table 3.4 summarizes the results from these printing tests.

Table 3.4: Summary of Printing Observations Using Different Amounts of Boric Acid as a Locking Agent

Grams Boric Acid per 100 Grams Steel Powder	Printing Observations
0.01	Insufficient locking, with occasional layer surface disruption
0.02	Minimal acceptable locking, with only infrequent surface disruption
0.05	Sufficient locking, with unprinted regions having appreciable strength
0.10	Sufficient locking, with unprinted regions having excessive strength

A coating level of 0.05g boric acid per 100g steel powder was chosen for all future printing tests. Although this quantity of coating provided more than sufficient powder locking, it was considered better to have an initial excess of locking capability, so that increases in powder coating would not have to be made later in the research.

Powder preparation and recycling

To attain fluidity levels comparable to those of uncoated powders, all the coated powders, both new or recycled from previous printing runs, were milled in a ball mill for one hour immediately before printing. The ball milling successfully broke up all the salt bonded agglomerates in the powder mixture, thereby restoring powder fluidity. A complete description of powder preparation and recycling procedures is given in appendix D.

Powder preheating

To inhibit the absorption of atmospheric moisture onto the coated powder surfaces after ball milling, the milled containers of powder were preheated to approximately 150°C prior to printing. A heating plate was used to maintain the powder container at this temperature during printing.

Moisture delivery

The quantity of moisture delivered by an ultrasonic humidifier was judged to be insufficient to consistently activate the powder coating. Also, since the ultrasonic mist was at room temperature, it would not readily "condense" on the powder surfaces. A preliminary evaluation of steam generated by a hand-held steamer (the type used to remove wrinkles from clothing) indicated that this was a promising approach. The quantity of water delivered by the steamer was more than adequate to activate the powder coating, and the temperature differential between the steam and powder caused the steam to condense when it hit the powder surface. To improve the consistency with which the steam was delivered to the powder surface, a semi-automated steamer bar assembly was constructed. This assembly is illustrated in figure 3.12.

Steam was generated in an electrically heated metal evaporation chamber which had been obtained from one of the hand-held steamers. A 3/8" I.D. bent copper tube was used to deliver the steam to the powder surface. Several small holes, 1/8" in diameter, were drilled in the length of the tube to act as steam vents. The copper tube was wrapped with electrical heater cord (not shown in the figure) and heated to above 100°C to prevent premature condensation of steam within the tube, which otherwise would have resulted in droplets of water being expelled from the steam vents. Water was fed into the evaporation chamber from the body of a 30cc syringe (no plunger) using a gravity head control mechanism. The water height Z above the evaporation chamber was maintained at a near-constant value, once a water height was found which gave an appropriate steam flowrate. The water height was manually monitored and adjusted as needed. A valve at the bottom of the syringe was used to turn the steam on and off.

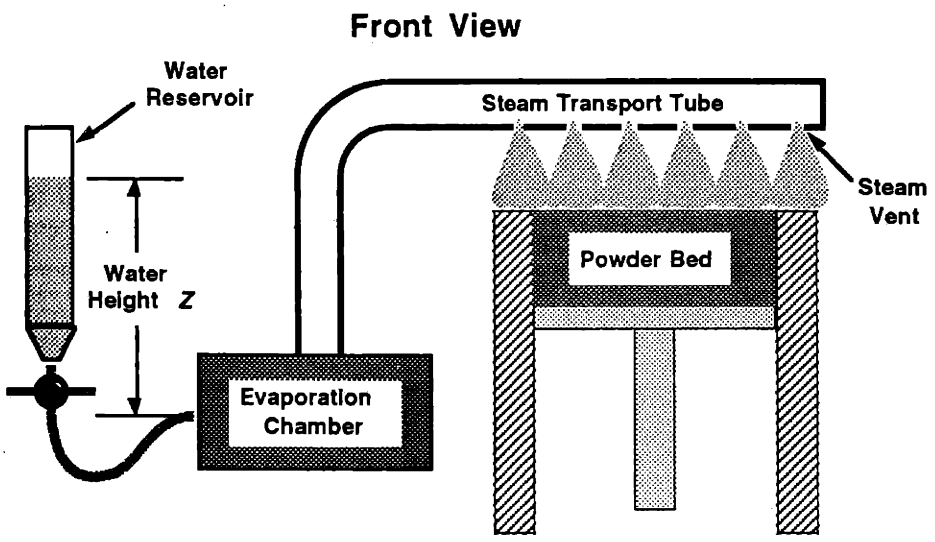

Figure 3.12: A schematic of the semi-automated steamer bar assembly.

The entire steamer bar assembly was attached to the slow axis of the 3DP machine. In operation, the steamer bar would be slowly swept across the surface of the new powder layer. The vents from the steamer bar were positioned approximately 25mm above the powder surface. A slow axis velocity of 0.25"/minute, and a steam flowrate of approximately 2cc/minute, were found to provide sufficient moisture to activate the boric acid powder coating.

Printed line drying

The final process improvement was the replacement of the manually applied forced hot air used to remove residual moisture from the top layer. The solution approach taken replaced the forced hot air from the heat gun with unforced convection from two Inconel electric heater bars, which had a maximum output of 120 watts each. Figure 3.13 is an illustration of the heater bar assembly. The heater bars were rectangular, and measured approximately 5mm x 15mm x 120mm. The heater bars remained powered during the entire printing cycle, continuously delivering heat energy to the powder surface. As in the case of the steamer bar, the heater bars were attached to the slow axis of the 3DP machine, and were positioned so binder delivered from the printhead impacted the powder surface along a line between the bars. In this way, one bar acted as a pre-heater of the powder surface before printing, while the other acted as a post-heater after printing. The height of

the bars was adjusted so that there was a 5mm gap between the powder surface and the bottom of the bars.

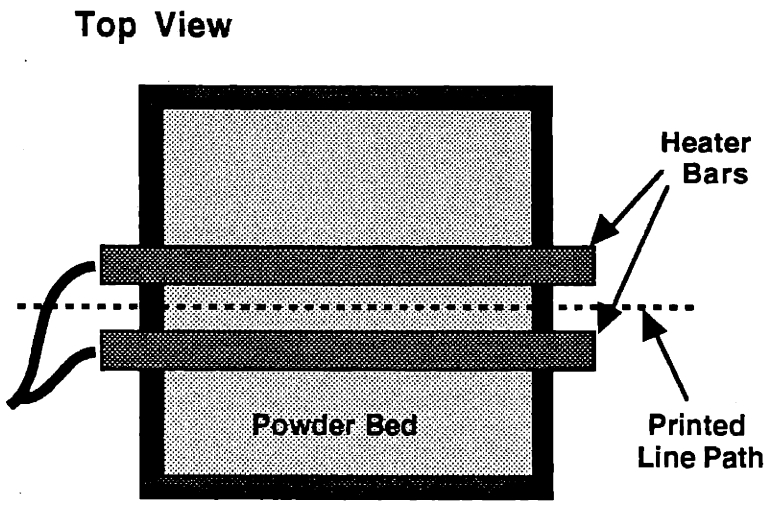

Figure 3.13: An illustration of the heater apparatus used to remove residual moisture.

The heat output from the bars was controlled with a variable transformer. Several bar power settings were evaluated during printing tests. It was found that the critical variable was the temperature of the powder surface between the bars. This temperature was measured by inserting a micro-thermocouple probe approximately 1mm into the powder surface between the bars. A surface temperature between 80 and 100°C gave the best drying results. (This required a total power input between 60 and 80 watts.) Lower temperatures would sometimes result in incomplete drying of the printed regions, while higher temperatures were discovered to prevent condensation of steam during the locking activation of the next layer. Also, excessively high temperatures (over 200°C) would cause the binder to instantly vaporize upon impact with the powder surface, which prevented inter-layer bonding.

Figure 3.14 provides two views of the new printing equipment, showing the relative positions of the spreader rod, steamer bar and heater bars in relation to the powder piston. All these devices moved in tandem with the motion of the slow axis. Figure 3.15 is a photograph of the actual setup used in this research. The electrical heater cord which wraps the steamer tube is visible in this photo.

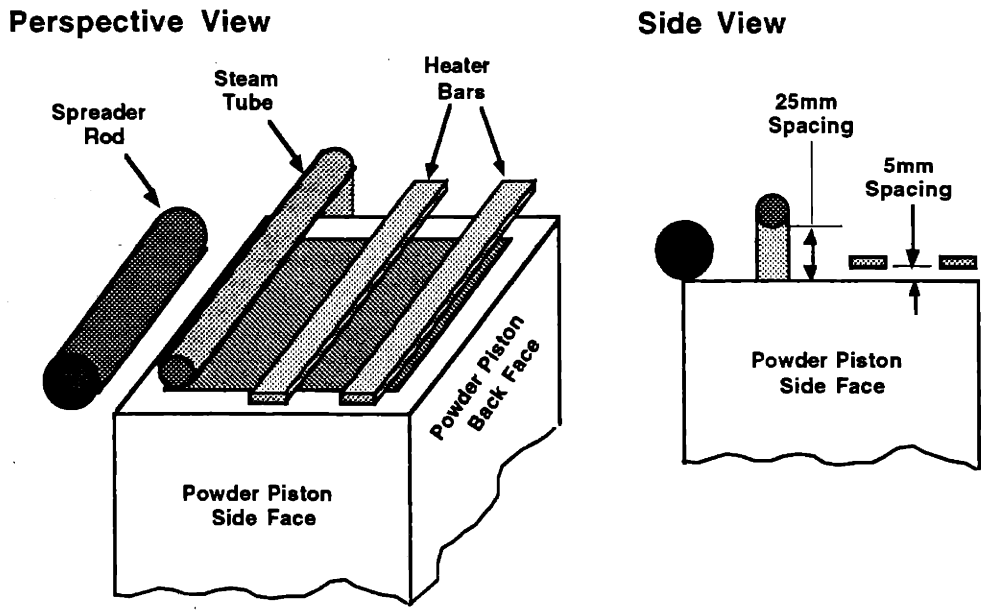

Figure 3.14: Layout views of the new printing equipment, showing the relative positions of the individual pieces.

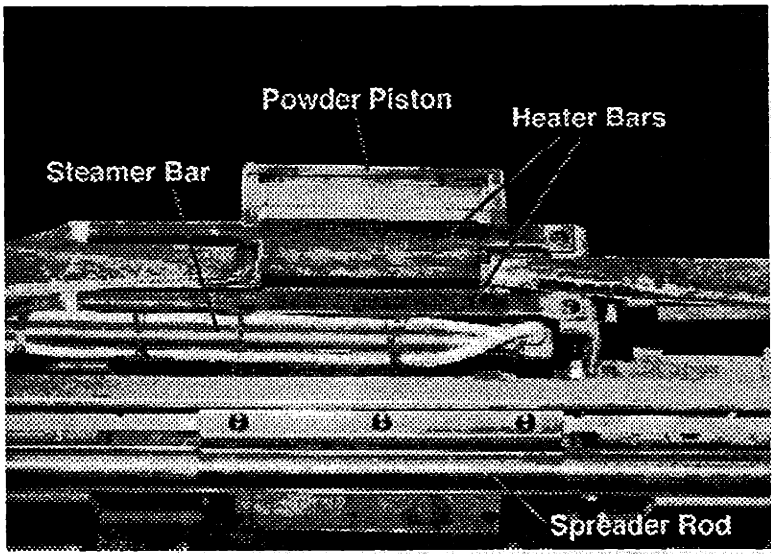

Figure 3.15: A front overhead view of the new printing equipment.

3.3.3 Preliminary Bimodal Printing Results

After all the new equipment and procedures were in place, several printing runs were made with the three bimodal powder mixtures to evaluate the new printing process.

Rectangular bars which measured 2mm x 10mm x 70mm were used as the printing test geometries. A description of the preliminary printing cycle used during this evaluation is as follows.

1. Manually dispense preheated powder in a pile in front of the spreader rod.

2. Spread the new layer with the spreader rod, with the slow axis moving from the front to the back of the piston at 0.5"/second.

3. On the return pass of the slow axis to the front of the piston, turn on the steamer bar to activate the powder coating. Slow axis speed is 0.25"/second for this second pass.

4. Perform layer printing.

5. Lower the piston one layer thickness.

For the most part, the initial printing of bimodal runs were successful. Bars were printed with all three bimodal powder mixtures. A critical printing parameter which was identified in these tests was the binder flowrate. Too low a flowrate would result in complete delamination of the printed bars, especially in the case of the 71/9μm 316L and 66/9μm 420 bimodal mixtures. For these powders, a flowrate in excess of 1.25cc/minute was necessary to prevent delamination. (Recall that the layer thickness in all cases was 175μm.) The cause of this delamination effect was believed to be the very small pores which existed in these bimodal mixtures. When tightly packed, these mixtures have a pore size on the order of 3μm, which is significantly smaller than any previous metal powder printing. The presence of these small pores within the layer was inhibiting the transport of binder across layers, where the average pore size tends to be much larger due to inter-layer defects.

Another observation was that the coated bimodal mixtures were found to be extremely susceptible to tearing defects when spread over moist regions. This effect was again attributed to the small pore size of the bimodal powders. The presence of these very small pores produced elevated levels of capillary suction in the powder pile, as compared to the larger monomodal powders. Moisture was drawn up into the powder pile as it was spread across the previous layer, causing adhesion and subsequent tearing. Two time

delays were added to the printing cycle to allow for more thorough removal of residual moisture. A 30 second delay was added to the start of the printing cycle to allow time for evaporation of the condensed steam from the steamer bar. This initial delay also prevented binder bleeding, which has been observed to occur when printing into wet powder. A 30 second delay was also added to the end of the printing cycle to more completely remove water from the printed regions before spreading of the next layer.

Finally, it was discovered that the combination of steam activation and the new boric acid powder coating produced a significant bonding effect between the powder layer edges and the piston walls. If the piston bottom was dropped after these bonds had been formed, the powder immediately adjacent to the piston walls was prevented from lowering, causing damage to the layer in this vicinity. Layer damage only occurred if the piston bottom was dropped after the wall bonds had formed. If instead the piston was raised, no damage occurred since the underlying powder regions could support the shear forces generated at the wall. A piston raise-and-lower cycle was added to each layer in the printing cycle to break these wall bonds.

After incorporating these changes to the printing procedure, the modified printing cycle was as follows:

1. Lower the piston one layer thickness (175μm).

2. Manually dispense preheated powder in a pile in front of the spreader rod.

3. Spread the new layer with the spreader rod, with the slow axis moving from the front to the back of the piston at 0.5"/second.

4. Lower the piston an additional 250μm.

5. On the return pass of the slow axis to the front of the piston, turn on the steamer bar to activate the powder coating. Slow axis speed is 0.25"/second for this second pass.

6. Move the slow axis to a position where the heater bars are over the first line to be printed and pause 30 seconds to allow removal of condensed steam.

7. Perform layer printing.

8. Stop the slow axis with the heater bars positioned over the last printed line and pause 30 seconds to allow removal of residual moisture from the printed binder.

9. Raise the piston 250μm to break any powder wall bonds.

3.3.4 New Printing Process Parameters

The parameters for the entire bimodal printing process are summarized below. New parameters are indicated in the shaded regions.

The bimodal layer generation parameters were as follows:

Layer Generation Parameter	Value
direction of spreader rod rotation	counter-rotating
method of powder pile dispensing	hand dispensed
mass of powder in the initial pile	approximately 300% of what was required to strike the layer height
single or distributed powder piles	single pile placed on the front lip of the powder piston
number of spreading passes	one
piston motion sequence	see above
horizontal spreading speed	0.5 inches / sec
vibration condition	200Hz diagonal motion and 2 mil peak-to-peak displacement
final layer thickness	175μm
powder preheat temperature	150°C

The bimodal printhead parameters were as follows:

Printhead Parameter	Value
nozzle type	wire bonding tool
nozzle orifice diameter	1.8 mils
piezo simulation frequency	50 to 60 KHz
binder flowrate	1.25 cc/minute minimum
printhead rastering speed	60 inches / sec
binder concentration	20 weight % polymer

The miscellaneous bimodal printing parameters were as follows:

Miscellaneous Parameter	Value
spacing between printed lines	175μm
number of prelayers spread before printing of the first part layer	minimum of 4
type of locking activation	steam on return pass
steam flowrate	approximately 2cc / minute
slow axis speed during steaming	0.25 inches / second
heater method	natural convection from bar heaters
heater power	60 - 80 watts
distance from bed	5mm
bed temperature	80°C to 100°C in region of the printed line

Chapter 4. Analysis of the Baseline Bimodal Printing Process

4.0 Introduction

In this chapter the "baseline" bimodal printing process, in which a counter-rotating rod was used to spread the powder layer, is thoroughly analyzed to serve as a standard of comparison for future layer densification techniques. To perform this baseline analysis, it was necessary to develop new measurement techniques which could more precisely characterize the current printing procedures. Quantitative comparisons between printed parts generated by both current and future methods would then be possible.

A review of those microstructural parameters which were to be measured, and the techniques available at the outset of this research for measuring them, is presented in section 4.1. A summary of the new measurement techniques which were developed specifically for this research is also given. Results from the baseline analysis are given in section 4.2, followed by a discussion of these results in section 4.3.

4.1 Measurement of the Baseline Printing Process

The primary metric which had been used prior to this research to evaluate 3D printed parts was the average green density. This quantity was usually obtained by measuring the volume and mass of a printed rectangular bar. Although average green density was certainly a valuable parameter for comparing printed parts, it was far from a complete characterization of the printed microstructure. Microstructural images obtained from part cross-sections revealed a variety of packing density variations and defects which occurred on a length scale similar to the layer thickness dimension. Figure 4.1 is a cross-sectional image of a bar printed with the 71/9μm 316L bimodal powder. The layer packing defects generated during the printing process are quite apparent in this image.

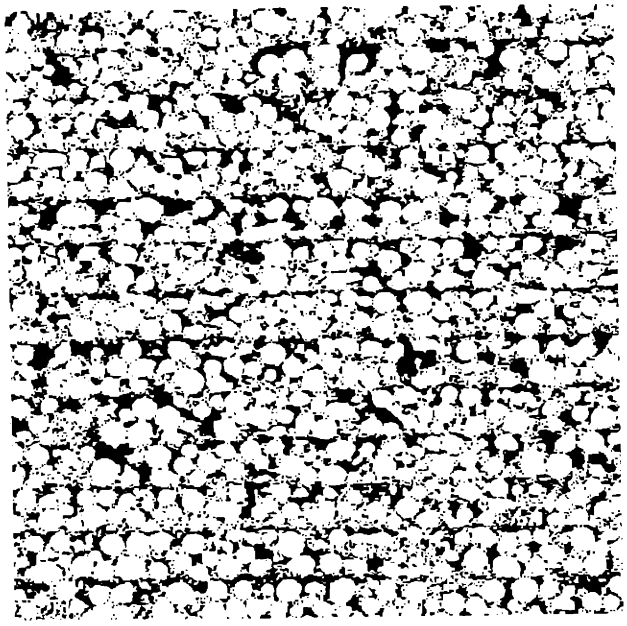

Figure 4.1: Microstructural image from a bar printed with the 71/9μm 316L bimodal powder mixture. The part layers, each 175μm thick, run horizontally across the image. 40x magnification.

Since packing defects which occurred across the printed layers and lines of parts had been observed to be an dominant microstructural characteristic, being able to quantitatively measure these layer and line packing defects was a desirable measurement capability. This capability would provide important additional information with which to compare part microstructures.

Packing defects had been observed in most printed parts, whether they were made from ceramic or metal powders, with either monomodal or bimodal distributions. A different microstructural characteristic which was unique to the bimodal metal parts was the local bimodal composition. If segregation of the bimodal powder components occurred during the printing process, it would lead to local variations in part composition. Another desirable measurement capability, therefore, would be determination of part composition on a micro-scale.

This section describes the techniques which were developed to provide a more complete characterization of the printed part microstructures. The characteristics which were to be quantitatively measured included green density (both average and local), the extent of packing defects across the printed layers and lines, and local bimodal

composition. We begin with a review of methods which existed at the start of this research for measuring some of these microstructural characteristics.

4.1.1 Review of Microstructural Measurement Techniques

Measuring green density

Three established methods for determining the green density of printed parts were available at the start of this research. These were direct measurement, hydrostatic weighing, and photographic analysis. In the direct technique, the volume of the printed part was determined by measuring it with calipers, and the part mass was obtained with a precision scale. The green density, $\emptyset_{green}$, was determined from the expression

$$\phi_{green} = \left(\frac{\text{part mass}}{\text{part volume}}\right)\left(\frac{1}{\rho_{theoretical}}\right), \qquad 4.1$$

where $\rho_{theoretical}$ was the theoretical density of the alloy. The pros and cons of this method were as follows:

Pros

1. Fast.
2. Relatively easy to employ.

Cons

1. Difficult to measure complex shapes (usually limited to rectangular bars).
2. Could not measure local green density.
3. Binder must be removed or the binder mass known a priori before bar mass can be determined.

Measurement error was also a concern using the direct approach. The error originated primarily from the determination of part volume. Accurately measuring the length, width and height dimensions of a printed bar was difficult because the external surfaces tended to be rather rough. (This was usually due to printing defects on the bottom, sides and ends of the bar.) Table 4.1 illustrates the percentage error in the volume

measurement for two different sized bars and four different levels of part dimension measurement error. For example, if there was a measurement error of +/- 50μm for each of the edge dimensions of a 2mm x 10mm x 70mm bar, then the volume calculation could be off by as much as 3.07%.

Table 4.1: Volume Measurement Error for Different Measurement Conditions

Part Edge Measurement Error (μm)	10mm x 10mm x 70mm Bar % Volume Error	2mm x 10mm x 70mm Bar % Volume Error
25	0.54%	1.54%
50	1.07%	3.07%
75	1.61%	4.61%
100	2.14%	6.14%

The green density calculation was directly affected by the bar volume measurement error. Error could be reduced by printing larger bars, but this could be an extremely time consuming task if multiple printing conditions were to be investigated. The green density measurement was also affected by the precision of the bar mass measurement, although this was usually much less of an issue since precision scales could determine the bar mass to +/- 0.001g.

In the hydrostatic weighing technique, part volume was determined by suspending the bar from a very thin wire and submerging it into a container of water. The container was positioned on a precision balance before the part was lowered. The amount of water which the part displaced in the container (i.e. the part volume) translated into an increase in the apparent mass of the container as follows:

$$\text{part volume} = \frac{\Delta_{\text{mass}}}{\rho_{\text{water}}}. \qquad 4.2$$

The density of the water (in g/cc), which is temperature dependent, was given by

$$\rho_{\text{water}} = 1.0017 - 0.0002315(T), \qquad 4.3$$

with T being the water temperature in °C. To prevent water from filling the pores of the part, the part was infiltrated with mineral oil prior to immersion. Once the part volume was

known, the part green density could be obtained using expression 4.x above. The pros and cons of this method were as follows:

Pros

1. Could be used to measure density of odd shaped objects.
2. Relatively easy to employ.

Cons

1. Tiny air bubbles that adhered to the part would cause great loss of precision, especially with small samples. Adding a surfactant to the water helped, but did not solve the problem.
2. Could not measure local green density.
3. Binder must be removed or the binder mass known a priori before bar mass can be determined.
4. The oil used to seal the pores often formed a film around the part, increasing the apparent volume. This resulted in green density measurement errors similar to those in the direct measurement technique.

The third method of measuring green density was with photographic analysis. In this technique, a digitized image of a polished cross-section from the part was obtained. Computer algorithms were used to count the number of pixels in the image which represented metal regions. The green density of the part was equal to the fraction of total pixels in the image which were in the metallic regions. The pros and cons of this method were as follows:

Pros

1. Could be used to measure density of odd shaped objects.
2. Could measure local packing density.

Cons

1. A complex technique, requiring extensive sample preparation, digital photographic equipment, and custom software.

2. Multiple images were required to obtain an average green density.

Measuring packing defects across printed layers and lines

Prior to this research, there was no quantitative method for measuring these quantities. The extent of packing defects had been previously judged by visual inspection of cross-sectional images.

Measuring bimodal composition

Three established methods existed for measuring part composition. These included sieving, liquid settling, and photographic analysis using different metal alloys for the large and small powder components. For both the sieving and liquid settling techniques, the printed part first had to be "dissolved" in a solvent which would attack the Acrysol binder. Ammonia was the solvent used. The part was placed in a glass beaker of ammonia and sonicated for 15 minutes to completely dissolve the Acrysol. After the powder had settled to the bottom of the beaker, the ammonia solution was carefully decanted so as to not remove any of the powder particles. The process was repeated once more with fresh ammonia, and then twice more with distilled water. Finally, the remaining water was evaporated in an oven, leaving behind all the original powder, in a loose, binder-free condition. At this point, either the sieving or liquid settling approach could be used to measure composition. In the sieving approach, the powder was sieved with a screen that would only allow the fine particles to fall through. By measuring the mass of all the particles before sieving, and the mass of either the large or small components after sieving, the composition could be determined.

In the liquid settling approach, the loose powder was redispersed in water using a surfactant. The water / powder mixture was poured into the top of a water filled, 1 meter tall acrylic cylinder, approximately 3" in diameter. The different powder sizes have settling velocities given by the expression

$$V = gD^2(\rho_s - \rho_l)/18\mu, \qquad 4.4$$

where V is the settling velocity of a given particle, g is the gravitational acceleration, μ is the water viscosity, and ρ_s and ρ_l are the densities of the steel and water, respectively. [20] Since settling velocity varies as the square of particle diameter, the large particles settled much faster than the small. At some point, all the large particles had reached the bottom of the cylinder, while the small particles were still settling. Using a siphon, the small particles and surrounding water were removed before they reached the bottom of the cylinder. Once separated, the remaining water could be removed by decanting and evaporation. Again, by measuring the mass of all the particles before dispersing, and the mass of either the large or small components after separation, the composition could be determined.

Although the sieving and liquid settling approaches to compositional measurement were straightforward in concept, they were actual very difficult to implement in practice. The pros and cons of these two methods were as follows:

Pros

1. Could be used to measure average composition of a part.

Cons

1. Printed part was destroyed in the process.
2. Neither technique could measure local composition.
3. Removing all the Acrysol binder was extremely difficult, resulting in some agglomerates of small particles which would be improperly identified as large particles.
4. Sample sizes were very small (usually less than 15g). Loosing any particles during processing could result in large errors. Particles could be lost by:
   - getting stuck in the sieve mesh
   - being lost during binder removal and decanting
   - adhering to the walls of the acrylic cylinder during freefall

The third established method for measuring composition was via photographic analysis. For this technique, the large and small components needed to be composed of differing alloys, which would appear at different brightness levels in the digitized image. A computer algorithm could then be used to analyze the image, counting the number of pixels

associated with each phase. Based on this pixel count, the composition of the image could be determined. The pros and cons of this method were as follows:

Pros

1. Could be used to measure local composition.
2. Only a portion of a sample needed to be used for the analysis.

Cons

1. A complex technique, requiring extensive sample preparation, digital photographic equipment, and custom software.
2. Multiple images were required to obtain an average composition value.
3. Bimodal mixtures with different alloys needed to be used. The printing behavior of a mixed alloy system may not be representative of an all steel system, however, and this difference could give misleading results.

4.1.2 Evaluation of Current Measurement Capabilities

After reviewing the pros and cons of the established techniques for measuring the microstructural features of interest, it was concluded that only the photographic analysis technique for measuring green density was acceptable. A development effort was undertaken to expand the capabilities of the photographic analysis technique so that all the features of interest could be quantitatively measured. Image acquisition techniques were developed and custom image analysis software was written to perform this task. A complete description of this development effort is given in appendix C. The reader is encouraged to thoroughly review this material before proceeding. A brief summary of the measurement techniques developed and the parameters generated is given below.

4.1.3 Summary of New Microstructural Measurement Techniques

To analyze the microstructures produced by a given printing procedure, several rectangular bars were printed using that procedure. The bars were removed from the bed, and furnace processed to remove the polymeric binder and lightly sinter the powder skeleton. The bars were then cross-sectioned halfway along their length, vacuum infiltrated with epoxy and polished to reveal the internal microstructure. Multiple high-

resolution images from a scanning electron microscope (SEM), operating in backscatter electron mode, were taken of the cross-section. Figure 4.2 is a illustration of the location in the printed bars where the SEM images were obtained.

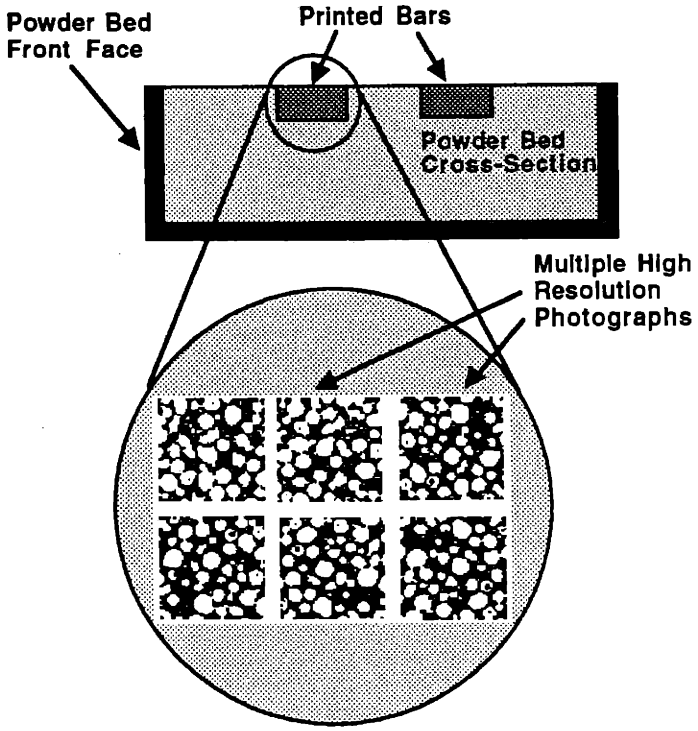

Figure 4.2: Orientation of printed bars for cross-sectioning.
The fast axis is into the page.

A group of ten images, taken at 100x magnification, were typically obtained from each microstructure. Each image had a viewing area of approximately 1mm x 1mm. These images were digitized into a 1024 x 1024 pixel format by the image acquisition hardware and software. The digitized images of the microstructure were then enhanced and analyzed using custom computer algorithms developed specifically for this research.

After processing, a summary data file was created for each batch of images. An example of a summary data file is given in figure 4.3.

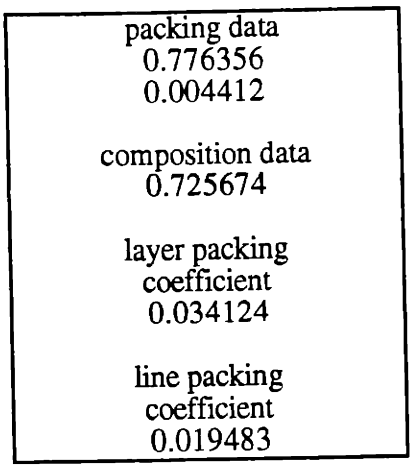

Figure 4.3: Example of a summary data file.

The average packing density of the images in the batch was given, along with the standard deviation of the individual image packing density values. From these two numbers, a packing density coefficient of variation (COV) was determined using the formula

$$\text{packing density COV} = \frac{\text{standard deviation of packing values}}{\text{average packing value}}. \qquad 4.5$$

The packing COV was used as a measure of the extent of powder packing variation across the part microstructure. Low values for the packing COV indicated a homogeneous, densely packed microstructure. The next quantity given in the summary data file was the average bimodal composition for the sample. (This quantity was irrelevant when analyzing monomodal samples for packing defects.) Finally, layer and line packing coefficients were generated. These coefficients described the extent to which packing defects existed across the spread layers and between the printed lines in the microstructure. Again, lower values were preferred for these coefficients, since this indicated more homogeneous powder packing.

The numbers generated in the summary data file could be used to compare the microstructures of parts produced using different printing and layer densification techniques. To serve as an additional standard for comparison, "cast" control samples were made from both the monomodal and bimodal powder feedstocks. A "cast" control

sample was made from loose powder which was tap densified in a ceramic crucible and lightly sintered to produce a representative microstructure for that powder. This method of producing a cast part ensures that there is no microstructural directionality to the part. The cast microstructure was taken to be the most densely packed and homogeneous microstructure possible for a given powder. The descriptive values generated by the image analysis algorithms for these control samples were considered the best values which could be obtained, and were the target values for the printed microstructures.

4.1.4 Baseline Printing Test Procedures

The tests which were performed during the baseline analysis are detailed in section 4.2 below. (Historical Note - The tests below only consider the two 316L bimodal powder blends. The 420 bimodal blend was not included.) A summary of these tests is as follows:

1. Spread Densities - Layering tests were performed on two monomodal and two bimodal blends to determine their spread density. Tests were made both with and without roller vibration to determine the effect of this parameter on layer packing.

2. Layering Segregation - A test was devised to determine if bimodal powder segregation was occurring during layer generation with the counter-rotating spreader rod. Spreading was again performed both with and without vibration.

3. Control Sample Analysis - Cast control samples, both monomodal and bimodal, were analyzed to serve as a basis for future comparison. Also, printed monomodal parts from previous research were analyzed.

4. Bimodal Bar Analysis - Bars were printed with both the 316L bimodal blends, using the baseline printing technique and parameters described in chapter 3. Printing runs were made both with and without roller vibration to determine the effect of this parameter on the printed bimodal microstructures.

4.2 Results from Baseline Printing

4.2.1 Spread Densities of Monomodal and Bimodal Powders

In this test, multiple layers were spread in the powder piston to determine the spread density of a given powder. The 120μm and 20μm 316L monomodal powders, and the 120/20μm and 71/9μm 316L bimodal powders, were tested. No powder locking was used, and no printing was performed between layers. Two spreading conditions were evaluated for each powder: one in which the spreader rod was vibrated, and one in which it was not. In the case of vibration, the excitation frequency was 200Hz, and the motion was diagonal with 2 mils total displacement. For the powders tested, 100 layers, each 175μm thick, were spread in the 9cm x 9cm powder piston. The spread volume of powder was therefore 141.5cc. After spreading was completed, the powder was removed from the piston and weighed to determine the spread packing density. Table 4.2 summarizes the results from this test. Information on the apparent and tap densities for the powders is also given for comparative purposes.

Table 4.2: Spread Densities for the Sample Powders

	120μm 316L	**20μm 316L**	**120/20μm 316L**	**71/9μm 316L**
Spread Without Roller Vibration	61.5%	58.0%	67.3%	64.2%
Spread With Roller Vibration	62.5%	61.0%	75.6%	66.8%
Apparent Density	58.8%	52.6%	60.5%	58.0%
Tap Density	62.8%	62.1%	76.2%	78.5%

Figure 4.4 presents the spreading results in graphical form. As would be expected, the two bimodal mixtures packed to higher values than the two monomodal powders. The use of vibration improved the spread density in all cases, however the 71/9μm bimodal blend showed very little improvement over the case of no vibration. This was attributed to the very high interparticle friction in the 71/9μm mixture, which had been initially observed in the very high angle of repose value for this powder. The spread density with vibration nearly reached the tap density of the powders in all cases except the 71/9μm blend, where there was still significant opportunity for further densification.

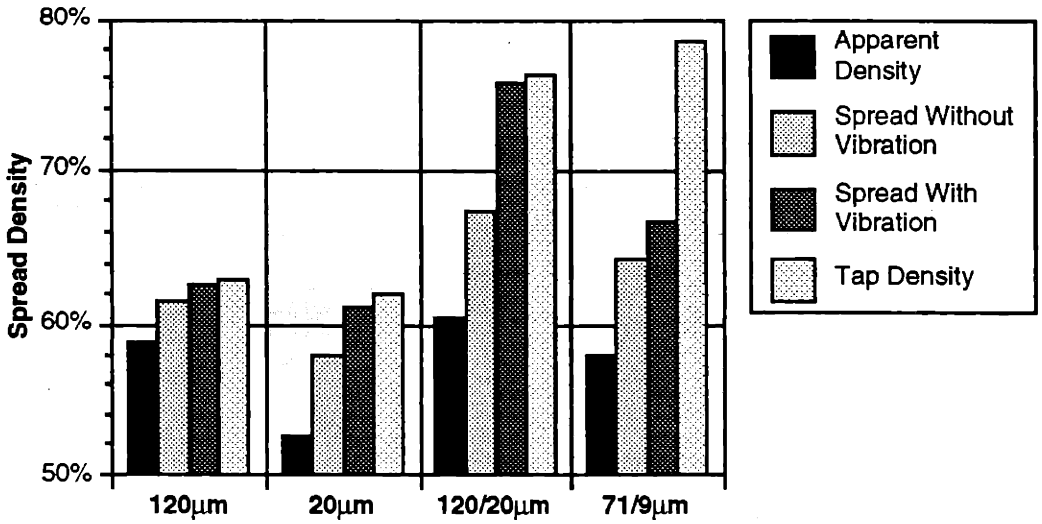

Figure 4.4: Results from the spread density tests.

4.2.2 Analysis of Bimodal Segregation During Layering

The counter-rotating spreader rod had been identified as a possible source of segregation during the spreading of bimodal powders. A test procedure was devised which would determine if this baseline spreading process was indeed causing segregation. For each of these tests, powder was layered over a stainless steel substrate. The substrates measured 1mm x 10mm x 200mm. The substrates were attached to the piston bottom using double-sided tape. Fifteen layers of powder were spread on each substrate, with the longest substrate dimension being the direction of spreading. (Note - The use of these steel substrates allowed for substantially longer spreading distances than would have been possible using the standard 9cm x 9cm powder piston on the prototype 3DP machine.) A total of four spreading runs were made, using the 120/20μm and 71/9μm 316L bimodal powder mixtures, both with and without roller vibration.

After spreading, the substrates were furnace processed to lightly sinter the powder layers. The strips of sintered powder were then potted and polished. Microstructural photographs were taken at 5mm intervals along the length of each strip. A magnification setting of 100x was used for the 120/20μm powder strips, and 150x for the 71/9μm powder strips. The individual photographs were analyzed for local compositional value and local packing density. The results from these tests are plotted in figures 4.5-6. (Note -

In these figures, compositional values are indicated by the percentage of large powder, which was 73.5% in the original bimodal feedstocks.)

Figure 4.5 shows the localized composition versus spreading distance for the tests conducted with the 120/20μm powder. Three sigma upper and lower statistical limits are also shown on the graph. These limits were previously determined by analyzing 30 photographs taken from the 120/20μm cast control sample. The composition for each of these 30 images was determined, and a standard deviation in composition was calculated. The region between the three sigma limits in figure 4.5 represents where compositional values from these spreading tests should fall if there was no segregation present. Inspecting the data for both the spreading conditions of vibration and no vibration, there is no indication of segregation present. All compositional variation falls between the upper and lower statistical limits, and there is no apparent upward or downward trend in the data. The mean compositional values do not precisely correspond to the 73.5% starting feedstock value, but this was attributed to slight errors in the calibration of the analysis software.

Figure 4.6 is a plot of local packing density versus spread distance for the 120/20μm spreading tests. Packing was also measured as a confirmation that composition was not being significantly altered. Since the maximum packing value of a bimodal mixture is very sensitive to mixture composition, it was expected that any deviation from the ideal composition of 73.5% large component would result in a drop in packing density. Although there is variation present in the local packing values shown in figure 4.6, there is no downward trend for either spreading condition. The average packing values for the conditions of vibration and no vibration are different, however, as had been previously determined by the spread density tests above.

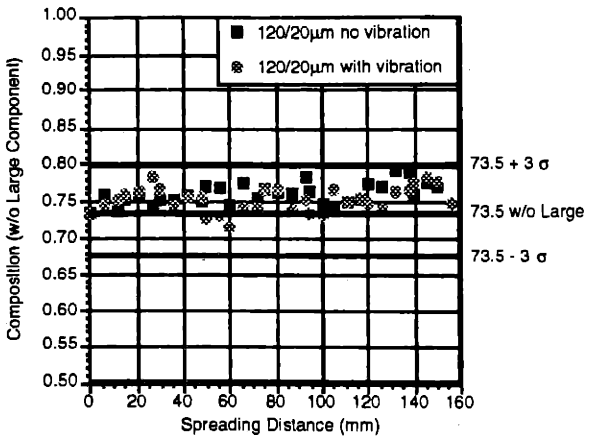

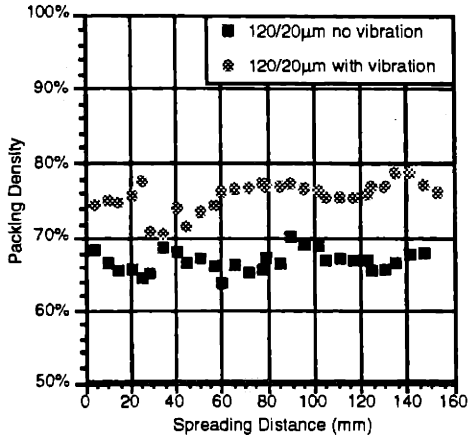

Figures 4.5 and 4.6: Localized composition (left) and packing density (right) vs. spread distance for the 120/20μm bimodal powder mixture.

Figures 4.7-8 are the data plots for the 71/9μm bimodal powder spreading tests. Again, there is no indication that segregation is occurring during the spreading of this powder, either with or without the use of spreader rod vibration.

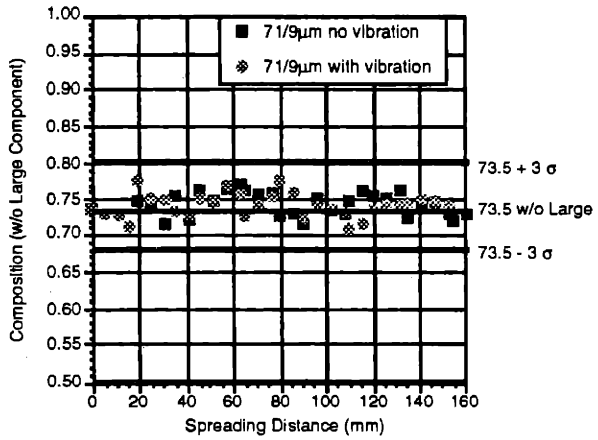

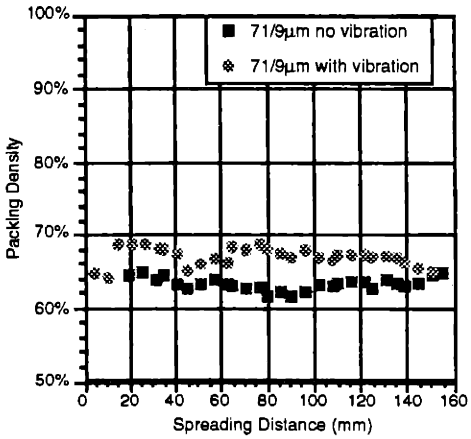

Figures 4.7 and 4.8: Localized composition (left) and packing density vs. spread distance for the 71/9μm bimodal powder mixture.

4.2.3 Microstructural Analysis of "Cast" and Printed Control Samples

Before performing microstructural analysis on the printed baseline parts, the following question was asked: For the hypothetical ideal case in which a printed part had a completely homogeneous microstructure, what values would the packing parameters

attained with the analysis procedure have ? Knowledge of these "ideal" parameters, for parts printed with either monomodal or bimodal powders, would prove useful for evaluating how far from ideal a given part was. Improvements in printed part uniformity would be indicated by packing parameter values which were closer to the values of ideal parts.

The method used to obtain ideal packing parameter values was to analyze "cast" powdered metal parts made from both monomodal and bimodal powders. A "cast" part was made by lightly sintering powder which has been poured into a ceramic tray and tap densified. A typical cast part measured approximately 1 x 1 x 2 cm. Cast monomodal microstructures made from the 71μm and 9μm powders, and cast bimodal microstructures made from 120/20μm and 71/9μm powder mixtures, were analyzed. The composition of both bimodal mixtures was again 73.5% large powder component. The microstructures of the 71μm and 9μm cast monomodal samples are shown in figures 4.9 and 4.10. The microstructures of the 120/20μm and 71/9μm cast bimodal samples are shown in figures 4.11 and 4.12.

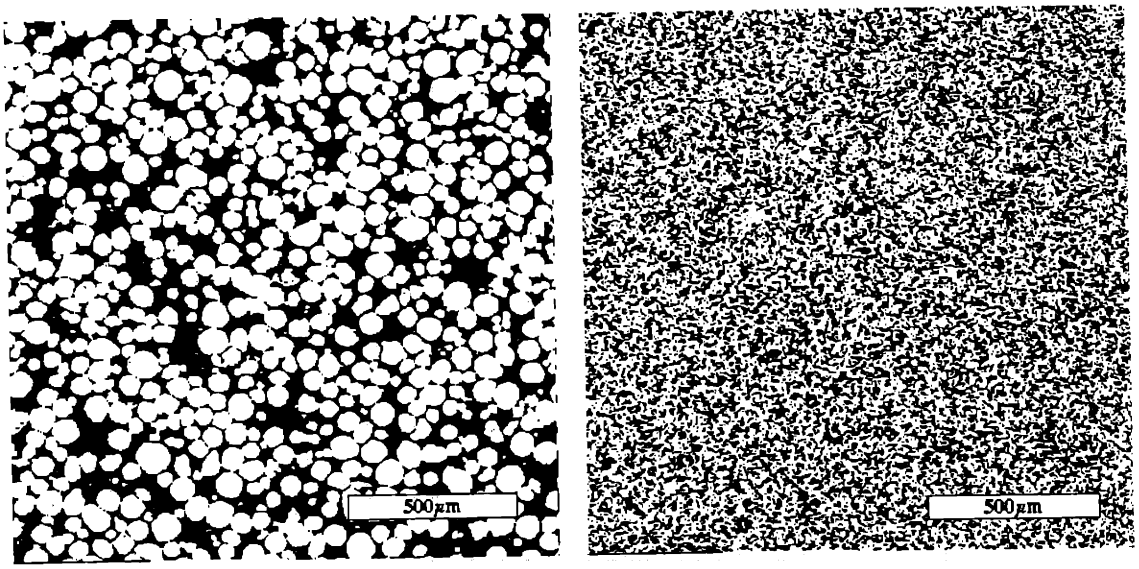

Figures 4.9 and 4.10: Microstructures of the 71μm (left) and 9μm "cast" monomodal baseline samples. Magnification 50x.

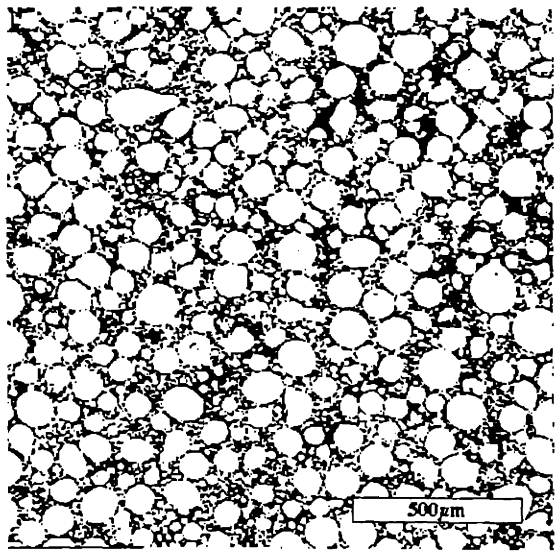

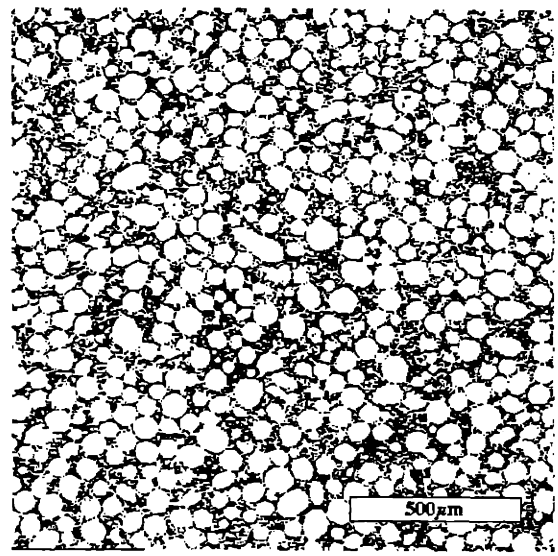

Figures 4.11 and 4.12: Microstructures of the 120/20µm (left) and 71/9µm "cast" bimodal baseline samples. Magnification 50x.

Results of the microstructural analysis of the monomodal and bimodal cast samples is given in table 4.3. Because the control samples have no inherent orientation to their microstructural defects, the values for the layer and line packing coefficients are nearly identical for each of the cast samples. A single, average value of the layer and line coefficients (given in the bottom row of Table 4.3) was therefore used as the ideal value for later comparisons.

Table 4.3: Microstructural Analysis Results for Cast Control Samples

Measurement Parameter	71µm monomodal	9µm monomodal	120/20µm bimodal	71/9µm bimodal
Average Packing Density	65.2%	58.0%	75.9%	76.4%
Packing COV	2.15%	8.33%	1.42%	1.34%
Layer Packing Coefficient	5.86%	8.06%	3.02%	2.59%
Line Packing Coefficient	5.63%	8.23%	3.10%	2.42%
Average of Layer and Line Coeff.'s	5.74%	8.15%	3.06%	2.51%

The vast majority of metal parts printed to date had been printed with monomodal 316L stainless steel powders. Powder size for these parts was usually 71μm, although a small number of parts had been printed with the 20μm powder. Packing densities for these monomodal parts were typically between 56 - 58%. The microstructures of these parts were analyzed using the photographic techniques to establish additional baseline values to be used for later comparison. Parts printed with new techniques could then be compared to these monomodal baseline values to indicate if the new techniques had improved on the current baseline process.

The microstructures of the 71μm and 20μm printed monomodal samples are shown in figures 4.13 and 4.14. Layers are in the horizontal direction. Obvious layering defects are present in the 20μm sample. There is no apparent layer or line structuring in the 71μm sample. Results of the microstructural analysis of the printed monomodal samples is given in table 4.4.

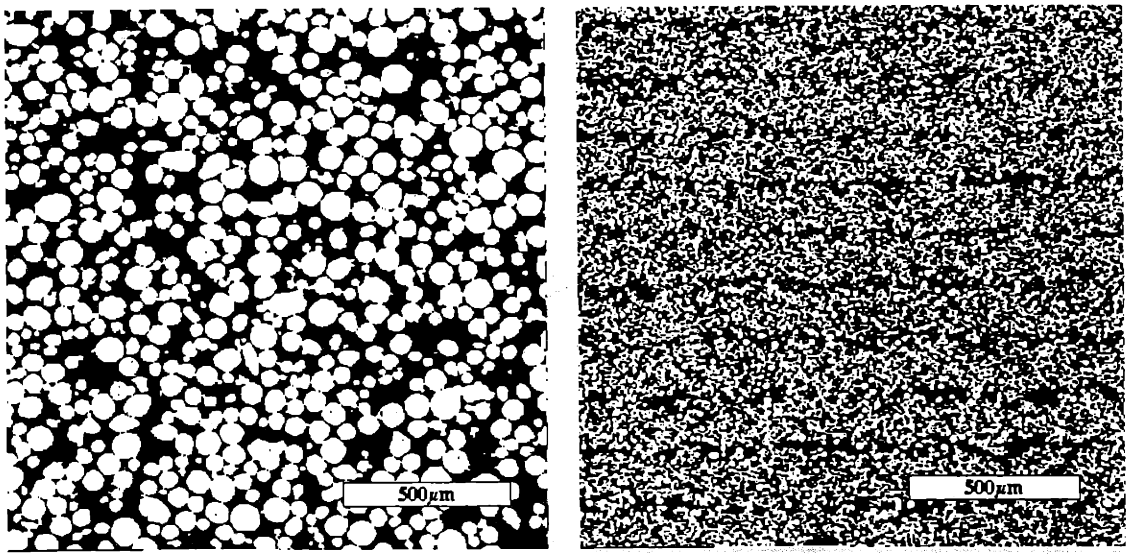

Figures 4.13 and 4.14: Microstructures of the 71μm (left) and 20μm printed monomodal baseline samples. Magnification 50x.

Table 4.4: Microstructural Analysis Results for Printed Monomodal Samples

Measurement Parameter	71μm printed monomodal	20μm printed monomodal
Average Packing Density	58.4%	52.7%
Packing COV	2.60%	3.47%
Layer Packing Coefficient	6.30%	8.54%
Line Packing Coefficient	6.37%	4.06%

The analysis results for both the cast control samples and the printed monomodal samples are summarized graphically in figure 4.15. The 9μm cast sample exhibited a significantly higher degree of packing variation, as indicated by its high value of packing COV. This was caused by both a large standard deviation in the individual packing densities of the images analyzed, and a low average packing density. The 20μm printed sample had the highest layer packing coefficient, which resulted from the significant layering defects shown in figure 4.14. The cast and printed 71μm samples had nearly identical values for both the layer and line packing coefficients, indicating that the printing process was not significantly affecting the microstructure of parts printed with the 71μm powder. The cast bimodal controls had the lowest values for all the measured parameters, which was a result of their extremely dense packings.

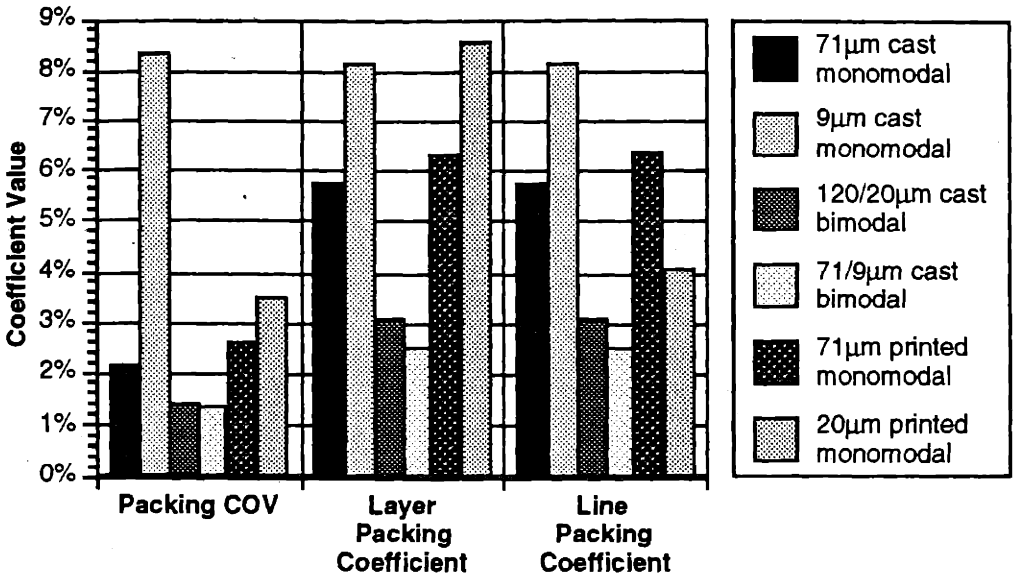

Figure 4.15: Results from analysis of cast control samples and printed monomodal samples.

4.2.4 Analysis of Bimodal Bars Printed with the Baseline Techniques

Four sets of bimodal bars were printed with the baseline technique, using the 120/20μm and 71/9μm powders, and spreading conditions with and without vibration. Figures 4.16-17 are micrographs of the samples printed without vibration. Large voids and layering defects are apparent, especially in the case of the 71/9μm powder. Figures 4.18-19 are micrographs of the samples printed with vibration. Packing defects are still present, although in smaller numbers.

Table 4.5: Microstructural Analysis Results for Printed Bimodal Samples

Measurement Parameter	120/20μm no vibration	120/20μm vibration	71/9μm no vibration	71/9μm vibration
Average Packing Density	62.7%	64.0%	62.3%	65.0%
Packing COV	3.46%	2.50%	2.54%	2.03%
Layer Packing Coefficient	7.22%	5.41%	10.91%	5.29%
Line Packing Coefficient	5.63%	3.81%	5.02%	3.45%

Figure 4.20 graphically summarizes the microstructural defect analysis results, and includes bimodal control sample data for comparison. In all cases, the values of the packing defect parameters improved (i.e. were reduced) with the use of spreader rod vibration. This is especially apparent in the improvement of the layer packing coefficient for the 71/9μm powder. In none of the test cases, however, was the target value of the control sample reached.

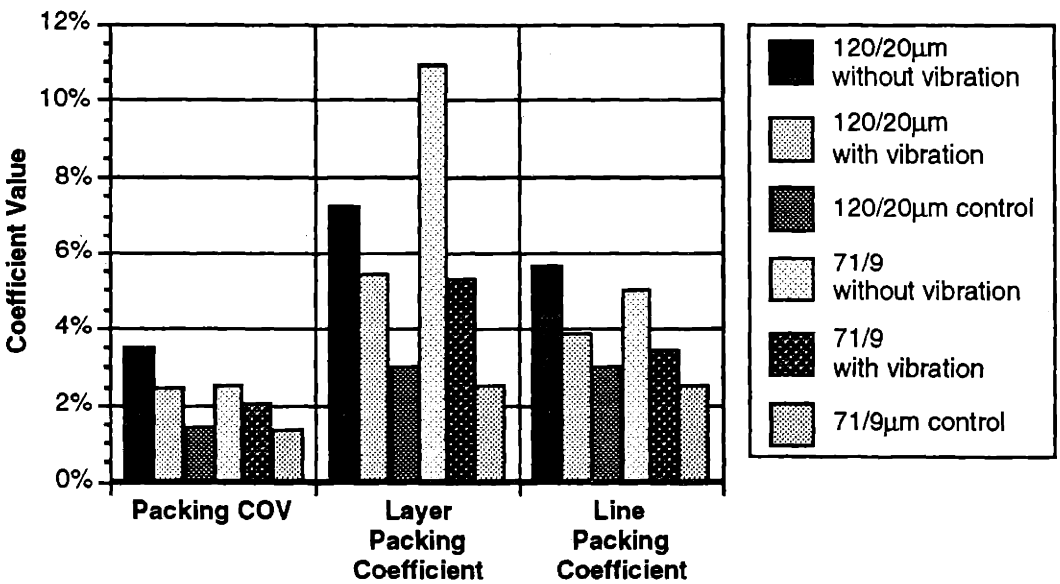

Figure 4.20: Results from analysis of printed bimodal samples.

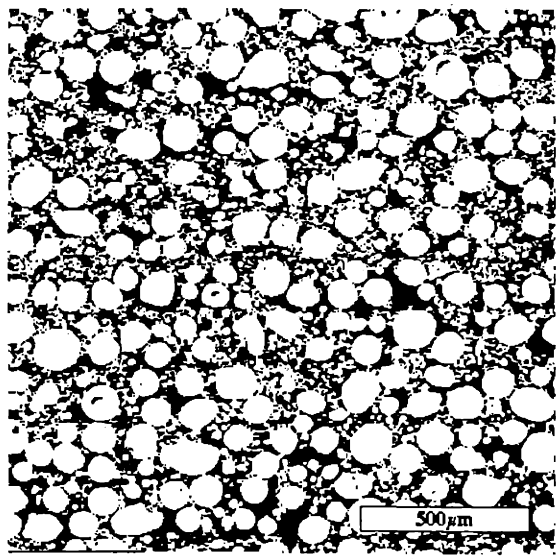

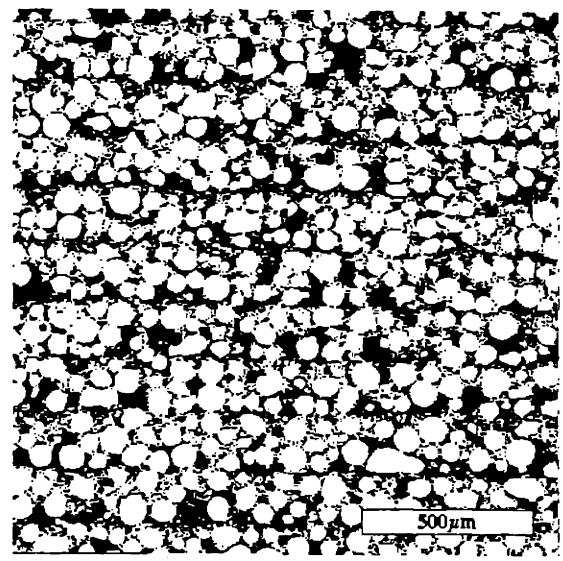

Figures 4.16 and 4.17: Microstructures of the 120/20μm (left) and 71/9μm printed bimodal baseline samples. Magnification 50x. No vibration.

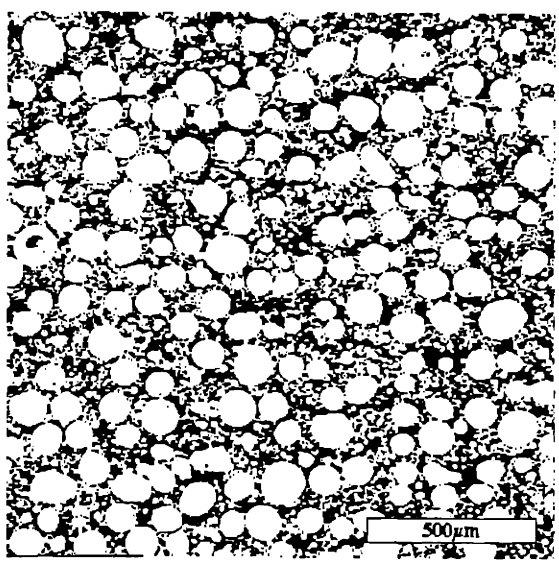

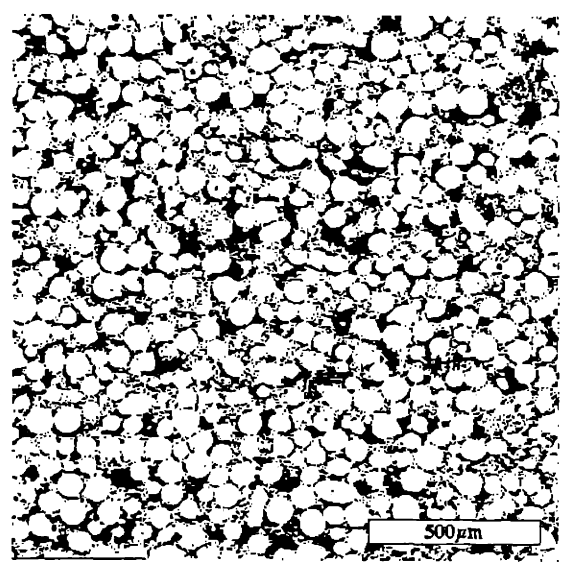

Figures 4.18 and 4.19: Microstructures of the 120/20μm (left) and 71/9μm printed bimodal baseline samples. Magnification 50x. With vibration.

Analysis results from the bimodal printing are given in table 4.5. The use of roller vibration caused a slight improvement in green density for both powders, but the packing values are still far below the powder tap densities.

4.3 Discussion

The green densities for the bimodal parts printed with the baseline techniques were higher than those for any previously printed monomodal parts. This was an encouraging result, as it indicated that metal parts with improved properties could be printed simply by altering the powder feedstock. There was, however, significant room for improvement. The bimodal green densities were far below the tap densities of the powders used. Also, the presence of significant packing defects, especially in the case of the 71/9μm powder, was a concern, since these defects would invariably lead to irregular shrinkage during sintering and anisotropic material properties in the final parts.

The printed green densities for the bimodal powders were also far below the spread densities which were obtained using the same spreading conditions. An explanation for this packing decrease was that during the spread density tests, particulate adhesion forces - either from printed binder or powder locking - were not present. All the powder particles, both in the powder pile and in the previously spread layer, were mobile. This mobility allowed for a greater degree of accommodation in the positioning of the individual particles, and led to a higher degree of packing. During the actual printing tests, the particles in the previous layer were bound together, either weakly by the powder locking coating, or strongly by the polymeric binder. All particle accommodation had to be accomplished by the mobile particles in the spread pile, which was less than that necessary to completely pack the new layer.

In general, the higher the fluidity of a powder, the more homogeneous the resulting printed microstructure. For monomodal powders, the 71μm printed sample had a much more homogeneous microstructure than the 20μm sample. This was again true with the bimodal powders, where the 120/20μm blend, with its lower interparticle friction, produced more homogeneous parts than the 71/9μm blend. Unfortunately, parts printed with these larger powders are less desirable, since the large particle sizes place limitations on the minimum layer thickness which can be used, and the minimum feature size which can be obtained. As the resolution demands on the 3DP process continue to increase, there will be a greater trend towards the use of finer powders. New layer densification techniques must be able to fully pack these finer powder feedstocks.

The remainder of this thesis will describe the work performed in the development of new layer densification processes. The goal of this work was to print parts from the 316L

and 420 bimodal powder blends with green densities at or near the tap densities for these powders, and part homogeneity values which approached those of the control samples.

Chapter 5. Investigation of Layer Densification Mechanisms

5.0 Introduction

To successfully design a new layer densification mechanism for the 3DP process, the following questions needed to be addressed:

1. What were the densification characteristics of the metal powders being studied in this research ?

2. How would variations in vibrational direction, frequency, amplitude and stress level affect the densification of these powders ?

3. Was there a resonant frequency (as in foundation modeling) at which the densification mechanism should operate ?

4. What was the time scale for densification ?

5. What method of densification was best suited for the printing of parts ?

6. What were the process requirements and constraints imposed by the 3DP system in the selection of a densification mechanism ?

These questions, and others, are considered in this chapter. Of the many compaction processes available, only some would be potentially applicable to the 3DP process. Answering the above questions would help in focusing on those methods which were useful to this research.

An overview of this chapter is as follows. A densification mechanism design selection methodology is presented in section 5.1. Potential designs for the next generation spreader / layer densification device are considered. In order to chose from these potential designs, tests from soil and powder mechanics were performed on the metal powders to better understand how applied stresses, both static and oscillatory, influenced their densification behavior. These tests are described in sections 5.2 through 5.5. Based on

the results from these tests, the potential designs were ranked in order of effectiveness. This discussion is presented in section 5.6.

5.1 Selection Process for a New Densification Mechanism

The question of how to go about determining the best way to densify powder layers in the 3DP process was rather open-ended. To approach this problem in a structured manner, a design selection methodology was proposed that specifically outlined the steps which were to be taken in creating a new layer densification mechanism. Although this methodology was certainly not the only one possible, it nevertheless helped to focus and direct this research effort.

5.1.1 A Design Selection Methodology

The goal for this portion of the research plan was to develop a new layer densification mechanism which met the following criterion:

1. Densified the layer the most, in the best case to the tap density of any given powder.

2. Densified the layer the fastest. With the current baseline process, each layer was spread at 0.5 inches/second. Improving on this rate while still increasing the spread density would be ideal, but it was desirable to not reduce the layer formation speed too much below this baseline rate.

3. Did not damage or distort the previously printed regions.

A design selection methodology was proposed in order to determine the best possible layer densification technique in a structured manner. Using this methodology, the design selection process proceeds through the following steps:

1. Propose several potential designs for the new layer densification mechanism. These potential designs were limited to those which would work within the constraints of the 3DP process. For example, any potential design need to be scaleable to work over a range of powder bed sizes. A design which only worked for evaluation on the small 9 x 9cm prototype piston would not be acceptable. Within the constraints of the 3DP process, the proposed designs should be as varied as possible, allowing

for the broadest possible selection options. Later steps in this design selection methodology would aid in predicting which of these designs would work best.

2. Utilize information from soil and powder mechanics to understand the relationship between applied stress fields and the densification behavior for the powders being considered. Each of the densification mechanisms proposed above would impose a unique stress field on the powder layer and underlying regions during the densification process. Some of these applied stress fields would presumably work better than others at densifying the powder. Theoretical considerations from powder mechanics should help to indicate which of the proposed designs would work best.

3. Perform tests from soil and powder mechanics to develop a better understanding of the relationship between applied stress and densification for the powders being considered. Information from these tests is then compared to existing theoretical models of densification, or used to create new models more applicable to the 3DP process. Information from these tests further aids in selecting the optimal layer densification mechanism from the proposed set of designs.

4. Construct the top design and evaluate it in actual printing conditions. It was expected that when the new design was used in actual printing conditions, new interactions would occur which would further modify the selection process. These printing tests would also confirm or refute the theoretical predictions of which design should work best. Ultimately, the final design selected is the one which best met the three design criterion listed at the beginning of this section.

Step one in this selection methodology, in which several potential designs for the new layer densification mechanism were proposed, is presented below. Steps two and three, in which tests from soil and powder mechanics were utilized to better understand the densification behavior of the metal powders, are described in the subsequent sections. Step four, in which the selected design is evaluated in actual printing conditions, is reserved for the next chapter.

5.1.2 Design Constraints

Before theoretical considerations, any potential spreader / densifier design needed to work within a set of pre-existing constraints. Some of these constraints were imposed by the 3DP process itself, while others were self-imposed due to practical considerations. The list of design constraints was as follows:

1. The compaction device needed to be scaleable. It could not operate on the entire powder surface at once, since this would require a potentially very large device in the case of a very large powder bed. Therefore, the design feature of current spreading method, in which only a strip of the powder bed is acted upon at any one time, would be kept in future designs. The spreader / densifier must therefore move across the powder bed during layer creation and densification. Specific design details, such as the speed with which this device moved, and the width of powder bed which was acted upon at any one time, were design parameters to be specified later.

2. It has been previously shown that a non-vibrating, counter-rotating spreader rod does not cause segregation of bimodal powders during layer spreading. Therefore, the initial powder spreading action, in which a single large powder pile was spread across the previous layer surface, would still be accomplished with such a spreader rod. This initial layer would be an extra-thick "prelayer", and would be subsequently compacted by the new densification mechanism. This prelayer / compacted layer approach had the benefit that all types of compaction equipment which were tested would have the same prelayer "starting point" on which to act, and therefore densification results would be more comparable. This constraint would also make the design of a new densification device easier, since this densification mechanism would act on a uniformly spread prelayer instead of a powder pile which decreased in size during the layer spread.

3. The quantity of powder distributed in the extra-thick prelayer would be more than was necessary to complete the final, compacted layer. This implied that the densification apparatus would, in addition to compacting the prelayer, be removing some quantity of powder and rejecting it off the rear of the piston. Although it was conceptually possible to spread a prelayer which contained exactly the amount of powder necessary to complete the final compacted layer, from a practical standpoint

it was better to have a small excess of powder in the prelayer prior to compaction. This would eliminate any possibility of have an insufficient quantity of powder in the prelayer to complete the compacted layer.

4. Any stress field generated by the densification mechanism must be transmitted into the prelayer through the top surface. The densification mechanisms would therefore be limited to the application of normal stresses acting downward on the powder surface and shear stress acting across the powder surface.

5. The preferred method of compaction would be one which employed a continuous motion across the powder bed, in tandem with the spreader rod which was striking the initial layer surface. Although it was possible to utilize a non-continuous approach, in which the motion of the densification mechanism across the bed was incremental, this approach was less desirable since it might require separate mechanisms for the spreader and densifier, which would add complexity and would likely be slower.

6. The maximum permissible stress applied normal to the surface of the prelayer was 1.0 psi (6895 Pa). This constraint was intended to prevent any significant increase in load capacity requirements for the powder piston. Additionally, based on previous experience with the printing process, it was unlikely that the powder bed could support loads in excess of 1.0 psi without damaging the previously printed regions. This constraint might be relaxed slightly if it could be shown that significant improvements in powder packing could be attained at higher stress levels without part damage.

5.1.3 Proposed Densification Mechanism Designs

Working within the above constraints, four concepts for a new spreader / layer densification mechanism were proposed. These are illustrated in figures 5.1-2. In all four concepts, a wedge shaped plate moves in tandem with the spreader rod, densifying the prelayer which has already been struck. The wedge shape was chosen because it provided a well defined, measurable bottom surface area through which densification stresses would be applied. Also, some type of forward facing surface was necessary to push excess powder along. The wedge shaped plate was a preliminary concept, however, and would be altered as necessary when additional design information became available.

The primary difference in the design concepts is the manner in which densification stresses are generated and applied to the prelayer. Figure 5.1 illustrates two of the four design concepts. In the first concept, the wedge plate oscillates through a defined vertical motion as it steadily moves across the layer surface in the positive x direction. The plate can be modeled as a displacement source in the z direction, and the resulting z axis reaction forces will depend on the underlying powder properties. In the second concept, both static and oscillatory vertical stresses are imposed on the plate in the z direction. The plate can be considered a force source in the z direction, and the resulting vertical motion of the plate over time will again depend on the underlying properties of the powder. These two design concepts create static and oscillatory stress fields in the powder regions directly below the wedge plate which are predominately compressive in the z direction.

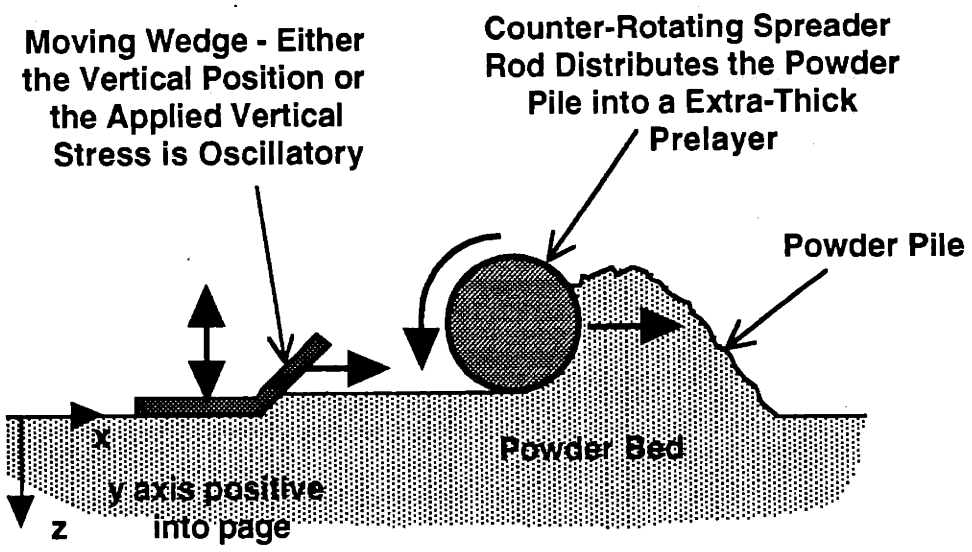

Figure 5.1: Illustration of the two densification mechanism concepts which impose a predominately normal stress distribution on the prelayer.

Figure 5.2 illustrates the third and fourth design concepts. In both concepts, the wedge plate oscillates through a defined displacement along the y axis. The plate is modeled as a displacement source in the y axis, and the y axis reaction shear forces will depend on the underlying powder properties. In the third concept, the vertical height of the wedge plate is constrained, and the resultant reaction forces in the z axis direction will depend on the underlying powder properties, and possibly the shape of the wedge plate itself. In the fourth concept, a monotonic vertical stress is imposed on the wedge plate.

The plate is allowed to move freely in the vertical direction, and reaches a stable position in which the applied and resultant vertical forces balance. Because the wedge plate is oscillating horizontally in these latter two design concepts, the oscillatory stresses transmitted to the powder regions directly below the wedge plate are predominately shear stresses along planes parallel to the powder surface. The static stress fields are again predominately compressive in the z direction.

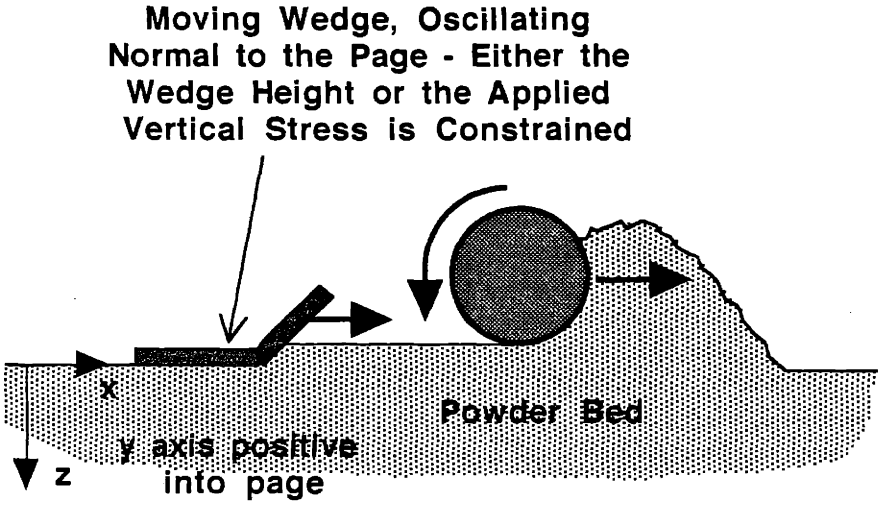

Figure 5.2: Illustration of the two densification mechanism concepts which impose a predominately shear stress distribution on the prelayer.

Choosing between these four concepts (or identifying any additional ones) required information on the densification behavior of metal powders when subjected to various stress distributions. To obtain this information, extensive testing was performed on the metal powders, using techniques borrowed from soil and powder mechanics. The different test areas are described in sections 5.2 through 5.5.

5.2 Powder Bed Vibrational Response

Two preliminary tests were performed to gather information about the vibrational response characteristics of the powder bed when it was filled with a metal powder. In the first test, the speed of sound through a bed of bimodal powder was measured. From the speed of sound data, the bed stiffness (i.e. Young's modulus) in the vertical direction could be estimated. Knowledge of the bed stiffness would help indicate if the powder bed had a

resonant frequency, and if the bed could be modeled using a lumped-parameter approach, as is sometimes done in soil mechanics.

In the second test, the attenuation with depth of a vibrational stress applied vertically to the top surface of the powder bed was measured and compared to attenuation predictions based on elastic body theory. This test helps indicate how fast the vibrational energy produced by a densification mechanism dissipates in the powder bed, and if the elastic body approximation was applicable. Ideally, energy that was put into the new layer to densify it will not travel too much farther, where it might cause damage to the lower regions in the powder bed.

5.2.1 Speed of Sound Measurement

Procedure

The 120/20μm and 71/9μm 316L bimodal powders were measured in this test. Figure 5.3 shows the setup used for the speed of sound (SOS) measurements. A 15 mil thick RAINBOW piezo transducer (see appendix B) was attached to the bottom of the powder piston and used as a vibrational transducer. It was assumed that the slew rate of the piezo was much faster than the speed of pressure waves through the powder. Time lag between any applied pressure to the piezo and the voltage output from the piezo was taken to be zero. The powder bed was filled with powder, and the powder was tap densified by pressing on the top surface with a plate while repeatedly striking the piston side with a metal block. A level surface was struck, and the input transducer was placed on top of the powder surface. The input transducer was a 30mil thick RAINBOW piezo which had a small aluminum block attached to act as a striking surface. Both the input and output transducers were attached to an oscilloscope.

The input transducer was struck with a small steel hammer, producing a voltage response and transmitting a pressure wave through the powder. After a time delay, the output transducer responded. The time delay between input and output voltages was recorded.

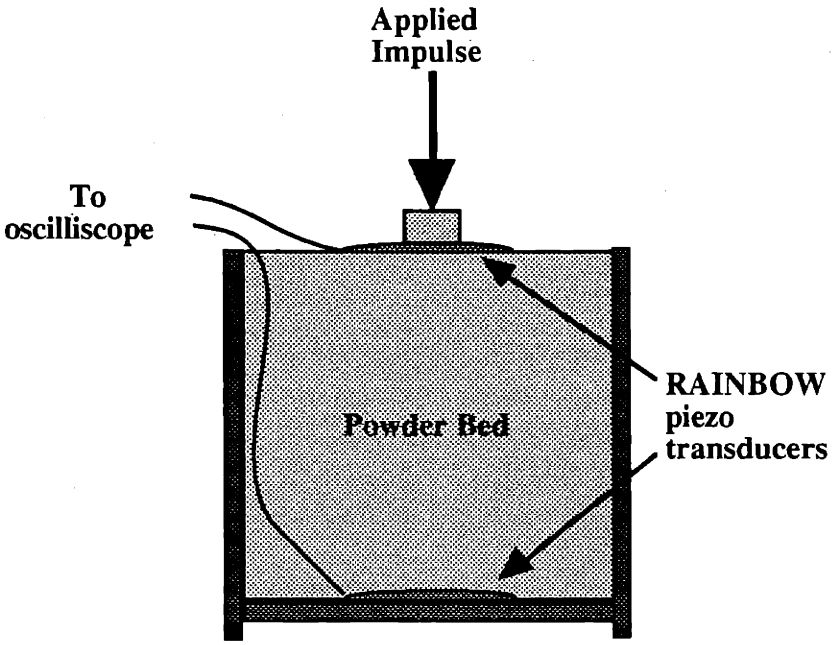

Figure 5.3: Schematic of the speed of sound experimental setup.

Results

Multiple tests were performed for each powder, and the results averaged. The results from the speed of sound tests are given in table 5.1.

Table 5.1: Results from the Speed of Sound Tests

Powder	Depth (cm)	Time Delay (μs)	SOS (m/s)
120/20μm	4.29	253	170
71/9μm	4.36	276	160

The velocity V_c of a compressive wave through particulate material is given by the expression

$$V_c = \sqrt{E/\rho}, \qquad 5.1$$

where E is the Young's modulus and ρ is the bulk density of the material. [29] By measuring V_c and ρ, E can be obtained. The calculated values for Young's modulus are given in table 5.2

Table 5.2: Young's Modulus for the Two Bimodal Powders Tested (at the Tap Density)

Powder	Young's Modulus (GPa)
120/20μm	0.173
71/9μm	0.154

For comparison, the Young's modulus for solid steel is 207GPa. The stiffness of the bimodal powders at the tap density is therefore approximately 0.08% that of solid steel.

5.2.2 Vibrational Stress Attenuation Measurement

Procedure

Figure 5.4 is an illustration of the setup used for the vibrational stress attenuation measurements. Measurements were made using the 120/20μm and 71/9μm 316L bimodal powders. The powder bed was filled with powder and densified as described above. Vertical static and dynamic stresses were applied through an aluminum pressure plate. The surface of the plate in contact with the powder measured 1.5cm x 8.5 cm. (The device used to produce the stresses is described in section 5.4.) The static compressive load applied was $10g/cm^2$. The superimposed dynamic load was +/- $4g/cm^2$. Loads were applied at 200, 500 and 1000Hz. The amplitude of the output voltage from the pickup piezo was measured for several depths of powder. For a given frequency, the output voltage from the transducer was proportional to the vertical stress at the transducer location.

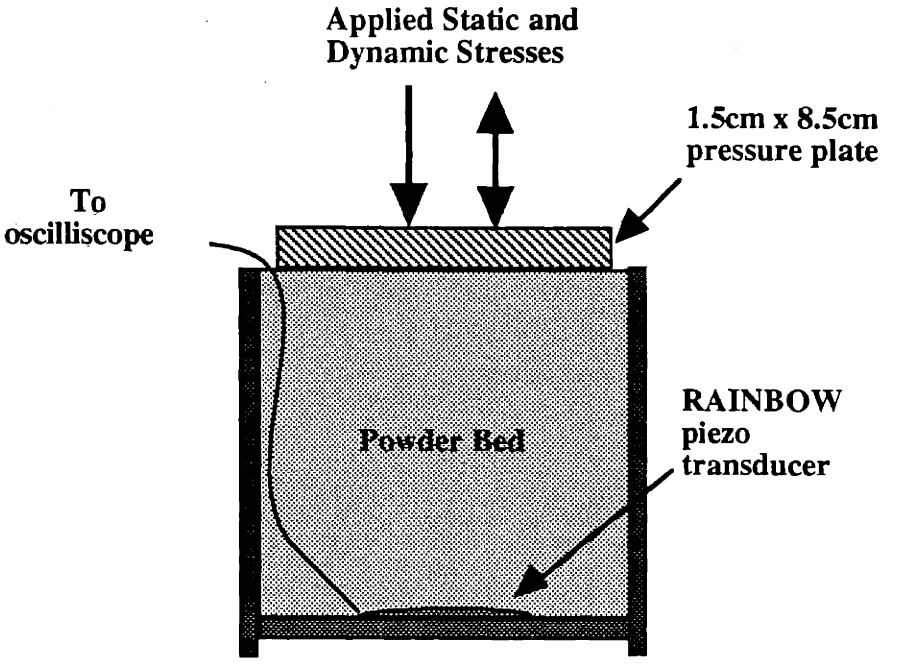

Figure 5.4: Schematic of vibrational energy attenuation measurement setup.

Results

The results from the attenuation tests are shown in figure 5.5. Also plotted is the theoretical attenuation of stress in a semi-infinite elastic body subjected to a strip load. The vertical stress transmitted in an elastic body by a strip load is given by the expression

$$\sigma_z = \left(\frac{\text{applied stress}}{\pi}\right)(\sin(2\beta) + 2\beta), \qquad 5.2$$

where

$$\beta = \arctan\left(\frac{\text{footing width}}{2 * \text{depth}}\right). \qquad 5.3$$

[ref. 58, p.228]

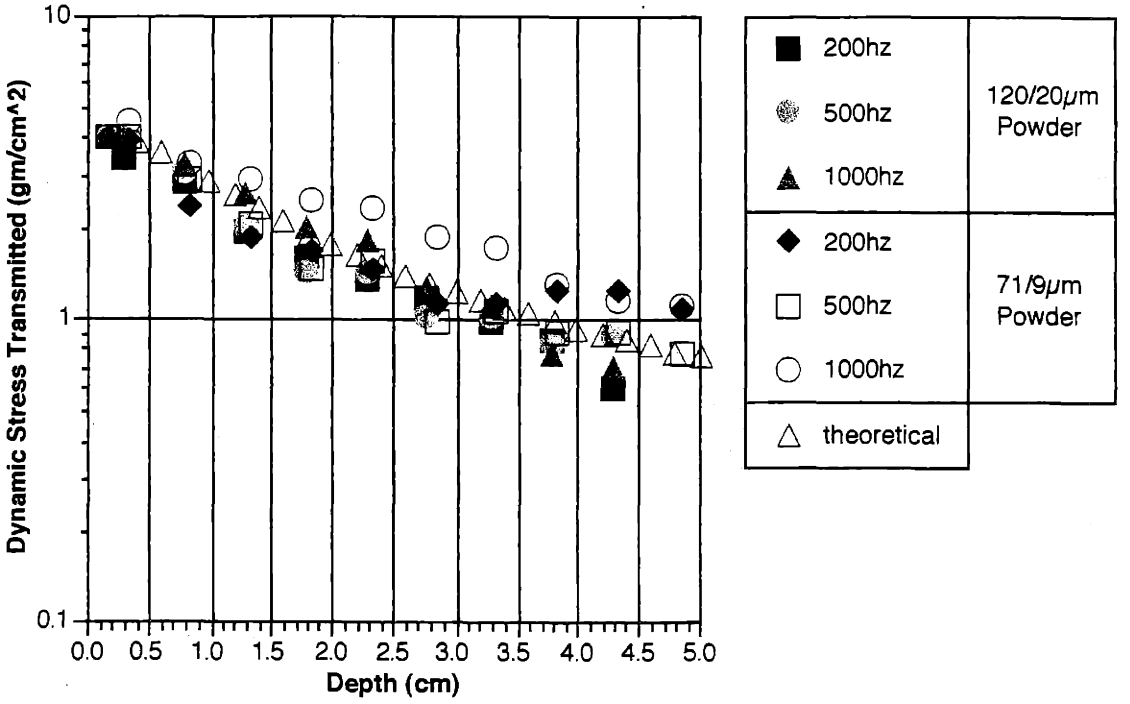

Figure 5.5: Vibrational energy attenuation measurements for powders at the tap density. Vertical static and dynamic applied stresses.
Static stress = $10g/cm^2$. Dynamic Stress = +/- $4g/cm^2$.

All the vibrational test conditions closely tracked the theoretically predicted values, with only a slight variation in the case of the 71/9μm powder tested at 1000Hz.

5.2.3 Conclusions from the Vibrational Response Tests

The stiffness of the powder bed using either of the bimodal mixtures was significantly lower than that of solid steel. In the review of soil mechanics literature, it was shown how soil masses which are dynamically loaded can exhibit a resonance frequency at which densification proceeds the fastest. To determine if a powder bed filled with metal powder might have a similar resonance frequency, a crude estimate of the spring constant k of the powder bed in the vertical direction was made. For a volume of powder bed measuring 1cm deep x 1cm wide x 9cm long (a typical volume of powder bed which might be acted on during densification), k can be obtained from the expression

$$k = \frac{EA}{t}, \qquad 5.4$$

where A is the surface area (=9cm^2) and t is the thickness (=1cm). Furthermore, if we assume a resonant mass m equal to the powder mass in the volume, then a resonant frequency f_r can be obtained from the expression

$$f_r = \frac{1}{2\pi}\sqrt{\frac{k}{m}}. \qquad 5.5$$

Assuming a 75% packing density, the resonant mass m is equal to 53g. This results in a resonant frequency of approximately 26KHz. Whether or not this calculated resonance frequency was realistic is unclear, and would certainly need to be verified experimentally. In any case, this value was far above the range of vibrational densification frequencies which could be considered in this research. Modeling the powder bed using a lumped-parameter approach is therefore inappropriate. In soil mechanics, the thickness of the particulate volume being considered is usually on the order of several meters, the soil stiffness are much lower, and the resonant mass includes the mass of the building foundation and machinery. All these factors contribute to producing resonant frequencies in the range of 1 to 100Hz.

From the results of the attenuation experiments, we can conclude that an elastic stress distribution approximation is acceptable for determining the stresses transmitted through the powder bed from any given densification mechanism. The frequency of the dynamic stress does not alter the attenuation response, at least over the frequency range tested. Furthermore, the decrease of stress intensity with depth has an approximately exponential relationship over the range of depth tested.

5.3 Shear Cell Tests

One of the most basic and simple tests from soil and powder mechanics for the measurement of powder stress / strain properties is the shear cell test. A schematic diagram of a shear cell was previously shown in figure 2.32. In the shear cell test, a specified normal load is applied to the shear plane. The top half of the shear cell is moved at a constant shearing rate, and the resultant shear stress is recorded over time. In soil mechanics, the shear cell test is used primarily to determine under what stress conditions a given sample of soil will fail. This information can later be used, for example, to predict the level of loading which an area of soil can support in actual field conditions. For this

research, we are primarily interested in using the shear cell tests as a means to further understand the densification behavior of metal powders.

5.3.1 Additional Background in Shear Cell Testing

The shear cell test characterizes the powder stress condition at the point of initial failure, and during continuous sliding. A typical response curve from a shear cell is shown in figure 5.6. The shape of the response curve depends on the applied normal stress (which is held constant throughout the test), and the initial packing density of the powder in the cell. As was explained earlier in the literature review, the only packing density which can be reliably repeated in the cell is the tap density. Starting from this packing density condition, the shear cell is always over-consolidated at the start of the test. The shape of the response curve in figure 5.6 is typical of an initially over-consolidated sample.

During the shearing test, shear stress builds along the shear plane until dilation and failure occur. During failure, the packing density along the failure plane drops below the tap density. The point of initial failure is represented by point *A* in figure 5.6. The shear stress value at point *A* is referred to as the "peak" shear stress for the test. According to the Jenike yield locus theory, point *A* lies on the yield locus which corresponds to the tap density of the powder being tested. With continued straining, the resultant shear stress eventually drops to a steady value, represented by point *B*. The powder packing density along the shear plane is unknown at this point. The shear stress value at point *B* is referred to as the "sliding" shear stress for the test. Point *B* is a *critical point*, and lies on the *effective yield locus*. (Refer to chapter 2 for a complete discussion of these terms.)

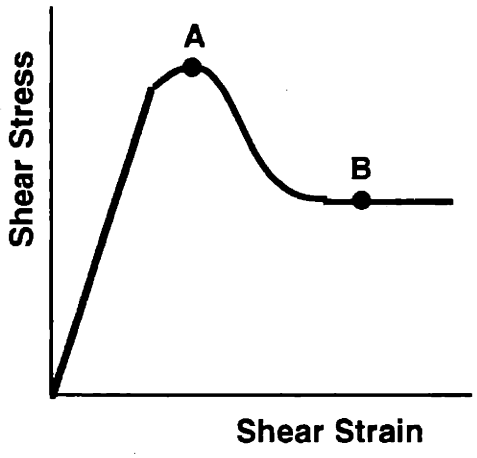

Figure 5.6: Shear cell stress / strain response for a powder at the tap density.

By performing multiple shear cell tests in which the normal stress is varied, the yield locus for the tap density of the powder, in addition to the effective yield locus, can be reconstructed. This is illustrated in figure 5.7. The points *A* and *B* in this figure correspond to those in figure 5.6, and were obtained from a single shear cell test.

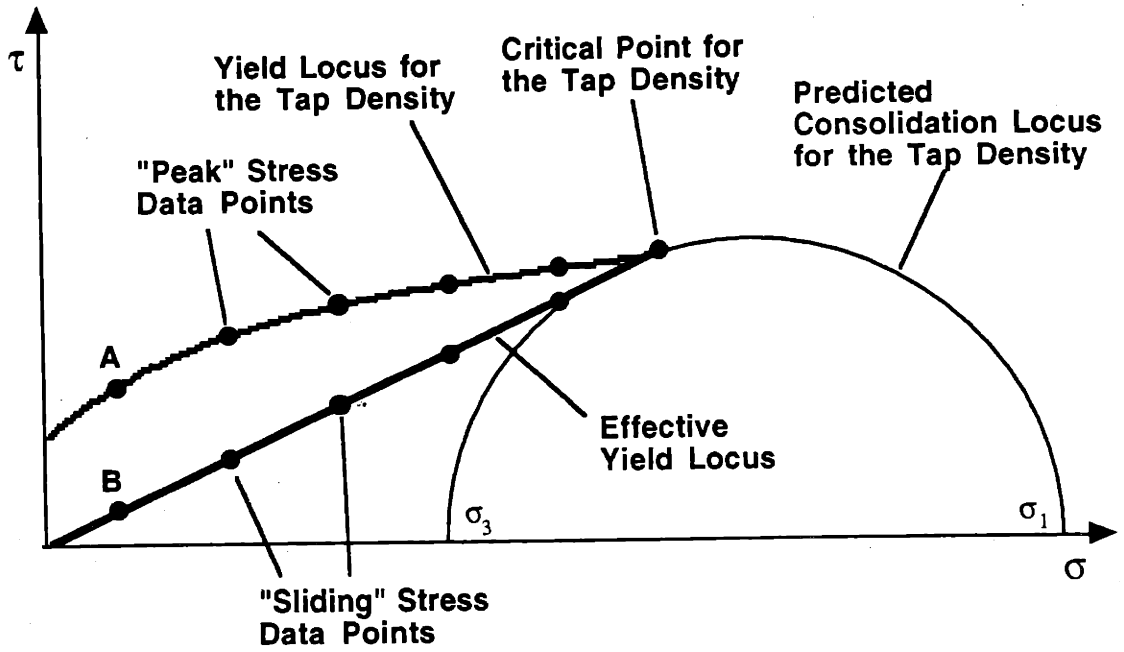

Figure 5.7: Reconstruction of yield and consolidation loci from data obtained in the shear cell test.

The intersection of the yield locus for the tap density and the effective yield locus corresponds to the critical point for the powder at its tap density. In theory, the powder should flow freely at this point, while remaining at the tap density. (It is uncertain that a powder could actually flow if it was at the tap density, since the particles would be so tightly packed that rearrangement would be very difficult. For the purposes of this discussion, when referring to the tap density, it is implied that we mean points at or *near* the tap density. This slight adjustment to the theory should not significantly affect its validity.)

Taking the analysis one step further, once the critical point for the tap density is known, a consolidation locus which passes through the critical point and is tangent to the

yield locus can be constructed. From the intersection of this consolidation locus with the normal stress axis, the principal stress required to bring a powder to its tap density can be estimated.

5.3.2 Objectives for the Shear Cell Tests

It was anticipated that data gathered from the shear cell tests would provide a better understanding of the stress levels required to achieve the tap density for a given powder. Other objectives for the shear cell tests were:

1. To determine if a linear approximation for the Jenike yield locus at the tap density was appropriate.

2. To compare the yield and effective yield loci for different powders.

3. To locate the critical point at or near tap density for different powders.

4. To construct a consolidation locus from the data gathered.

In the "standard" shear cell test, the applied normal and shear stresses are non-oscillatory. Since a goal of this research was to understand the use of vibration in the densification of powders, a modified shear cell test was devised in which an oscillatory stress component could be superimposed on either the applied normal or shear stresses. The additional objectives for these modified shear cell tests were:

5. To determine (qualitatively and / or quantitatively) the effect of vibration and direction of vibration on the location of the yield and consolidation loci.

6. To observe the effect of different vibrational frequencies and stress levels.

7. To provide additional insight into how vibration affects the behavior of particulate materials.

5.3.3 A Modified Shear Cell Apparatus

A shear cell apparatus was constructed for these tests which could perform both the "standard" shear cell tests and those modified tests in which an oscillatory stress component was added. A schematic of the entire apparatus is shown in figure 5.8, and a detailed illustration of the shear cell itself is given in figure 5.9.

A unique feature of this shear cell, as opposed to those described in the literature, is that the bottom portion of the cell was mobile and the top portion was stationary. This design approach was chosen so that majority of the cell components, which were positioned above the actual cell, could also remain stationary during testing. This alteration from the standard approach greatly simplified the design and construction of the modified apparatus.

Referring to figure 5.8, the shear cell bottom was mounted on a linear slide which constrained the cell motion to the horizontal direction. A load cell attached to the lower portion of the cell provided data on the shearing forces generated during testing. The shear force load cell was attached via a steel cable to a DC gear motor assembly (note shown) which moved the cell at a constant shearing rate. The upper portion of the cell assembly was fixed in position.

Normal stress was applied via a pressure plate. The pressure plate was attached to a linear bearing which constrained motion to the vertical direction. The normal force applied to the plate, both static and oscillatory, was measured by a load cell attached to the top of the plate.

The static normal forces were generated by a counter-balanced 1kg metal block. By altering the amount of mass in the counter-weight, the resultant static normal force could be quickly adjusted. The 1kg block was also mounted to a linear slide which limited its motion to the vertical direction. The oscillatory normal forces were generated with the RAINBOW resonant force source described in appendix B. The resonant system was mounted to the top of the metal block. The resonator was driven by a function generator and electrical amplifier.

To generate oscillatory shear forces, the resonator assembly was instead mounted horizontally to the bottom of the shear cell. (Not shown in the diagram.)

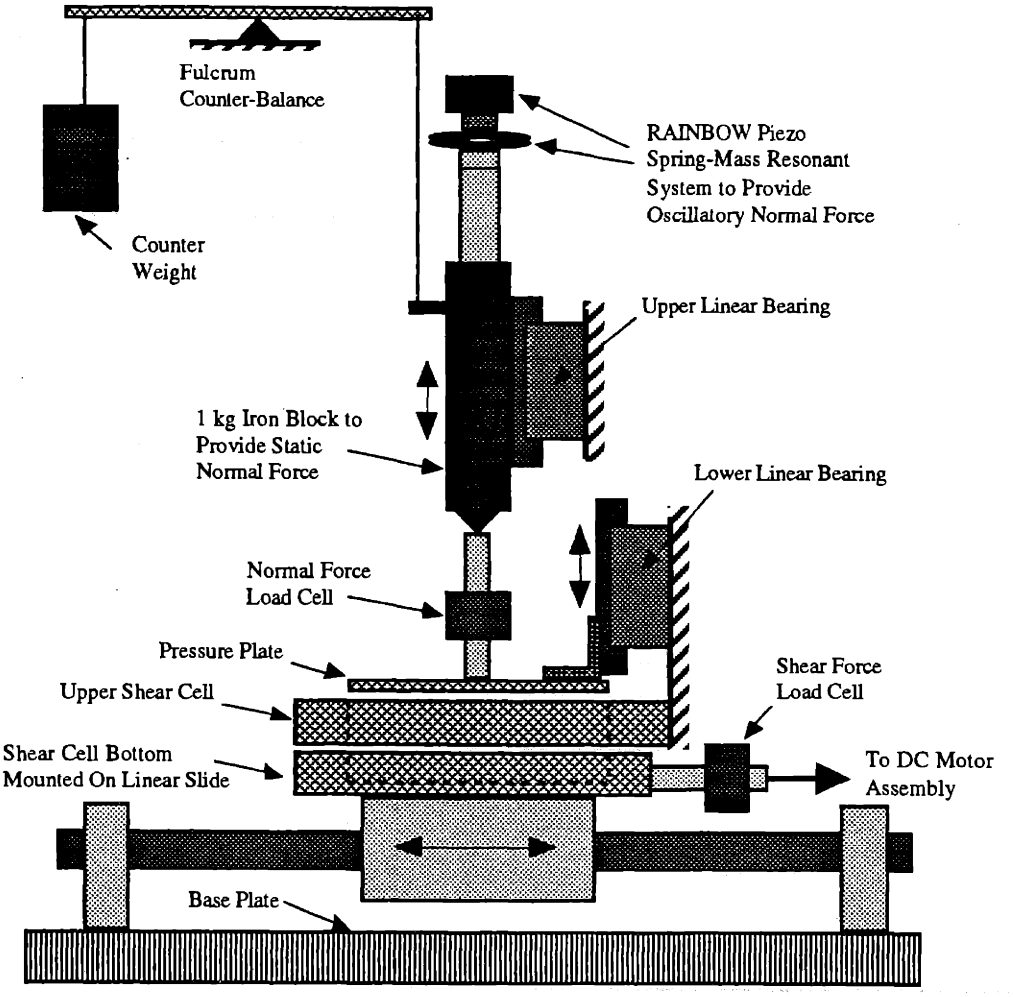

Figure 5.8: The modified shear cell test apparatus.

Figure 5.9 shows a cross-section close-up of the shear cell itself. The area of the shear plane was a square measuring 5.0 x 5.0 cm. A 250μm gap was provided between the halves of the cell. This gap needed to be sufficiently large to prevent the wedging of powder particles between the edges of the cell halves, which would have created significant errors in the shear forces measured during testing. Too large a gap, however, would prevent precise location of the shear plane.

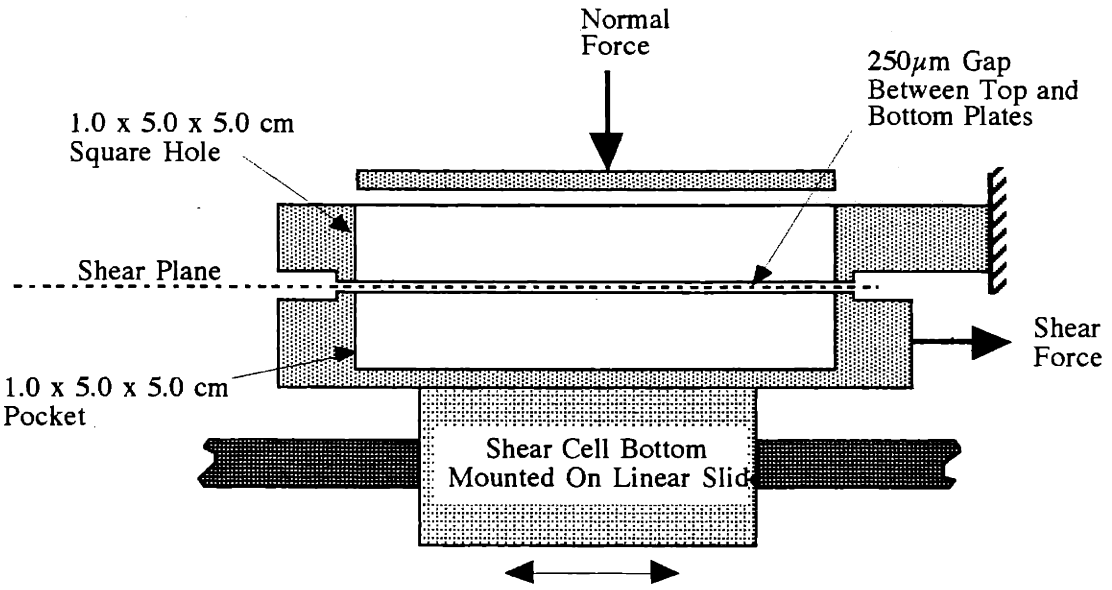

Figure 5.9: Detail view of the shear cell.

The load cells which measured the shear and normal forces were attached to an Apple Macintosh computer running Labview data acquisition software. Measurements were taken from each load cell at a rate of 100 samples / second.

5.3.4 Shear Cell Test Procedures

For each of the shear cell tests performed, the operating procedure was as follows:

1. Fill the cell with powder and compact to the tap density by striking the pressure plate several times with a small hammer.

2. Adjust the counter-weight to provide the required normal load. Normal loads were typically varied between 200 and 6000Pa, the later value being roughly equal to 1psi.

2a. (Variation) Apply a superimposed oscillatory normal stress component, varying the stress frequency and amplitude.

2b. (Variation) Apply a superimposed oscillatory shear stress component, varying the stress frequency and amplitude.

3. Shear the powder at a shearing rate of 0.11mm / second. (This was a typical shearing rate for a shear cell test.) Record shear force data over time.

4. Plot shear force versus time. Determine the peak and sliding shear stresses.

5. Perform a minimum of three runs for each normal stress condition.

The shear cell was frequently cleaned during these tests to ensure that the shear resistance was due only to powder sliding along the failure surface. The shear cell response for a variety of monomodal and bimodal powders was examined. These results are presented below.

5.3.5 Results from the Shear Cell Tests

The first shear cell test performed was the "standard" test, in which the normal and shear loadings were non-oscillatory. Results for five different powders are shown in figure 5.10. In these graphs and all the graphs that follow, the left-hand graph is a plot of the peak shear stress versus normal stress (i.e. the yield locus for the tap density condition), and the right-hand graph is a plot of the sliding shear stress versus normal stress (the effective yield locus for the powder). This graphing scheme was chosen because it allowed for presentation of the greatest amount of data using the fewest figures.

Linear curves were fitted to the data, and indicated that a linear approximation for the yield locus was valid over the range of stresses tested. Referring to the peak shear stress plot, there was a direct correlation between the location of the yield loci for the different powders and the values of their angles of repose. (Angle of repose values for the tested powders were previously given in Table 3.3 and Appendix A.) Of the powders tested, the 71/9μm 316L bimodal mix had the highest angle of repose, and the 66μm 420 monomodal powder had the lowest. Similarly, the 71/9μm blend had the highest yield locus, and the 66μm powder had the lowest. This correlation indicated that the resistance of a particular powder to dilation and shear failure was in part governed by the level of interparticle friction in the powder.

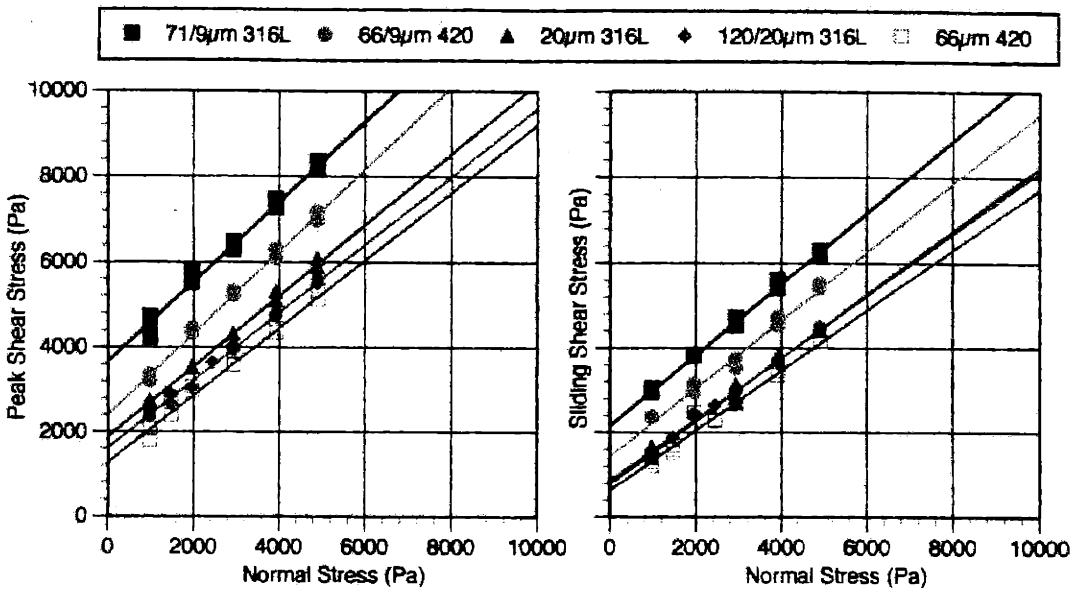

Figure 5.10: Plots of yield loci for the tap density (left) and effective yield loci (right) for a non-oscillatory loading condition.

In comparing the yield and effective yield loci for each of the powders tested, a startling discovery was made. In *none* of the cases did the lines intersect. This was true not only for this series of tests in which no vibration was used, but also for *all* the tests which followed (and are described below). This result was rather disappointing, since locating the critical point for each powder, and the construction of a corresponding consolidation locus, depended on knowing the location of this intersection. An explanation for this condition is illustrated in figure 5.11.

In the Jenike model, the yield locus of a powder at a given packing density was stated to be a curve which was concave down. The slope of this curve near the condition of zero normal stress would therefore be larger the slope near the critical point. Assuming that the range of normal stresses tested was much less than the range over which the yield locus curved, then the linear approximation of the yield locus over the range tested would have a slope greater than that of the effective yield locus. The measured yield and effective yield loci would, therefore, not intersect.

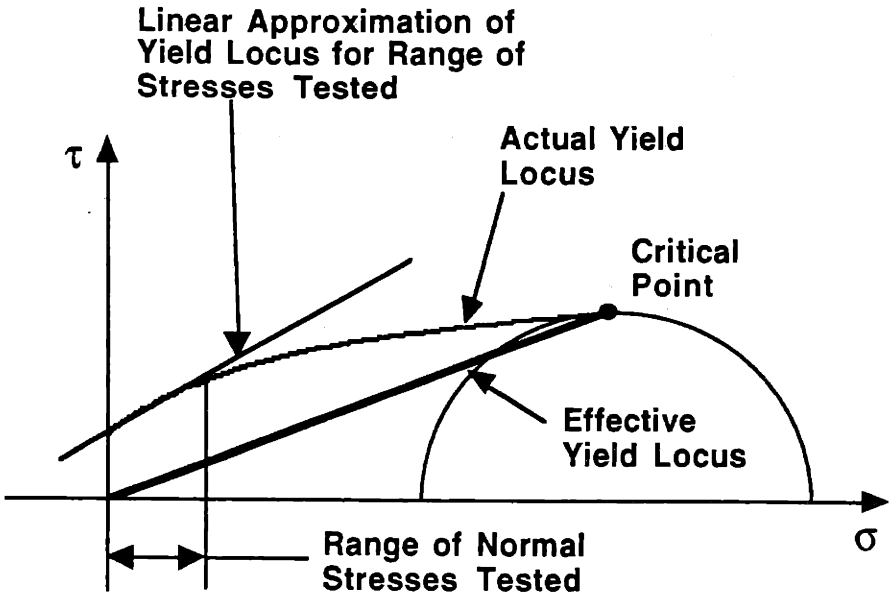

Figure 5.11: Illustration of why the measured yield and effective yield loci did not intersect.

Testing the metal powders at stress levels higher than those shown in figure 5.10 was not possible with the shear cell equipment which had been constructed. In any event, these higher stress levels would have been beyond what was considered permissible in the 3DP process.

The highly linear relationship between the applied normal stress and both peak and sliding shear stresses shown in figure 5.10 suggests an alternative, and possibly more intuitive, interpretation of the shear cell results. The most basic model of frictional resistance between two solid, flat surfaces relates the normal and shear forces applied to the surfaces with the static and kinetic coefficients of friction. [10] These coefficients are μ_s and μ_k, respectively. Referring to figure 5.12, the shear force τ_s required to initiate sliding between two solid surfaces is given by the expression

$$\tau_s = \mu_s \sigma, \qquad 5.6$$

and the shear force τ_k required to maintain sliding between two solid surfaces is given by the expression

$$\tau_k = \mu_k \sigma. \qquad 5.7$$

In general, it is the case that $\mu_k < \mu_s$, indicating that, for a given normal stress, it is easier to maintain sliding than it is to initiate it.

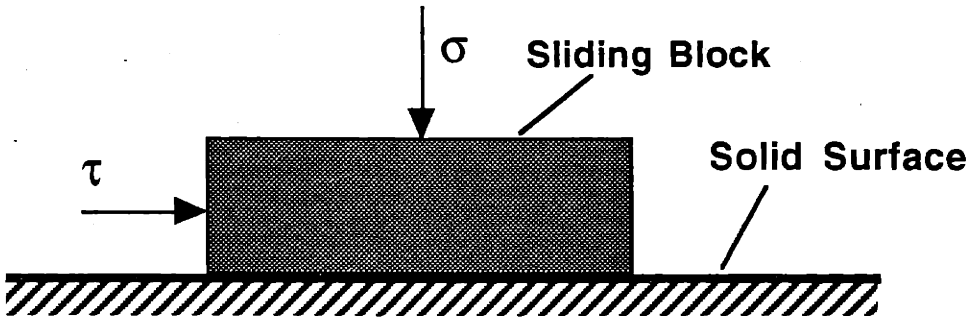

Figure 5.12: Illustration of a blocking sliding on a solid surface.

The observed shear cell behavior for both the peak and sliding conditions can be described by two relations which are analogous to equations 5.6-7. For the peak results, the relation has the form

$$\tau_p = \sigma \tan(\theta_p) + c_p, \quad 5.8$$

where θ_p is the angle of internal friction for the powder at the onset of failure from the tap density, and c_p is the shear axis intercept which defines the powder cohesion at the onset of failure from the tap density. Similarly, for the sliding results, the relation has the form

$$\tau_s = \sigma \tan(\theta_s) + c_s, \quad 5.9$$

where θ_s is the angle of internal friction for the powder during continuous sliding, and c_s is the shear axis intercept which defines the powder cohesion during sliding.

If the powder cohesion c is ignored, then the angle of internal friction θ for a given powder can be expressed in the same "terms" as the coefficient of friction μ for sliding solid surfaces by using the relationship

$$\tan(\theta) = \mu. \quad 5.10$$

Figure 5.13 is an illustration of how the observed failure and sliding behavior along the shear plane is analogous to the sliding behavior of solid surfaces.

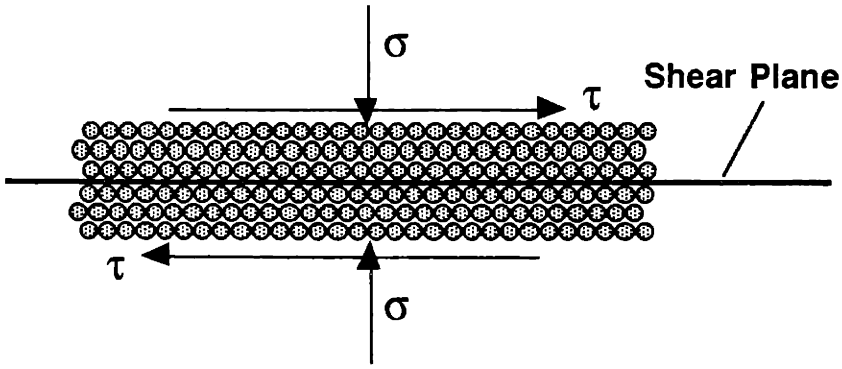

Figure 5.13: Illustration of how the observed failure and sliding behavior along the shear plane is analogous to the sliding behavior of solid surfaces.

Figure 5.14 is a graph of the peak and sliding angles of internal friction for the non-oscillatory shear cell tests. As we have already seen in studying the slopes of the data in figure 5.10, in all cases θ_p was greater that θ_s.

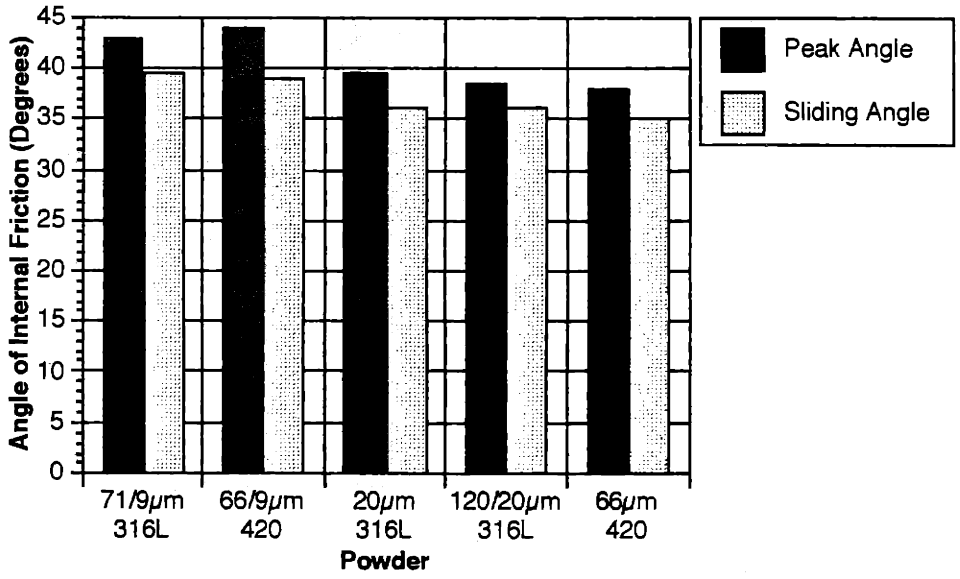

Figure 5.14: Peak and sliding angles of internal friction for the non-oscillatory shear cell tests.

In the next series of shear cell tests, an oscillatory component was added to the normal stress. The frequency and amplitude of the oscillatory normal stress were varied to observe the effect on the location of the yield loci. Figure 5.15 shows the results for the 120/20μm 316L powder, in which the vibration frequency was held constant at 159Hz and

the normal stress amplitude was varied. The data in figure 5.15 is plotted as *mean* normal stress versus shear stress. In figure 5.16, the normal stress amplitude was held constant at +/- 500Pa, and the excitation frequency was varied. Again, the horizontal axes represent the mean applied normal stress. The shearing condition of no vibration, which was measured in the previous tests, is also plotted for the purposes of comparison.

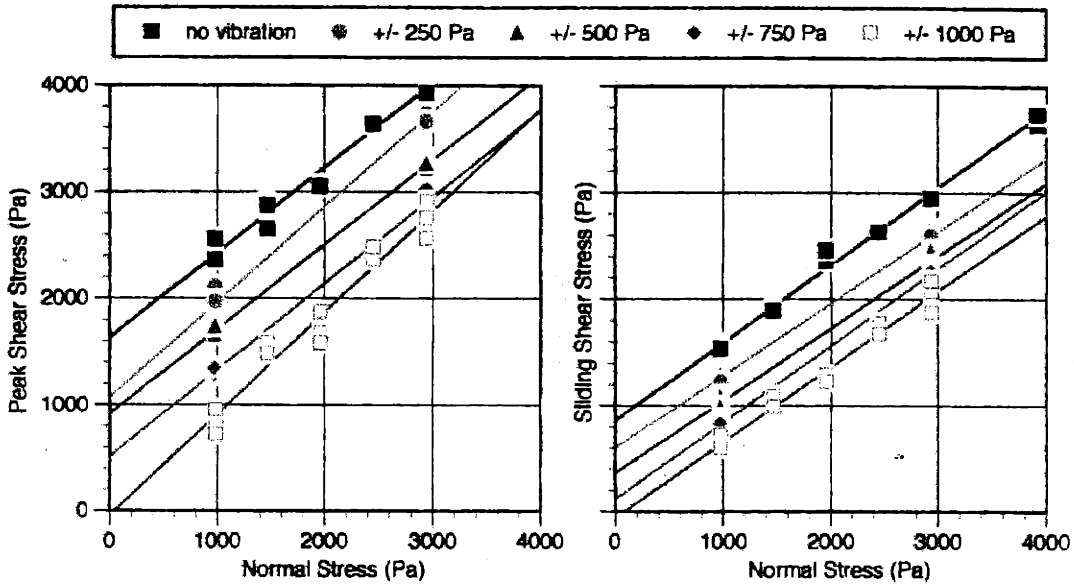

Figure 5.15: Results for the 120/20μm 316L powder with an oscillatory normal stress component at 159Hz and various stress amplitudes.

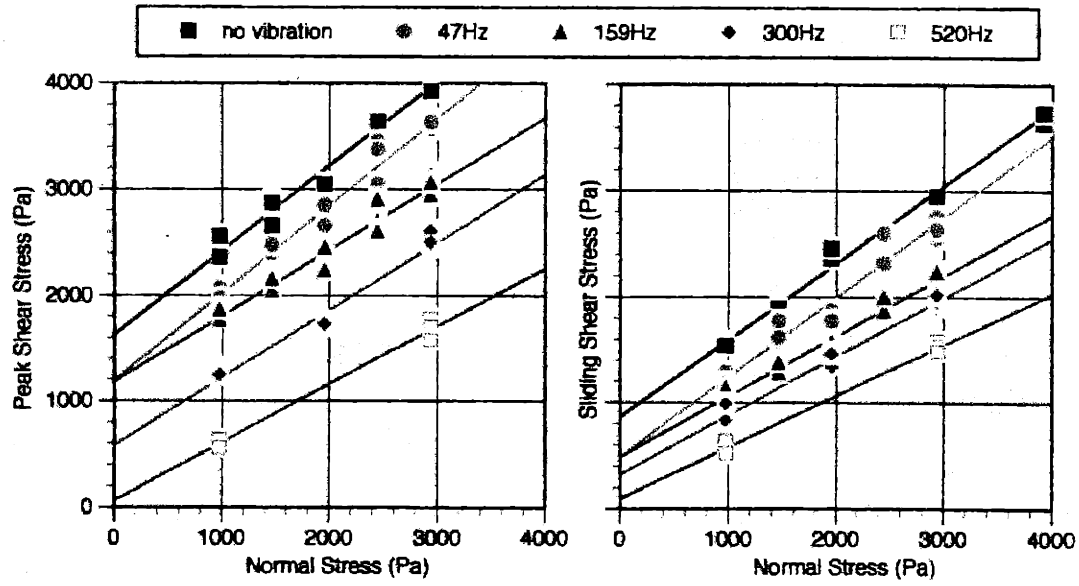

Figure 5.16: Results for the 120/20μm 316L powder with an oscillatory normal stress component at +/- 500Pa and various frequencies.

In all cases, the presence of an oscillatory component in the applied normal stress had the effect of depressing the yield and effective yield loci. In other words, it became easier both to initiate failure and to maintain continuous sliding. Increasing either the excitation frequency or amplitude caused further depression of the loci.

Figure 5.17 is a graph of the peak and sliding angles of internal friction taken from the data shown in figure 5.16. Compared to the shear cell test in which no vibration was used (this data is shown in the first column), there was a definite decrease in the angles of internal friction as the normal stress excitation frequency was increased. Again drawing an analogy to the case of sliding solid surfaces, the addition of an oscillatory normal stress component made it easier for the powder particles on either side of the failure plane to "slide" past each other.

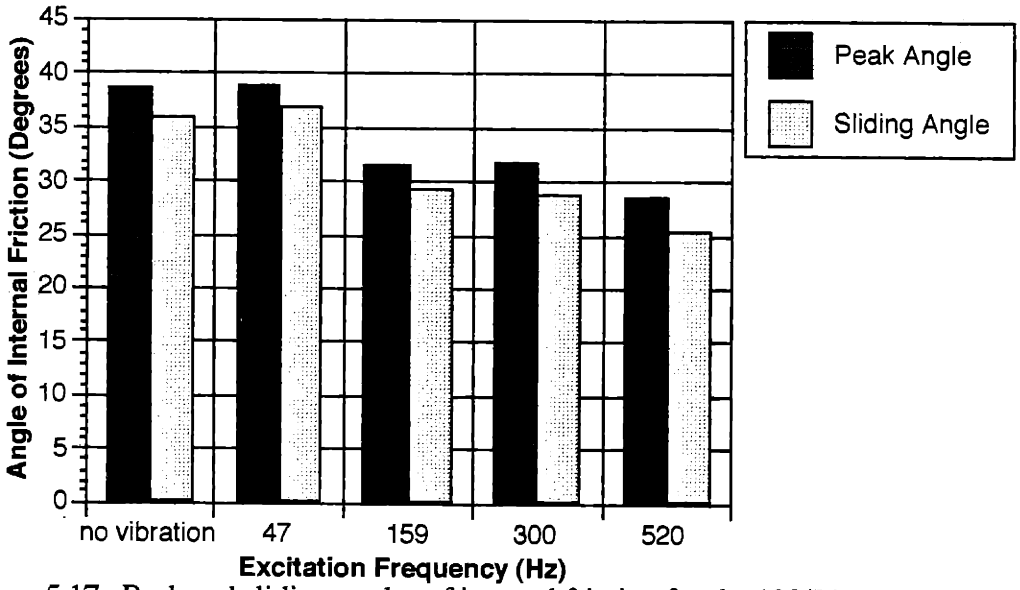

Figure 5.17: Peak and sliding angles of internal friction for the 120/20μm 316L powder with an oscillatory normal stress component at +/- 500Pa and various frequencies.

The effect of adding an oscillatory component to the applied shear stress was investigated next. Figure 5.18 shows the results for the 120/20μm 316L powder, in which the shear stress amplitude was held constant at +/- 200Pa, and the excitation frequency was varied. A similar depression resulted in the yield and effective yield loci, but to a greater extent, and at a lower oscillatory stress level, when compared to the above results.

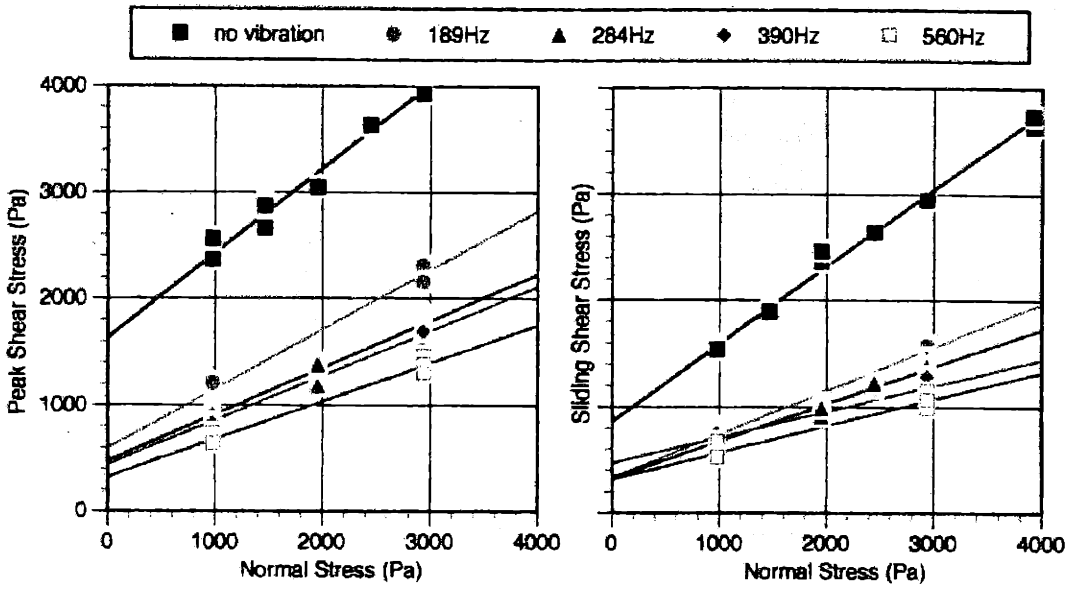

Figure 5.18: Results for the 120/20μm 316L powder with an oscillatory shear stress component at +/- 200Pa and various frequencies.

Figure 5.19 is a graph of the peak and sliding angles of internal friction taken from the data shown in figure 5.18. The use of an oscillatory shear stress resulted in even greater reductions in the angles of internal friction compared with the previous results shown in figure 5.17 in which an oscillatory normal stress was used.

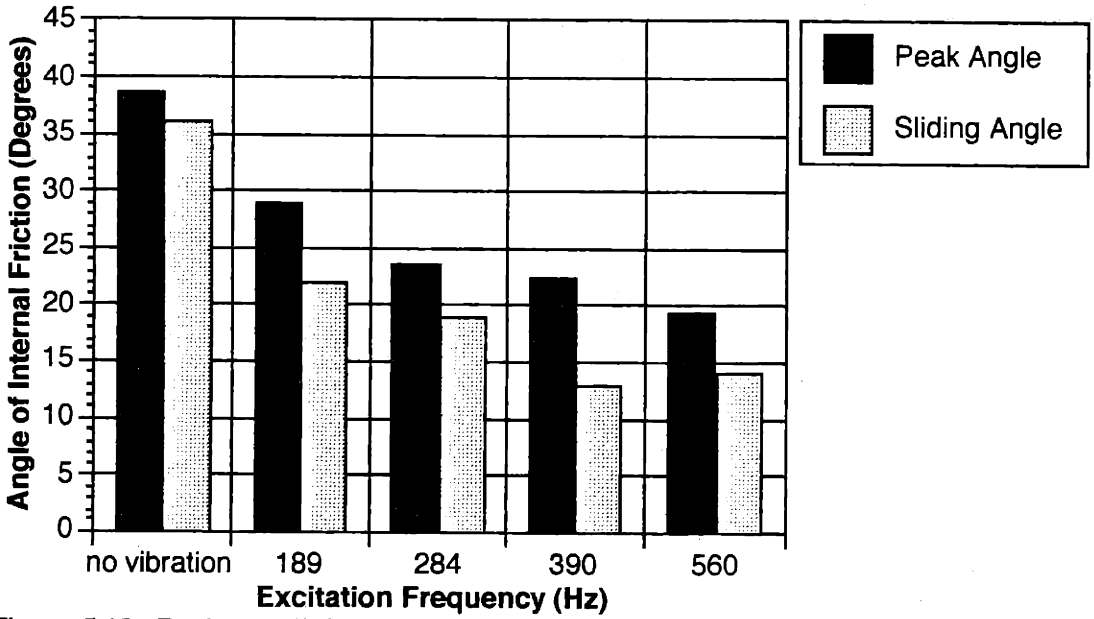

Figure 5.19: Peak and sliding angles of internal friction for the 120/20μm 316L powder with an oscillatory shear stress component at +/- 200Pa and various frequencies.

In figure 5.20, additional results for the 71/9μm 316L powder are shown, in which either an oscillatory normal or shear component was applied. These results are typical of all the powders tested. Increases in either vibration frequency or stress level depressed the yield loci. The application of an oscillatory shear component was much more effective at doing so, compared with the application of an oscillatory normal component.

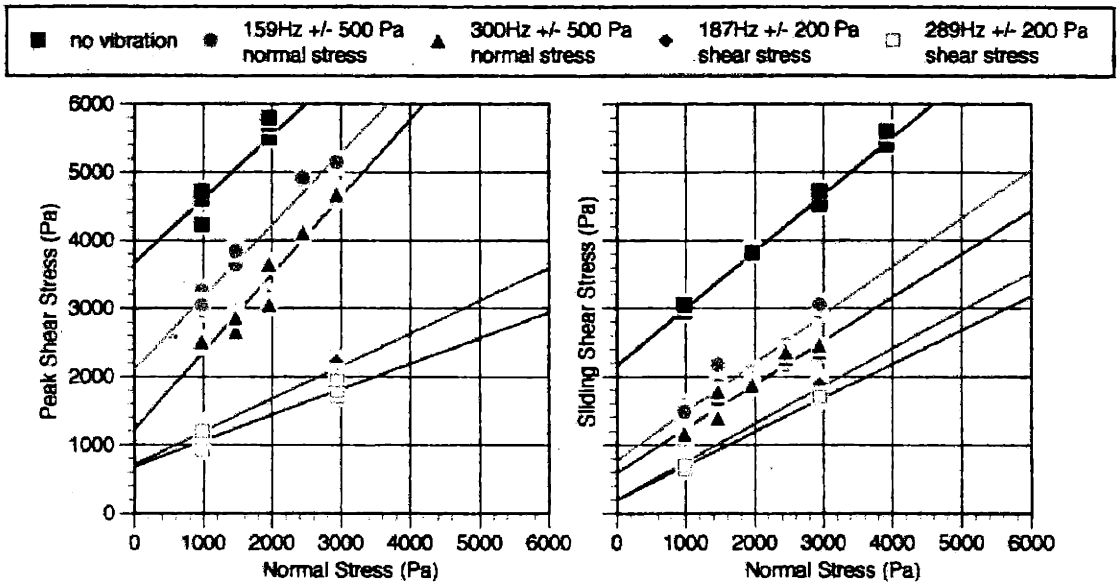

Figure 5.20: Results for the 71/9μm 316L powder with either an oscillatory normal or shear stress component.

A discussion of all the above results is reserved for the next section. However, several last tests were performed to answer the following question: If, for a given oscillatory stress amplitude, the frequency and *shearing rate* (i.e. the horizontal velocity of the upper-half of the shear cell, expressed in units of mm/s) were adjusted such that their ratio was held constant, would the locations of the yield and effective yield loci also remain constant ? The concept here was that perhaps the reduction in failure and sliding stresses was related to the *number of stress reversals* which the shear plane experienced over a *given distance of travel.* If during a stress reversal particles were given the opportunity to slide or "jump" past each other with greater ease, then it might be the case that an increase in the number of these opportunities over a given distance of travel would result it greater reduction in the peak and sliding shear stress levels. If the number of these opportunities over a given distance of travel was held constant, by maintaining a constant ratio of

excitation frequency to shearing rate, the perhaps the locations of the yield and effective yield loci would also remain constant. The final shear cell tests investigated this possibility.

Figure 5.21 shows the test results for the 71/9μm 316L powder in which an oscillatory normal stress component of +/- 500Pa was applied. Two tests were first performed at different frequencies, where the shearing rate was kept at the standard 0.11mm / second. In two additional tests with the same frequencies, the shearing rate was adjusted to keep the stress cycles per millimeter of strain constant at 1450.

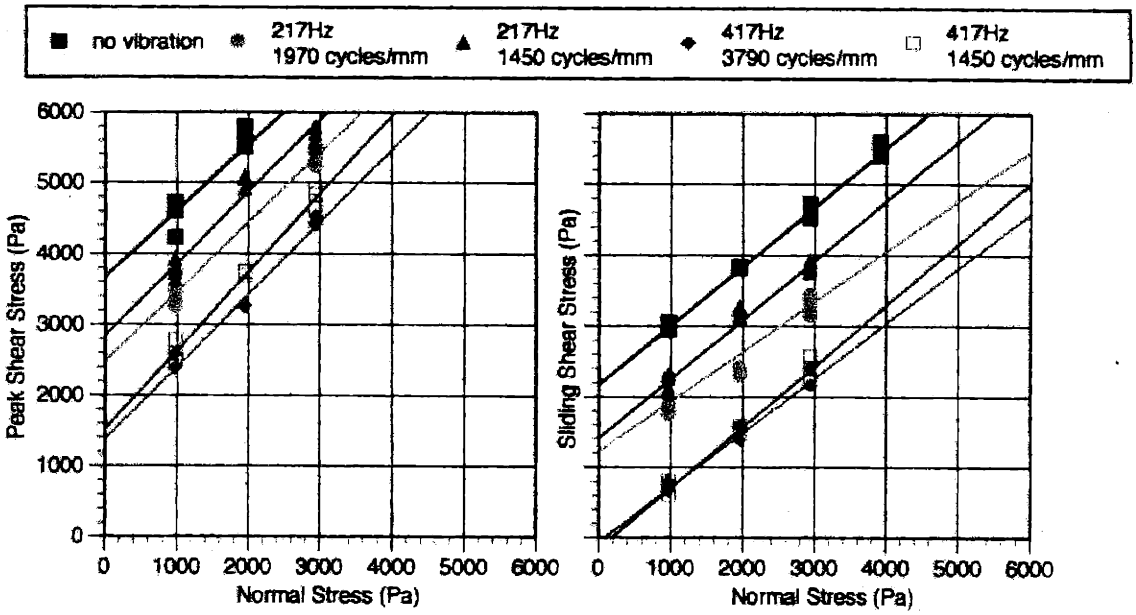

Figure 5.21: Results for the 71/9μm 316L powder with an oscillatory normal stress component of +/- 500Pa. The frequency and shearing rate were varied to keep stress cycles per millimeter of strain constant at 1450 in two of the four tests.

Figure 5.22 shows the results for the 71/9μm 316L powder in which an oscillatory shear stress component of +/- 200Pa was applied. The frequency and shearing rate were varied in two of the four tests to keep stress cycles per millimeter of strain constant at 1700.

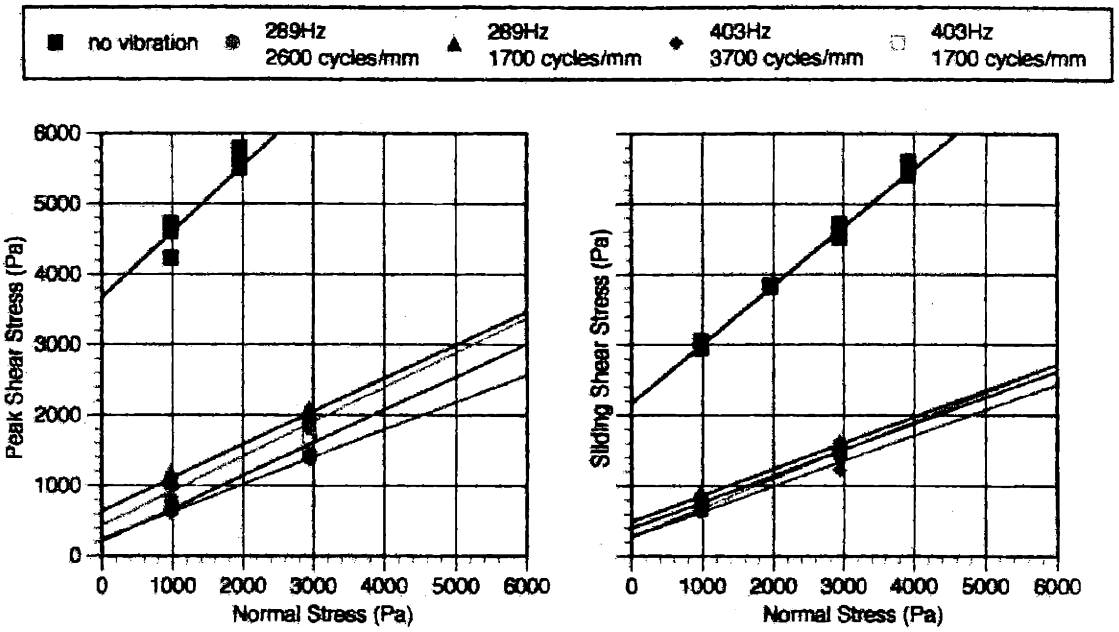

Figure 5.22: Results for the 71/9μm 316L powder with an oscillatory shear stress component of +/- 200Pa. The frequency and shearing rate were varied to keep stress cycles per millimeter of strain constant at 1700 in two of the four tests.

Maintaining the ratio of stress cycles per millimeter of strain constant had the effect of moving the yield and effective yield loci to different positions, but did not bring them significantly closer to each other.

5.3.6 Discussion

From the results of the shear cell tests, the following conclusions were made about the powder behavior:

1. Over the range of normal stress levels tested, the tap density yield locus and the effective yield locus were linear. This result led to a new interpretation of the data which used an analogy between the shear cell data and the frictional sliding behavior of solid surfaces. The coefficient of internal friction for the peak and sliding shear cell results was observed to be analogous to the coefficient of static and kinetic friction for solid surfaces over the range of normal stresses tested.

2. Powders with poor fluidity had higher yield and effective yield loci.

3. It was not possible to determine a critical point or draw a consolidation locus for any of the test conditions. In all cases, both with and without vibration, the slope of the tap density yield locus was larger than the slope of the corresponding effective yield locus. A proposed explanation was that the range of normal stresses tested was too small to fully determine the shape of the yield locus. It should be noted that shear cell tests used in soil mechanics typically operate a much higher stress levels.

4. In all cases, application of vibration lowered the yield conditions.

5. Increasing either vibration amplitude or frequency lowered the yield loci for a given powder, and frequency had a stronger effect.

6. Applying an oscillatory component to the shear stress had a much greater effect at lowering the yield loci for a given powder than applying a normal stress oscillation.

7. Maintaining a constant value of stress cycles per millimeter of strain did not offset the effect of different vibrational frequencies on the position of the yield loci.

Although the shear cell tests failed to provide a quantitative first estimate of the stress levels required to reach the tap density, the results added insight to the conceptual model of how powder particle rearrangement occurs. The depression of the yield loci with the addition of vibration indicates how the effects of powder particle locking and wedging, both of which contribute to shear resistance, can be diminished with the application of a vibrational stress component. In addition, the direction in which the vibrational stress is applied, in relation to the orientation of powder failure plane, is critical. Powder mobility appears to be enhanced the most when these directions are identical.

5.4 Layer Densification Tests

The primary deficiency of the shear cell test was its inability to provide information about the packing density of the powder along the shear plane after failure had occurred. The only standard test from soil and powder mechanics which could track changes in the packing of a powder sample was the confined compression, or oedometer, test. An illustration of an oedometer was shown in figure 2.36. In the oedometer test, powder is loaded into a chamber and uniaxially compressed. Changes in the height of the oedometer

piston directly correspond to changes in the packing density of the sample, as long as the sample depth is small compared to the horizontal dimensions of the test cell.

Testing similar to that accomplished with an oedometer was performed to better characterize how metal powders would compact under the influence of a new densification apparatus. This section describes these layer densification tests. The primary difference between the tests performed below and oedometer testing was the absence of confining vertical cell walls. For these tests, an horizontally *unconfined* layer of powder was vertically compacted by a pressure plate. This pressure plate could apply static and oscillatory vertical loads, and could also be vibrated horizontally to induce shear loads on the top surface of the powder layer. Measurement of the vertical displacement of the pressure plate into the powder layer directly correlates to changes in packing density for the powder under the plate, as long as significant amounts of powder were not ejected from underneath. The testing concept is illustrated in figure 5.23.

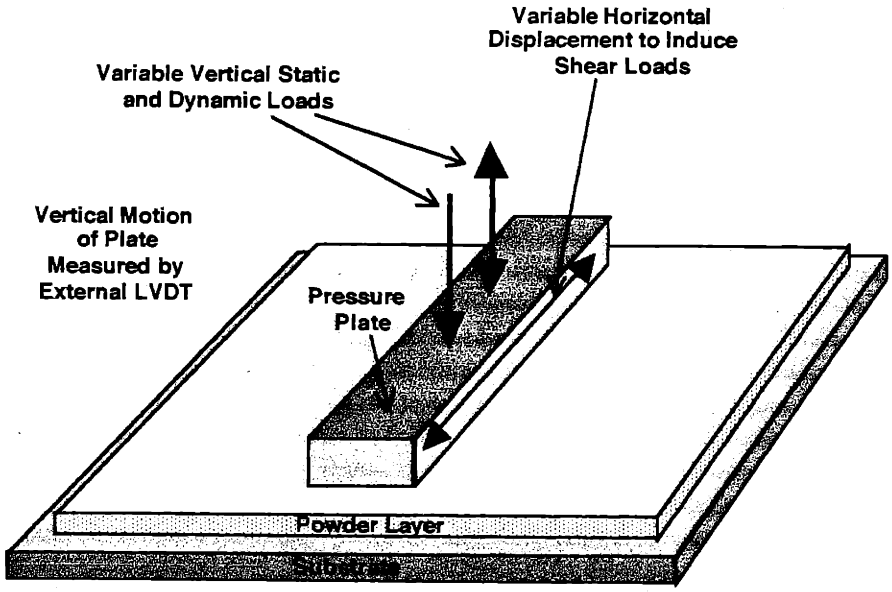

Figure 5.23: A schematic drawing of the layer densification tests.

An unconfined compression test more closely resembled how actual layer packing might be done, compared to an oedometer test, since in actual layer densification the strip of powder being densified would be horizontally confined only by the adjacent powder. Also, because the powder was unconfined, the initial powder layer could be generated by the standard non-vibrating spreader rod. This would again more closely resemble how the envisioned layer densification process would be performed.

5.4.1 Objectives for the Layer Densification Tests

The objectives for the layer densification tests were as follows:

1. To determine if vertical or horizontal applied stress vibrations were the best way to compact the metal powder. Also, to observe if (as in the case of the shear cell test) horizontal oscillations generated greater particle mobility than vertical oscillations.

2. To determine the effects of vibrational frequency and amplitude on densification behavior.

3. To determine the levels of stress required to achieve densification near the tap density.

4. To determine the time frame for densification. This information would prove valuable in later determining the speed with which the layer densification device should act on the prelayer.

5.4.2 The Layer Densification Test Apparatus

The layer densification apparatus which was constructed for these tests is illustrated in figures 5.24-26. (Several of the components were borrowed from the shear cell test apparatus.) Referring to the side view illustration in figure 5.24, an aluminum pressure plate with horizontal dimensions of 1.5cm x 8.3cm was mounted to a linear slide, which constrained the plate motion to the vertical direction. Vertical static and oscillatory stresses were applied to the pressure plate by the same counter-balance assembly used in the shear cell tests. Vertical stresses were again measured using an in-line load cell.

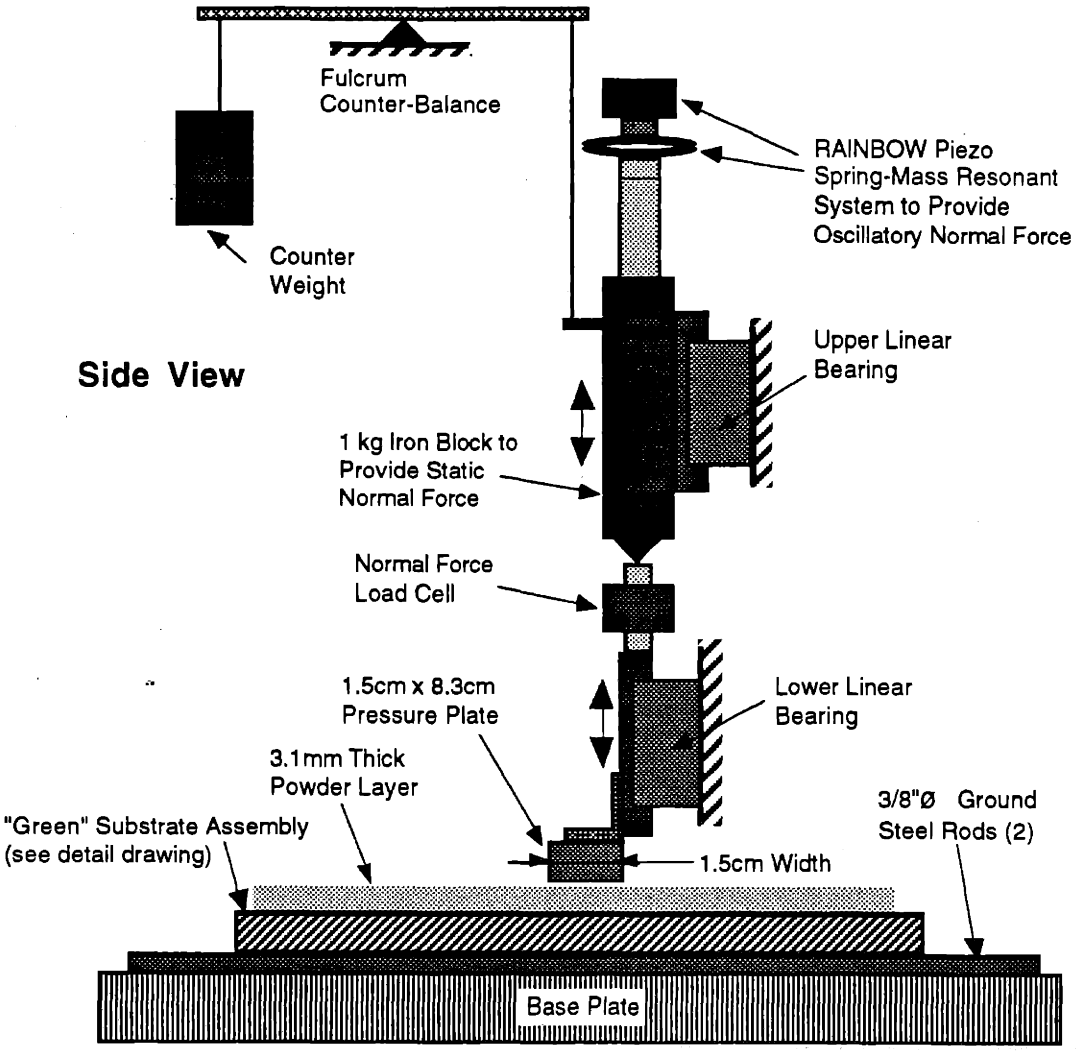

Figure 5.24: Side view of the layer densification apparatus.

Figure 5.25 is a front view of the layer densification apparatus. The powder layer to be densified was spread onto a special "green" substrate (described below), and this substrate was in turn placed on top of the base plate, using two ground steel rods for support. These horizontal steel rods completely supported the substrate, and allowed for precise vertical registration of the substrate with respect to the base plate, which was critical for these tests. Also, the steel rods prevented any powder particles which might have been inadvertently attached to the bottom of the substrate from altering the vertical registration, since these particles would tend to be pushed to the side by the rods when the substrate was placed on the base plate.

A linear voltage-displacement transducer (LVDT) was used to monitor the vertical position of the pressure plate. The LVDT measured only the time-averaged lowering of the plate into the powder. Oscillatory vertical displacements caused by stress excitation inputs were not recorded. The transducer had a resolution of +/-30μm. Output from the LVDT was recorded using the Labview data acquisition system described above.

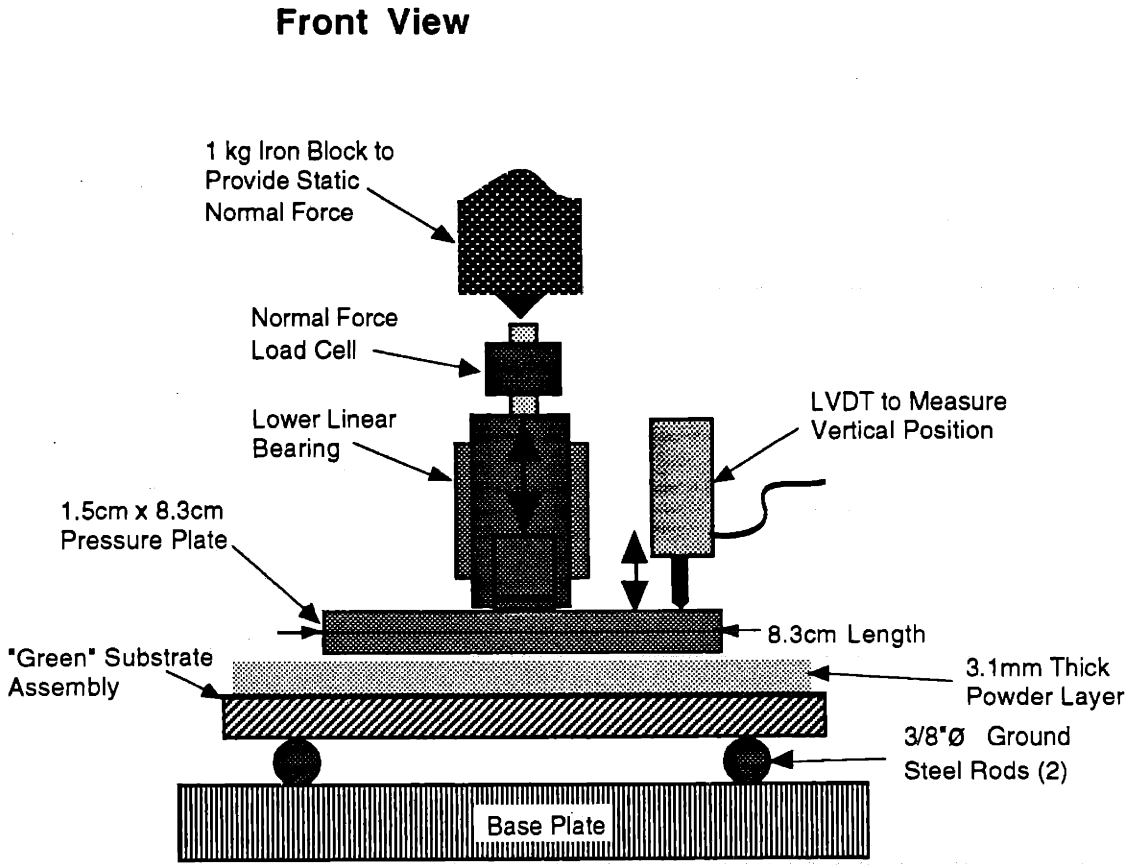

Figure 5.25: Front view of the layer densification apparatus as equipped to apply static and oscillatory vertical stresses.

Figure 5.26 is a detail of the modifications which were made to the test apparatus in order to generate horizontal shearing motions in the pressure plate. In this case the pressure plate was mounted to an additional linear bearing, oriented to move only the horizontal direction. An accelerometer, attached to the end of the pressure plate, was used to determine the amplitude of the horizontal plate oscillation. The RAINBOW resonant force generator was mounted to the horizontal linear bearing and used to drive the shearing motion of the pressure plate.

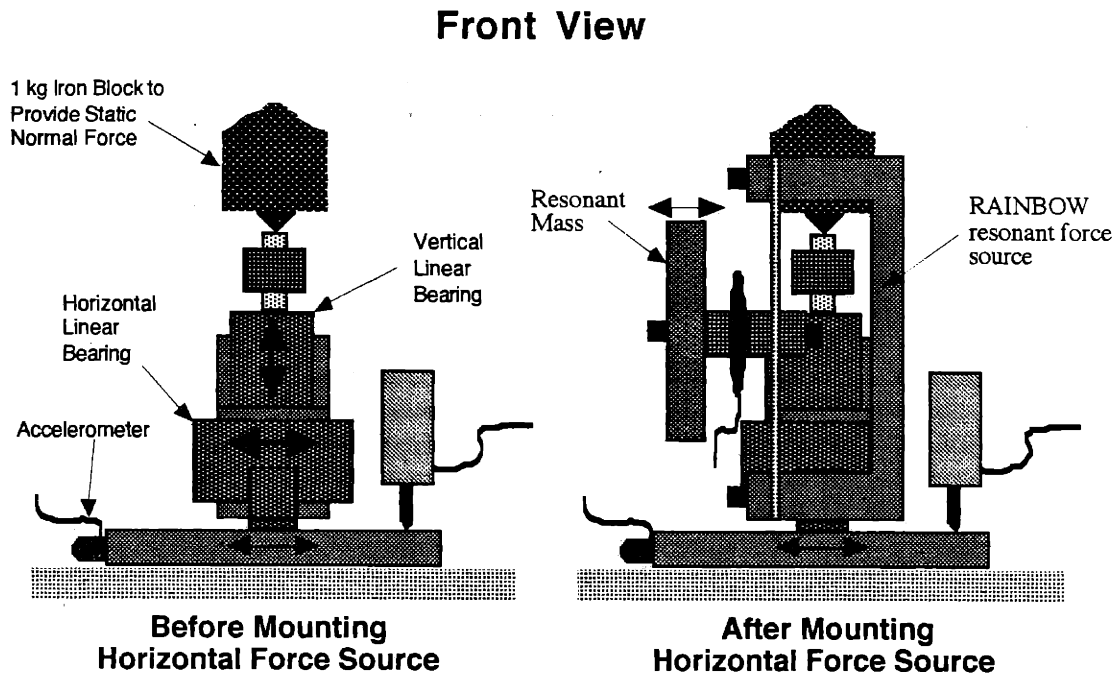

Figure 5.26: Front view of the layer densification apparatus as equipped to apply a static vertical stress and an oscillatory shearing motion. The apparatus is shown before and after the addition of the RAINBOW resonant force source.

The powder layers which were to be densified were spread onto a special substrate which was intended to simulate the properties of a green part in the powder bed, thereby more closely simulating the actual printing process. This "green" substrate is illustrated in figure 5.27. The substrate was composed of a 1/2" thick sheet of plexiglass with 320 grit adhesive-backed sandpaper laminated to one side. (The sandpaper gave the surface more grip prior to spreading of the green powder layer.) A single layer of 60μm steel powder, approximately 3/8" thick, was spread over the sandpaper, and the entire layer was saturated with Acrysol binder. After curing the polymer, the powder layer was machined flat to a final thickness of 1/4".

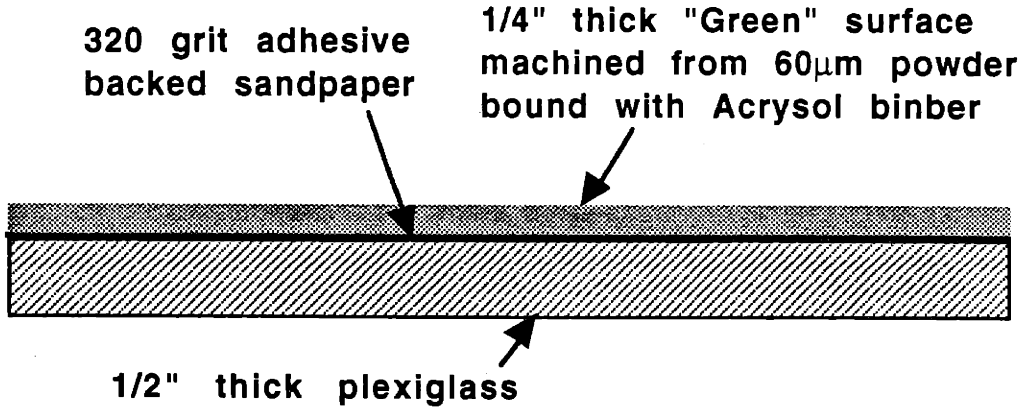

Figure 5.27: A schematic of the "green" substrate used to better simulate the densification behavior of powder over previously printed regions.

5.4.3 Determination of Layer Packing Density

During testing, the packing density ø of the powder beneath the pressure plate was determined from the expression

$$\phi = \phi_o\left(\frac{t_0}{t}\right), \qquad 5.11$$

where ϕ_o was the initial packing density in the test layer, and t and t_o were the current and initial thicknesses of the powder layer beneath the plate, respectively.

An initial layer thickness of 3.1mm was chosen to limit packing density measurement error to 1% or less. These layers were generated by placing the green substrate on the piston mount of the prototype 3DP machine and spreading a single, thick layer with the non-vibrating, counter-rotating spreader rod. The slow-axis spreading speed was set at 0.5"/second. The initial packing density ϕ_o of this single, 3.1mm thick layer was measured for several powders. For this measurement, a 10cm x 10cm rectangular area of powder was removed from the spread layer and then weighed to determine the packing density. The results are given in table 5.3.

Table 5.3: Packing Densities for the 3.1mm Thick Initial Layers.

Powder	Average Spread Density
71/9μm 316L	65.4%
120/20μm 316L	68.9%
66/9μm 420	69.2%
20μm 316L	57.8%

5.4.4 Tests with no Vibration

Initial tests were performed where only a non-oscillatory vertical load was applied to the pressure plate. Although all the powders listed in table 5.3 were evaluated in this and subsequent tests, only the results for the 71/9μm powder are presented. In all test cases, the results of the 71/9μm powder were representative of the other powders. The procedure for the zero vibration tests was as follows:

1. Lower the pressure plate gently onto the layer surface.

2. Slowly increase the vertical stress, at a rate of approximately 200Pa / second. This was accomplished by attaching an empty 500ml beaker to the top of the 1kg weight, and then slowly filling it with bronze shot, thereby steadily increasing the load transmitted to the pressure plate. The bronze shot was dispensed into the beaker via a large funnel. The funnel exit size was adjusted to dispense the shot at the required rate.

3. Record the applied load and the vertical displacement of the pressure plate over time.

The results from four separate compression runs using the 71/9μm powder are shown in figure 5.28. Each run took approximately 60 seconds to complete. The right-hand plot is a close-up of the low stress region from the left-hand plot.

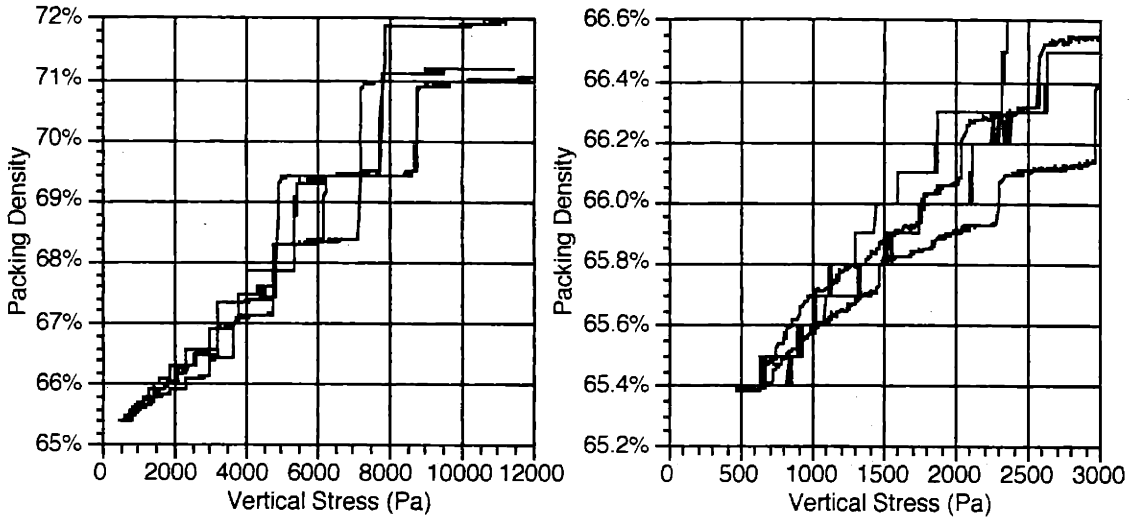

Figure 5.28: Results from four separate compression tests using the 71/9μm powder.

The most prominent feature of these results was the sudden, incremental increases in packing density which occurred as the static load was steadily increased. It was believed that these incremental jumps in packing corresponded to the sudden collapse of internal void structures which had grown unstable. The increases in packing occurred even at low stress levels, although these incremental gains were small, indicating that only a small fraction of the pore structures were unstable at these low stress levels. At higher stress levels the incremental packing increases were much larger, indicating that each pore collapse event was effecting a larger region of the total pore structure. Note that at an applied vertical stress 3000Pa (or nearly 1/2psi), there was only a modest increase in packing density.

A separate test was performed in which the vertical stress was increased rapidly in three discrete steps. The results from this test are presented in figure 5.29, where vertical stress and packing density are plotted separately over time.

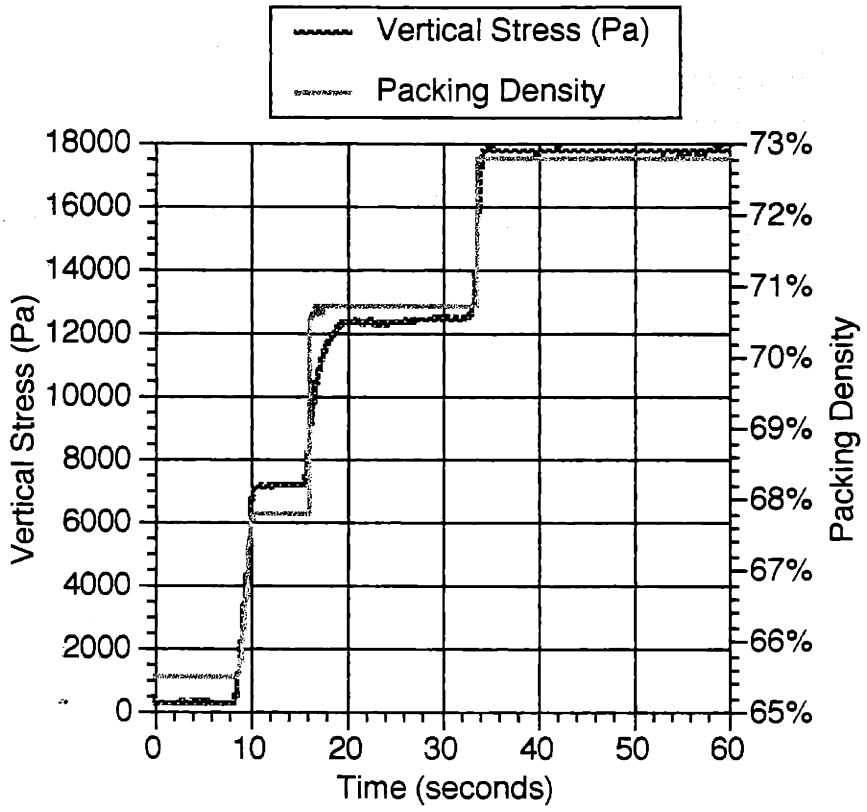

Figure 5.29: Response of the 71/9μm powder to three rapid, discrete increases in vertical stress.

The packing density increased immediately to its new value with each increase in vertical stress. There was no change in packing density during the times between the loading increases, however.

5.4.5 Tests with Static and Oscillatory Vertical Stresses

In the next series of tests which were performed, a constant vertical static stress was applied, and then an oscillatory vertical component was superimposed. The magnitudes of the static and oscillatory stresses, in addition to the frequency of vibration, were varied to observe the effects of these parameters on the powder densification behavior. In the previous shear cell tests it had been observed that the addition of a vibratory stress component lowered the stress levels required for powder to flow, and that higher frequencies produced greater stress reductions. It was expected that the presence of a vibratory component in the vertical stress would have a similar effect on the powder under the pressure plate, and would lead to greater levels of densification.

Results for the 71/9μm 316L bimodal blend are presented below. For this powder in was observed that ejection from underneath the sides of the pressure plate did not occur until the packing density exceeded approximately 72%. In all the graphs of results presented below, packing density values above 72% are shaded in gray, to indicate that the measurement technique was in error for these values. All data are presented, however, for the purposes of comparison.

In the first set of tests, the magnitudes of the static and dynamic stresses were varied, while the excitation frequency was kept constant at 185Hz. The results from this test are shown in figure 5.30. As might be expected, larger stress magnitudes in general produced greater levels of densification. More important, however, was the observation that the greatest levels of densification occurred when the magnitudes of the static and oscillatory stresses were approximately equal. For example, the level of densification after five seconds of vibration was greater for the condition of 2000+/-2000Pa, than for the condition of 6000+/-2000Pa, even though in the later case there was a much larger initial vertical strain caused by the greater static load. The proposed explanation for this effect was that by allowing for complete unloading of the powder mass with each stress oscillation, the greatest amount of powder mobility was obtained. Pore structures which were mechanically locked and stable due to the applied load had an opportunity for slight amounts of particle shifting and rolling a the low point in the stress cycle. With each oscillation, a few pore structures which had been previously mechanically stable were altered just enough that they become unstable, and collapsed during the next loading peak. Once collapsed, it was highly unlikely than a group of particles would reform a stable structure, especially if complete unloading and the lifting of the pressure plate off of the powder surface was avoided.

Another observation made from this test was that the majority of densification occurred within the first second of vibrational excitation. Smaller packing gains were made after one second, especially in the case of the higher stress levels, in which case a portion of the vertical strain was due to powder being slowly pushed out from underneath the pressure plate. Finally, in was observed both for the 71/9μm mixture and the other powders tested, that very high vertical stress levels were required to approach the tap density. (Recall that a stress limitation of 1psi, or 6900Pa, had been imposed for the new densification process.)

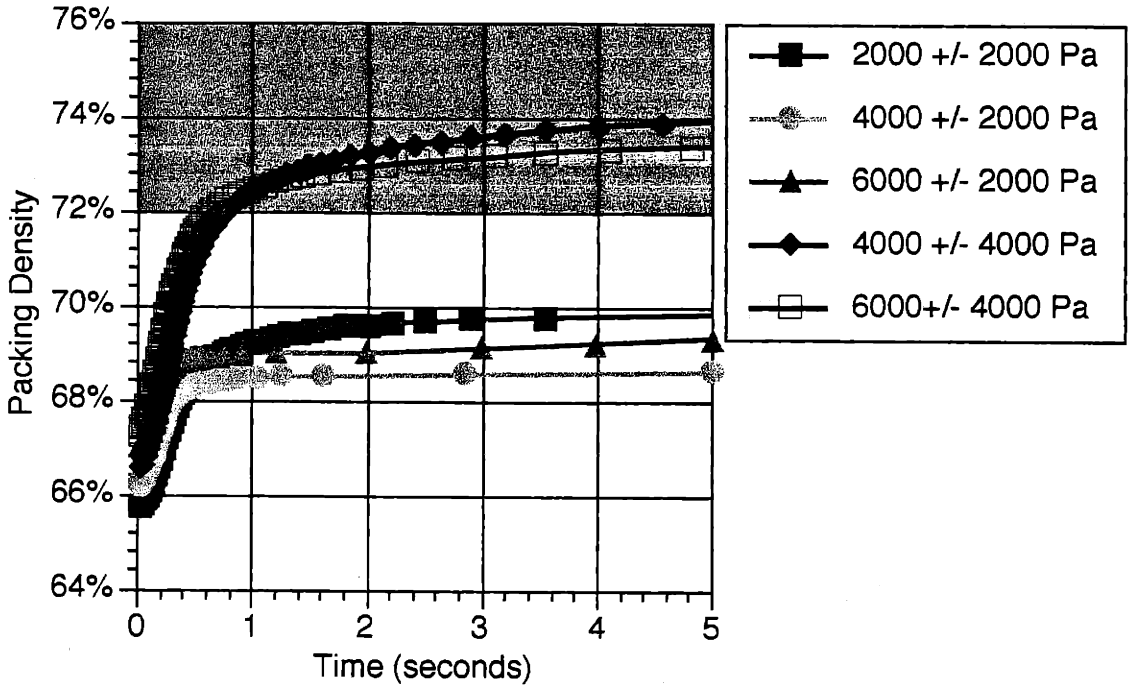

Figure 5.30: Effect of static and dynamic stress level on densification behavior. 71/9μm powder. 185Hz excitation.

In a second series of tests, the vertical stress levels were fixed at 2000+/-2000Pa, and the excitation frequency was swept through a range of 52 to 300Hz. The results from these tests are plotted in figure 5.31, both with time and number of stress reversals on the horizontal axes. The final packing density is plotted against the excitation frequency in figure 5.32.

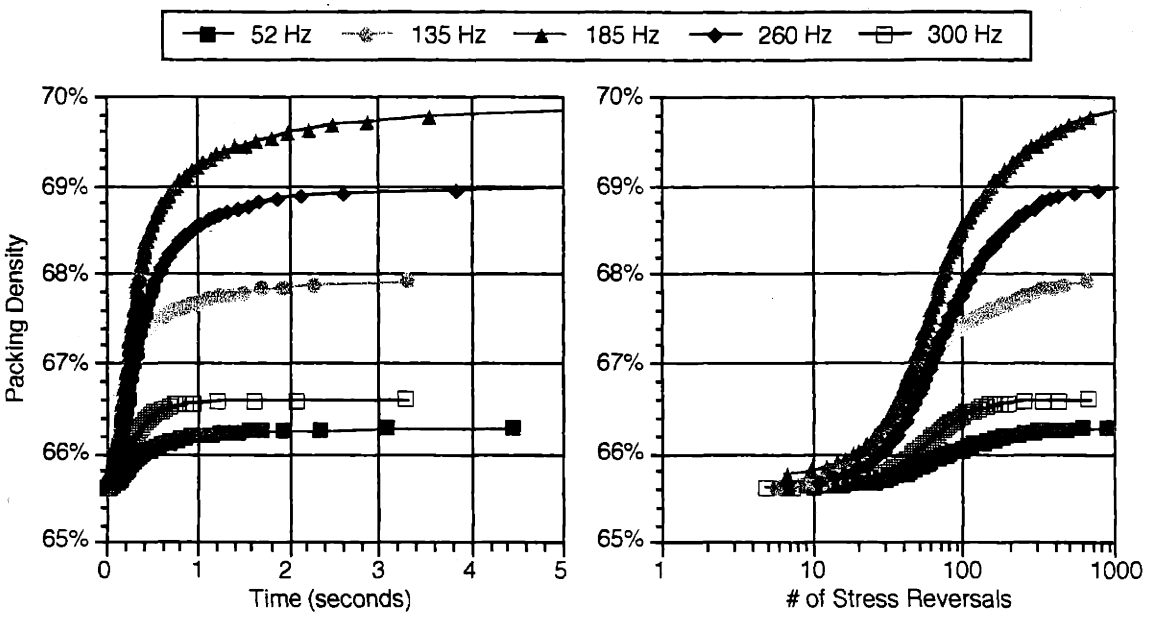

Figure 5.31: Effect of frequency on densification behavior. 71/9μm powder. Vertical stress condition of 2000 +/- 2000Pa.

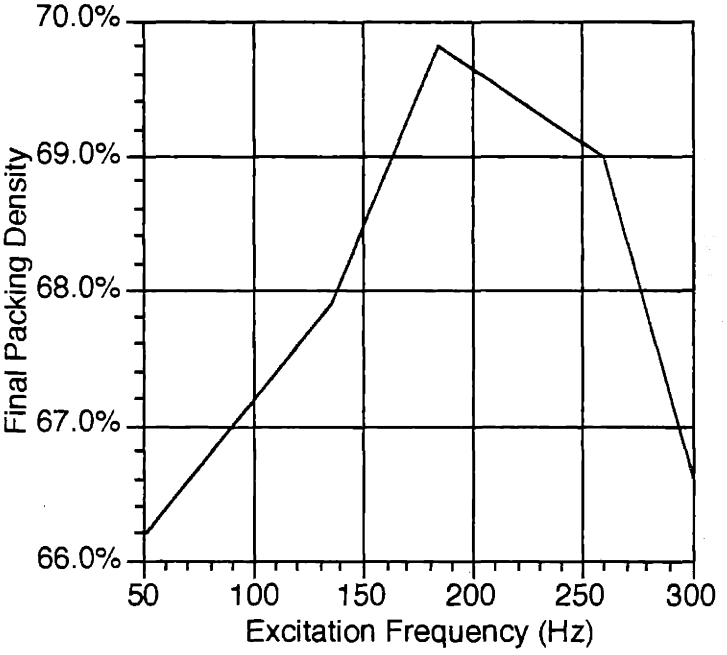

Figure 5.32: Final packing density vs. excitation frequency. 71/9μm powder. Vertical stress condition of 2000 +/- 2000Pa.

Very little densification occurred at the extremes in the frequency range, while the greatest packing was obtained at a frequency of 185Hz. This frequency dependency was

contrary to the expectation that higher excitation frequencies would result in greater particle mobility and hence higher packing densities. Two possible explanations for this preference towards an intermediate frequency were proposed. First, it was possible that the entire test apparatus had a weak mechanical resonance near this intermediate frequency. Second, it may have been the case that for some of the test frequencies the magnitude of the oscillatory stress component slightly exceeded that of the static stress component. (This was not intended, but may have been a result of insufficient resolution in the vertical stress transducer.) In this case, the pressure plate would have lifted off the powder surface during the low point in the stress cycle, and then impacted back into the surface with every oscillation. This unintentional pressure plate behavior could explain the higher packing densities obtained at some frequencies. Unfortunately, neither possibility was investigated at the time of the testing, so a definitive explanation could not be given.

An additional purpose for this test was to determine if, for a given static and oscillatory stress condition, the rate of densification was determined solely by the number of stress reversals. If this was true, then increases in excitation frequency would have the effect of speeding up the densification process, but the ultimate level of densification would remain the same. In the right-hand graph of figure 5.31, the densification results are plotted against the number of stress reversals. Note that the horizontal axis is in logarithmic units. From these results in was clear that both the rate and final level of densification ware complex functions of the excitation frequency, and could not be predicted solely on the basis of the number of stress reversals.

In summary, the conclusions drawn from this series of tests were as follows:

1. Most densification occurred in less than one second.

2. Higher stress levels provided better densification. The best densification condition was where the static and dynamic stresses were nearly equal.

3. The stress levels for significant densification were very high.

4. The relationship between excitation frequency and densification behavior was unclear. For these tests, frequencies of about 200Hz achieved the greatest densification, which was contrary to the expectation that higher excitation

frequencies would encourage greater particle mobility and result in higher packing density values.

5.4.6 Tests with Static Vertical Stress and Horizontal Shear

In the final series of layer densification tests, a static vertical stress was applied, and then the pressure plate was oscillated horizontally at a set amplitude. In most of the tests performed, the bottom surface of the aluminum pressure plate was smooth. In one instance, however, the bottom was intentionally "roughened" by laminating it with adhesive-backed sandpaper in order to increase the shear stress transmitted to the powder. In all these tests, the actual shear stress generated by the oscillating horizontal motion of the pressure plate was not measured or controlled. In was felt that, in the actual densification apparatus to be later developed, controlling displacement amplitude would be far easier than controlling the shear stress applied to the powder surface. Again, based on the results from the earlier shear cell tests, it was expected that the presence of a vibratory component in the shear stress would enhance powder mobility under the pressure plate, and would lead to greater levels of densification.

In the first set of tests performed, the low stress response of the 71/9μm powder was evaluated. The vertical static stress was limited to 1000Pa, and low oscillatory frequencies were used. The results for this test are shown in figure 5.33.

Even at these low levels of applied stress, modest amounts of densification occurred, compared to the above test results in which the oscillatory stress was in the vertical direction. Similar to the densification behavior in the case of no applied oscillation, small, incremental jumps in the packing density were observed after the majority of densification was accomplished. Again, these small jumps were believed to correspond to the sudden collapse of pore structures.

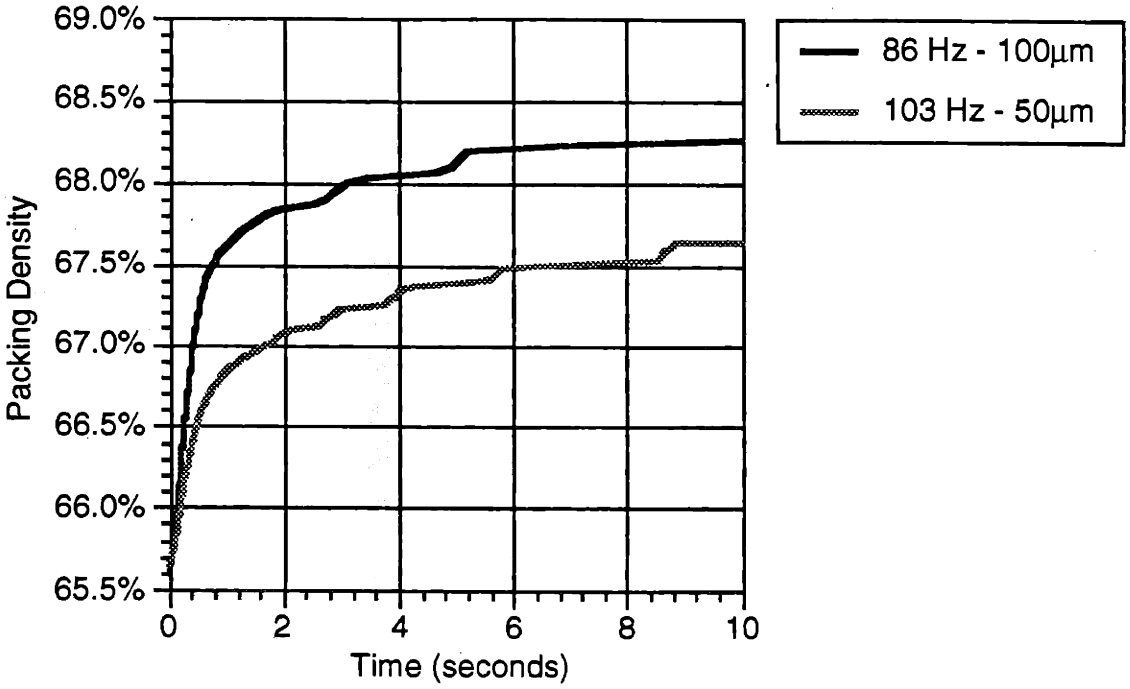

Figure 5.33: Collapse of internal pores at low excitation frequencies. 71/9µm powder. Smooth surface pressure plate. 1000Pa static vertical stress.

In the second set of layer densification tests, the applied vertical stress was again fixed at 1000Pa, and the excitation frequency was fixed at 225Hz. The peak-to-peak amplitude of the pressure plate was varied between 40 and 100µm. The results from these tests are shown in figure 5.34.

Increases in horizontal displacement resulted in higher packing densities. It was again observed that the packing levels achieved were reasonably high for the level of applied vertical stress, as compared to earlier testing.

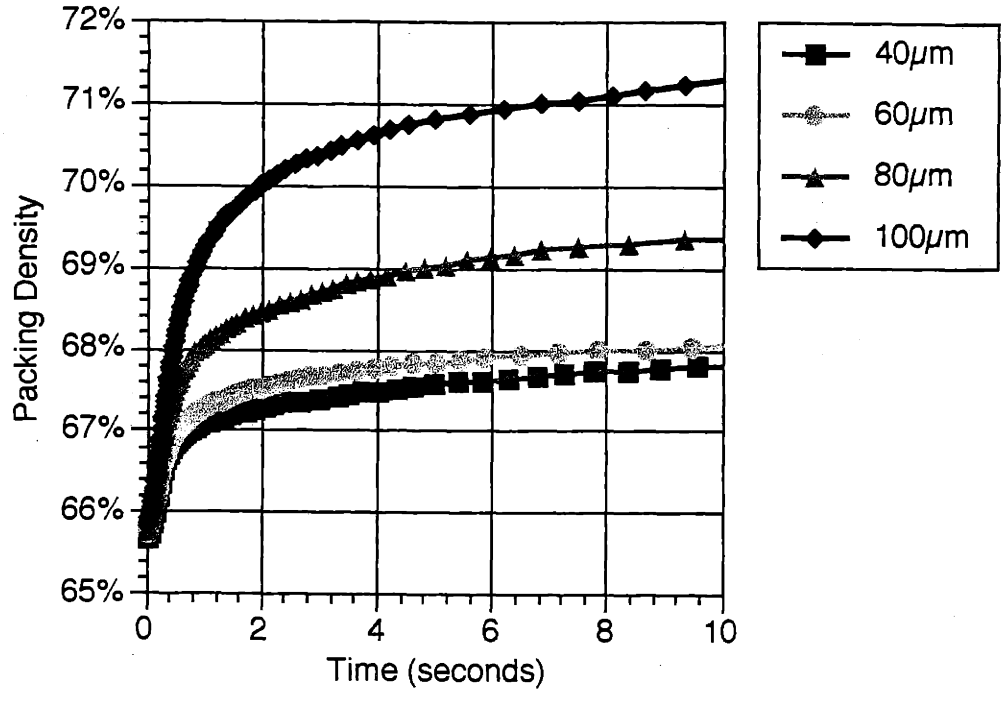

Figure 5.34: Effect of horizontal shear amplitude on densification behavior. 71/9μm powder. Smooth surface pressure plate. 225Hz excitation. 1000Pa static vertical stress.

Next, the effect of excitation frequency on densification behavior was studied. The applied vertical stress was again fixed at 1000Pa. The horizontal peak-to-peak displacement was fixed at 100μm, except at the higher frequencies where the RAINBOW resonator assembly could not generate sufficient oscillatory force. The excitation frequency was varied between 86 and 400Hz. The results from these tests are shown in figure 5.35. The final packing density is plotted against the excitation frequency in figure 5.36.

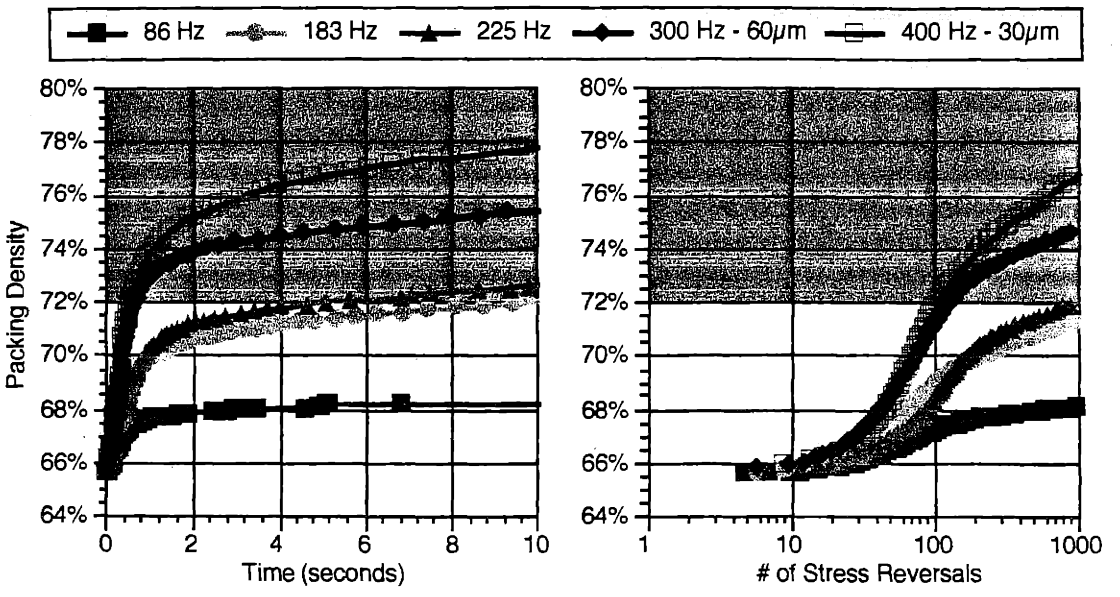

Figure 5.35: Effect of horizontal shear frequency on densification behavior. 71/9μm powder. Smooth surface pressure plate. 100μm peak-to-peak horizontal displacement (unless otherwise noted). 1000Pa static vertical stress.

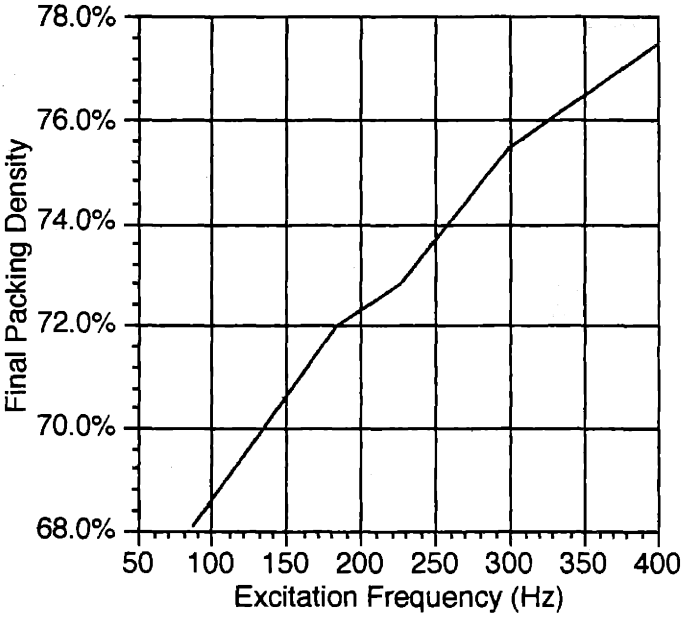

Figure 5.36: Final packing density vs. excitation frequency. 71/9μm powder. Smooth surface pressure plate. 100μm peak-to-peak horizontal displacement (unless otherwise noted). 1000Pa static vertical stress.

Higher excitation frequencies resulted in significantly higher packing densities. This result was in agreement with the expected frequency dependency that was initially observed during the shear cell tests. Even though the displacement at 400Hz was only

30μm, the indicated packing densities were near the tap density of the powder. The higher shear excitation frequencies were more effective at destabilizing the pore structures within the powder layer, thereby resulting in greater densification.

The packing results were also plotted against the number of stress reversals, with the intention again being to investigate the possibility that the rate and level of densification for a given stress condition might be dictated by this parameter. Again, however, the results indicated that the densification behavior was a more complex function of the input variables.

A final set of tests was performed to investigate the effect of changes in applied shear stress for otherwise identical conditions. Two series of tests were made, one in which the smooth-bottomed pressure plate was used, and one in which the bottom was roughened, as described above, by laminating it with 320 grit silicon carbide sandpaper. Although the shear stress was never actually measured, it was assumed that the shear forces delivered to the layer surface by the roughened plate were significantly higher than those from the smooth plate, as long as other parameters were equal. In all cases, the peak-to-peak horizontal displacement was 50μm, and the excitation frequency was 300Hz. The static vertical stress was varied between 200 and 2000Pa. The results from these tests are shown in figures 5.37-38.

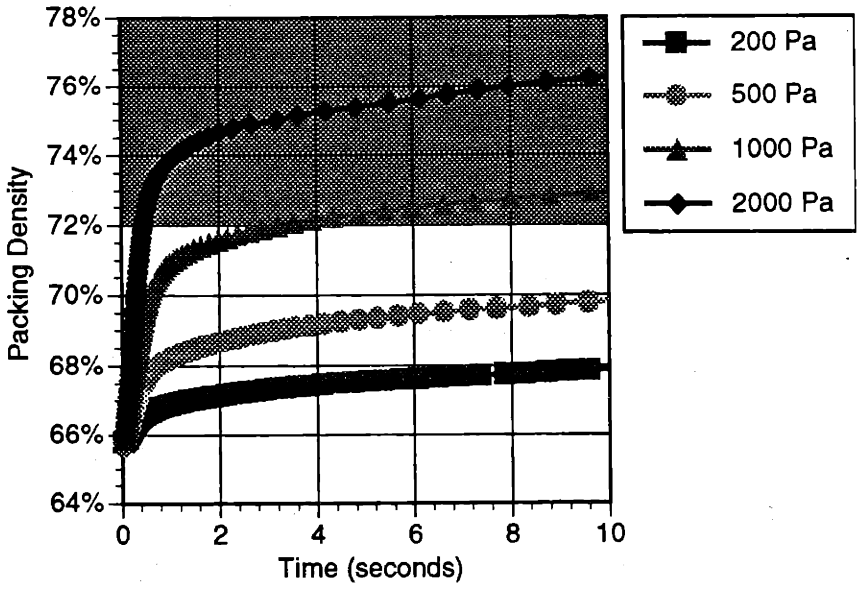

Figure 5.37: Effect of static normal stress on densification behavior. 71/9μm powder. Smooth surface pressure plate. 50μm peak-to-peak horizontal displacement. 300Hz excitation.

Increases in static normal stress, for either the smooth or rough plate, resulted in significant increases in densification. More prominent, however, was how the roughened plate produced results which rapidly became "off the scale" for the higher normal stress conditions. Although the packing density measurements above 72% were again in error due to powder being lost from under the pressure plate, the high rate at which the powder densified immediately after the application of vibrational excitation was significant. It was clear that increasing the shear stresses transmitted to the layer, either by increasing the applied normal stress, or by roughening the pressure plate surface, was an effective method for improving densification. Also of note was how there was little difference in the densification behavior of the two pressure plates for the lower normal stress levels. This might imply that a certain minimum normal stress was required in order for the pressure plate to effectively transmit shear forces.

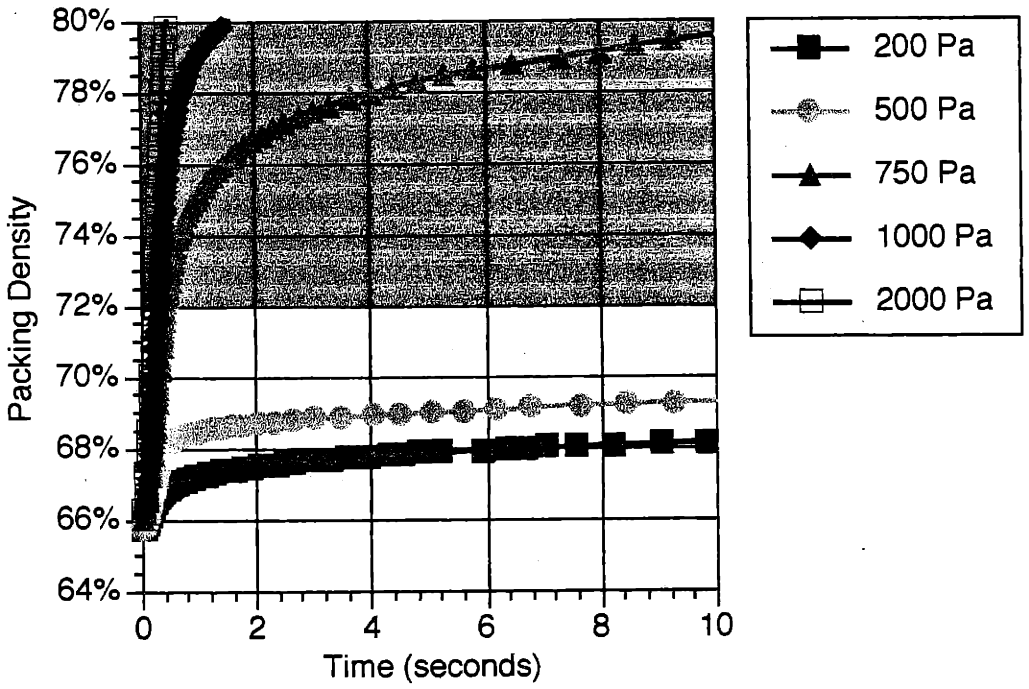

Figure 5.38: Effect of static normal stress on densification behavior. 71/9μm powder. Rough surface pressure plate. 50μm peak-to-peak horizontal displacement. 300Hz excitation.

In summary, the conclusions drawn from this series of tests were as follows:

1. Oscillatory horizontal shearing was much more effective at producing densification than vertical vibration. The required normal stress levels were significantly lower.

2. Increases in the transmitted shear force for a given normal force had a strong influence on densification.

3. Higher frequencies produced better densification, even when the peak-to-peak displacement of the pressure plate was as low as 30μm.

4. Most densification again occurred in less than one second.

5.4.7 Discussion

The powder underneath the pressure plate in these layer densification tests experiences compaction due to both the static and dynamic stresses which are applied. The total vertical strain, ε_z, is the summation of the strains due to the static and dynamic loadings, or

$$\varepsilon_z = \varepsilon_{static} + \varepsilon_{dynamic}. \qquad 5.12$$

Each strain quantity, in turn, is a function of various other parameters. For example, ε_{static}, is a function of (at least) the following quantities:

$\varepsilon_{static} = f$[static vertical stress,
initial packing density,
degree of interparticle friction, locking, wedging, etc.,
ultimate (tap) density for the powder]

As we have seen from the above tests, $\varepsilon_{dynamic}$ is a function of (at least) the following parameters:

$\varepsilon_{dynamic} = f$[static vertical stress,
initial packing density,
degree of interparticle friction, locking, wedging, etc.,
vibrational frequency, amplitude and direction,
the time vibration is applied for (or number of stress reversals),
ultimate (tap) density for the powder]

In soil and powder mechanics, $\varepsilon_{dynamic}$ is usually plotted as a function of the number of stress reversals, and typically exhibits a logarithmic or exponential behavior. Previously, we have seen how uniaxial vibratory compaction (similar to an oedometer test) was modeled using the relation

$$\frac{d\varepsilon_{dynamic}}{dN} = \frac{K_1}{N}, \qquad 5.13$$

where N was the number of *stress reversals*, and K_1 was a constant determined by the specific testing conditions. [12] This relationship stated that the amount of densification which occurred during any given stress reversal was inversely proportional to the number of stress reversals which had already occurred. Since vibratory compaction is usually performed at a fixed frequency, N was a multiple of the time of application of the vibratory excitation.

The solution to the above differential equation is the logarithmic relationship

$$\varepsilon_{dynamic} = K_1 \cdot \ln(N) + K_2. \qquad 5.14$$

The shape of this strain response model is a good representation of the behavior observed in actual confined compression tests (refer to figure 2.45). Confined compression differs from the layer densification tests performed above, however, in that the powder is enclosed by vertical walls during compaction.

An alternative model which describes the observed behavior for a uniaxial densification process is that the amount of vertical strain which occurs during any given stress reversal is proportional to the difference between the maximum and current amounts of strain. In differential form, this relationship is

$$\frac{d\varepsilon_{dynamic}}{dN} = K_1\left(\varepsilon_{ultimate} - \varepsilon_{dynamic}\right), \qquad 5.15$$

where $\varepsilon_{ultimate}$ is the maximum amount of strain possible (based on the tap density of the powder), and K_1 is again a constant determined by the specific testing conditions (but different from the constant in relation 5.14). For this model, as the powder is compacted closer and closer to its tap density (i.e. $\varepsilon_{dynamic}$ approaches $\varepsilon_{ultimate}$), it becomes progressively more difficult to further compact the powder. The strain response for this second model is given by the exponential decay relationship

$$\varepsilon_{dynamic} = K_2\left(1 - e^{-K_1 N}\right) + K_3, \qquad 5.16$$

where $\varepsilon_{ultimate} = K_2 + K_3$.

Both of the above models predict response curves which are similar in shape to those observed in these tests. Sample responses for the two models are shown in figure 5.39. The packing density $\emptyset$ is plotted on the vertical axis, instead of $\varepsilon_{dynamic}$, so that these plots resemble the experimental results presented earlier.

Referring to the left-hand plot in figure 5.39, we see that both models exhibit response characteristics which are comparable in shape to the experimentally obtained results. The logarithmic model in the left-hand graph appears to mimic the experimental data more accurately than the exponential decay model, since a final asymptotic packing density value is never reached. In the right-hand plot, a logarithmic horizontal axis is used. Comparing the shape of the exponential decay model in the right-hand plot to the experimental results shown previously in figures 5.31 and 5.35, we see an excellent response shape correspondence. From this simple comparison of the shape of the mathematical models to the actual experimental densification results, it is not possible to conclude that one model is superior to the other.

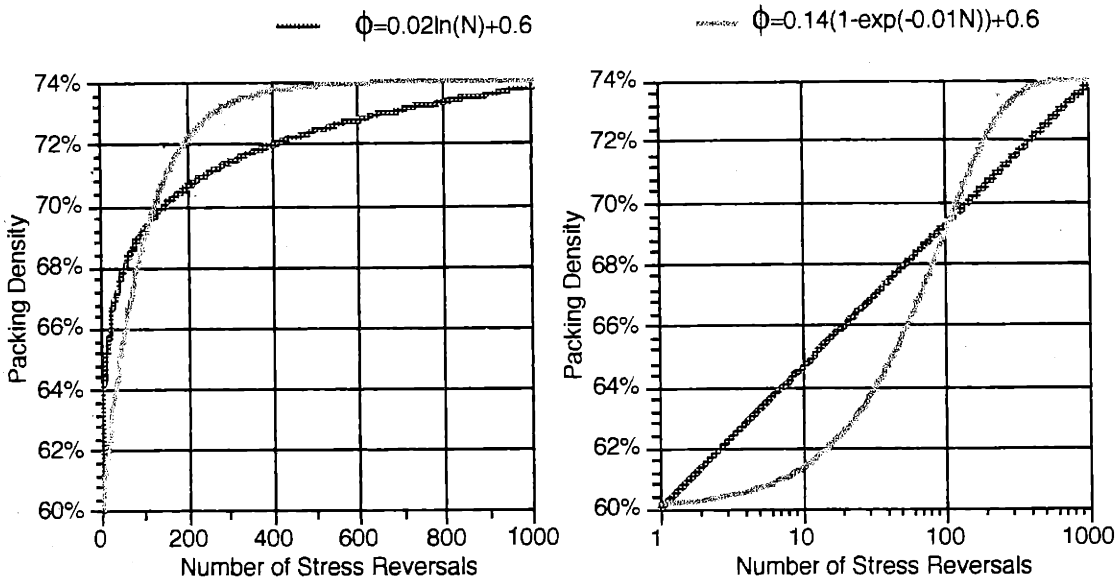

Figure 5.39: Shape of the response curves for the two proposed models.

The K constants used in the above models are, in general, complex functions of the various input parameters, such as vibrational frequency, amplitude, direction, etc., and of the specific characteristics for the powder being densified. Determining an exact relationship for a given powder and densification mechanism is usually not possible without direct experimental characterization. Nevertheless, the models provide a useful tool for predicting the shape of the layer densification response over time.

The main conclusion drawn from these layer densification experiments was that the direction in which vibrational excitation was applied to the powder layer was the dominant factor in layer densification behavior. The application of an oscillatory shear stress parallel to the layer surface, in combination with a small static normal stress, provided the best mechanism for inducing particle rearrangement and densification. Conceptually, this mechanism reduces the stabilizing effects of powder locking and wedging on pore structures in the layer by simultaneously keeping the applied normal stress levels low and the level of particle rolling and sliding high.

5.5 Characterization of Packing Evolution in a Powder Mass

One question not answered by the previous layer densification tests was how the powder packing density in the different regions underneath the pressure plate evolved over time. Specifically, did every portion of the powder mass under the plate simultaneously

begin to compact the moment vibration was applied, or did packing density changes propagate out from the regions immediately adjacent to the pressure plate, into areas further away ? Also unknown was the maximum depth of influence of the applied vibration into the powder layer. Information about the depth of influence for various vibration conditions would be useful if it were ever necessary to compact very thick layers.

Two final tests were devised to help understand how deeply and how fast packing density changes propagated through a powder mass. These tests are described below.

5.5.1 Depth of Influence Tests

The objective of these tests was to observe the powder densification patterns under the pressure plate for different applied stress conditions. These observations would allow a qualitative determination of how deeply into a powder mass the layer densification techniques developed in the previous section could densify powder. For each of these tests, a ceramic boat with internal dimensions of 1.5cm x 5cm x 10cm was filled with the 71/9μm powder. A flat top surface was struck using the non-vibrating spreader rod. The boat was filled by very gently pouring the powder into it, with the intention of leaving the powder as loosely packed as possible (near the apparent density). After filling, the average packing density in the boat was approximately 66%.

Using the pressure plate apparatus from the previous layer densification tests, a strip of powder in the top center of the boat was densified. (The pressure plate horizontal dimensions were again 1.5cm x 8.3cm.) Vibration was applied for 30 seconds to ensure that the packing limit had been reached in each case. Different variations of vertical stress and horizontal shear displacement were tried. Figure 5.40 is an illustration of the densification technique.

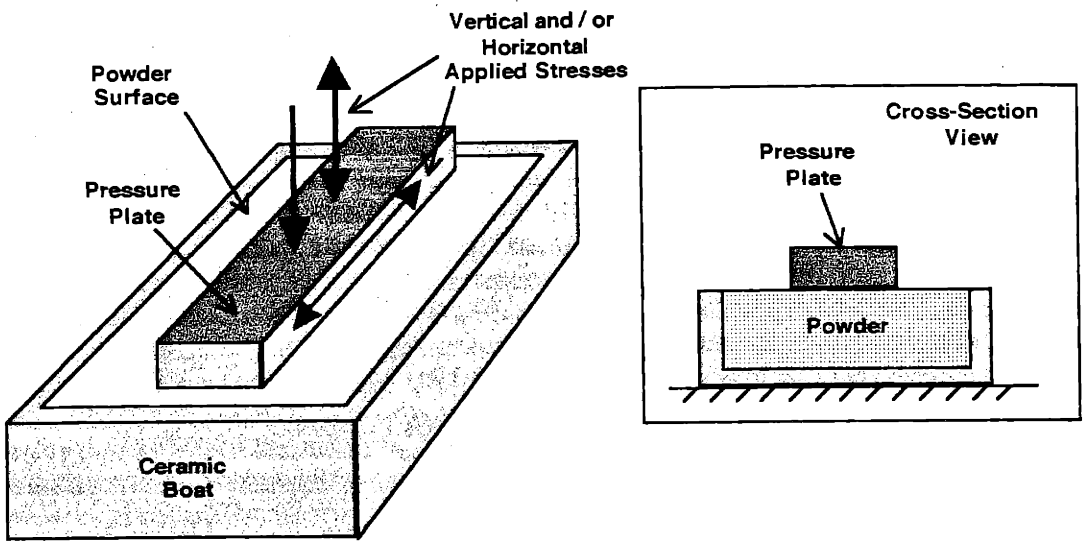

Figure 5.40: An illustration of how the depth of influence test samples were produced.

After compaction, the boat of powder was furnace processed to lightly sinter the powder particles. The sintered sample was then cross-sectioned halfway along its length, potted in epoxy and polished. Using digital photographic analysis techniques, the local packing density throughout the cross-section was determined at grid intervals of 2mm x 2mm. The array of packing data obtained was then used to create a packing density topographical map, which revealed the packing contours generated beneath the pressure plate for a given densification technique. Packing density values in the maps below have been adjusted to compensate for shrinkage which occurred during sintering.

The process of obtaining a single packing density map was extremely labor intensive, requiring approximately 120 packing density photographs to be acquired and analyzed. For this reason, only three maps were generated. The three vibration conditions chosen for these tests were considered to provide the greatest spectrum of information about the layer densification process.

In the first test performed, a vertical stress condition of 4000+/-2000Pa was applied to the powder surface at a frequency of 185Hz. The packing density map for this test is shown in figure 5.41. Packing density increases were observed all the way to the bottom of the sample, approximately 15mm away from the pressure plate. Significant increases in packing, i.e. those which approached the tap density of the powder, were limited to a depth of approximately 4mm.

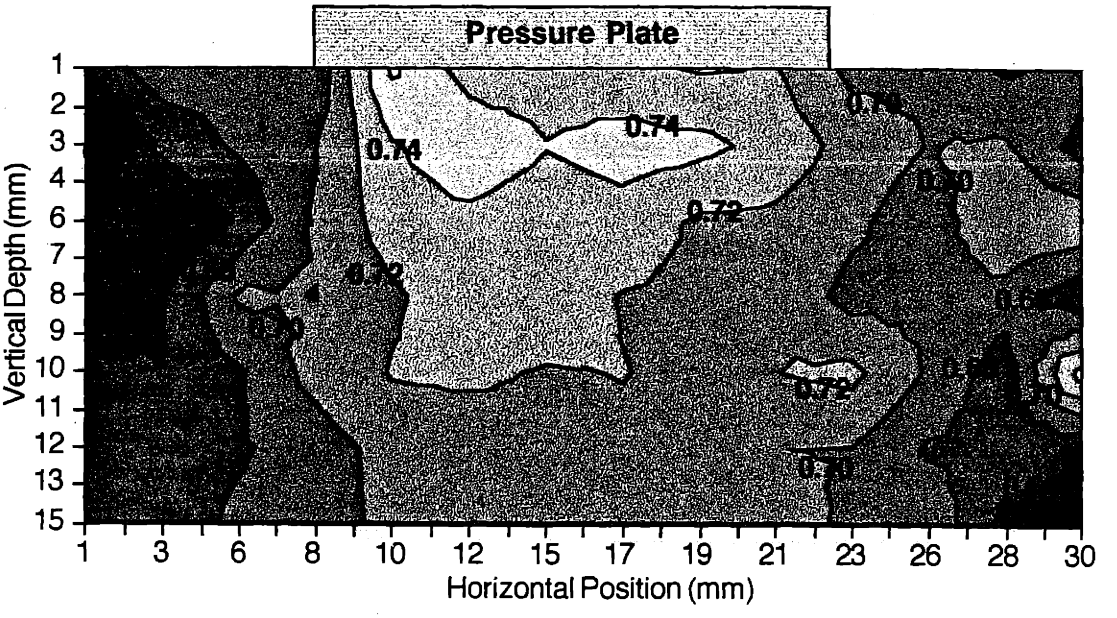

Figure 5.41: Packing density map for the condition of 4000+/-2000Pa vertical applied stress. 185Hz excitation. 71/9μm powder. Vibration was applied for 30 seconds.

The isobars for the major principal stress, σ_{1p}, were calculated using a strip load stress distribution approximation from elasticity theory. Refering to figure 2.18 and equations 2.20-22, the major principal stress σ_{1p} under a strip load is given by the expression

$$\sigma_{1p} = \frac{1}{2}\left[\sigma_1 + \sigma_3 + \sqrt{(\sigma_1 + \sigma_3)^2 + 4\tau_{13}^2}\right]. \qquad 5.17$$

[ref. 58, p.229]

These the major principal stress isobars were superimposed on the previous packing density map for the visualization purposes. This overlay is shown in figure 5.42. A rough correspondence between the locations of the packing and stress isobars can be seen. As might be expected, regions which experienced a higher overall stress level densified to a greater extent.

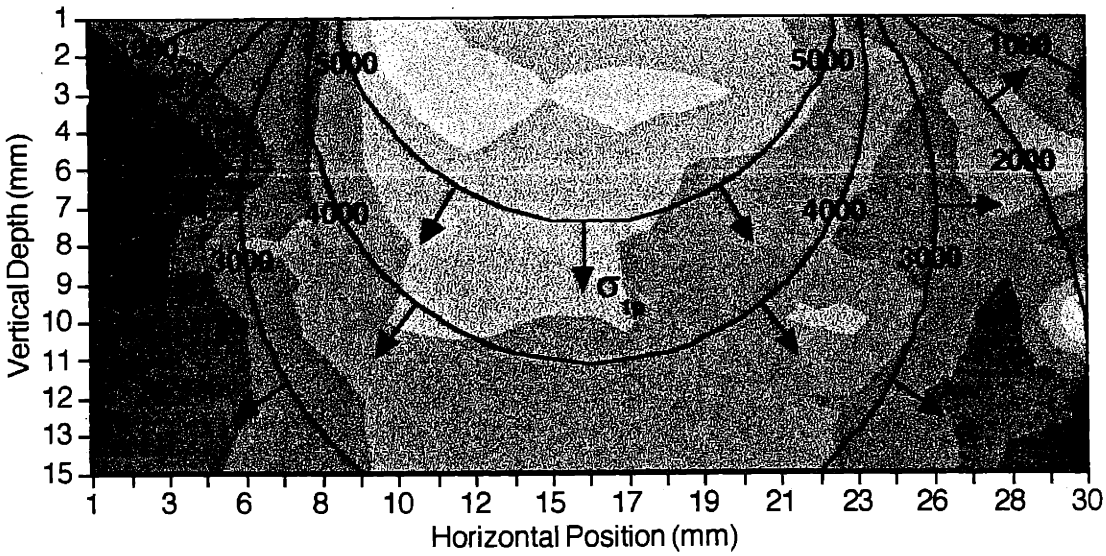

Figure 5.42: The packing density map shown in figure 5.41, with the isobars of the major principal stress superimposed.

In the second test performed, a vertical static stress of 500Pa was applied, and the pressure plate was horizontally oscillated through a peak-to-peak displacement of 60μm. The excitation frequency was 300Hz. The smooth-bottomed pressure plate was used. The packing density map for this test is shown in figure 5.43. In this packing map and the next, the pressure plate shown was oscillating normal to the page.

This map showed a depth of influence similar to the previous test, with a slight difference being that the highest packing density areas (those that exceeded 74%) were located in a tighter region directly below the plate. Note that these first two tests produced similar overall packing density values, even though the vertical stress level was significantly lower in the second test. The influence of vibrational direction on the powder densification behavior was again very apparent.

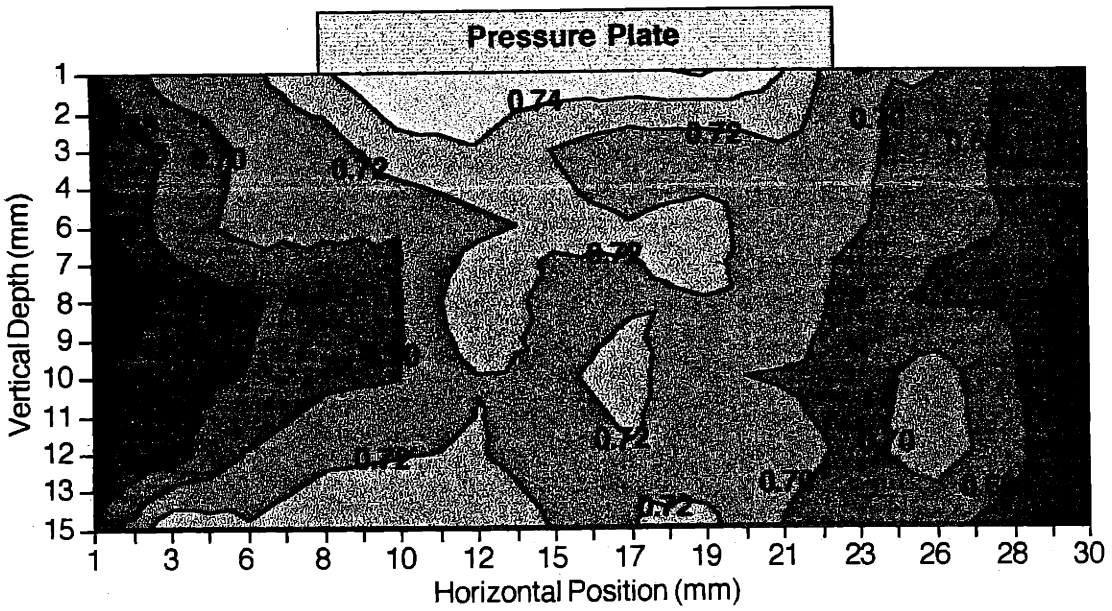

Figure 5.43: Packing density map for the condition of 500Pa vertical static stress and 300Hz, 60μm horizontal shearing oscillation. Smooth surface pressure plate. 71/9μm powder. Vibration was applied for 30 seconds.

The final packing test had vibrational conditions identical to the second, except the pressure plate bottom was roughened to observe the effect of increased shear stress on the packing density distribution. The packing density map for this test is shown in figure 5.44.

The highest packing density values were obtained in this test, demonstrating again that high transmitted shear stresses are critical to powder compaction. Highest packing was again concentrated to a region directly beneath the plate. The attenuation of shear stress with increasing distance from the pressure plate was believed to be the cause of the stratified packing density values near the bottom of the plate.

Little densification occurred below a depth of 6mm. No explanation could be given for this effect. With only one packing map generated for each vibrational condition, it was impossible to determine if this effect was real or an anomaly localized to the portion of the original sample which was sectioned.

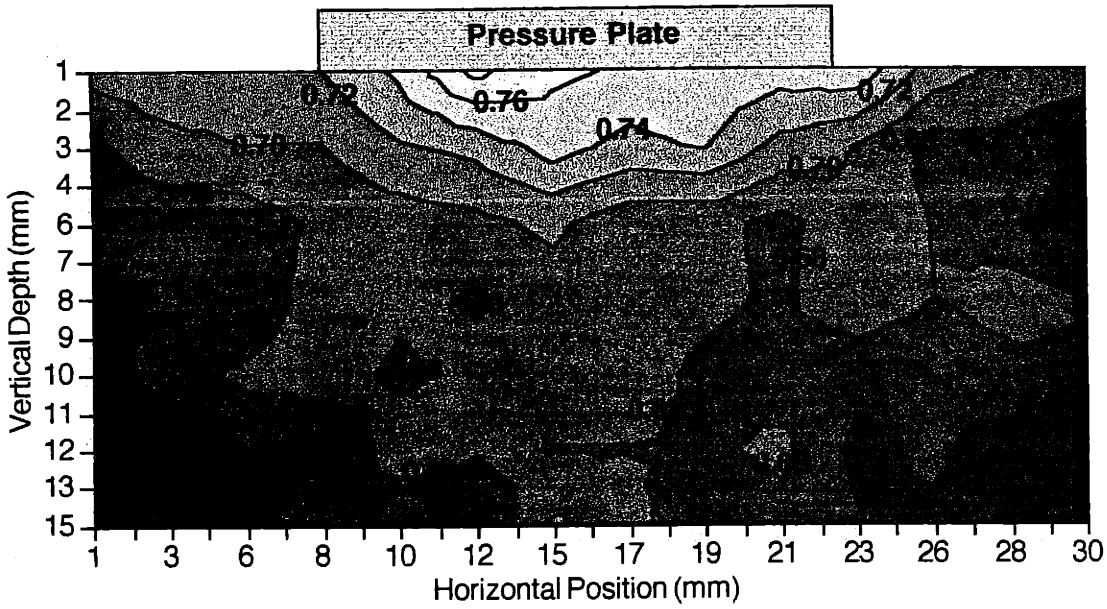

Figure 5.44: Packing density map for the condition of 500Pa vertical static stress and 300Hz, 60μm horizontal shearing oscillation. Rough surface pressure plate. 71/9μm powder. Vibration was applied for 30 seconds.

The conclusions drawn from the depth of influence tests were as follows:

1. For vibrational densification conditions similar to those used in the earlier layer densification tests, significant densification occurs at distances of 4 to 6mm from the pressure plate. Since a typical layer thickness in 3DP is 175μm, complete layer densification should not be an issue.

2. Horizontal shearing vibration, in the presence of a small static vertical stress, was again observed to be the preferred method for powder layer densification.

5.5.2 Packing Density Propagation Tests

In the depth of influence tests above, the powder body was allowed to reach a state of packing equilibrium before the local packing densities were measured. During the time in which packing density changes were occurring, one of two possible behavior patterns was expected. In the first possibility, packing density changes propagated outward from the pressure plate. In this case, regions further away from the plate remained unaffected during the first several moments of densification. This behavioral possibility was based on the premise that powder which had not yet been densified could not transmit significant

levels of stress (particularly shear stress). In the second possibility, packing density changes started everywhere in the powder mass simultaneously. In this second case, the transmission of stress away from the pressure plate was not significantly affected by the lower initial packing values throughout the sample.

To determine which possibility was correct, a series of tests similar to the depth of influence tests were performed, with the main difference being that the vibrational excitation was applied for only short periods of time. A horizontal shear oscillation condition was used with the smooth-bottomed pressure plate. A vertical static stress of 500Pa was applied, and the pressure plate was horizontally oscillated through a peak-to-peak displacement of 20μm. The excitation frequency was 300Hz. The 20μm 316L monomodal powder was used for these tests. The packing density in the ceramic boat prior to densification was approximately 56%.

Three tests were run, in which the durations of vibration were 0.5, 1 and 2 seconds. After each test, the samples received furnace processing and metallographic preparation similar to that described above. Instead of mapping packing density across the entire sample cross-section, only a vertical strip below the center of the pressure plate was measured. The packing density results for the three runs are plotted against distance from the pressure plate in figure 5.45.

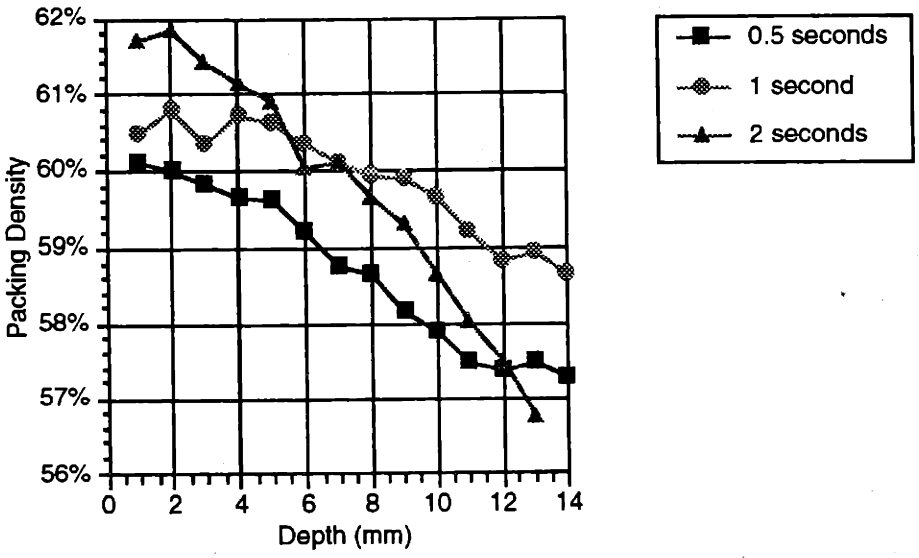

Figure 5.45: Packing density vs. depth for three durations of vibrational application. 500Pa vertical static stress and 300Hz, 20μm horizontal shearing oscillation. Smooth surface pressure plate. 20μm powder.

Longer periods of vibration produced higher packing densities in the first 5mm of powder beneath the pressure plate. In all three tests, packing dropped off steadily with increasing depth. No explanation is given for why the powder packing after 2 seconds of vibration was lower than after 1 second for depths greater than 7mm, but this effect may simply be a result of performing each test only once. Even after only 0.5 seconds of vibration, there was still densification evident at depths greater the 10mm. These results would indicate that the start of densification processes occurs in all regions simultaneously. Regions further from the pressure plate experienced attenuated stress levels, resulting in local packing density values which were consistently lower over time, compared to regions closer to the plate.

5.6 Densification Mechanism Design Selection

Having completed an extensive characterization of powder densification behavior, the task at hand was now to select a densification device from the four previously proposed designs.

5.6.1 Ranking of Potential Designs

In terms of overall expected effectiveness at densifying a powder layer to near the tap density, the four proposed designs were ranked in the following order:

1. Horizontally oscillating wedge with controlled vertical stress.

2. Horizontally oscillating wedge with fixed vertical position.

3. A wedge in which the vertically applied static and oscillatory stresses are fixed.

4. Vertically oscillating wedge in which the mean height of the plate is fixed.

Both the layer densification and packing density mapping experiments had indicated that a horizontal shear motion in the presence of a small static normal stress was the optimum method for layer densification. The design for a horizontal oscillating wedge with controlled vertical stress level was selected as the better of the first two choices, since all previous testing had been performed with a controlled vertical stress. Using the design in

which the vertical position was fixed would have resulted in an unknown vertical reaction stress, and it was felt that this would make interpretation of the later printing evaluation results more difficult.

The final two design concepts were also ranked, although it was not expected that these designs would be evaluated. The design in which the wedge applied a controlled static and oscillatory vertical stress, with the additional requirement that the magnitudes of these stresses be approximately equal, was considered better, simply because it would allow for a complete unloading of the powder surface during each oscillation. Complete unloading had been previously shown to be critical to densification behavior when using vertical oscillation, since in allowed the powder to become momentarily "unlocked".

Figure 5.46 is an illustration of the design mechanism which would be used during the final printing evaluation tests.

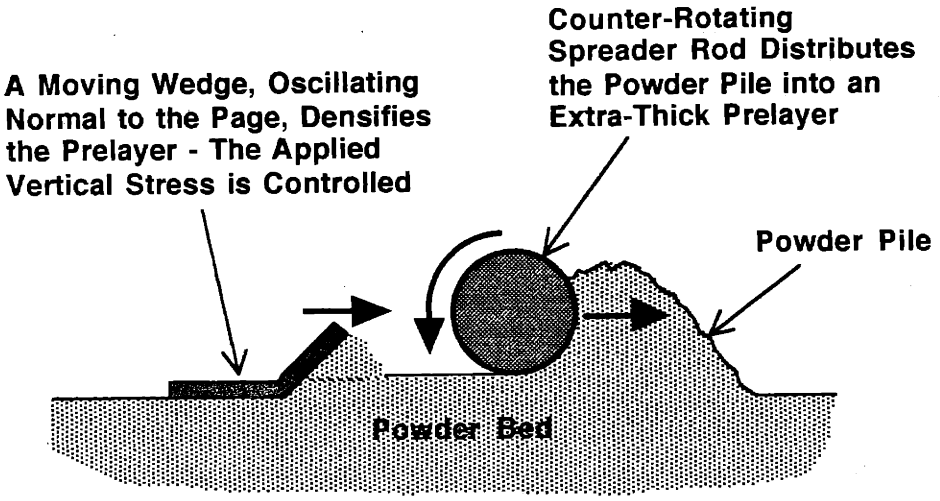

Figure 5.46: Illustration of the design selected to perform powder layer densification.

5.6.2 Selection of Design Parameters

Based on the results from the previous experiments, the optimum values for several of the design and operational parameters for the new layer densification mechanism could be estimated. The results from the layer densification tests indicated that most densification was accomplished in the first 2 seconds of vibrational excitation, regardless of the choice of vibrational frequency or amplitude. The width of the wedge bottom and the wedge

spreading speed would together determine the length of time which any given strip of powder bed experienced vibrational stresses. A wedge width of 0.5 inches, and a spreading speed of 0.25 inches / second, were chosen to meet the 2 second densification time requirements.

A roughened wedge bottom would be used to generate the maximum transfer of shear stress between wedge and powder. Confining normal stresses in the range of 500 to 2000Pa would be evaluated. Vibrational frequencies between 200 and 400Hz would be tested, with the expectation being that higher frequencies would work better. Finally, the maximum horizontal amplitude which could be generated for a given frequency would be used.

5.6.3 Design Evaluation in Actual Printing Conditions

The final step in this overall development effort was to evaluate the new layer densification mechanism in concert with the other printing equipment which had been previously developed. The horizontal shear spreader concept would need to be adapted to work on the prototype 3DP machine, and it was expected that some alterations in the concept would be necessary, simply due to practical constraints. An evaluation of the new densification mechanism in actual printing conditions is presented in the next chapter.

Chapter 6. Evaluation of the New Printing Techniques

6.0 Introduction

The final set of testing performed in this research was the demonstration of the new layer densification design during actual printing of metal parts, both with monomodal and bimodal powders. The ultimate goal of these tests was the creation of a printing process which could produce parts at or near the tap density of the powder used. Recognizing that 3D printing was a complex process, it was anticipated that several design modification / printing evaluation iterations would be necessary before establishing a new, usable printing technique.

6.1 Initial Printing with the New Densification Mechanism

To evaluate the new densification mechanism design in actual printing conditions, the concept first had to be adapted to operate in conjunction with the other equipment used on the prototype 3DP machine.

6.1.1 Design of the New Densification Mechanism

The design of the new densification mechanism, as it was incorporated into the prototype 3DP machine, is shown in figures 6.1-3. Because of space restrictions in adding the new densification apparatus, and the limited travel of the slow axis on the prototype machine, the printing cycle was altered so that the new layers were spread from the back to the front of the powder piston. Figure 6.1 shows the relative position of the new layer densification hardware to the other printing equipment, such as the spreader rod, and the heater and steamer bars. The horizontally oscillating wedge and its related support components were all mounted on a vertically oriented clear lexan sheet. Lexan was chosen instead of metal so that the printing process could be viewed through the mounting plate.

The support structure for the horizontally oscillating wedge used in these printing tests was identical to that used in the earlier layer densification experiments, with two orthogonally mounted linear bearings providing for horizontal and vertical motion of the wedge. A new approach, however, was taken for controlling the vertical stress which the wedge bottom applied to the powder layer. Instead of using a counter-balance assembly, a

small air cylinder and pressure regulator were used to modulate the vertical force. With no air pressure applied to the cylinder, the mass of the wedge plate and bearing assembly could provide a vertical stress of 3000Pa to the powder layer. As increasing air pressure was applied to the cylinder, the resultant vertical stress on the powder layer could be reduced to any lower value.

The oscillating wedge itself was fabricated from 50mil stainless steel sheet. The wedge strip was cut to size and bent to create a 45° inclined face, followed by a horizontal surface with a 0.5" width.

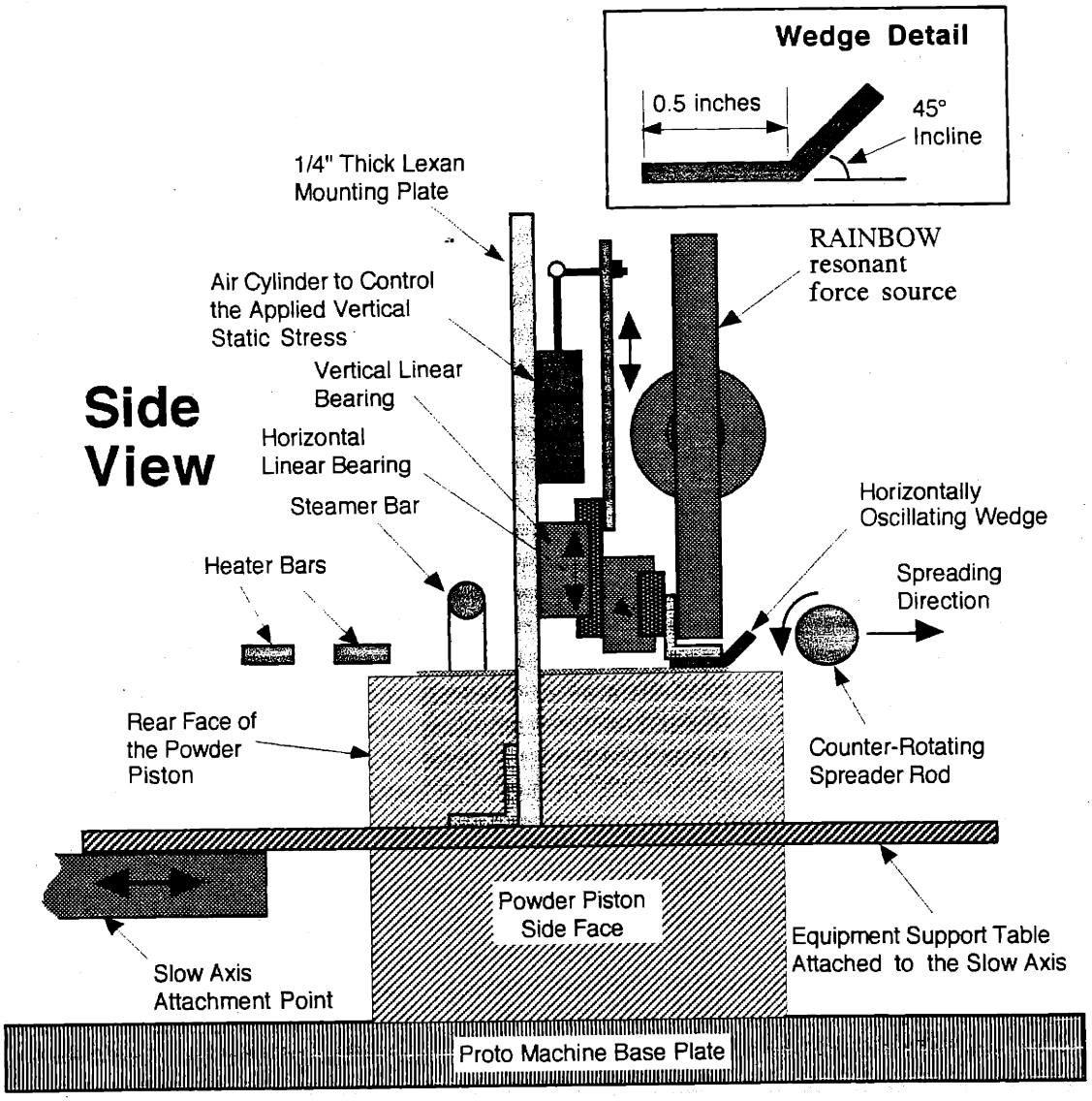

Figure 6.1: A side view of the new densification apparatus, showing its relative location to the spreader rod, steamer and heater bars. Note that the spreading direction was opposite that of early printing techniques, with the new layer being spread from back to front.

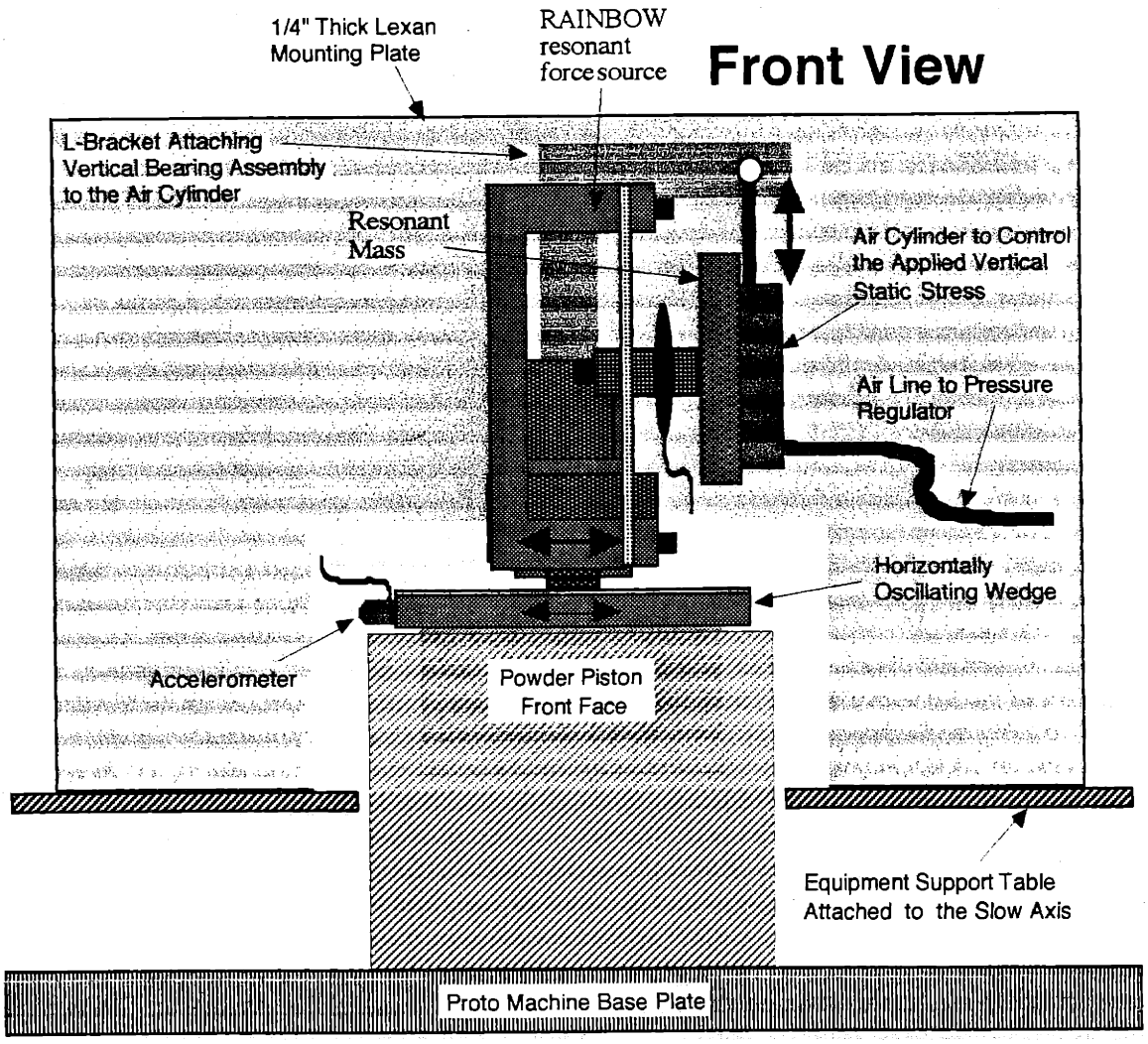

Figure 6.2: A front view of the new densification apparatus as mounted on the prototype 3DP machine.

Figure 6.3 is a photograph of the actual layer densification assembly as mounted on the prototype 3DP machine. The RAINBOW resonant force source, which was mounted to the horizontal linear bearing, is visible in this photograph.

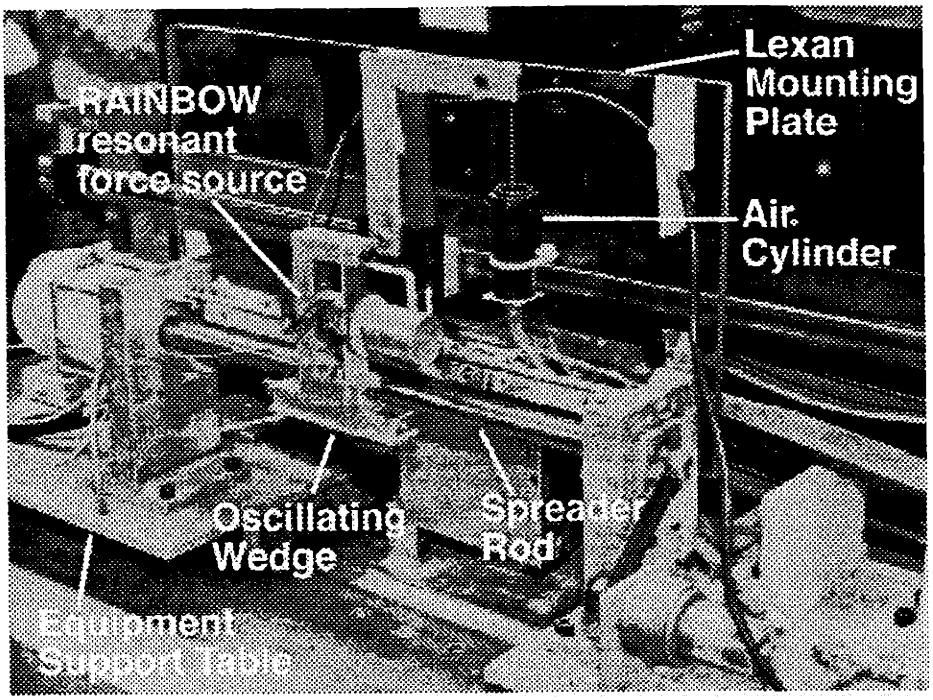

Figure 6.3: A front view of the new spreading equipment as mounted on the 3DP prototype machine.

In order for the oscillating wedge concept to be successfully employed in the final printing process, the compacted layer needed to be of uniform thickness across the entire powder bed. Since the vertical height of the shearing wedge was not fixed (only the applied vertical stress was), it was uncertain as to whether or not the height of the wedge would reach a steady-state condition during densification of the prelayer.

If powder in the prelayer was perfectly compressed and not skimmed away by the oscillating wedge during the densification process, then the packing density ϕ of the powder in the densified layer could be calculated from the expression

$$\phi = \phi_o\left(\frac{t_0}{t}\right), \qquad 6.1$$

where ϕ_o was the packing density in the prelayer, and t and t_o were the thickness of the densified and prelayers, respectively. This densification condition is illustrated in figure 6.4.

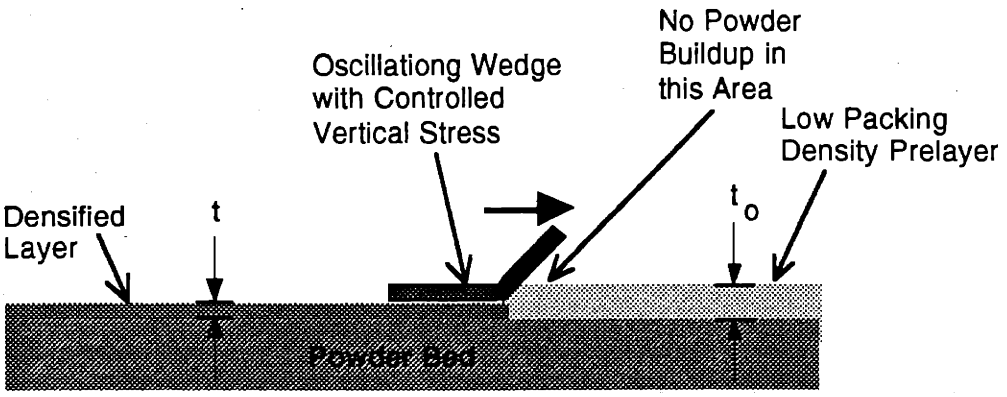

Figure 6.4: Illustration of the densification condition in which all the powder in the prelayer was compacted to form the densified layer.

If, however, it was the case that some of the powder in the prelayer was removed during the densification pass, then the final packing density could not be determined from the above quantities. In this later case, it would be necessary to spread an initial prelayer which contained a surplus of powder above that needed in the final layer. Exactly how much of a surplus of powder needed for any given printing condition would be based on numerous spreading parameters, such as the wedge shape and vibratory conditions, and most likely could not be calculated a priori. If, however, a *repeatable* amount of powder was removed with each densification pass, then after several powder layers had been generated, a steady-state condition would be reached in which the final layer thickness was identical to the vertical drop of the piston with each layer. The following example will help to clarify this point.

For this example, let the net downward travel of the piston be 175μm for each layer created, and let the target thickness for the each densified layer also be 175μm. Let us assume that 20% of the powder in the prelayer was removed by the wedge during any densification pass, with the remainder of the powder in the prelayer being used to create the densified layer. If the first prelayer generated was 175μm thick, then the corresponding densified layer would be too thin, both because the layer thickness was reduced due to densification and because 20% of the powder in the prelayer had been scraped away by the wedge. After the piston dropped 175μm, the subsequent prelayer would be thicker than 175μm, with the difference being the same amount by which the previous densified layer was too thin. For this second layer, the final densified layer thickness would be closer to the desired thickness of 175μm, since in this case the prelayer contained a surplus of

powder. After several more layer generation iterations, it would the case that the final layer thickness asymptotically approached the value of the piston vertical drop.

It was not possible, a priori, to determine which of these two densification conditions would result during actual layer creation. Printing tests were therefore performed to make this determination.

6.1.2 Initial Printing Sequence

The following printing procedure was used in conjunction with the new layer densification device. At the start of the procedure, the slow axis was positioned such that the spreader rod was at the rear of the piston. (Refer to figure 6.1.)

1. Lower the piston one layer thickness (175μm).

2. Manually dispense preheated powder in a pile in front of the spreader rod.

3. Generate the new layer, with the spreader rod striking the prelayer and the oscillating wedge performing the final densification. Pressure to the air cylinder was adjusted to provide the correct level of vertically applied stress. The slow axis was moved from the back to the front of the piston at 0.25"/second.

4. Lower the piston an additional 250μm.

5. Turn on the steamer bar to activate the powder coating. Move the slow axis from the front to the back of the piston. Slow axis speed for powder coating activation was 0.25"/second. On completion of the pass, turn off the steam.

6. Move the slow axis to a position where the heater bars were over the first line to be printed and pause 30 seconds to allow for removal of of condensed steam.

7. Perform layer printing.

8. Stop the slow axis with the heater bars positioned over the last printed line and pause 30 seconds to allow for removal of residual moisture from the printed binder.

9. Raise the piston 250μm to break any powder wall bonds.

6.1.3 Initial Printing Results

Initial printing tests were performed using the different monomodal and bimodal metal powders, and adjusting the frequency, amplitude and normal stress settings of the oscillating wedge. The texture of the bottom of the wedge was also varied between smooth and rough. Unfortunately, no operating condition could be found which generated a densified layer with uniform thickness. Even at the most moderate of wedge settings (i.e. peak-to-peak amplitude less than 10μm, normal stress less than 200Pa, and a smooth bottom surface to lower the transferred shear stress), the wedge would slowly dig into the powder prelayer during densification, instead of attaining a steady-state height. This effect is illustrated in figure 6.5. The quantity of powder removed by the wedge was not a function of the prelayer thickness. By the half-way point in each spreading pass, the wedge had effectively skimmed away all the powder in the prelayer and was scraping the previous layer. Powder in the prelayer was pushed out ahead of the wedge and off the sides of the piston.

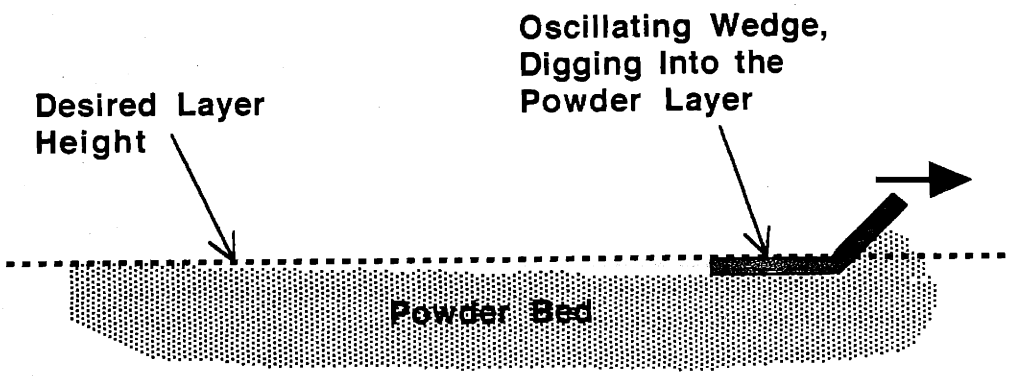

Figure 6.5: Illustration of the oscillating wedge digging into the powder surface during layer densification.

A variety of factors, such as the precise cross-sectional shape of the oscillating wedge, and the fluidity of the powders under examination, may have contributed to the poor performance of the initial design. An exact explanation of why the digging effect occurred was not determined. It may have simply been the case, however, that it was not possible to avoid uncontrolled digging into the prelayer in the presence of any applied normal stress, however small.

No printing was accomplished using the horizontally oscillating wedge with controlled normal stress due to this spreading difficulty. A modified densification process sequence was created to circumvent this problem.

6.1.4 An Incremental Densification Approach

In the modified densification sequence that was tried next, the 1.5cm x 8.3cm pressure plate from the layer densification tests in chapter 5 replaced the oscillating wedge shape. The modified sequence is shown in figure 6.6. After the spreading of the prelayer, the pressure plate was incrementally moved across the prelayer surface, locally densifying the powder. Each strip of powder received a minimum of 2 seconds of densification. There was a 2mm overlap for each repositioning of the pressure plate. The incremental approach avoided the skimming effect of the oscillating wedge. However, after the completion of each incremental densification pass, the top of the densified powder layer was unacceptably rough for the purposes of printing. This roughness resulted from small amounts of powder being ejected from the sides of the pressure plate during every densification increment. To remove this roughness, a final smoothing pass was performed with the spreader rod.

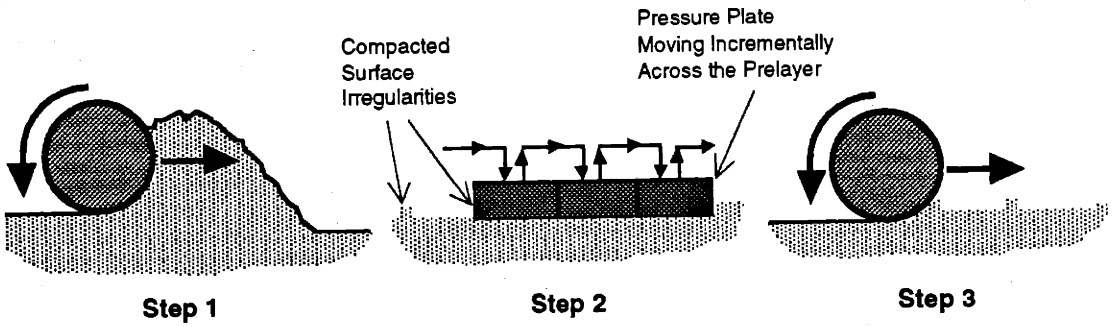

Figure 6.6: The incremental compression layer generation sequence.

It should be noted that it may have been possible to densify the entire 9cm x 9cm prelayer at once by using a pressure plate with the same horizontal dimensions as the powder piston. Doing so probably would have avoided the need for a final leveling pass with the spreader rod. This approach was not taken, however, for two reasons. First, the oscillatory force levels required to densify the entire layer simultaneously were beyond the

capabilities of the RAINBOW resonant force source which was being used, since the required horizontal shear stresses scaled with pressure plate surface area. Second, although an apparatus might have been constructed which would densify the small 9cm x 9cm area of the prototype 3DP machine, such a device would have been difficult to scale to larger, production 3DP machines.

The following printing procedure was used with the incremental layer densification approach. Again, at the start of each new layer, the slow axis was positioned such that the spreader rod was at the rear of the piston. The thickness of the prelayer was 350μm, which was certain to provide more than enough powder for layer densification and final layer smoothing.

1. Lower the piston two layer thicknesses (350μm).

2. Manually dispense preheated powder in a pile in front of the spreader rod.

3. Generate the prelayer with the spreader rod. The slow axis was moved from the back to the front of the piston at 0.5"/second.

4. On the return pass of the slow axis to the rear of the piston, perform the incremental densification of the powder layer. Again, pressure to the air cylinder was adjusted to provide the correct level of vertically applied stress. Each strip of powder received 2 seconds of horizontal shearing excitation.

5. Raise the piston one layer thickness (175μm).

6. Using the spreader rod again, smooth the densified layer surface and strike the final layer thickness. The slow axis was moved from the back to the front of the piston at 0.5"/second.

7. Lower the piston 250μm.

8. Turn on the steamer bar to activate the powder coating. Move the slow axis from the front to the back of the piston. Slow axis speed for powder coating activation was 0.25"/second. On completion of the pass, turn off the steam.

9. Move the slow axis to a position where the heater bars were over the first line to be printed and pause 30 seconds to allow for removal of the condensed steam.

10. Perform layer printing.

11. Stop the slow axis with the heater bars positioned over the last printed line and pause 30 seconds to allow removal of residual moisture from the printed binder.

12. Raise the piston 250μm to break any powder wall bonds.

6.1.5 Printing Results Using the Incremental Densification Approach

A variety of printing conditions were tried with the incremental densification approach. Packing density results for three test conditions using the 71/9μm bimodal powder are given in table 6.1. These results were typical of all the powders evaluated.

Table 6.1: Incremental Densification Testing Conditions and Packing Density Results. 71/9μm 316L Powder.

Test #	Pressure Plate Bottom Texture	Vibrational Frequency (Hz)	Vibrational Amplitude (μm)	Vertical Static Stress (Pa)	Packing Density
1	rough	310	20	1000	66.2%
2	rough	310	20	3000	63.6%
3	smooth	150	100	3000	66.0%

The packing density results using the incremental densification approach were not significantly different from the baseline analysis packing density results in which only the spreader rod was used. After reconsidering the entire incremental process illustrated in figure 6.6, it was concluded that the final smoothing pass of the spreader rod may have been "undoing" any densification caused by the pressure plate. The reasoning behind this assertion was based on the Jenike yield locus theory, which stated that a powder mass subjected to a shearing stress in the absence of a confining normal stress would tend to dilate and flow. Referring to figure 6.7, the region directly in front of the spreader rod during the final smoothing pass was subjected to a similar stress condition. A shearing stress generated by the moving rod was transmitted through the pile of excess powder to the layer below. However, no normal stress was present in this region. It was therefore

likely than any densification effect accomplished by the pressure plate was being negated by the final spreader rod pass.

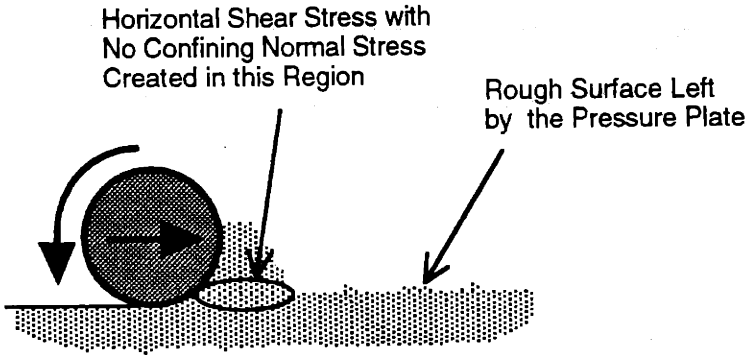

Figure 6.7: Illustration of how the spreader rod could potentially lower packing density during a smoothing pass.

To determine if powder layer dilation was indeed occurring during the final smoothing pass, was necessary to print directly into the compacted region before any subsequent spreading was performed. A modified incremental approach was developed which avoided the need for a final smoothing pass with the spreader rod. This modified approach is described in the next section.

6.2 A Modified Pressure Plate Layer Densification Approach

In order to ascertain the effectiveness of the new layer densification design concept in which a oscillatory shear stress was applied to the powder layer in conjunction with a small confining normal stress, the following process compromise was made. The ability to densify the entire 9cm x 9cm layer surface was sacrificed in order to print a single bar for which no smoothing passes with the spreader rod were required after each layer. To this end, an approach was taken in which a single, small portion of each prelayer measuring 2.0cm x 8.5cm was densified using an enlarged pressure plate. The center of this area was then immediately printed into, to create a single printed bar with horizontal measurements of 1.0cm x 8.0cm. The entire printing sequence is described below.

6.2.1 A Printing Sequence for Generating a Single Bar

The modified process sequence is shown in figure 6.8. As before, the spreader rod was used to generate an undensified prelayer. A single area at the center of the powder

prelayer was then densified using the enlarged 2.0cm x 8.5cm pressure plate. Small quantities of powder were ejected from the perimeter of the plate during densification, but this did not effect the printing process. The center of the densified region was then printed into.

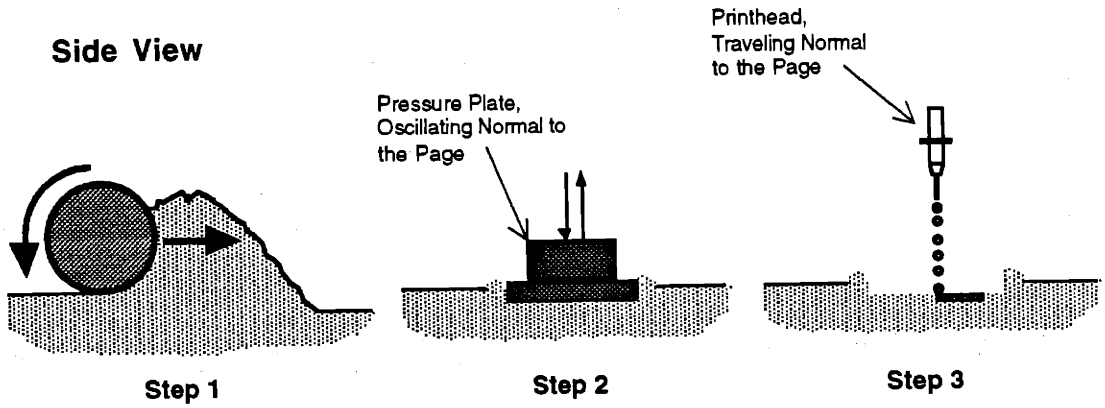

Figure 6.8: The process sequence used to create a single densified region within the powder bed.

The complete printing procedure was as follows:

1. Lower the piston one layer thickness (175μm).

2. Manually dispense preheated powder in a pile in front of the spreader rod.

3. Generate the prelayer with the spreader rod. The slow axis was moved from the back to the front of the piston at 0.5"/second.

4. Lower the piston an additional 250μm.

5. Move the slow axis to position the pressure plate over the center of the powder prelayer. Lower the pressure plate onto the powder surface and apply vibrational excitation for a minimum of 2 seconds. Turn off the vibrational excitation before lifting the plate in order to minimize disruption of the compacted layer surface.

6. Return the slow axis to the back of the piston. Turn on the steamer bar. Move the slow axis from the back to the front of the piston to activate the powder

coating. Slow axis speed for powder coating activation was 0.25"/second. On completion of the pass, turn off the steam.

7. Move the slow axis to a position where the heater bars were over the first line to be printed and pause 30 seconds to allow for removal of condensed steam.

8. Perform printing of a single bar in the densified powder region.

9. Stop the slow axis with the heater bars positioned over the last printed line and pause 30 seconds to allow for removal of residual moisture from the printed binder.

10. Raise the piston 250μm to break any powder wall bonds.

Prior to the start of printing, five layers were spread and the center regions densified to allow the layer thickness in the densified region to asymptotically approach the 175μm total downward piston travel for each layer. For each printing condition, a single bar was printed with a minimum of 12 layers in order to produce a representative microstructure.

6.2.2 Printing Results

The modified pressure plate densification approach was successful in generating a single printed bar for each printing condition. A variety of metal powders in combination with different pressure plate vibrational frequencies, shear amplitudes, and applied normal stresses were evaluated. It was also desired to evaluate the effect of different pressure plate textures on printed part microstructures, however, only the smooth-bottomed plate could be used successfully. When the roughened plate (laminated with 320 grit abrasive paper) was used with any of the powders, powder would stick to the bottom surface when the plate was lifted away after densification. The densified layer was disrupted and irregular, and was unacceptable for later printing. The problem of powder sticking and layer surface disruption also occurred using the smooth-bottomed plate, but only infrequently and to a greatly reduced extent. The results from all the printing runs using the modified pressure plate densification approach are given in table 6.2.

Table 6.2: Printing Results Using the Modified Pressure Plate Layer Densification Approach.

Powder	Vibrational Frequency (Hz)	Vibrational Amplitude (μm)	Static Stress (Pa)	Packing Density	Packing COV	Layer Packing Coeff.	Line Packing Coeff.
71/9μm 316L	120	200	500	74.7%	1.44%	4.84%	3.44%
	320	20	500	73.4%	1.26%	5.35%	4.02%
	320	20	2500	75.8%	1.00%	4.46%	2.19%
66/9μm 420	120	200	500	73.0%	1.71%	4.88%	2.87%
	320	20	500	75.8%	1.69%	5.21%	3.51%
	320	20	2500	73.8%	1.55%	4.66%	3.35%
120/20μm 316L	120	200	500	64.3%	2.43%	7.36%	4.89%
	320	20	500	66.2%	2.22%	7.57%	5.08%
20μm 316L	320	20	500	60.6%	2.47%	6.98%	4.85%

Except for the 120/20μm bimodal blend, all the metal powders tested showed significant increases in printed green density compared to the previous results from the baseline analysis. In several instances, the tap density of the powder was approached or equaled. It was believed that the poor results with the 120/20μm powder resulted from dilation of the powder due to vertical adhesion forces generated during removal of the pressure plate. The 120/20μm powder blend had one of the highest fluidities of all the powders tested, and therefore offered the least resistance to particle rearrangement and loosening during plate removal.

For any given powder, the differences in the packing density and the packing homogeneity results using different densification conditions were small in comparison to the improvement of these same parameters from the baseline printing results. Since only one bar was printed for each test condition, it was not known if these small differences in the packing and homogeneity parameters were real, or because of noise in the acquired data. (More bars were not printed and analyzed due to time constraints.)

Cross-sectional micrographs for three different printing conditions are shown in figures 6.9, 6.10 and 6.12. In studying the micrographs in figures 6.9-10, which shows the 66/9μm bimodal powder printed to the tap density, an important discovery was made. Although the powder in this printed sample was as densely packed as it could get, obvious layer defects still occurred. This observation brought into question the belief that a part

printed at the tap density would have a completely homogeneous microstructure. Further consideration of figures 6.9-10 led to the following explanation for the presence of the layer defects. What visually appeared as an inter-layer defect was actually a local reduction in the number of large particles. Since each layer in the microstructure was printed at the tap density, the top surface of each layer contained few or no large pores. During the spreading and densification of the subsequent layer, there were no surface pores big enough for any of the large particles to even partially fit into. The layer defect in the bimodal parts was therefore a result of the exclusion of large particles from the inter-layer region. This exclusion effect is illustrated in figure 6.11. No large particles crossed the boundary between layers, because the individual layers were so tightly packed. The absence of large particles in all the inter-layer regions resulted a visually identifiable layer defect.

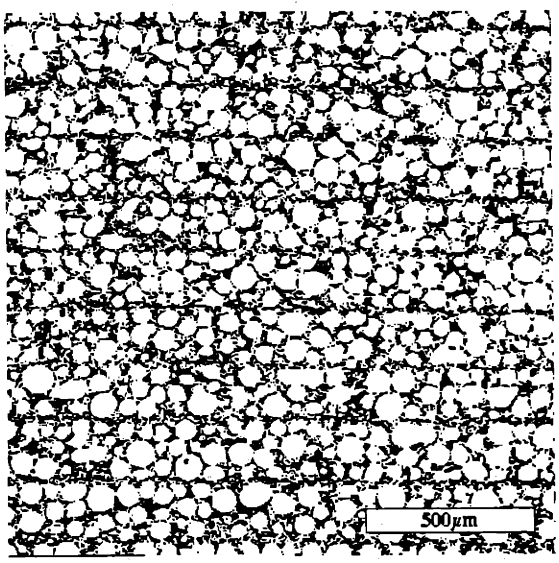

320Hz Excitation / 20μm Amplitude
500Pa Normal Stress

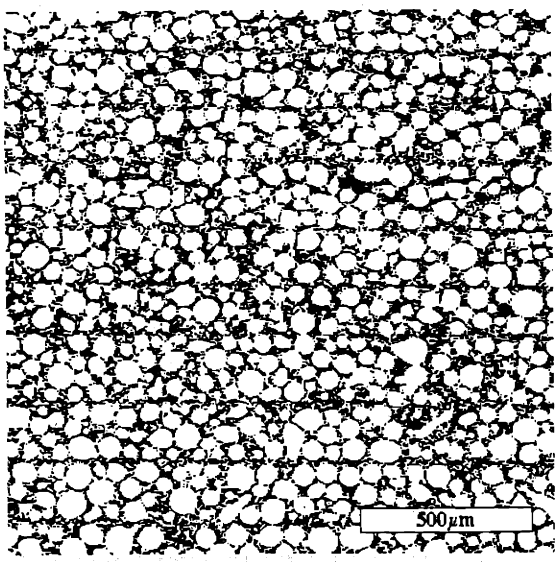

320Hz Excitation / 20μm Amplitude
2500Pa Normal Stress

Figures 6.9 and 6.10: Microstructures of bars printed with the 66/9μm 420 powder. Magnification 50x.

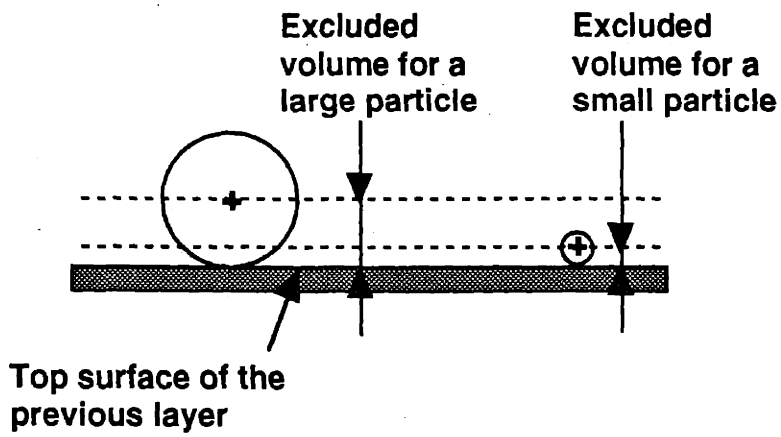

Figure 6.11: Excluded volume regions for the centers of the large and small particles.

The 20μm 316L monomodal microstructure shown in figure 6.12 also exhibited some small traces of layer packing defects, but the overall packing homogeneity was significantly improved over the baseline 20μm microstructure shown in figure 4.14.

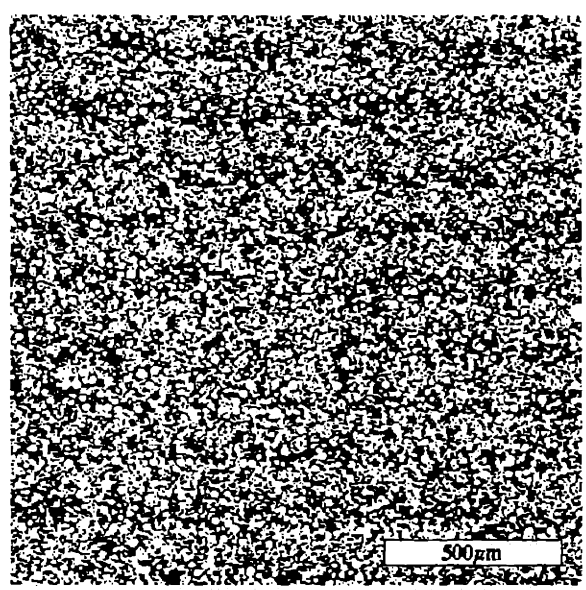

Figures 6.12: Microstructure of the bar printed with the 20μm 316L powder.
320Hz Excitation / 20μm Amplitude and 500Pa Normal Stress.
Magnification 50x.

Packing density and homogeneity results for the baseline, pressure plate and control samples are summarized in figures 6.13-15 below. Data for the 120/20μm, 71/9μm and

20μm 316L powders is presented. In comparing the packing density values in figure 6.13, we see that the bars printed with the pressure plate approached the "ideal" control sample values. Again, the printed density of the 120/20μm pressure plate sample showed little improvement over the baseline value due to layer dilation during removal of the pressure plate.

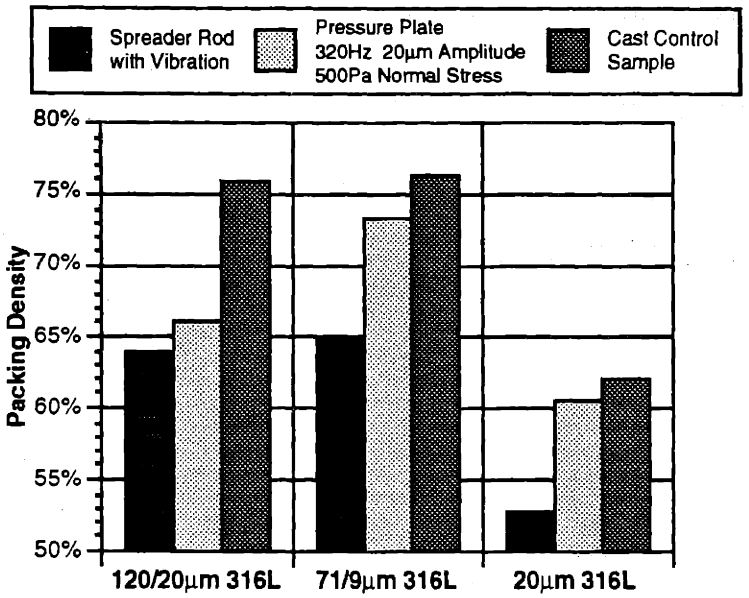

Figure 6.13: Comparison of the packing density values for the baseline, pressure plate and control samples.

In figure 6.14 the packing coefficient of variation (COV) for the different samples is compared. As might be expected, improvements in the average packing density for the pressure plate bars also resulted in decreased variation in the local packing density. Note that in the case of the 71/9μm bar printed with the pressure plate, the packing COV value was comparable to that of the control sample.

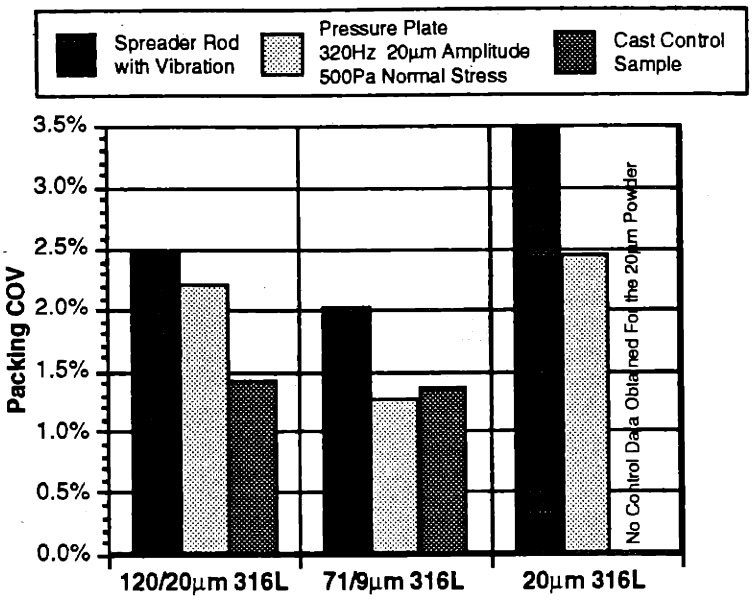

Figure 6.14: Comparison of the packing COV values for the baseline, pressure plate and control samples.

In figure 6.15 the layer and line packing coefficients for the different samples are compared. The increase in coefficient values between the 120/20μm baseline and pressure plate samples was not representative of the actual process due to the layer damage which occurred during densification. The lack of significant change between the 71/9μm baseline and pressure plate layer packing coefficient values was attributed in part to the presence of the layer packing defects in both samples.

For both the 71/9μm and 20μm powders, the line packing coefficient for the pressure plate bars was slightly higher than that of the baseline bars. This was contrary to expectation, since in both cases the packing density of the pressure plate bars was higher. In any event, there did not appear to be a significant level of packing defects across the printed lines for either the baseline or the pressure plate bars.

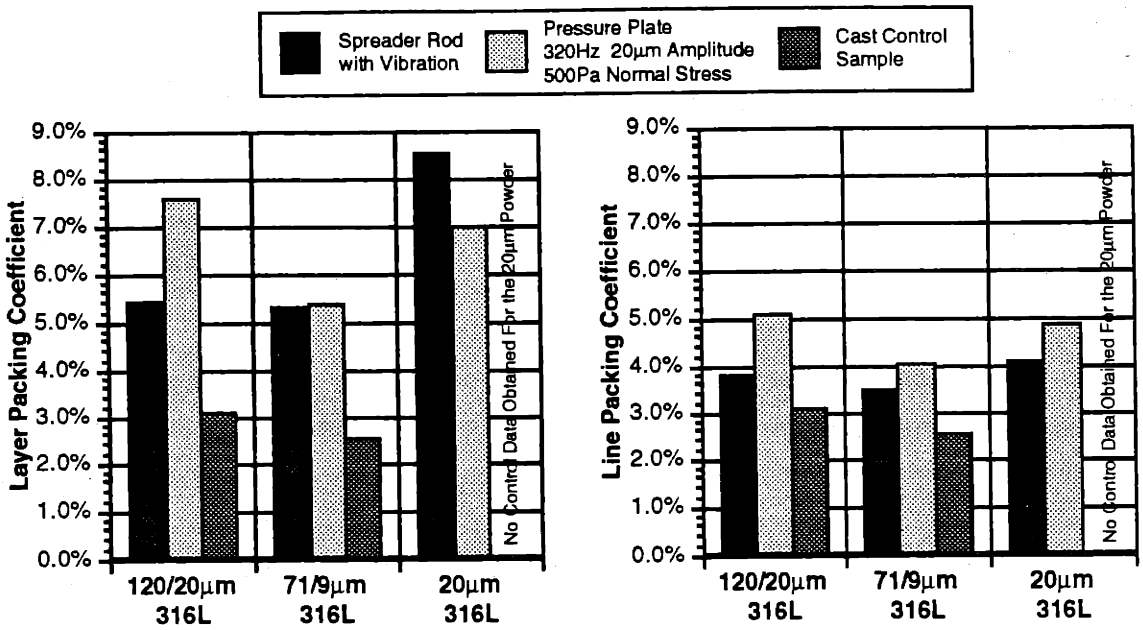

Figure 6.15: Comparison of the layer and line packing coefficient values for the baseline, pressure plate and control samples.

In order to evaluate the performance of the oscillating pressure plate over as broad a range of printing conditions as possible, bars were also printed with the standard 30μm platelet alumina used in the printing of casting shells. For comparison, cross-sections of bars printed with the alumina / colloidal silica material system on the Alpha 3DP machine using both the "raster" and "mushroom" print patterns were also analyzed. The results from these tests are given in table 6.3. For the bars printed on the Alpha machine, the green density values were calculated by measuring the mass of a bar using a precision balance, and the volume of the bar using the caliper technique. The bar mass values were adjusted to eliminate the mass addition from the presence of the colloidal silica. In this way, the packing density of the alumina in the bars was determined. Representative microstructures for the Alpha "mushroom" printed bar and the pressure plate printed bar are shown in figures 6.16-17.

Table 6.3: Printing Results Using the Modified Pressure Plate Layer Densification Approach with Alumina Powder.

Powder	Vibrational Frequency (Hz)	Vibrational Amplitude (μm)	Static Stress (Pa)	Packing Density	Packing COV	Layer Packing Coeff.	Line Packing Coeff.
30μm alumina	320	20	2500	40.9%	2.73%	7.83%	3.57%
alpha raster				34.3%	-----	12.22%	8.60%
alpha mushroom				35.4%	-----	14.49%	7.44%

A two critical differences exist between the printing techniques used to produce the Alpha machine and pressure plate bars which need to be taken into consideration when comparing the analysis results. First, Acrysol binder was used to print the pressure plate bars, while colloidal silica was used to print the Alpha machine bars. Also, powder locking and layer drying were used during the printing of the pressure plate bars, whereas the Alpha machine bars were printed with the standard printing procedure.

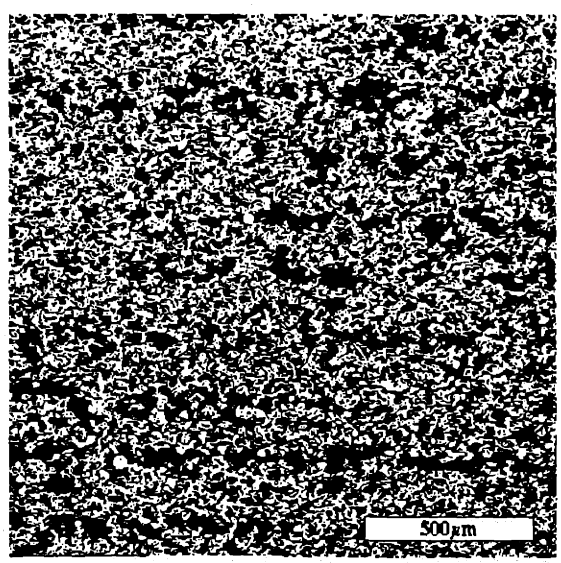

Standard alumina printing process using the Alpha 3DP machine and a "mushroom" printing pattern.

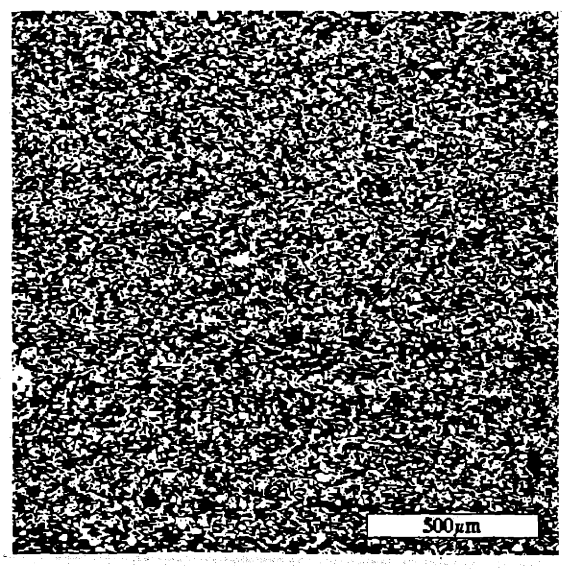

320Hz Excitation / 20μm Amplitude
2500Pa Normal Stress
Pressure plate printing.

Figures 6.16 and 6.17: Microstructures of bars printed with the 30μm platelet alumina. Magnification 50x.

The results from the printed alumina bar comparison showed a significant improvement in the alumina packing density, and a dramatic reduction in packing variation

and defects using the pressure plate approach. The large macro-voids which existed between the layers of the Alpha printed bars were completely eliminated.

6.2.3 Discussion

The modified pressure plate layer densification tests demonstrated that a layer compaction device which applied an oscillating horizontal shear stress in combination with a small confining normal stress provided significant improvement in printed part properties compared with parts generated using the standard spreader rod. Due to the small differences in the values of microstructural parameters for the various test conditions, and also because only one bar was printed per test, it is not possible to pinpoint any specific trends between changes in vibrational conditions and printed part properties. However, except in the cases where printing problems were observed, all the conditions evaluated produced bars with green densities at or near the tap density. It is therefore concluded that the pressure plate layer densification process is not sensitive to the specific values of the vibrational frequency, amplitude and applied normal stress which are used in any given test.

It is also concluded, based on a simple geometrical argument, that it is impossible to print a bimodal part at the tap density without the presence of layer defects. These defects are identified as local reductions in the frequency of large powder particles between layers. Whether or not these layer defects would result in anisotropic final part properties is unknown, and has to be determined by future research.

Finally, the pressure plate densification approach was shown to improve packing density and homogeneity not only in metal parts but also those printed with alumina powder.

The primary drawback of the modified pressure plate densification approach is its limited area of densification in the powder bed. As discussed earlier, although it is conceivable that the area of the pressure plate can be increased to cover the entire powder prelayer surface, both on the prototype or other, larger 3DP machines, the size and complexity of such a device might become unwieldy. If it is possible to combine the compact size of the horizontally oscillating wedge with the densification performance of the pressure plate, then the entire layer surface can be compacted without the need for a much larger device. A final layer densification mechanism prototype which met these goals was

constructed and a preliminary evaluation was performed. This prototype "shear sled" is described below.

6.3 A Prototype Shear Sled Layer Densification Mechanism

The oscillating wedge concept described in section 6.1 failed to perform adequately because it could not strike a uniform layer thickness. By fixing the vertical height of the wedge, the generation of a uniform layer would be guaranteed. In fixing the height, however, the resultant vertical stress would then become uncontrolled, making this approach fundamentally different from all previous densification concepts. (Note that the fixed height wedge was initially proposed as one of the four possible layer densification mechanisms in chapter 5.) Many new unknowns enter into a fixed-height design, such as how the specific shape of the powder wedge affected the resultant vertical stress levels.

A preliminary evaluation of a fixed-height, horizontally oscillating wedge design (renamed below as the shear sled concept) was performed as the final set of testing in this thesis. It was believed that, based on the previous layer densification results, the shear sled would densify the powder layer in a similar fashion to the pressure plate. In both cases, the powder particles in the layer would be subjected to an oscillatory horizontal shearing motion which should encourage densification. Also in both cases, a confining vertical stress would be present, except that in the case of the shear sled the magnitude of this vertical stress would not be known.

A single shear sled geometry was evaluated, and only the horizontal shear frequency and amplitude were measured. As a further simplification of the layer generation apparatus, the spreader rod was no longer used to strike the extra-thick prelayer prior to densification. Instead, the shear sled was used to both distribute the powder pile and densify the powder layer simultaneously. This testing was intended to be a "proof of concept" for the shear sled design. If successful, it would serve as a starting point for future work.

6.3.1 Design of the Prototype Shear Sled

The layer densification mechanism illustrated in figures 6.1-3 was used for the final shear sled tests, with the only modifications being that the vertical position of the sled was

now fixed and the spreader rod was removed. The general technique for layer generation using the shear sled is illustrated in figure 6.18.

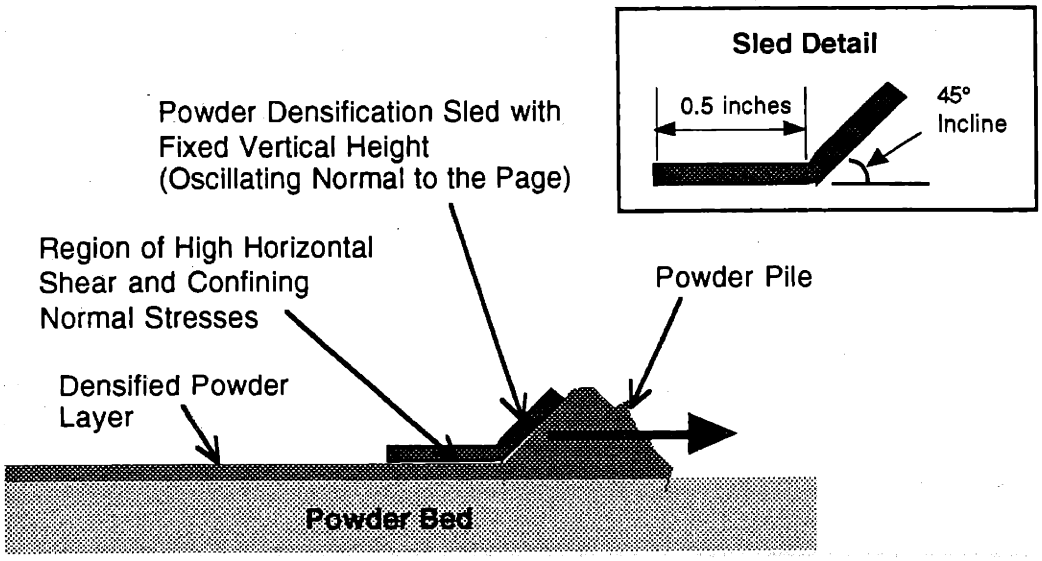

Figure 6.18: Illustration of the prototype shear sled concept.

The complete printing procedure used in conjunction with the shear sled was as follows:

1. Lower the piston one layer thickness (175μm).

2. Manually dispense preheated powder in a pile in front of the sled.

3. Turn on the sled horizontal vibration. Move the sled from the back to the front of the piston at 0.25"/second to generate the densified layer.

4. Lower the piston an additional 250μm.

5. Turn on the steamer bar. Move the slow axis from the front to the back of the piston to activate the powder coating. Slow axis speed for powder coating activation was 0.25"/second. On completion of the pass, turn off the steam.

6. Move the slow axis to a position where the heater bars were over the first line to be printed and pause 30 seconds to allow for removal of condensed steam.

7. Perform printing.

8. Stop the slow axis with the heater bars positioned over the last printed line and pause 30 seconds to allow for removal of residual moisture from the printed binder.

9. Raise the piston 250μm to break any powder wall bonds.

For each printing condition, test bars were printed with a minimum of 12 layers in order to produce a representative microstructure. The smooth surface texture on the bottom of the sled was used for all tests.

6.3.2 Printing Results Using the Prototype Shear Sled

The shear sled mechanism was successful in generating printed bars for several different operating conditions. Monomodal and bimodal metal powders were tested in combination with different sled vibrational frequencies and shearing amplitudes. The results from all the printing runs using the prototype shear sled densification mechanism are given in table 6.4.

Table 6.4: Printing Results Using the Prototype Shear Sled Layer Densification Mechanism.

Powder	Vibrational Frequency (Hz)	Vibrational Amplitude (μm)	Packing Density	Packing COV	Layer Packing Coeff.	Line Packing Coeff.
71/9μm 316L	120	200	76.8%	1.40%	3.38%	2.08%
printed region	320	20	74.4%	1.52%	6.21%	3.21%
unprinted region	320	20	73.7%	1.58%	6.37%	3.24%
66/9μm 420	320	20	73.4%	0.99%	5.29%	3.03%
120/20μm 316L	320	20	70.8%	1.70%	4.86%	4.38%
20μm 316L	320	20	60.6%	0.88%	4.04%	2.88%
30μm alumina	320	20	38.9%	2.23%	7.34%	3.42%

Packing densities using the shear sled were comparable to those produced with the controlled vertical stress pressure plate, with values again nearing or equaling the tap densities of the individual powders. Cross-sectional micrographs for several different printing conditions are shown in figures 6.19-22.

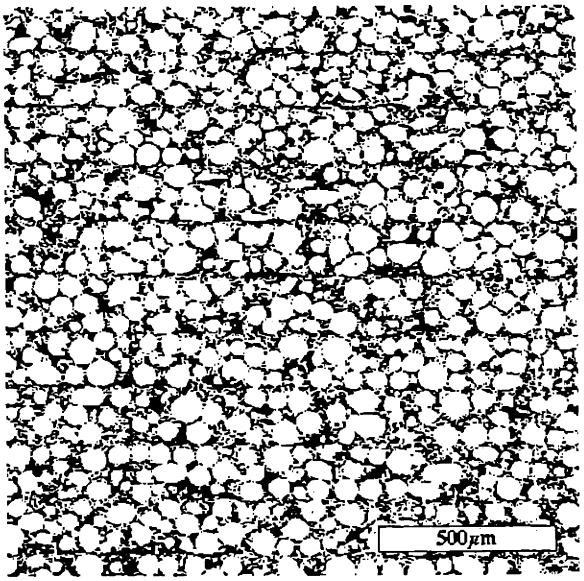

Figures 6.19: Microstructure from a bar printed with the 71/9μm 316L powder. 120Hz excitation and 200μm amplitude. Magnification 50x.

After the printing of bars using the 71/9μm 316L powder and a 320Hz / 20μm sled vibration condition, both a printed region and an adjacent "unprinted" region of the powder bed were analyzed. The goal of this test was to determine if the printing process was significantly altering the powder bed microstructure of each layer after densification with the shear sled had been performed. The results of this test are also given in table 6.4, and representative microstructures from both the printed and unprinted regions are shown in figures 6.20-21. Analysis of the adjacent regions revealed no significant differences in the powder bed microstructures. Based on this result, it was concluded that little or no powder rearrangement occurred due to impact and absorption of the binder stream into the densified and locked powder layer.

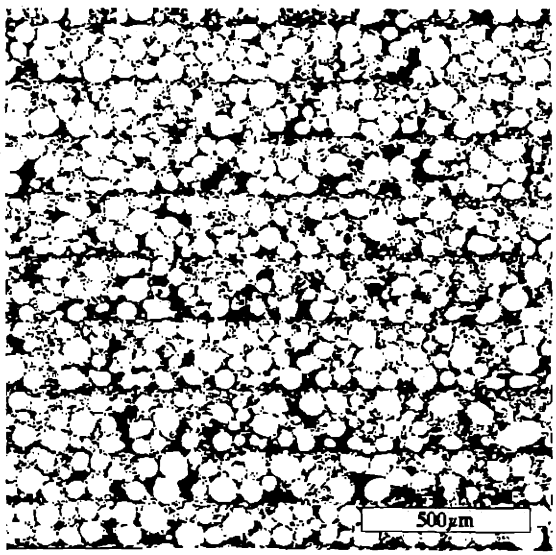

Printed Region

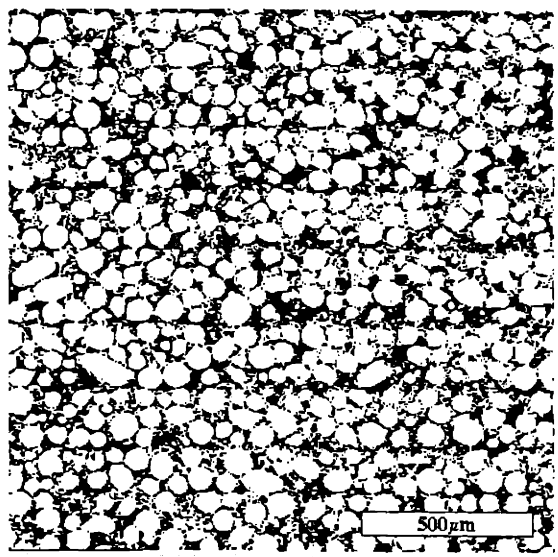

Unprinted Region

Figures 6.20 and 6.21: Microstructures from adjacent printed and unprinted regions. 71/9µm 316L powder. 320Hz excitation and 20µm amplitude. Magnification 50x.

The shear sled was also tested with the 30µm platelet alumina to complete its evaluation. As before, Acrysol binder was used and the alumina powder was chemically locked before the printing of each layer. A representative microstructure from an alumina bar is shown in figure 6.22. As in the case of printing with the pressure plate, no inter-layer macro-voids were present, although there was a slight drop in the printed density.

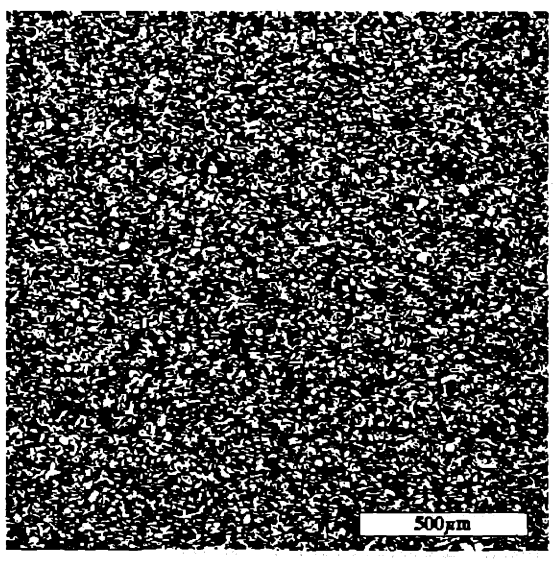

Figures 6.22: Microstructure from a bar printed with the 30µm platelet alumina powder. 320Hz excitation and 20µm amplitude. Magnification 50x.

Packing density and homogeneity results for the baseline, pressure plate, shear sled and control samples are summarized in figures 6.23-25 below. Data for the 120/20μm, 71/9μm and 20μm 316L powders is presented. Similar to the printing results with the pressure plate densification approach, the packing density values for the bars printed with the shear sled approached (and in the case of the 71/9μm powder slightly exceeded) the "ideal" control sample values.

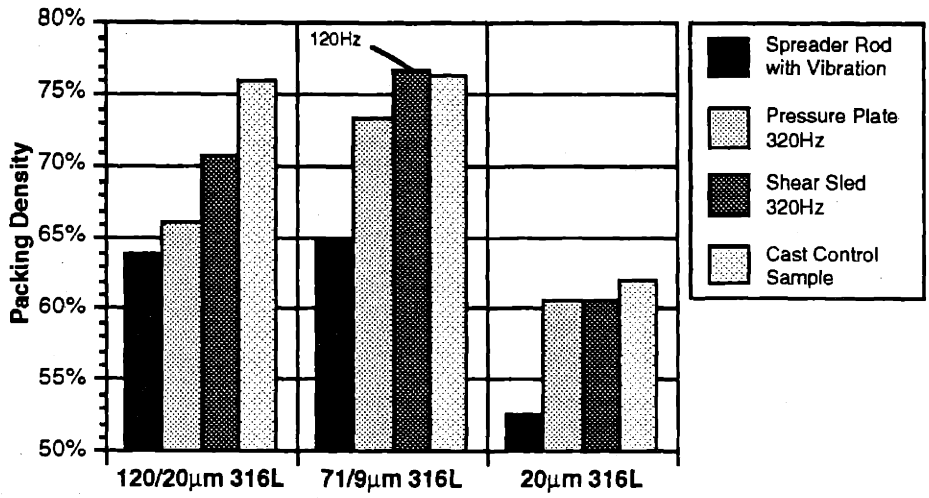

Figure 6.23: Comparison of the packing density values for the baseline, pressure plate, shear sled and control samples.

Packing homogeneity results are shown in figures 6.24-25. Compared with the pressure plate results, the use of the shear sled improved the packing uniformity and homogeneity of the printed bars, especially in the case of the 20μm monomodal powder.

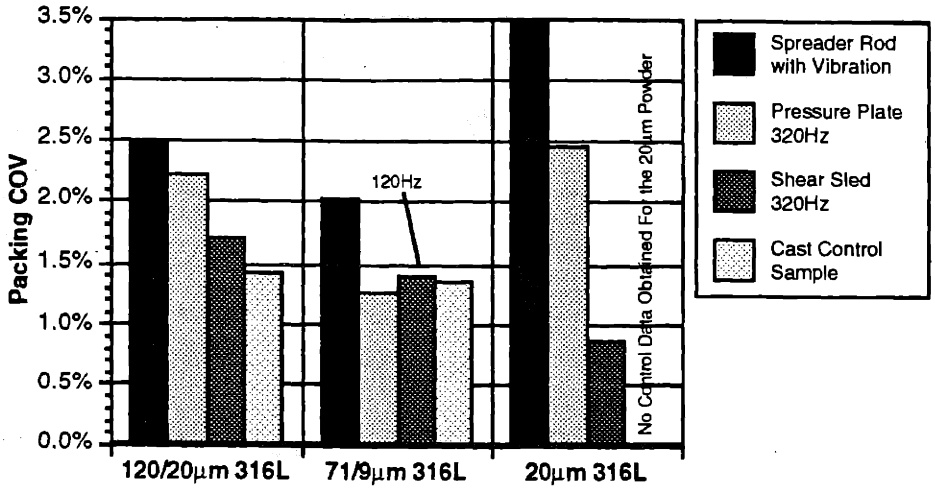

Figure 6.24: Comparison of the packing COV values for the baseline, pressure plate, shear sled and control samples.

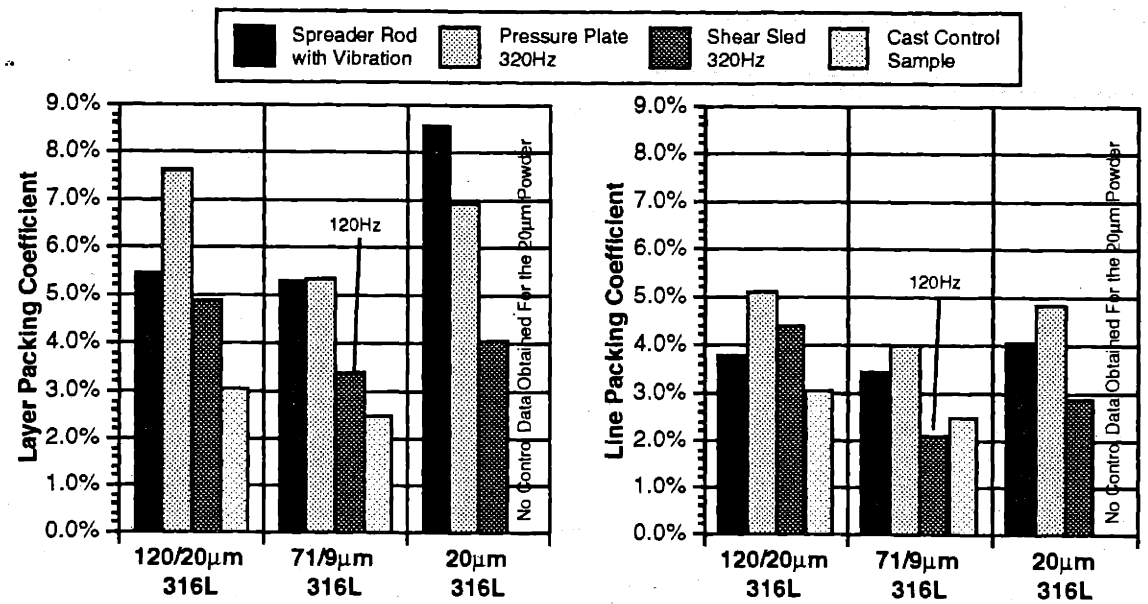

Figure 6.25: Comparison of the layer and line packing coefficient values for the baseline, pressure plate, shear sled and control samples.

6.3.3 Impact of the Shear Sled on Delicate Part Features

A concern with the shear sled design was than the stresses generated in the underlying printed regions during the layer creation and densification operations might be sufficient to damage or distort the partially printed areas. To investigate this possibility, "delicate part" test bars with the cross-section shown in figure 6.26 were printed using the

71/9μm powder. The bars were oriented in the powder bed as shown in figure 6.27. The bar design shown in figure 6.26 consisted of a rectangular base region, with three vertical strips of different thicknesses attached. If the shear forces generated in the powder bed by the shear sled were indeed excessive, then it was expected that some or all of these vertical strips would be distorted or sheared off at some point during the printing process.

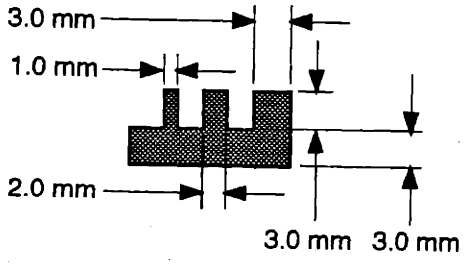

Figure 6.26: Cross-section of the delicate part test bar.

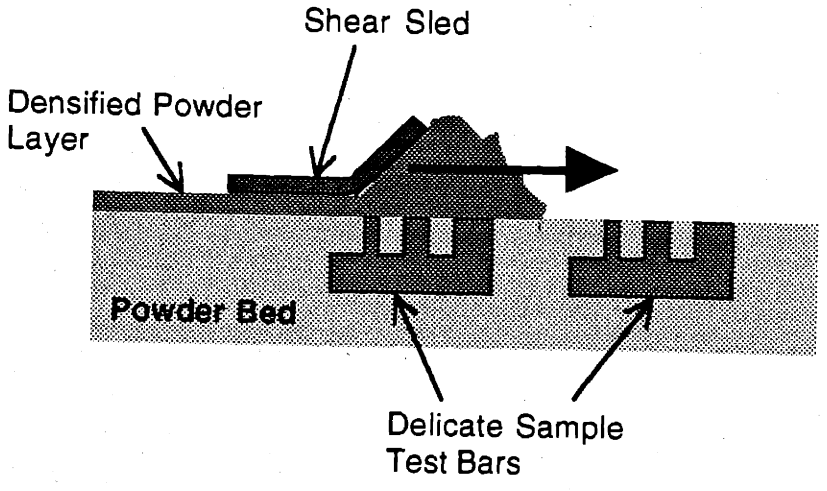

Figure 6.27: Orientation of the delicate part test bars in the powder bed during layer creation using the shear sled.

Results from the delicate part tests indicated that no damage or distortion occurred to the test bars during printing. In considering this result, however, it is certainly the case that the chemical powder locking used throughout the bed had some impact on the deformation resistance of both the printed and unprinted regions. Material systems which do not require or utilize powder locking during printing may still be susceptible to shear damage induced by the shear sled.

6.3.4 Discussion

Printing test results using a prototype shear sled design indicated that this concept had excellent potential for producing high green density printed parts, both with metal and ceramic powder systems. The ability of the shear sled to produce more densely packed layers compared to the spreader rod was believed to result from the manner in which the sled design separated the functions of powder pile distribution, densification, and layer height definition during layer generation process. This concept is illustrated in figure 6.28.

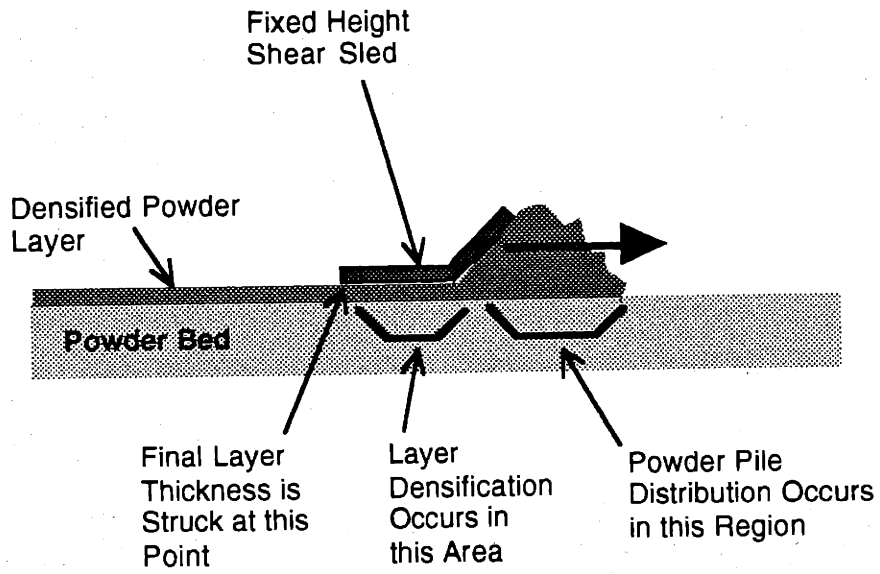

Figure 6.28: Illustration of why the shear sled was successful in producing densely packed layers.

In the earlier analysis of why the incremental pressure plate densification process was ineffective in producing densely packed parts, it was concluded that the final spreader rod pass which was used to smooth the powder layer was also causing dilation of the compacted powder. (Refer to figure 6.7) In this case, as the spreader rod moved excess powder over the densified surface, shear stresses transmitted to the powder caused layer dilation in front of the spreader rod. In the original baseline case in which a vibrating spreader rod was used to generate the powder layer, it was similarly the case that a condition of powder dilation (or lack of densification) existed in the region in front of the moving spreader. Only in the small strip of powder directly beneath the spreader rod did a

confining normal stress condition exist. The time duration for which this strip of powder was exposed to densification was insufficient to fully compact the powder.

In the shear sled design, a similar region of unconfined shear stress existed in front of the sled as the powder pile was distributed. This region was separated, however, from the back edge of the sled where the final layer thickness was struck. In between these two regions was an extended area over which any strip of powder received a full two seconds of vibratory shear excitation. It was concluded that the ability of the shear sled to fully densify the powder layer was related to this unique separation of pile distribution, densification and layer height definition functions.

This conceptual model of how the shear sled operates is certainly a simplification of the actual densification processes which were occurring beneath the sled. Knowledge of the stress distributions throughout the regions of powder compaction, and particularly at the pinch point region in front of the sled, would aid in creating a more complete model of the densification process.

Chapter 7. Conclusions and Recommendations for Future Work

7.0 Overall Conclusions

The central goal of this research, which was to produce a printed metal part with a green density between 75 - 80%, was reached. The use of bimodal powder mixtures was critical in reaching this goal. The increased green density should have a profound effect on the properties of the fully post-processed parts, moving them that much closer to those required by the industrial users of injection molding tooling.

A complete printing process, in addition to a new spreader apparatus, was developed. Process improvements were made to the layer drying, powder coating activation, powder preparation and recycling procedures. Some processes were partially automated in order to produce more consistent results. Because of the additional steps in the new printing process, however, the overall printing rate was lowered. Further optimization of the printing process is possible, and several suggestions are provided below.

Photographic analysis techniques were developed which could quantitatively measure local packing variation in the 3D printed parts. Local compositional variation could also be measured in parts printed with bimodal powder mixtures. These techniques allowed for a more rigorous comparison of the printed part microstructures than was previously possible, and also acted as an indicator for which printing process variations were indeed producing better parts.

Using a baseline printing process in which the original spreader rod was used to strike each powder layer, monomodal and bimodal printed parts were produced to serve as a benchmark for future comparison. These parts were found to have green densities far below the tap densities of the powders used, indicating that the spreader rod was far from an ideal layer densification mechanism. Parts which contained fine powder components below 20μm were found to exhibit significant packing defects across the printed layers.

The densification behavior of monomodal and bimodal powders was studied using modified versions of standard test equipment from the fields of soil and powder mechanics. These tests provided new insights into powder packing behavior over what might be considered a "very low stress" range of test inputs. The direction in which vibrational

energy was applied with respect to the shear plane was found to be the single most important factor for influencing densification behavior. Based on the results from these tests, a preliminary design for a new layer densification mechanism was selected.

A new layer densification mechanism was developed which improved part green density and packing uniformity not only in metal, but also ceramic parts. This mechanism provided a horizontal oscillatory shear stress in combination with a confining normal stress in order to achieve layer packing levels near the tap density. The mechanism also supplied vibrational energy for a sufficient time to ensure that the maximum packing level was reached. Printing tests revealed that it was possible, however, to undo the effects of a densification mechanism and cause dilation of the powder layer by the unintentional application of unconstrained shear stresses. Any future design modifications to the layer densification apparatus should take into account the possibility for this dilation effect.

Improvements in part packing uniformity and homogeneity were obtained, in both monomodal and bimodal parts. The large layer defects present in parts printed with fine, monomodal powders were eliminated in both the metal and ceramic material systems.

A important discovery was made about the connection between the use of bimodal powders and the presence of packing irregularities across the spread layers. The generation of individual bimodal layers at or near the tap density by default guarantees that a certain degree of inhomogeneity will exist, because large powder particles are excluded from the inter-layer zone. There appears to be no solution for this effect.

Finally, an analysis of adjacent printed and unprinted regions revealed no significant differences in the packing microstructure. This result indicates that the printing process itself, in which the binder stream impacts the powder surface and subsequently wicks in, is not causing significant rearrangement of the powder particles in the layer. It is likely that the use of powder locking techniques, which create chemical bonds between the individual particles prior to layer printing, restricts the rearrangement of particles which would otherwise occur due to ballistic impact and capillary forces. Also, the presence of dried binder in the printed regions during the spreading of the next layer does not appear to alter the packing behavior of the powder particles.

7.1 The Current Understanding of Vibrational Densification Processes

An additional goal of this research was to further the understanding of why vibrational energy was effective in densifying powders, and how it could be most effectively utilized to produce highly packed powder layers in the 3DP process. The literature on vibrational densification presented a long list of parameters which had been observed to influence the densification process, and more than one author concluded that only empirical investigation of a specific application could reveal which densification parameters were critical, and how the individual parameters affected the ultimate level of densification. The formulation of a quantitative model of vibrational densification processes, which took as input parameters variables such as powder size and layer thickness, and produced as output parameters variables such as optimum vibrational frequency and amplitude, would have been ideal. Because of the extremely complex nature of vibrational densification processes, however, such a model was not possible to create.

It was shown, based on the results of speed of sound tests, that describing the powder layer with a lumped parameter model was not appropriate, because the stiffness of the powder layer was too high. No optimum resonance frequency at which to perform densification could therefore be determined.

Powder stress / strain / packing relationships such as the Jenike yield locus theory helped to explain why certain forms of vibrational densification worked better than others. The yield locus theory related the normal and shear forces which were present along any plane in a powder mass with the stability of the powder mass, and the tendency of the powder mass to either dilate or densify during failure. A qualitative, conceptual explanation was given for why the application of an in-plane oscillatory shear stress, in combination with a small confining normal stress, achieved the best densification results. In this situation, particle interlocking was minimized because the applied static stresses were low. The vibratory excitation which was applied helped to further reduce interlocking, and enhanced particle mobility within the layer. Although certain trends were observed between vibrational parameters such as frequency and amplitude and the ultimate packing which a powder layer obtained, no specific relationship was determined. It was observed that most densification took place in the first two seconds of vibrational excitation, and that only moderately low applied stress levels were required to obtain near complete densification. This information was valuable, since it was likely that the

application of large stress levels to the new layer surface would damage the previously printed regions below. Finally, maps of powder packing density changes which occurred in the powder regions beneath a pressure plate apparatus indicated that significant densification was present at distances of 2mm from the plate. Also, densification increases in all regions beneath the plate started simultaneously with the application of vibrational excitation, rather than propagating outward over time.

7.2 Using Bimodal Powders to Increase Spread Layer Density

The bimodal powders which were used in this study performed as anticipated in raising the maximum green density of the printed parts. The bimodal blends were definitely more difficult to work with, however, than monomodal powders. Although the bimodal powders tested did not segregate in use on the prototype 3DP machine, they nevertheless needed to be carefully and deliberately handled to eliminate the potential for segregation. New methods of automatic powder dispensing, which do not depend on gravitational freefall for powder transport, will have to be developed prior to using bimodal powders in a production setting.

The size ratio of the large and small particles in the bimodal blend was found to be a critical parameter, with a balance needing to be struck between mixture fluidity, maximum particle size (minimum feature size), and maximum packing density. Ideally, a size ratio greater than 10:1 would be used to obtain the maximum packing density benefits, but this ratio was not attainable in practice. Powders finer than approximately 10μm are expensive and difficult to obtain. These fine powders have very poor fluidity, which transfers over to any bimodal blend of which they are a significant component. Powders larger than 100μm are typically not acceptable, because of the impact on minimum feature size.

7.3 Microstructural Characterization Using Photographic Analysis Techniques

New photographic analysis techniques were developed which could quantitatively measure average packing density, local packing density and variation, and local composition in a printed part. The average packing density measurement was certainly of great value throughout this research, primarily because the very small size of the dozens of different test bars which were produced would have made green density measurement by other available techniques too inaccurate. Similarly, the local compositional measurement

capability has been and will continue to be of value in determining if powder segregation is occurring during the printing process.

The photographic analysis technique did present certain challenges in use. In order for results to be comparable, all analyzed photos needed to be of the same magnification. Because of the diversity of powders which are typically evaluated with the 3DP process, it is doubtful that a single magnification setting would be effective in all instances. A single microstructure could be analyzed at several different magnifications, but this would become a very labor intensive process. A fully automated image acquisition system, with a SEM microscope equipped with a computer controlled X - Y table and automatic data acquisition, would have greatly sped up the analysis process. Finally, regular calibration of the analysis process was absolutely essential for producing analysis results that were comparable over time.

Another concern about the photographic analysis technique was that it operated on a single cross-section from a printed part, and therefore assumed that the cross-sectional microstructure being analyzed was representative of the rest of the part. Multiple sections from each part would have been preferred, but again this would have significantly increased the time for analysis of a single part.

Finally, it is still the case that the most accurate and reliable approach for measuring the average green density is to print large bars, perhaps 1.0" x 1.0" x 6.0", and then determine the green density by direct measurement of bar mass and volume. This measurement approach will become more readily available as the new metals printing techniques are transferred to the Alpha or other large 3DP machines.

7.4 Recommendations for Future Work

At the conclusion of this research, several areas of study were identified as ideal starting points for the continued improvement of high green density metals printing procedures. These areas of study are presented below.

7.4.1 Printing Process Development

The development of new binder systems is critical to expanding the capabilities of the metals printing process. The current Acrysol binder exhibits good thermal

decomposition behavior during debinding, but has rather poor strength compared to other polymers. The glass transition temperature for the cured polymer is very low (approximately 30°C), which allows large parts to experience significant visco-elastic creep due to gravitational forces. Also, the cured binder is not water resistant, which eliminates the possibility of removing chemically locked powder which surrounds a printed part by submerging the powder mass. (Recall that the chemical locking agent is a highly soluble metal salt, and therefore the salt bonds would dissolve almost instantaneously after immersion in water.) Any new binder still needs to contain a volatile component, preferably water, so that after drying the printed part contains a continuous network of open porosity. Recently introduced water-based epoxies might meet all the above requirements.

The techniques used to provide cohesion to the powder surface by chemical locking can be improved in several ways. First, the minimum quantity of metal salt necessary to achieve sufficient surface cohesion should be more precisely determined. For the tests presented in this thesis, all the powders were treated with 0.05g of boric acid per 100g of metal powder. This quantity of coating was more than what was needed to provide resistance to particle rearrangement and ballistic ejection. Using the least amount of locking agent necessary will be of benefit later during removal of the part from the powder bed. Also, it is likely the case that different powders will require different amounts of metal salt to achieve sufficient locking, since the specific surface areas of the powders will be different.

The bars printed in this research were freed from the locked powder bed by removing the adjacent locked regions with a stiff bristle brush. This approach worked well for simple, rectangular geometries, but will become less effective as part complexity increases. As mentioned above, an ideal way for cleaning the printed part is by washing it in water, but this will require the development of new water-resistant binders. More study about locked powder removal is therefore required.

A final modification to the printing process involves improvement of the layer drying equipment in order to reduce overall cycle time. The current heater bar assembly relies on heat transfer by natural convection. The overall heat transfer rate to the powder surface can be increased by using low velocity forced hot air directed from a conduit similar in construction to the steamer bar. Air velocity and temperature should be controlled to prevent powder blowing and overheating. An alternate approach would be the use of infra-

red heat lamps, which would dry the bed with radiative heat transfer. A concern with the use of heat lamps, however, is that the radiative energy can be more difficult to direct in confined spaces compared with forced hot air from a simple conduit, with the possible danger of inadvertently heating and damaging delicate components of the 3DP apparatus such as the printhead.

7.4.2 Optimization of Bimodal Powder Mixtures

All the bimodal powders used in this research were blends of 73.5% large component and 26.5% small component. This composition was predicted to be the optimum for obtaining maximum packing density based on calculations made for an "ideal" bimodal mixture, in which all particles were one of two discrete sizes and the diameter ratio was infinite. For the actual powders used in the 3DP process, this composition may not be the best for obtaining the highest green density. Experimental work should be performed to find the optimal bimodal composition for a given powder.

Further experimental work should also be performed to determine the smallest sized powders which can effectively be used for printing metal parts. For this study, the 71/9μm 316L and 66/9μm 420 bimodal blends contained the smallest particles, although it is certainly the case that still smaller powders would be preferred in actual printing practice. A better understanding should be obtained for the balance between maximum green density and minimum feature size.

7.4.3 Characterization of Post-Processed Bimodal Parts

The end product of this study - a high green density printed metal part - is actually only an intermediate point in the entire tool production process. The high green density parts must still go through furnace post-processing in order transform the microstructure to a fully dense condition. Research into the post-processing characteristics of the high green density bimodal parts needs to be performed in order to answer the following questions:

1. How much shrinkage is required prior to infiltration ?

2. What is the shrinkage along each axis ? Is it uniform ?

3. Does the unique layer defect present in bimodal parts cause a problem for dimensional control ?

4. What is the best dimensional accuracy attainable ?

5. What are the material properties of a fully dense, infiltrated part ?

7.4.4 Additional Investigation of Layer Densification Mechanisms

The operation of the prototype shear sled concept presented in the final part of this thesis needs to be better understood before the design can be used in a production environment. A detailed study of shear sled should be performed with measurement of the reaction stresses generated in the vertical and spreading directions by various sled geometries. Using the reaction stress test results as a guide, additional modeling of the densification process over the regions directly in front of and below the sled should be performed. This extended investigation of the shear sled concept should include not only spherical metal powders, but also other powder material systems such as platelet alumina.

A bimodal powder segregation study should be performed on the shear sled in a manner identical to previously performed tests. This will help determine if the new sled design has a greater tendency to segregate powder that the spreader rod.

Finally, the shear sled design can be further refined and simplified compared with the apparatus used in this research. The horizontal linear ball slide should be eliminated from the design, because it significantly added to the total reciprocating mass, and because it was susceptible to contamination from the powder environment. A new shear sled design might instead use steel leaf spring supports to provide vertical rigidity while still allowing the needed amount of horizontal flexibility for the oscillatory shearing motion. This design is illustrated in figure 7.1. Note that the oscillatory driving mechanism for the shear sled is not shown in the illustration.

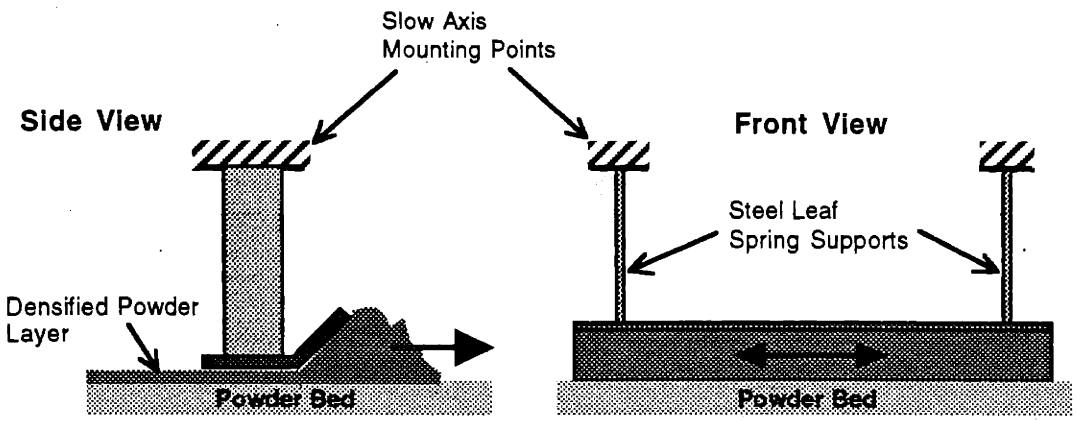

Figure 7.1: Illustration of a simplified shear sled concept.

The following question-and-answer section is offered as an aid in furthering the development of the shear sled concept and as a guide to future research in this area. The information below contains opinions and speculations about the key performance characteristics of the shear sled design.

Question: How important is the shape of the shear sled as described above, and how might changes in this initial shape affect densification performance ?

Answer: The cross-sectional shape and dimensions of the prototype shear sled were really a first guess at what might work. The forward-facing, angled portion of the sled was necessary for pushing excess powder in the pile along during spreading, and for directing the powder to the pinch-point where the layer thickness was initially struck. It is almost certainly the case that the angle of attack of the front wedge portion of the sled, in addition to its length, will affect the resultant shear and normal forces which are generated. The exact description of this relationship, however, is unknown, and will need to be determined experimentally. Hopefully, it will be the case that after experimental reaction force measurements are made using different powders and various sled shapes, a mathematical expression can be proposed which indicates the most appropriate shape for a given type of powder. From the powder densification tests we already know that a certain minimal amount of normal and shear stress is required to achieve densification for any given powder, but it also the case that an excess of applied stress will damage the underlying printed regions.

Question: Will the shear sled design have the same difficulties as the counter-rotating spreader rod in creating layers from very fine powders which have poor fluidity ?

Answer: In general, when sticky, non-flowable powders were used with the spreader rod, is was observed that the powder pile was simply pushed along in front of the rod, with very little powder going under the rod to form the new layer. In some initial work performed using the shear sled to spread 9μm monomodal powders, the sled appeared to be more capable of generating smooth, uniform layers than the spreader rod, although it still had some difficulties. It may be the case that both the spreader rod and shear sled would have improved results with fine powders if they were only used to strike the final thickness of an extra-thick prelayer which was laid down by some other means. For example, the fine powder could be deposited into a prelayer by sieving it from a wire screen onto the previous layer.

Question: What range of excitation frequencies should be investigated ?

Answer: This research focused on excitation frequencies up to about 500Hz. The single biggest factor which prevented the use of higher frequencies was the high force levels required to oscillate the mass of the pressure plate assembly, since these forces scaled as the square of the excitation frequency. Based on the results of the frequencies used, however, it seems likely that higher frequencies would not be necessary, since excellent densification results were obtained over this range.

Question: What surface textures should be used on the bottom surface of the shear sled ?

Answer: Although it was observed that laminating abrasive paper to the bottom of the pressure plate was a means of increasing the shear stresses transmitted to the powder layer and thereby increasing packing density, transferring this approach to the shear sled is not recommended. The central difficulty in using roughened plate textures is that powder particles tend to adhere to or become wedged in the plate surface. This resulted in dilation of the compacted areas in some of the pressure plate tests, and would likely prevent the striking of a smooth powder surface if incorporated into the shear sled design.

Question: Will there be variations in packing density from the front to the back of the layer due to the reduction in powder pile size in front of the sled as the layer is spread ?

Answer: Possibly. The creation of a powder bed with gradient properties along the direction of spreading has always been a possibility, since the spreader rod creating each layer is forced to operate on a powder pile which is continuously decreasing in size during the layer spread. Tests performed in the baseline analysis section of this research gave a preliminary indication that packing density gradient creation was not a problem using the spreader rod. The possibility of generating irregular layer properties also exists for the shear sled design, and may be even more of a danger since the resultant stress levels generated by the sled at any moment in time may be a function of the size of the powder pile in front of it. Again, a better understanding of how sled shape and powder pile size interact to create the normal and shear stresses used to densify the layer will help in predicting if gradient powder bed properties are likely to occur. Of course, direct measurement of packing density along the direction of spreading is the most definite method of determining the presence or absence of packing density gradients.

Question: Would it be preferable to spread a low-density, extra-thick prelayer with the spreader rod, with an appropriate thickness such that the shear sled completely densified the prelayer with none of the powder being scraped away ?

Answer: If such an approach could be accomplished, then concerns about producing gradient structures across the powder bed would be greatly reduced, since the shear sled would not be acting on a powder pile which was changing in size during layer densification. Experience has shown, however, that the exact "metering" of a prelayer with just the right amount of powder to create a densified final layer with the shear sled is rather difficult. Operating the shear sled in a mode in which there is always a surplus of powder in front of the sled compared to the amount required for completion of the densified layer eliminates the possibility of running out of powder before the densified layer is completed.

7.5 Closing Remarks

Powder mechanics is a challenging research area because no two powders react to a given set of conditions in the same way. In fact, a single powder can behave in a variety of different ways, based on subtle changes in variables such as room humidity or degree of agglomeration. Powder behavior is also *highly* influenced by the different levels of packing density throughout the powder mass, which makes modeling of stress transmission and densification processes extremely difficult. As a crude analogy, imagine the complexity of solving a viscous flow problem in fluid mechanics in which the viscosity

of the fluid was highly non-uniform throughout the volume of interest, and was also changing over time ! Because of this complexity, the modeling and understanding of the densification behavior of dry powders is still predominantly qualitative in nature. Nevertheless, the use of a basic conceptual model of densification processes was successful in guiding the design for a new layer densification mechanism.

The 3D printing process has the potential to produce metal tooling with properties and capabilities which cannot be duplicated with conventional manufacturing techniques. Tools with conformal coolant channels, functionally gradient microstructures, user-defined surface textures and extremely complex geometries are all possible. To attain these capabilities, all aspects of the printing and post-processing of metal parts will need continued improvement. The accomplishments of this work represent a single step towards the goal of making 3DP an industrially competitive tool manufacturing process.

Appendix A: Metal Powder Data Base

This appendix contains the characterization information for all the monomodal and bimodal powder mixtures used in this research.

120μm 316L Monomodal Powder

Alloy:	316L
Designation:	ANVAL -100/+170
Shape:	Spherical
Apparent Density:	4.65 g/cc (58.8%)
Tap Density:	4.97 g/cc (62.8%)
Pycnometer Density:	7.91 g/cc
Angle of Repose:	27°
Particle Size Ranks	
10% =	88 μm (estimate from 170 mesh sieve)
50% =	N/A
90% =	149 μm (estimate from 100 mesh sieve)
Estimate Average Size:	120 μm
Estimate Size Std. Dev.:	23 μm

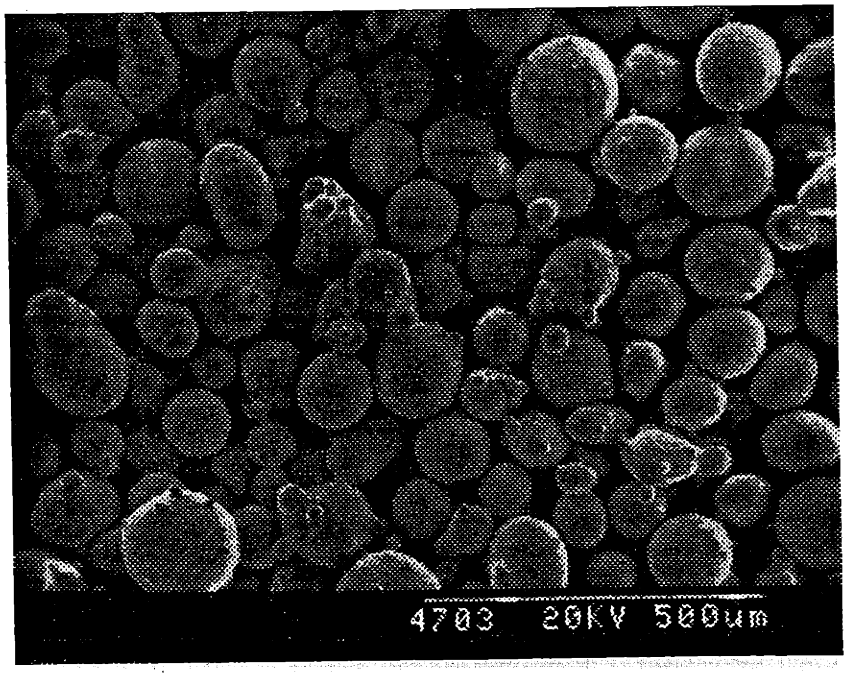

71μm 316L Monomodal Powder

Alloy:	316L
Designation:	ANVAL -170/+270
Shape:	Spherical
Apparent Density:	4.32 g/cc (54.6%)
Tap Density:	4.93 g/cc (62.3%)
Pycnometer Density:	7.91 g/cc
Angle of Repose:	26°

Particle Size Ranks

10% =	53 μm (estimate from 270 mesh sieve)
50% =	N/A
90% =	88 μm (estimate from 170 mesh sieve)

Estimate Average Size:	71 μm
Estimate Size Std. Dev.:	13 μm

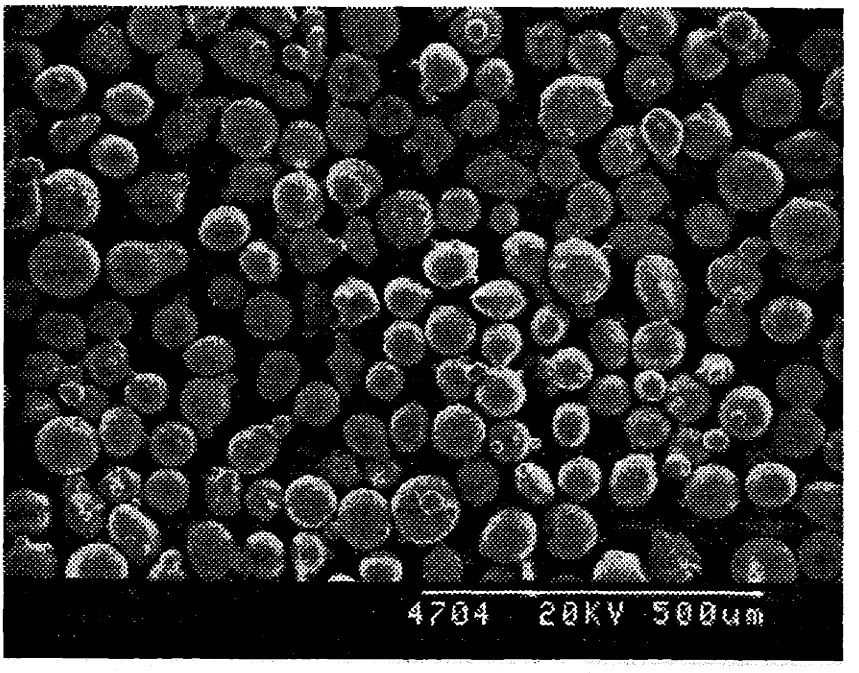

66μm 420 Monomodal Powder

Alloy:	420
Designation:	ANVAL -170/+325
Shape:	Spherical
Apparent Density:	4.32 g/cc (54.6%)
Tap Density:	4.93 g/cc (62.3%)
Pycnometer Density:	7.8 g/cc
Angle of Repose:	26°

Particle Size Ranks

10% =	44 μm (estimate from 325 mesh sieve)
50% =	N/A
90% =	88 μm (estimate from 170 mesh sieve)

Estimate Average Size:	66 μm
Estimate Size Std. Dev.:	

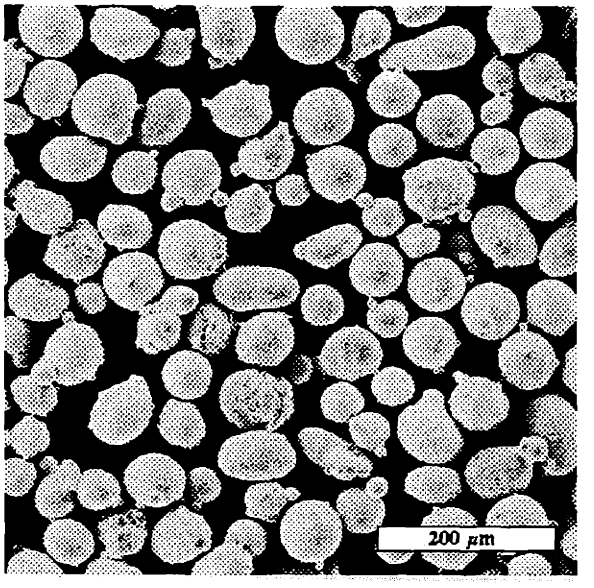

20μm 316L Monomodal Powder

Alloy:	316L
Designation:	Ultrafine Powder Technology (UFP) 15-30 Micron
Shape:	Spherical
Apparent Density:	4.16 g/cc (52.6%)
Tap Density:	4.91 g/cc (62.1%)
Pycnometer Density:	7.91 g/cc
Angle of Repose:	28°

Particle Size Ranks

10% =	10.58 μm
50% =	19.1 μm
90% =	30.85 μm

Estimate Average Size:	19.1 μm
Estimate Size Std. Dev.:	7.9 μm

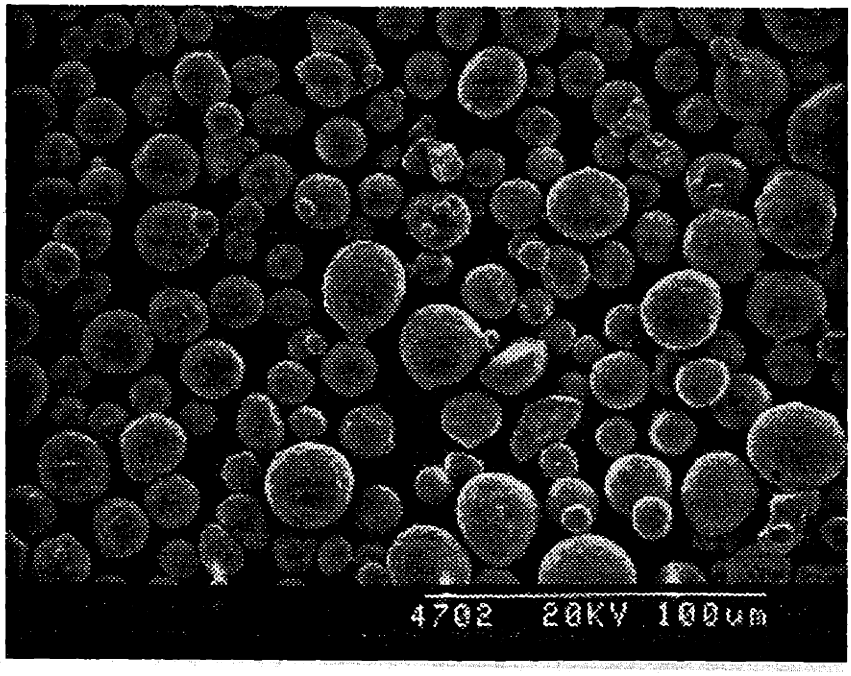

9μm 316L Monomodal Powder

Alloy:	316L
Designation:	Ultrafine Powder Technology (UFP) -15 Micron
Shape:	Spherical
Apparent Density:	3.35 g/cc (42.4%)
Tap Density:	4.28 g/cc (54.2%)
Pycnometer Density:	7.91 g/cc
Angle of Repose:	51°

Particle Size Ranks

10% =	4.05 μm
50% =	9.20 μm
90% =	15.79 μm

Estimate Average Size:	9.20 μm
Estimate Size Std. Dev.:	4.6 μm

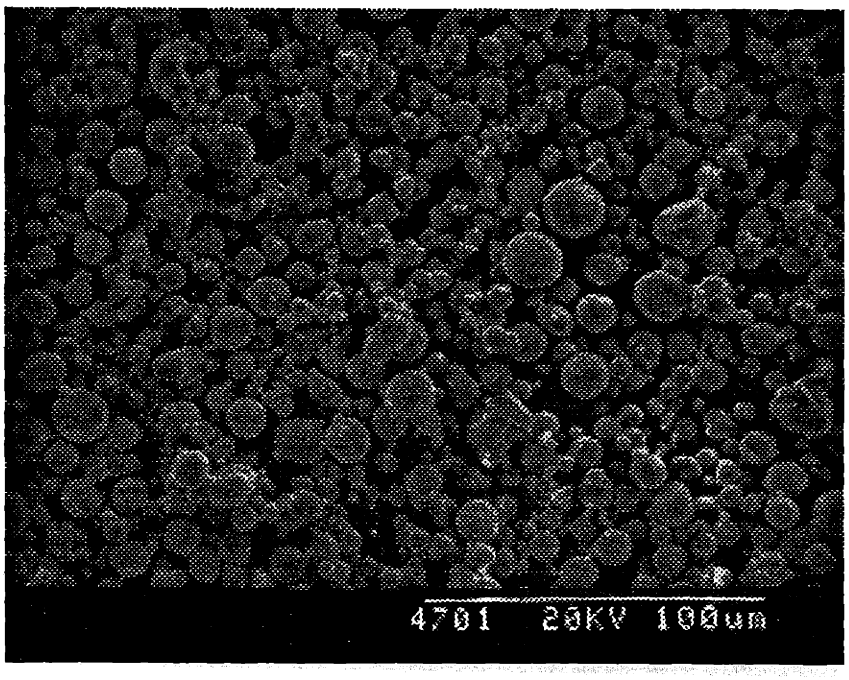

9μm 420 Monomodal Powder

Alloy:	420
Designation:	Ultrafine Powder Technology (UFP) -15 Micron
Shape:	Spherical
Apparent Density:	3.52 g/cc (45.1%)
Tap Density:	4.67 g/cc (59.9%)
Pycnometer Density:	7.8 g/cc
Angle of Repose:	28.5°

Particle Size Ranks

10% =	N/A
50% =	9 μm
90% =	N/A

Estimate Average Size:	9 μm
Estimate Size Std. Dev.:	

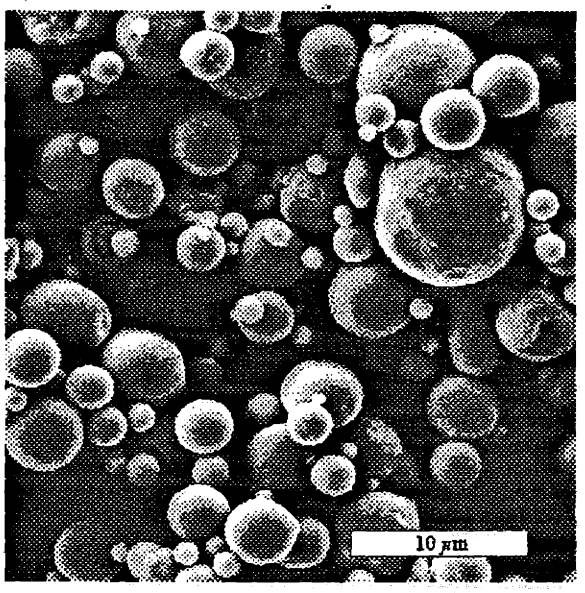

120/20μm 316L Bimodal Powder

Large Particle:		
Alloy:	316L	
Designation:	ANVAL -100/+170 mesh	
Shape:	Spherical	
Average Size:	120 μm	
Small Particle:		
Alloy:	316L	
Designation:	Ultrafine Powder Technology (UFP) 15-30 Micron	
Shape:	Spherical	
Average Size:	19.1 μm	
Composition:	73.5 w/o large	26.5 w/o small
Size Ratio:	6.3	
Apparent Density:	4.79 g/cc (60.5%)	
Stdev. App. Density	0.05 g/cc	
Tap Density:	6.03 g/cc (76.2%)	
Stdey. App. Density	0.01 g/cc	
Angle of Repose:	36°	
Coating Chemistry:	Boric Acid	
Coating Amount:	0.05 g per 100 g powder mixture	

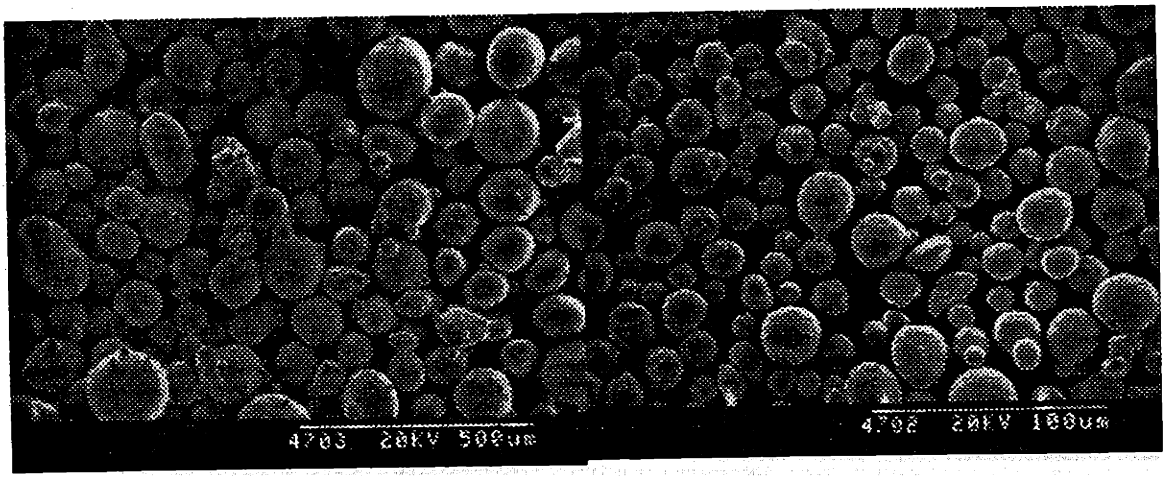

Large Particles

Small Particles

71/9μm 316L Bimodal Powder

Large Particle:	
Alloy:	316L
Designation:	ANVAL -170/+270 mesh
Shape:	Spherical
Average Size:	71μm
Small Particle:	
Alloy:	316L
Designation:	Ultrafine Powder Technology (UFP) -15 Micron
Shape:	Spherical
Average Size:	9.1μm
Composition:	73.5 w/o large 26.5 w/o small
Size Ratio:	7.8
Apparent Density:	4.59 g/cc (58.0%)
Stdev. App. Density	0.06 g/cc
Tap Density:	6.21 g/cc (78.5%)
Stdev. App. Density	0.02 g/cc
Angle of Repose:	45°
Coating Chemistry:	Boric Acid
Coating Amount:	0.05 g per 100 g powder mixture

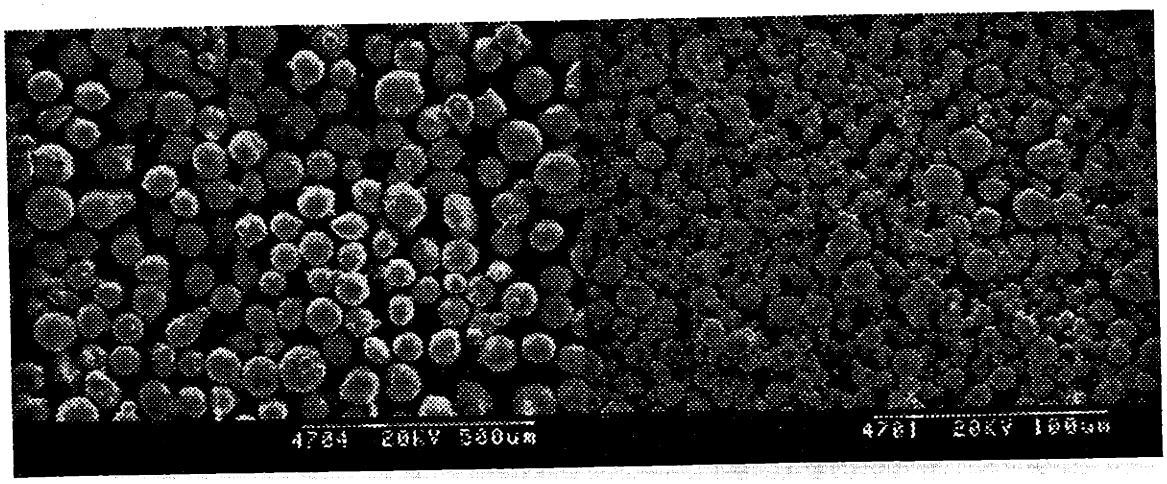

Large Particles Small Particles

66/9μm 420 Bimodal Powder

Large Particle:	
Alloy:	420
Designation:	ANVAL -170/+325 mesh
Shape:	Spherical
Average Size:	66μm
Small Particle:	
Alloy:	420
Designation:	Ultrafine Powder Technology (UFP) -15 Micron
Shape:	Spherical
Average Size:	9.1μm
Composition:	73.5 w/o large 26.5 w/o small
Size Ratio:	7.3
Apparent Density:	5.02 g/cc (64.4%)
Stdev. App. Density	0.07 g/cc
Tap Density:	5.90 g/cc (75.6%)
Stdev. App. Density	0.03 g/cc
Angle of Repose:	38°
Coating Chemistry:	Boric Acid
Coating Amount:	0.05 g per 100 g powder mixture

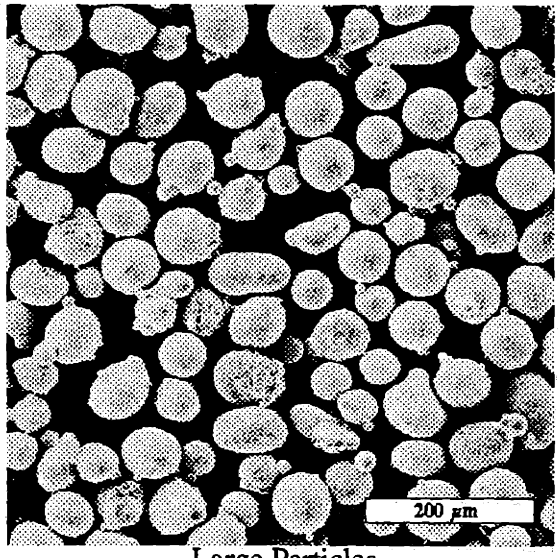

Large Particles

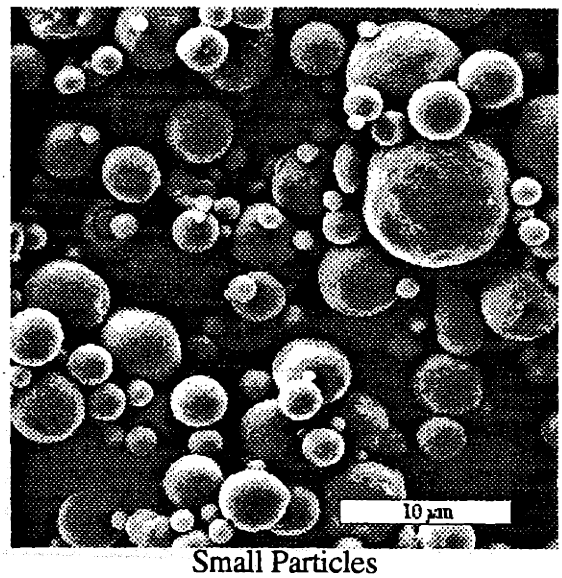

Small Particles

Appendix B: Construction and Use of RAINBOW Piezoelectric Transducers

B.0 Introduction

The vibrational motions and stresses which were used to densify powders in this research needed to be generated via an electromechanical transducer. This would allow convenient adjustment of vibrational frequency and amplitude output from a driving function generator and electrical amplifier. Both the current prototype and Alpha 3D Printing machines generate vibrational energy with a model 102A transducer manufactured by Ling Electronics, Inc. This transducer is pictured in figure B.1. This transducer is essentially the voice coil assembly from a low frequency stereo speaker. Internally, a large permanent magnet provides a stationary magnetic field. A very low mass electrical coil, mounted on a rubber spider, generates an opposing magnetic field when energized with an AC voltage, thereby producing motion. The transducer is non-resonant, and has a claimed operating range of 0 to 12KHz.

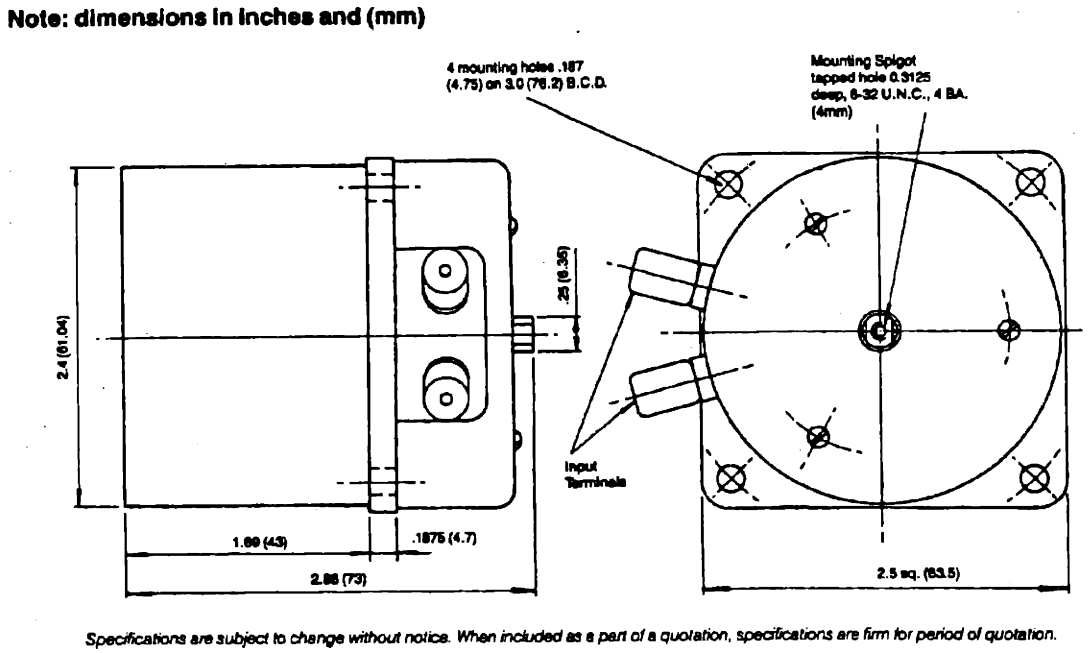

Figure B.1: A Ling Electronics transducer.

The Ling Electronics transducer has several drawbacks which make it less than ideal for use in prototype systems. The transducers are expensive, costing in excess of $300 each. They are large and weigh almost two pounds. This means that sufficiently

strong and rigid support structures must be built around the transducer, even when the load being driven by the transducer is relatively small. Although the electrical inputs can be fused to protect the internal coil from overload, experience has shown that this is not complete protection from coil burnout. Repair of the coil is difficult at best. Finally, transducer output falls off rapidly with increasing frequency.

B.1 Rainbow Piezoceramic Wafers

For these reasons, an alternate transducer for generating vibrational forces was sought. Requirements were low cost, small size and output capabilities to 1000Hz and 10 mils displacement. Piezoceramic wafers are used in a variety of applications to generate high frequency vibrations, but their output amplitudes tend to be very small. Many single wafers can be laminated together to form a piezo "stack" with a larger displacement, but these devices are very expensive and are not intended to be operated a high frequencies. Bimorph piezo transducers can produce larger displacements, but have very low load capacity. A recent piezoceramic invention called Rainbow (for reduced and internally biased oxide wafer) meets all of the requirements listed. The device is a domed circular piezo wafer which tends to flatten when an electrical bias is applied. By applying a bias voltage of 300 to 500 volts, displacements of up to 50 mils can be obtained. A Rainbow wafer is shown in figure B.2.

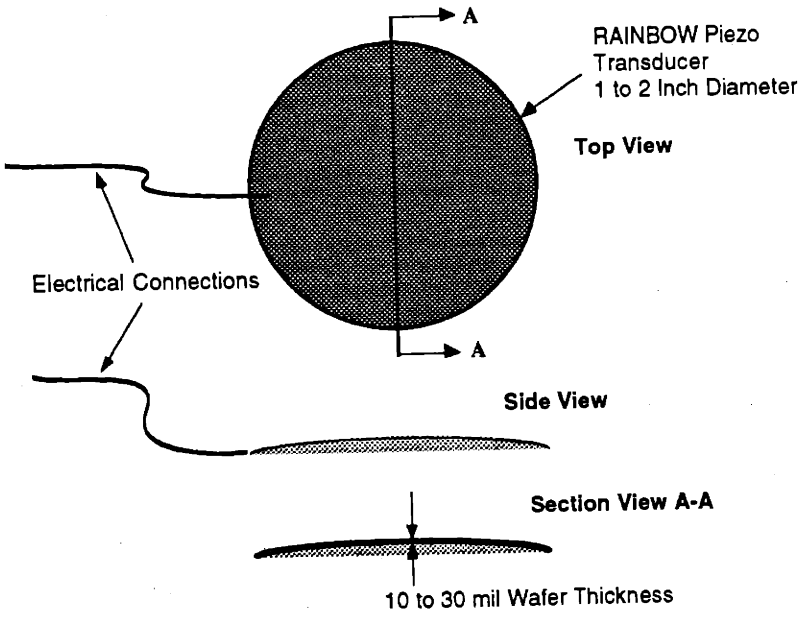

Figure B.2: A Rainbow wafer.

Individual wafers weigh less than 20 grams and cost less than $30 each. Rainbow wafers are available in a variety of diameters (typically 1 to 2 inches) and thicknesses (10 to 30 mils). Output displacement increases with increasing diameter and decreasing thickness. Load carrying capacity increases with decreasing diameter and increasing thickness. Selection of the appropriate diameter and thickness therefore depends on the specific application.

B.2 Construction Techniques for a Rainbow Transducer

As received from the manufacturer, the Rainbow wafers have no mounting points or connections. The wafer must therefore be fabricated into a transducer with additional components. Figure B.3 is an assembly drawing of a transducer constructed from two Rainbow wafers. The individual wafers are 1.25" in diameter with a 15 or 30 mil wall thickness. The wafers are laminated together by a RTV rubber bond. The rubber bond is compliant and can flex as the wafers flatten or bow. Note that the use of two rainbow wafers effectively doubles the displacement output of the transducer. (Aura Ceramics Inc., the manufacturer of the Rainbow wafers, claims that displacements of up to 0.2" can be obtained by stacking 4 transducers, each constructed of 2 piezo wafers, together.)

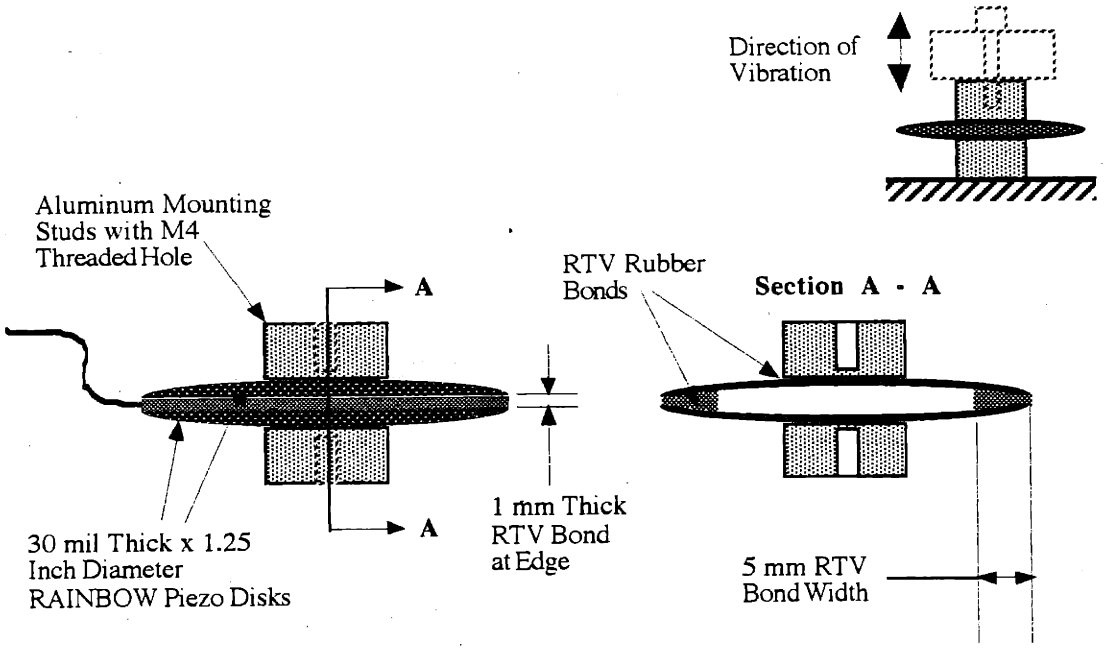

Figure B.3: A Rainbow transducer assembly.

Threaded aluminum studs are adhered to the top and bottom of the dual wafer assembly to serve as mounting points. RTV rubber adhesive is again used, since the adhesive joint must be able to deform slightly as the wafers bend. The aluminum studs which were used to construct the transducers were actually SEM microscope sample mounts, thereby eliminating the need for custom fabrication of multiple pieces.

B.2.1 Transducer Fabrication Procedure

The following procedure was used to fabricate the Rainbow transducer assemblies used in this research. Figure B.4 illustrates the key steps.

Step 1) A bead of RTV adhesive (GE Red RTV 106 Silicone rubber adhesive sealant) approximately 3mm thick is applied to the concave side of the first wafer, along the edge. Dispensing the RTV with a small 3cc syringe gives the best control of adhesive bead placement.

Step 2) Cut three pieces of 1.0mm diameter stainless tubing approximately 1 inch in length. Apply an extremely thin coating of silicone grease to the outside of the tubing, and place them onto the first wafer in a radial pattern, as shown in figure B.4. These tubes will act as spacers when the second wafer is applied. The grease coating will allow for easy removal of the tubes once the RTV rubber has dried. Finally, when the tubes are later removed, they will leave three small passages through which air can pass from the outside to the inner cavity between the wafers. Without these passages, the trapped air between the wafers would act as a spring, partially inhibiting wafer motion.

Step 3) The second wafer is positioned onto the RTV bead with its concave side facing the first wafer. Note that the electrical wires from each wafer are offset by about 45°, since clearance between the wafers is smaller at the wire connections. Slight pressure is applied by hand to squeeze the excess RTV out of the joint and seat both wafers against the stainless tubing. The excess RTV can be easily scraped away while it is still liquid, or it can be cut away after curing.

Step 4) After the RTV bond is cured, the stainless tubes are removed. Two aluminum studs are attached to the top and bottom wafers with a thin layer of RTV

adhesive. Since the top and bottom surfaces of the wafers are slightly curved, precise alignment of the two studs so that their mounting surfaces are parallel and their central axes are aligned may require external fixturing.

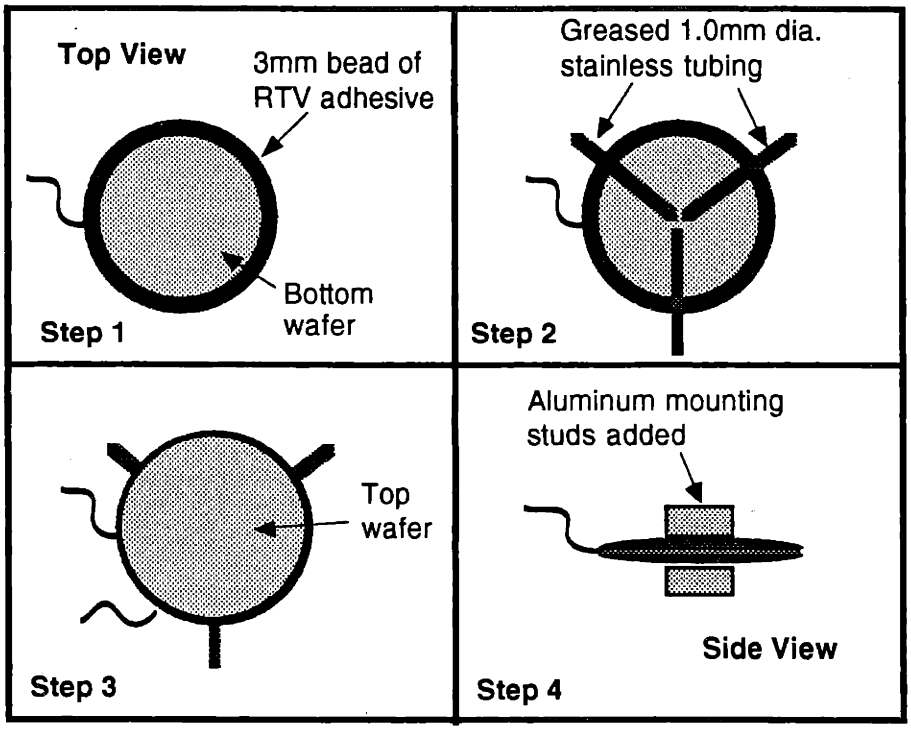

Figure B.4: Assembly procedure for a Rainbow dual wafer transducer.

B.3 Output Response

Rainbow transducers were constructed from 15 and 30 mil thick wafers and evaluated for output performance. In both cases, the transducers were constructed with 1.25" diameter wafers. One side of the transducer was mounted to a rigid surface. An accelerometer was attached to the other side of the transducer to determine output amplitude. In some cases a 20g mass was also attached to the free end of the transducer to see how output was affected by a small load. The input voltage was varied and the frequency varied between 50 and 1000Hz. The maximum driving voltage for the 15mil wafer was 100VAC, and was 200VAC for the 30mil wafer. Figures B.5 and B.6 show the output response for the transducer constructed from the 15 mil thick wafers.

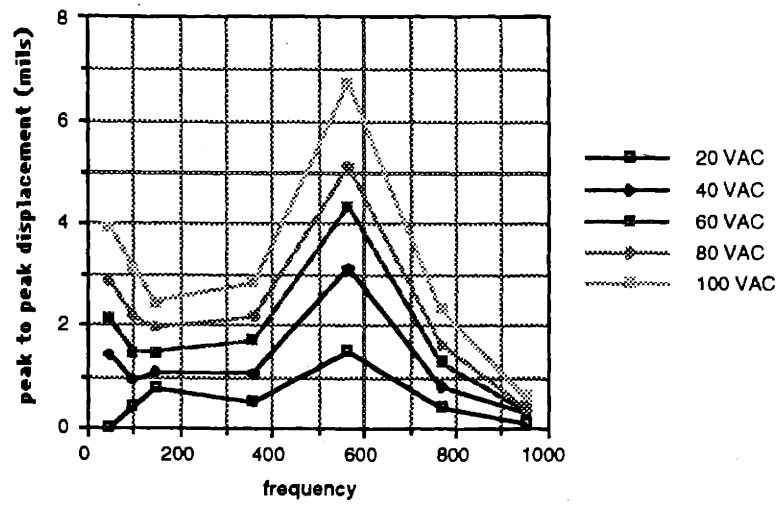

Figure B.5: Zero load output response for transducer constructed with 15 mil thick wafers.

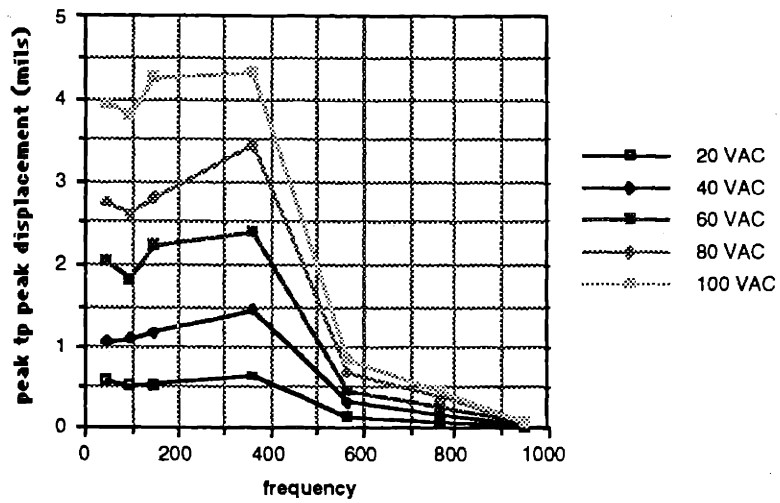

Figure B.6: Output response for 15 mil transducer driving a 20g load.

In the unloaded condition, the transducer had a resonance at approximately 575Hz. Once loaded, the resonance frequency dropped to approximately 250Hz.

Figures B.7 and B.8 show the output response for the transducer constructed from 30 mil thick wafers.

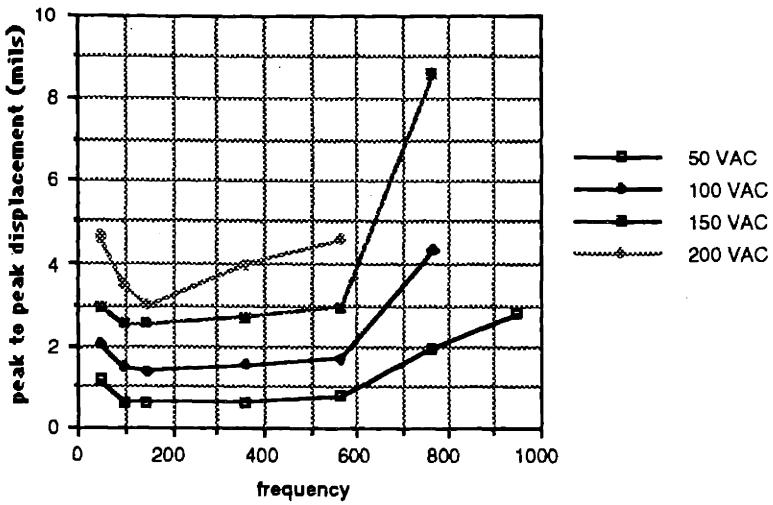

Figure B.7: Zero load output response for transducer constructed with 30 mil thick wafers.

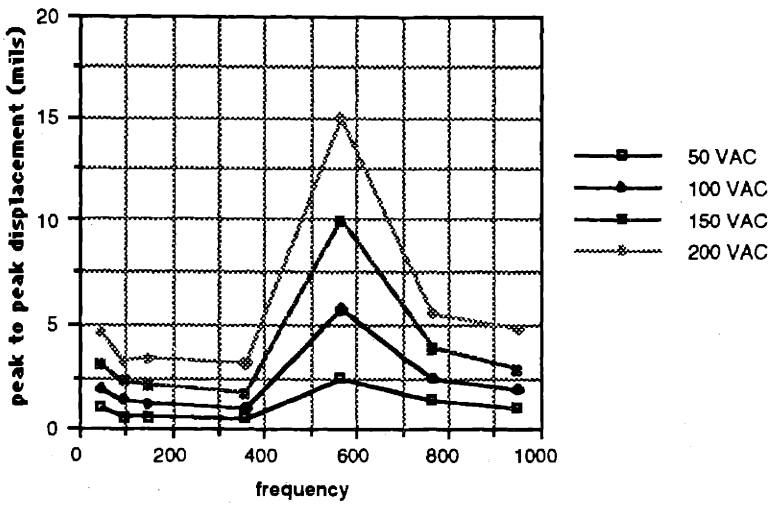

Figure B.8: Output response for 30 mil transducer driving a 20g load.

In the unloaded condition, the transducer had a resonance above 1000Hz. Higher frequencies were not tested because the transducer gave audible indications of being near failure. Once loaded, the resonance frequency dropped to approximately 560Hz.

B.3.1 Failure Modes

During the course of these tests, several transducers were destroyed while exploring their maximum output potential. The dominant failure mode during operation is

over-driving, especially near resonance. Although the Rainbow wafers are rather rugged compared to other types of piezos, they still exhibit the brittle characteristics of ceramic materials. Once the transducer is over-driven, a crack rapidly forms across one or both of the wafers. (Note: If only one of the wafers in the transducer is damaged, the good wafer can be salvaged by cutting the center RTV joint with a razor blade and attaching a new wafer.) The second primary failure mode was accidental shock while handling. Although the transducers can absorb large loads along their central axis, they are rather weak when loaded from other directions. The transducers constructed from 30 mil thick wafers were found to be much more durable compared to the 15 mil thick wafers. All further testing in this work was performed using the 30 mil wafer transducers.

B.4 A Resonant Force Source

The above results show that a transducer and attached mass have a second order response characteristic. The compliance in the system originates primarily from the RTV adhesive used in the transducer construction, with a slight contribution from the wafers themselves. As such, best output from a transducer can only be obtained at or near a specific resonance frequency. Since during this research it would be desirable to easily vary the operating frequency of the transducer while still maintaining high output, a spring / mass resonator assembly powered by a Rainbow transducer was constructed. The intention was to design a resonator assembly which could operated over a large range of frequencies and be easily attached at arbitrary orientations to whatever device needed an oscillatory force input. The resonator assembly is shown in figure B.9.

A thin metal strip, mounted in a U-shaped aluminum bracket, acted as a spring. The Rainbow transducer was attached between the spring and a variable mass. The resonant frequency of the spring / mass system could quickly be adjusted by changing the thickness of the spring or the amount of the attached mass. Since the aluminum strip spring was compliant in only one direction, the orientation of the entire assembly could be varied without affecting performance.

The resonant frequency of the assembly, f_r, can be calculated from the expression

$$f_r = \sqrt{k/m}, \qquad \text{B.1}$$

where k is the spring constant and m is the attached mass. The spring constant for a strip spring can be approximated from the expression

$$k = \frac{192EI}{l^3}, \qquad \text{B.2}$$

where E is the Young's modulus of the spring material, l is the length of the spring, and I is the area moment of inertia, given by

$$I = \frac{(\text{width})(\text{thickness})^3}{12}. \qquad \text{B.3}$$

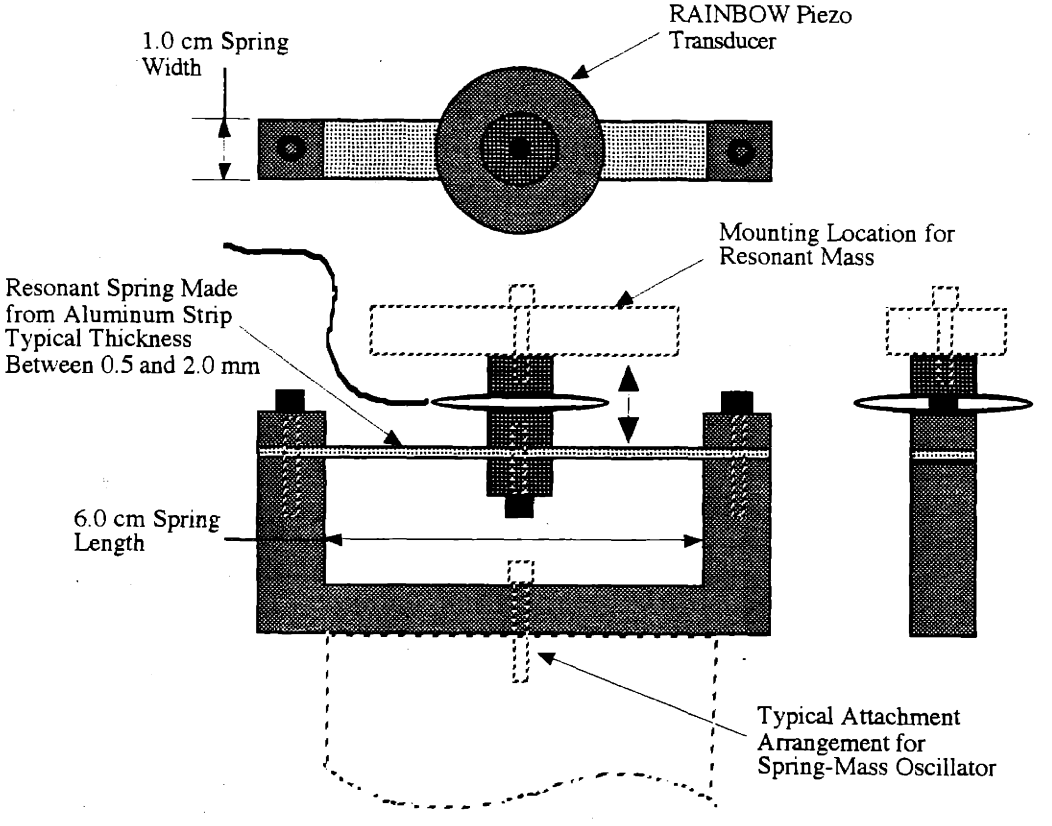

Figure B.9: A resonant force source powered by a Rainbow transducer assembly.

As built, the resonant force source had a effective frequency range of 50 to 600Hz.

B.5 Equipment Suppliers

Ling Electronics, Inc. 4890 E. La Palma Ave. Anaheim, CA 92806 (714) 779-1900
Aura Ceramics, Inc. 5121 Winnetka Ave. N., Minneapolis, MN 55428 (612) 535-9660

Appendix C: Measuring Packing and Compositional Homogeneity Using Photographic Analysis Techniques

C.0 Introduction

The microstructure of parts made with the 3DP process is the key determinate in many post-processing and final part property issues. Shrinkage and distortion in post-processing, and material properties such as hardness, fracture toughness and modulus are all affected by the microstructure of the green printed part. Bulk property measurements, such as the average green density of a large bar, cannot reveal vital microstructural information. To obtain this information, a close-up view of the printed part has to be studied, both qualitatively and quantitatively. The use of photographic analysis techniques as a means of analyzing printed part microstructure is the topic of this appendix.

The goal of this development work was to quantitatively measure several aspects of printed part microstructures. Specifically, these were:

1) Average packing density for a part, and variation in packing throughout a part on a microstructural level.

2) The extent of packing defects in a printed part, as caused by the spreading operations used to create each layer, and the printing operations which bond individual printed lines.

3) The amount of mixture segregation in parts printed with bimodal powders.

There are a variety of commercially available photographic analysis packages which are used to quantify various aspects of metallographic samples. Operations such as grain sizing and grain boundary reconstruction, volume fraction measurement of different phases and image enhancement are standard. Although these packages are very powerful, it was felt that they could not meet most of the measurement goals listed above. The development of custom image analysis algorithms, although a substantial undertaking, would allow output to be tailored to the exact needs of this research. Also, by developing these new techniques independently, a thorough understanding of their capabilities and limitations would be obtained.

The content of this appendix was not included in the main text because, although it represents a substantial amount of the work done in this thesis, these photographic analysis techniques are, in the end, simply a tool to be used to better understand the packing behavior of dry powders. The organization of this appendix is as follows. First, an overview of the entire analysis process, from sample preparation to final data output, is given. Next, the preparation of the different types of metallographic samples studied in this work is described in detail. The different methods for obtaining images of the samples are discussed, followed by a description of the development of the various algorithms for analyzing the images. Finally, the operation of the analysis software is reviewed.

C.1 Process Overview

The photographic analysis process develop here can be broken down into four distinct steps. These steps are illustrated in figure C.1.

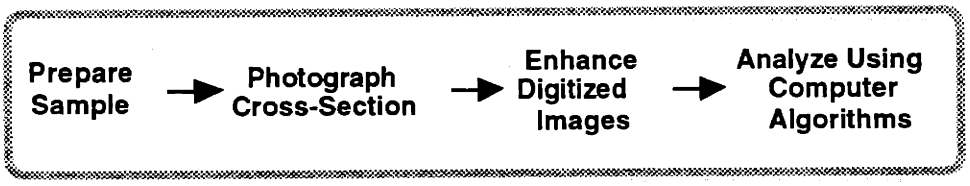

Figure C.1: Process overview for studying the microstructures of printed parts using photographic analysis techniques.

After printing, the green part must be lightly sintered to remove the polymer binder and form weak interparticle bonds. Ideally, sintering would be avoided, because in causes a small amount of shrinkage and particle rearrangement. However, green parts respond poorly to the subsequent steps of potting and polishing, primarily because individual particles tend to be pulled out of the cross-sectional surface during polishing. A light sinter is used, therefore, to ensure the part microstructure is not damaged during polishing.

After polishing, an image (or multiple images) of the part cross-section is obtained, using either an optical metallographic microscope or an SEM. If the original image is captured onto photographic film, then it must be digitized into a 256 gray level image. This step is not required in image acquisition techniques which directly create a digitized image.

The gray scale image is then enhanced by algorithms which distinguish the metal regions from the pores which are filled with potting compound. After enhancement a black and white remains, with the black regions representing the pore structure and the white regions representing the metal particles.

Finally, the enhanced digital image is analyzed using the custom algorithms in order to quantify the properties of interest, such as packing density, extent of packing defects, and bimodal composition.

C.2 Sample Preparation

During sample preparation, the printed part is lightly sintered, potted in epoxy resin, cross-sectioned along the plane of interest and polished to reveal the microstructure. In this research, three different types of metallographic samples were prepared for photographic imaging. These included small samples, large samples, and packing density map samples. Preparation differences for the three types of samples were primarily in the potting and polishing stages. A description of the entire sample preparation procedure is given below.

C.2.1 Furnace Operations

All samples were debound and lightly sintered in a argon / 5% hydrogen atmosphere. The furnace schedule for all samples was:

10°C / minute to 1050°C
hold 60 minutes at 1050°C
30°C / minute to room temperature

This schedule provided adequate strength for all samples, although samples which contained a greater percentage of fine powders would sinter slightly more than coarse samples. Although it would be possible to determine an optimum minimum sintering schedule for each type of sample, this added effort was avoided in the interest of simplicity. Linear part shrinkages after light sintering varied between 0.6% to 1.3%.

C.2.2 Potting the Sample

All samples were potted using Struers Epofix epoxy. This epoxy has very low viscosity immediately after mixing, which was critical for filling the small pores (often less than 10μm) in some of the samples. The samples were placed in suitable molds, and the molds were placed in a vacuum chamber. After pumping down, epoxy was added to the molds via a small tube. The epoxy was forced through the tube by external atmospheric pressure. After the molds were filled, the epoxy was allowed to degas for an additional 5 minutes before pressure was restored. This sequence of epoxy addition is *critical* to successful infiltration of all the small pores. In earlier attempts, epoxy was poured into the molds before they were placed in the vacuum chamber, with the belief that the gases trapped in the pores would escape once vacuum was pulled. In this case, the epoxy would only infiltrate about the first millimeter of surface, leaving a porous region in the center of larger parts. These parts could not be successfully polished and had to be discarded.

Small parts were potted in standard 1.25" diameter cylindrical molds. Larger parts, which would not fit into these molds, were potted in paper cups which were approximately 3" in diameter. After curing, the paper cup was torn away.

C.2.3 Polishing Procedure

Polishing the samples involved wet grinding with progressively finer grades of silicon carbide wet / dry paper, followed by a wet polish using a water-based alumina slurry. For the 1.25" samples, a Struers Rotopol-1 automatic polisher was used to provide the most consistent results. The initial wet grinding procedure was as follows:

Paper Grit	Polishing Time (min)	Polishing Force (N)	Platter RPM
80	2	20	150
220	2	20	150
500	5	20	150
1200	5	20	150

Note - The grit numbers used for Struers silicon carbide grinding papers do not correspond to U.S. standards. After grinding, the samples received a finish polish using a 0.3μm alumina slurry on a Texmet cloth wheel. This final polish was performed by hand. Each sample was hand polished for 1 minute.

After grinding and polishing of the 1.25" samples, it was often the case that the final polished surface was no longer parallel with the mounting surface at the opposite end of the sample. If not corrected for, when an SEM mounting stub was glued to this mounting surface and the sample placed in the SEM chamber, the facing polished surface would be at an angle to the scanning electron beam, causing changes in focal depth as the sample was moved in the chamber. To avoid these problems, a stub gluing fixture was built to ensure that the polished plane of the sample and the mounting plane of the stub were parallel for all samples.

For the large samples, including the packing density map samples, an initial machining operation was performed to create a flat surface for later grinding and polishing. Samples were generally machined into rectangular blocks for easier handling and mounting onto SEM stubs. All grinding and polishing steps were performed by hand, using the same paper grits, polishing times and platter speeds as for the 1.25" samples.

C.3 Photo Acquisition and Image Enhancement

Once the metallographic sample is prepared, the microstructural analysis begins with the acquisition of multiple photographic images from the cross-section. The processes used to acquire these photographic images, or micrographs, represent the most important step in the entire image analysis procedure. The micrographs contain all the information which will be available for later study. No amount of image correction or enhancement can completely compensate for poor initial image quality. A great deal of effort was spent in determining what form of image acquisition would best meet the needs of this research. The different image acquisition approaches which were investigated are described in this section. A review of the process requirements for any image acquisition procedure is presented first.

C.3.1 Process Description and Requirements

The application of photographic analysis to the 3D printed sample microstructures is considerably simplified because they contain only a single metallic phase. In other types of metallographic analysis, multiple phases such as impurities, inclusions or carbides need to be discriminated from the overall metal matrix, placing greater requirements on the image acquisition procedure. Because there is only a single phase present (steel, in this case)

surrounded by a pore structure filled with epoxy, the primary requirement of the image acquisition process is to provide maximum contrast between the metal and epoxy. Ideally, the process would generate a black and white image in which the black regions represented the epoxy and the white regions represented the steel. The image acquisition processes investigated, however, do not operate in just black and white, but over a continuous gray scale. As we will see, how well a given process can produce a highly contrasted gray scale image is an indication of process capability.

Before discussing the different types of image acquisition processes, some of the commonalties of the procedures will be reviewed. Figure C.2 is an illustration of how a sample cross-section is converted into a digitized image. This figure shows how the edges of a single particle are detected. As the particle is scanned, an analog video signal is produced which is proportional to the reflectivity of the particle and surrounding epoxy. This analog signal is then quantized into 256 distinct levels to create a digital signal. The quantity zero represents complete black, and 255 represents complete white. Gray levels are represented by intermediate values. The region in the transition from epoxy to metal along the scan line will exhibit a continuous level of values between 0 and 255. The digitized signal is then delineated into metal and epoxy regions using a *threshold* value somewhere between 0 and 255. This threshold value is determined based on the gray levels at the centers of epoxy and metal regions. One might expect a threshold value exactly between 0 and 255, or 127, to be the correct value. However, this would be the case only if the average of the gray levels for the epoxy and metal regions was also 127. Selection of the correct thresholding level is critical, since this level has a direct effect on the accuracy of particle size measurements.

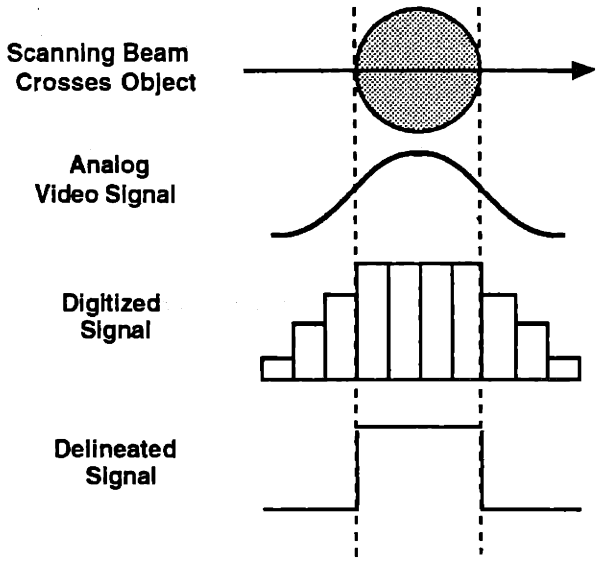

Figure C.2: The process of converting an analog video signal from a scanned image into a digital format.

The suitability of a gray scale image for the types of image analysis developed in this work can be evaluated by studying a histogram of the pixel values in the image. In figure C.3, what would be considered an "ideal" histogram has been drawn for the purposes of discussion. The horizontal axis in the histogram contains the pixel values 0 to 255, while the vertical axis indicates what percentage of the total pixels in the image have that gray scale value. The main features of this ideal histogram are a strong grouping of pixel values towards the extreme values, with a large range of intermediate values for which there are no pixels in the image. For a digitized image with such a histogram, any threshold value between about 30 and 220 would convert the original gray scale image into the same final black and white image. The sensitivity to the choice of threshold value is therefore greatly reduced.

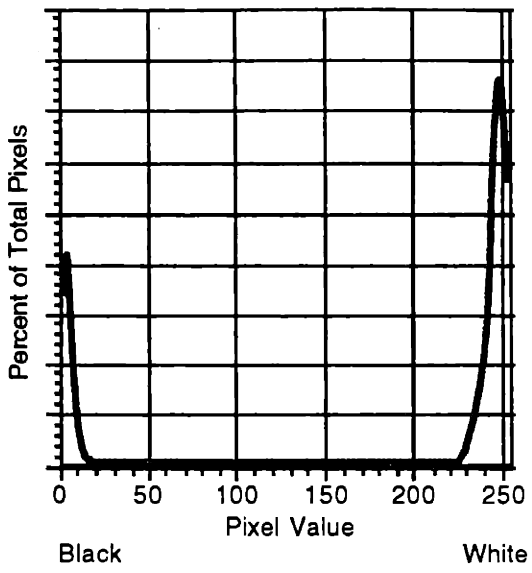

Figure C.3: An "ideal" histogram for pixel values from a 256 gray level image.

A final comment about all the image acquisition procedures to be considered is the need for absolute consistency during use. All the different approaches use equipment which can be adjusted in many different ways. An optical microscope, for example, has adjustments for light source intensity and the use of different optical filters, to name a few. For whatever procedure was to be finally utilized, it was appreciated that the results gathered during a photo session and between photo sessions would only be comparable if *exactly* the same procedure was used each time. The reader is cautioned to take heed of this warning, otherwise large volumes of data can be gathered which have little meaning.

C.3.2 Different Image Acquisition Approaches

Several possible photographic techniques existed for capturing images of the metallographic specimens. Three such methods are reviewed here. These included digitized 35mm film, direct capture ccd, and scanning electron microscope (SEM). In the digitized 35mm film procedure, an optical metallographic microscope is used to photograph images with a 35mm camera attachment. After exposure, the film is sent to a photographic lab for developing and scanning of the negatives. Using very high resolution scanners, the film images are digitized into a standard computer graphic file format and the information is stored onto a PhotoCD. (Note - film developing and scanning can be performed in-house, if the equipment is available.) Each image is scanned and stored at several resolutions, ranging from 192 x 128 pixels to 3072 x 2048 pixels. The PhotoCD format is ideal for

multiple image storage since at the highest image resolution, each gray scale image requires 6 Mbytes of storage space. A single PhotoCD can store over 100 images.

In the direct capture ccd method, an optical microscope is again used to magnify the image, but image acquisition is performed by a high resolution ccd camera. A ccd camera directly converts the image into digital format. The camera is attached to a microcomputer which is running dedicated image acquisition software. Each image is stored to the computer's hard drive for later retrieval. Image resolution for a high end camera is typically 1024 x 1024 pixels. If the required magnification is low enough, then a macro 35mm lens can be used instead of a metallographic microscope.

In the SEM imaging technique, the video output from the SEM is digitized by an external microcomputer running image acquisition software. Images are again stored to the computer's hard drive. A maximum resolution of 1024 x 1024 pixels is typical.

Table C.1 lists the pros and cons associated with each method. The pump-down time of the high vacuum system in an SEM makes analysis of multiple samples time consuming. The SEM, however, offers a variety of methods with which to scan the sample, such as with backscatter electrons. With both direct ccd and SEM, the final image is viewed at the time of acquisition. With the 35mm film approach, the final image isn't seen until the PhotoCD is received from the processing lab. File storage can become an issue when hundreds of images are acquired over time. The PhotoCD approach avoids this problem.

Table C.1: Pros and Cons of the Different Image Acquisition Approaches.

Acquisition Method	Pros	Cons
35mm film	PhotoCD format convenient for storage of large quantities of images Optical microscope can scan multiple samples quickly	Development and scanning of images handled by external photo lab
Direct CCD	Optical microscope can scan multiple samples quickly Direct digitization of image	All images must be stored on hard drive
SEM	Many different types of operating modes i.e. backscatter Direct digitization of image	All images must be stored on hard drive Use of SEM is slow for multiple samples

The order in which the different approaches were evaluated was determined by availability of the required equipment at the time. At the early stages of this work, only the 35mm film approach was viable, so this was investigated first.

C.3.3 Initial Work Using the 35mm Format

An Olympus metallographic microscope was used to obtain the images. The 35mm camera attachment had automatic shutter speed adjustment. Film speed was selected with an external dial. After a discussion with the technical support staff at Kodak corporation, the Kodak T-Max 100 black and white film was selected. T-Max 100 is a very high contrast black and white film, and has an extremely fine grain size for optimum resolution.

To select an exposure setting which would provide the most contrasted images, multiple photos were taken of a single sample while adjusting the film speed setting on the camera. The automatic shutter speed in the camera would then alter the exposure time accordingly. Film speed settings of 200, 100, 50, 25 and 12.5 ASA were evaluated. After transfer to PhotoCD, a histogram for each image was generated. In addition, the digitized images were compared visually for contrast and edge definition. From this evaluation, a camera film speed setting of 25 ASA was chosen. All microscope settings, such as light

source intensity, were recorded so that all future work would produce identical results. No microscope optical filters were used in this procedure.

After transfer to the PhotoCD, images were downloaded to a Macintosh Quadra 610 computer for processing. Adobe Photoshop v.2.0.1 imaging software was used to perform the transfer. For maximum resolution, only the 3072 x 2048 pixel images were used. Although black and white film was used, the outside photo lab stored the images on the PhotoCD in the standard RGB color format. The Photoshop software was first used to convert these images to gray scale, and then to threshold the images to a black and white form.

The 35mm film approach was used to gather microstructural information from many samples over the course of several months. After several iterations of film exposure, developing and transfer to PhotoCD format, subtle inconsistencies in image quality became apparent. Specifically, the overall brightness and contrast of images could vary among different metallographic samples and different PhotoCD's. Figures C.4-5 are gray scale images taken from two different PhotoCD's. These images have clear differences in brightness and contrast.

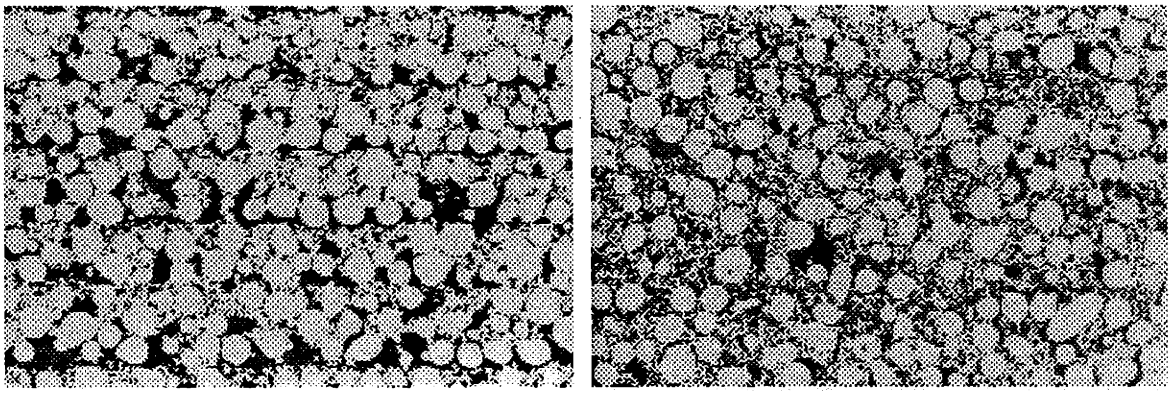

35mm photo A

35mm photo B

Figures C.4 and C.5: 256 gray level CD ROM images from two different photo sessions. Note the differences in image brightness and contrast level between the metal and epoxy regions.

Figure C.6 is a pixel value histogram for the images in figures C.4-5. Neither histogram would be considered "ideal" based on the definition given earlier, although the histogram for sample "B" is inferior to that for sample "A".

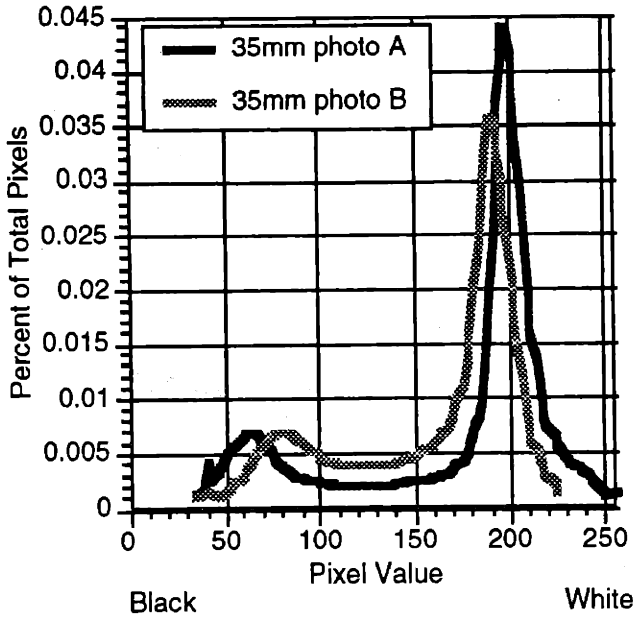

Figure C.6: Histogram of pixel values for the above CD ROM images obtained from 35mm photographs.

Several potential sources of variation were identified which might have caused the differences in image brightness and contrast. Since developing and scanning took place at an external photo lab, there was no information about how the lab procedures may have varied from batch to batch. Differences in the age of the chemicals used to develop each roll of film, in addition to the equipment settings on the scanning hardware, are two sources of potential variation. The 35mm camera attachment may also have been a source of variation. Although film speed could be set manually, shutter speed was automatically set based on the amount of light being received by an internal sensor. It was later noted that the reflectivity of a given sample would be proportional to its packing density. More tightly packed samples would have more polished metal surface with which to reflect light. This might result in a faster shutter speed for these samples.

Several solution approaches which might overcome the variations in brightness and contrast were considered. These approaches were intended to reduce the sensitivity of the final black and white image conversion to threshold level. A simple approach would be to use higher magnification images. The particles in these images would be larger, making

the precise location of particle perimeter less sensitive to threshold level. This approach, however, would have required re-imaging all previous samples, and was not a guaranteed fix.

A second solution approach was to apply a dynamic threshold algorithm to the individual images. Instead of having a single threshold value for every pixel in the image, the algorithm would raster scan the image, deciding what the correct local threshold level should be based on local brightness and contrast. Figure C.7 is a plot of pixel gray level vs. position for a portion of a single row of pixels from an actual image. High values indicate the presence of metal particles along the row. The pixel data was smoothed to remove background noise.

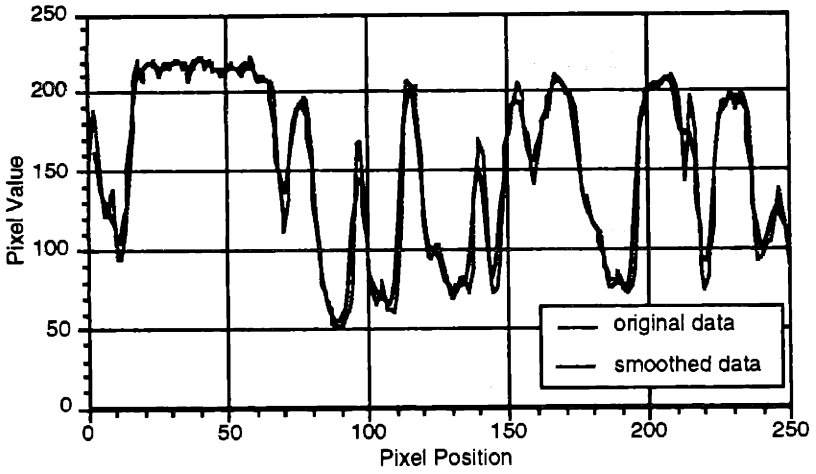

Figure C.7: Pixel values from a single raster scanned line across a digitized 35mm photograph.

In figure C.8, a small portion of the smoothed data from figure C.7 has been expanded for illustration of the dynamic thresholding algorithm. The algorithm used local maximum and minimum points in the data to mark the centers of light and dark regions in the gray scale image. A pixel value halfway between these points was chosen as the local threshold value. In figure C.8, points A and C are local minimum and maximum values, respectively, and point B is the chosen threshold value for the AC segment of data. After thresholding, all pixels along segment AB are given the value zero to represent black pixels, and all pixels along the segment BC are given the value 255 to represent while pixels. The process is continued to mark other maximum and minimum points E and G, and other thresholding values D and F. Every row of pixels in the image is individually thresholded in this manner.

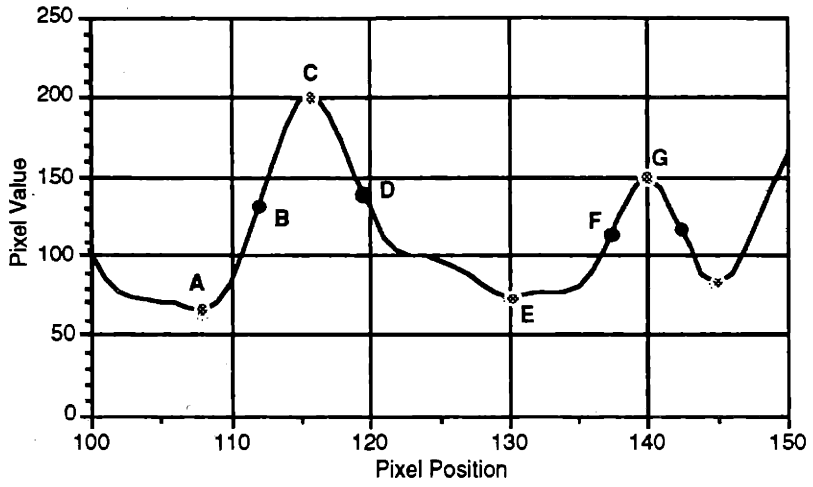

Figure C.8: A close-up view of a segment of smoothed data from figure C.7, showing inflection points (A, C, E, G) and thresholding points (B, D, F) as selected by the dynamic thresholding algorithm.

After an initial evaluation of the dynamic thresholding procedure, it became apparent that to be used successfully, a much more detailed study about the intricacies of the procedure would need to be made. Also, the procedure was itself a "band-aid", attempting to compensate for poor initial image quality. At this point in the photographic analysis development, new equipment which would allow the acquisition of digital images from an SEM became available. Effort was switched to the evaluation of this new technique, with the intent of improving the initial image quality and consistency. In this way, complex image post-processing could be avoided.

C.3.4 Working with Backscatter SEM Images

A Hitachi scanning electron microscope (SEM), coupled with image acquisition hardware and Link Isis v.3.00 software from Oxford Instruments, Inc. were used to obtain microstructural images. Image resolution was 1024 x 1024 pixels. In order to obtain the best possible contrast between metal and epoxy, backscattered electrons (BSEs) were detected instead of the standard secondary electrons (SEs). BSEs primarily result from electrons which have been scattered elastically by the nucleus of an atom. The higher the atomic number (Z) of a material, the more likely it is that backscattering will occur. Thus, as the scanning electron beam passes from a low-Z (low atomic number) area into a high-Z area, the signal due to backscattering, and, consequently, the image brightness, will increase. [7] Contrast is produced because of compositional differences with the specimen.

Since the epoxy regions of the samples were composed of very low-Z elements such as carbon and hydrogen, and the steel areas were composed of high-Z elements such as iron, nickel and chromium, images produced by backscattered electrons had exceptional contrast. Samples were not gold coated before SEM imaging, since this high-Z coating was found to effect the image contrast.

Two gray scale images of bimodal microstructures obtained using backscattered electrons are shown in figures C.9-10. Note that the images appear nearly black and white before any image post-processing was applied.

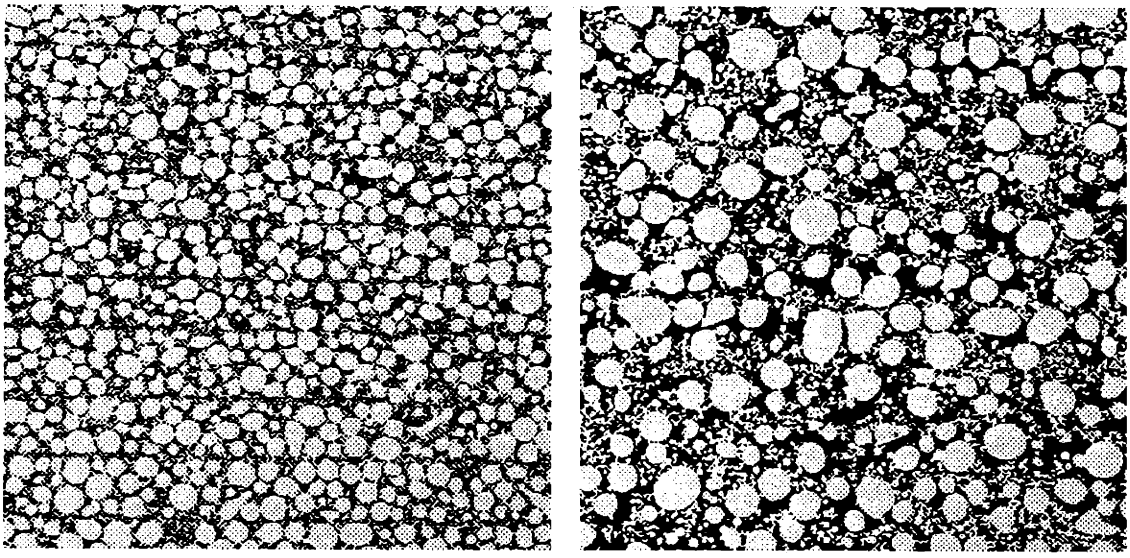

SEM backscatter image A SEM backscatter image B

Figures C.9 and C.10: Gray scale images obtained using the backscatter operating mode of a scanning electron microscope.

A pixel value histogram for the images in figures C.9-10 is shown in figure C.11. Note that this histogram is even more "ideal" that the conceptual histogram illustration in figure C.3. The same histogram with a logarithmic vertical axis is shown in figure C.12. From these two histograms, it was concluded that any threshold value between about 100 and 150 would be acceptable. A value of 127 was chosen for all subsequent work with backscatter images.

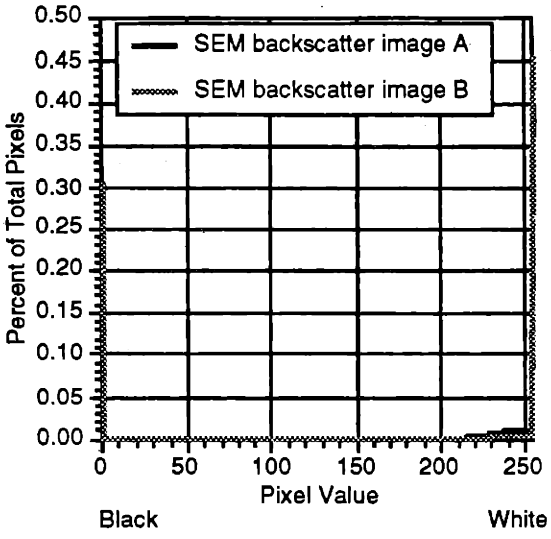

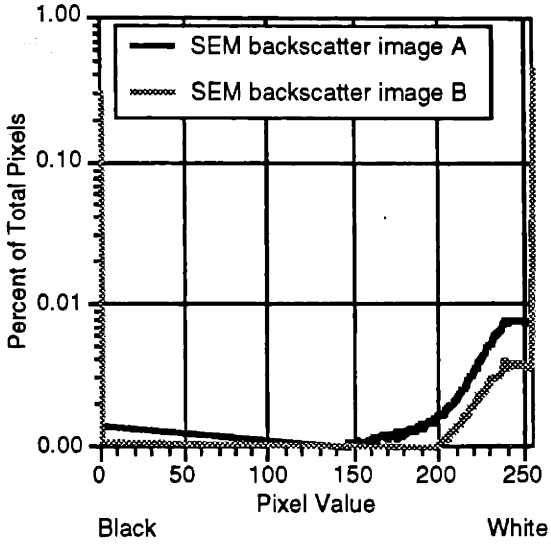

Histogram for backscatter images

Histogram with logarithmic vertical axis

Figures C.11 and C.12: Histograms of pixel values for the backscatter SEM images shown in figures C.9 and C.10.

After image acquisition, the images were stored as TIFF format files by the Isis software. The specific details of image thresholding and other file handling procedures are discussed in the final section of this appendix.

C.4 Measuring Packing Density and Variation

The measurement of packing density in printed parts is critical to determining how different methods of layer generation and densification compare. Additionally, information about how the packing density varies within a part on a microstructural level is necessary in order to optimize techniques which reduce this variation. In this section, the issues associated with the local measurement of packing density using image analysis are discussed. Packing density measurement approaches other than image analysis are discussed in the main text.

Determining the packing density $\emptyset_{image}$ of an individual image is straightforward. In this case, $\emptyset_{image}$ is determined with the expression

$$\phi_{image} = \frac{\text{number of white pixels in the image}}{\text{total number of pixels in the image}}. \qquad \text{C.1}$$

To determine the average packing density $\emptyset_{avg}$ of a part, several images are analyzed. The algebraic average of the packing densities of all the images is equal to $\emptyset_{avg}$. The more images which are analyzed, the higher the accuracy of the average packing density measurement.

Printed part packing density in this work was determined by averaging the packing density values for 10 images from a given part. A magnification of 100x was used in all cases. With this magnification, the analyzed area measured 1.0 x 1.0 mm. The images were taken from a single zone in the top center of a bar, using a 5 x 2 pattern, as shown in figure C.13. The top region of a printed bar is preferred because the first few printed layers of a bar can sometimes be unique due to transient effects.

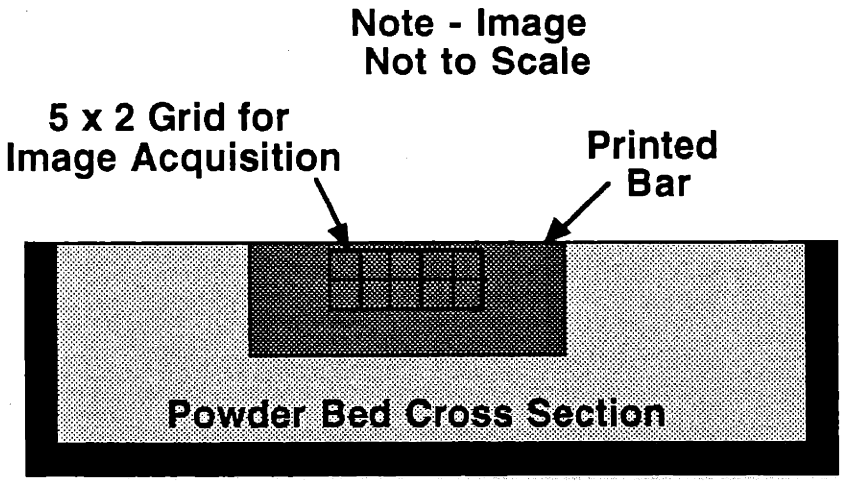

Figure C.13: A cross section of the powder bed, showing where images were acquired for packing density measurements. In this view, the fast axis of the 3DP machine is into the page.

In addition to determining the average packing density of the printed part, an indication of the local variation in packing can be obtained from the standard deviation of the packing values for the 10 individual images. The variation which is obtained for a given microstructure is dependent on two factors. The first factor is image magnification. If two sets of 10 images are taken from a given microstructure at two different magnifications, then the variation in image packing density will be higher in the set with the higher magnification. This is because a smaller area is being considered in each image. By

keeping image magnification constant at 100x for all packing density measurements in this work, this effect is eliminated. The second factor which affects packing variation is real differences in packing from image to image caused by voids and other packing defects. It is this variation that we are, of course, interested in, both for determining its source and ways to eliminate it.

The coefficient of variation (COV) from statistical theory will be used to compare packing density variation between parts. We can define Δ_{image}, the packing density variation parameter, as

$$\Delta_{image} = \frac{\text{stdev of packing in the individual images}}{\text{average packing of the individual images}}. \qquad \text{C.2}$$

The COV is a better comparative tool than the standard deviation, since it also considers the average packing density of the sample. In general, lower values of Δ are desirable because they indicate lower packing variation. If, using the above technique, two different samples are determined to have a standard deviation in packing of 3%, then the sample with the higher average packing density will have the lower value for Δ. Stated another way, a given level of packing variation is considered more "acceptable" in a sample with a higher average packing density.

An adjustment must be made to the average packing density numbers obtained from image analysis to compensate for any sintering shrinkage which occurred during sample preparation. This adjustment factor is determined by measuring the dimensions of a printed bar before and after firing. If l_0, w_0 and h_0 are the dimensions before firing, and l, w and h are the dimensions after firing, then the average packing density of the original green printed part, $\emptyset_{green}$, is given by

$$\phi_{green} = \phi_{image,average}\left(\frac{l \cdot w \cdot h}{l_o \cdot w_o \cdot h_o}\right). \qquad \text{C.3}$$

The packing variation parameter Δ is not affected by the sintering shrinkage, since both the numerator and denominator in expression C.3, are multiplied by the adjustment factor. Therefore,

$$\Delta_{green} = \Delta_{image}. \qquad \text{C.4}$$

When referring to packing density Ø and packing variation Δ, it will be assumed that it is the green part properties which are being referred to. The subscripts will be dropped for clarity.

C.5 Quantifying Packing Defects

Achieving printed parts with completely homogeneous microstructures has always been a goal for the 3D printing process. Unfortunately, the manner in which the printed parts are produced - the spreading of layers and the printing of lines - conspires against this goal in the form of packing defects. Packing defects can occur during spreading of the powder layer (lamination defects, tearing) or during the printing process (line pairing, ejection, balling, etc.) The end result of these packing defects will likely be anisotropic shrinkage during post-processing and anisotropic material properties in the finished material. Having a means of measuring inter-layer and inter-line defects would prove helpful in comparing microstructures of parts created with different spreading and printing techniques. The goal of this section was to develop a procedure which could quantitatively measure the extent to which packing defects existed between printed lines and across printed layers.

Figure C.14 is an SEM micrograph from a bimodal bar printed early on in this development work. The image was taken from a cross-section identical to that shown in figure C.13. The bar was printed with the 71/9μm 316L bimodal powder mixture. Layer and line spacing were both 175μm. The presence of layering defects is visible to the naked eye, although it is not readily apparent if line defects are also present.

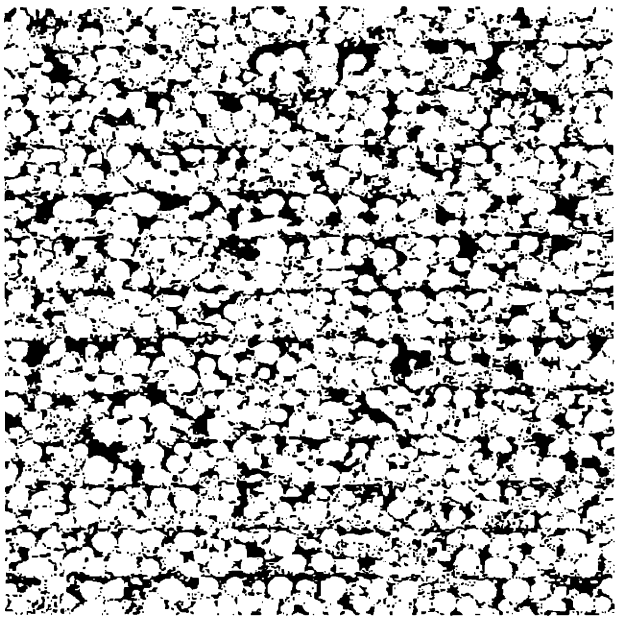

Figure C.14: Microstructural image from a bar printed with the 71/9μm 316L bimodal powder mixture. The part layers, each 175μm thick, run horizontally across the image. 40x magnification.

The development work on quantifying the extent of packing defects in microstructures similar to the one in figure C.14 begins with an approach called scanning line analysis. This approach is discussed next.

C.5.1 First Approach - Scanning Line Analysis

Any suitable metric for quantifying layer and line defects would, by design, increase in value with the increase of packing defects. An approach called scanning line analysis was the first concept considered which would provide such a metric. This approach will be explained by first considering how it would quantify the layer defects in figure C.14.

For layer defect interrogation using scanning line analysis, every horizontal row of pixels is individually scanned in a raster fashion. The scanning motion is illustrated in figure C.15. For each row analyzed, a scan ratio parameter S is calculated from the expression

$$S = \frac{\text{number of white pixels in the row}}{\text{total number of pixels in the row}}. \qquad \text{C.5}$$

Note that the S parameter has a functional definition similar to the packing density Ø. If there are i rows in the image, then i individual parameters S_1, S_2, ..., S_i will be calculated. When the scanning line passes through a layer defect region, the corresponding scan ratio parameters will have lower values because of the lower packing density in the area of the defect.

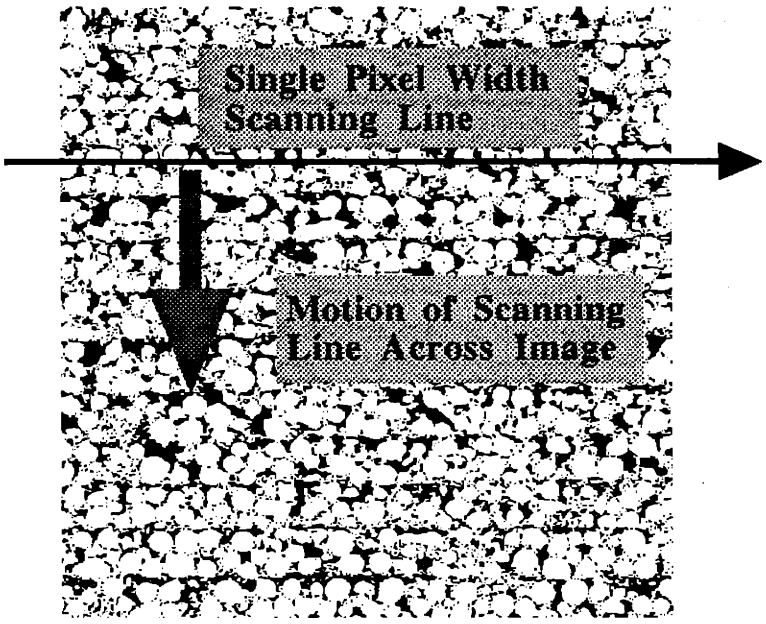

Figure C.15: Illustration of how a single pixel width scanning line is swept across the image to obtain packing defect data.

After the scan of the image is completed, a layer defect parameter D_{layer} is calculated from the expression

$$D_{layer} = \text{standard deviation}(S_1, S_2, ..., S_i). \qquad C.6$$

The layer defect parameter D_{layer} increases as the variation in the individual scan parameters S_1, S_2, ..., S_i increases. In this manner, D_{layer} quantitatively describes the amount of packing variation across the printed layers.

In a similar fashion, a line defect parameter, D_{line}, can be defined. In this case, the columns of pixels in the image are individually scanned to create the scan parameters T_1, T_2, ..., T_i . The parameter D_{line} is then defined as

$$D_{line} = \text{standard deviation}(T_1, T_2, ..., T_i). \qquad C.7$$

As variations in packing across the printed lines increases, the parameter D_{line} also increases.

Whereas the scanning line concept was conceptually straightforward and easy to implement, it had an unresolved issue associated with the meaning of the scan parameters on which the measurement was based. Although the scan parameters S_1, S_2, ..., S_i and T_1, T_2, ..., T_i had the functional form of a packing density measurement, these parameters were not truly measuring packing. A packing density measurement is associated with a volume within a part or an area within a cross-section which is significantly larger than the maximum particle size. The area associated with a single scanning line is too small to be used for a packing measurement. Admittedly, this is a subtle point. However, with some simple modifications to the scanning line procedure which are discussed in the next section, this concern can be resolved.

C.5.2 Second Approach - Scanning Window Analysis

A modification to the scanning line concept which would resolve the packing measurement issues was to expand the "width" of the scanning line, changing it into a scanning window. In a manner identical to the scanning line technique, a scanning window would be swept across the microstructural image to gather information about packing defects. An illustration of the scanning window approach is given in figure C.16.

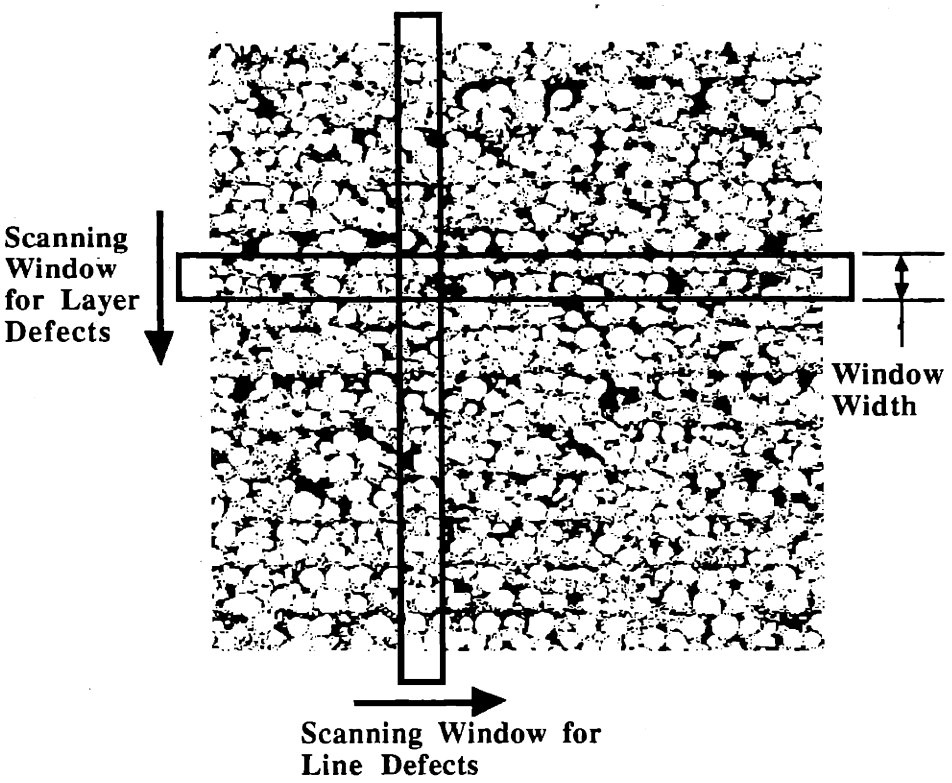

Figure C.16: Illustration of how scanning windows are swept across the image. Packing data gathered during the window sweep is used to quantify packing defects between lines and across layers.

The scanning window, which has a fixed width, is moved in single-pixel increments across the image. As the window is swept across, the packing density in the window is recorded, again producing a set of scan parameters $S_1, S_2, ..., S_i$ during the layer defect sweep and $T_1, T_2, ..., T_i$ during the line defect sweep. Note that in this case, the scan parameters are clearly representative of packing densities as long as the window width is suitably large. The layer and line defect parameters, D_{layer} and D_{line}, are calculated using the previously defined expressions.

The choice of window width has a direct effect on the minimum defect size which the procedure will detect. If the window width is made greater than layer or line spacing, then layer and line defects will be missed by the procedure. A window width of 88μm, which equaled half the layer and line spacing used in this research, was chosen for use with this procedure. (For an image with taken with 50x magnification, 88μm was equivalent to approximately 140 pixels.) This window width value provided a window area which was

sufficiently large to measure packing density, but small enough to detect defects with a length scale on the order of the layer and line spacing.

In order to accurately measure the green packing density at each window location, the scan parameters $S_1, S_2, ..., S_i$ and $T_1, T_2, ..., T_i$ must each be multiplied by the sintering shrinkage adjustment factor described in the previous section. This multiplication is performed before the calculation of D_{layer} and D_{line}.

To demonstrate the use of the scanning window procedure, the microstructural image in figure C.17 was analyzed. This image was obtained from a part printed with a 20μm 316L monomodal powder. Layer and line spacing were the usual 175μm. Image magnification was 50x.

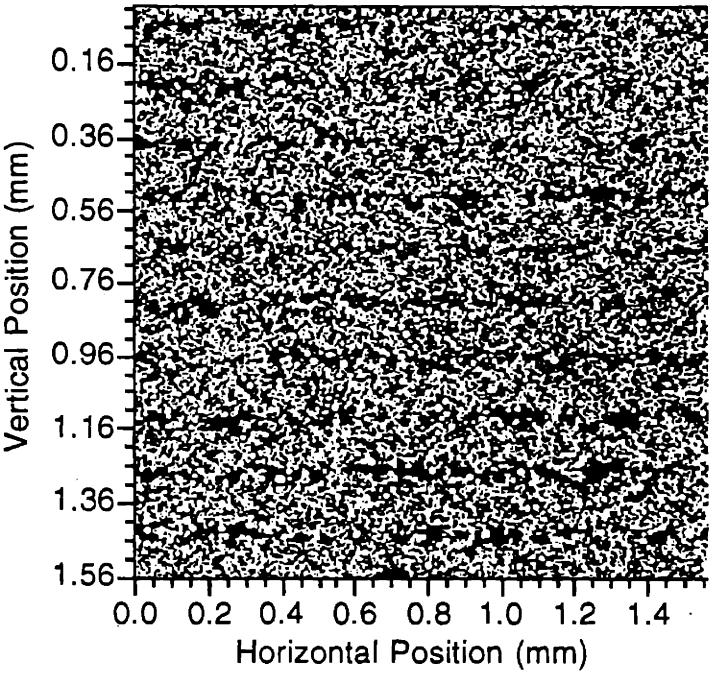

Figure C.17: Microstructural image from a bar printed with a 20μm 316L monomodal powder mixture. 175μm layers. 50x magnification.

After the image was analyzed, the packing density values of the scan parameters S_1, $S_2, ..., S_i$ and T1, $T_2, ..., T_i$ were plotted against window position. In figures C.18-19, the results of the vertical scan, which tested for layer defects, and the horizontal scan, which tested for line defects, are shown. The vertical layer defect scan clearly shows a

repetitive packing variation with a 175μm spacing. The horizontal line defect scan also shows variation in packing, but no repetitive pattern is obvious.

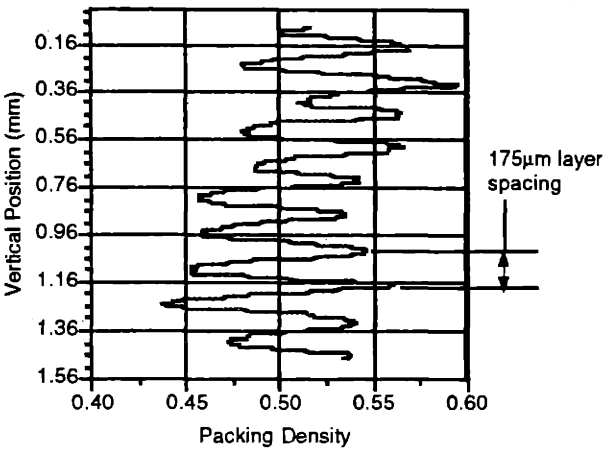

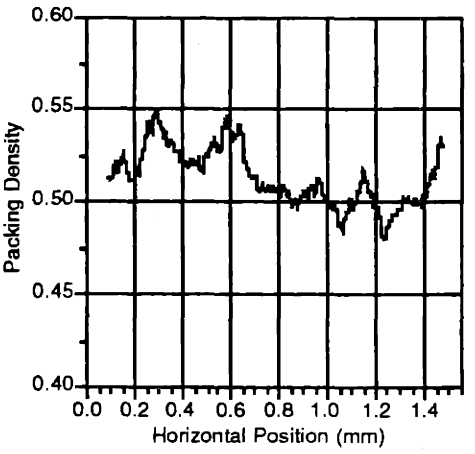

Vertical scan of 20μm image

Horizontal scan of 20μm image

Figures C.18 and C.19: Plots of packing density vs. scanning window position for the image in figure C.17. The scans are for layer defects (left) and line defects (right).

To make the comparison of layer and line defects between different parts more meaningful, two modified defect parameters based on the coefficient of variation of the scan parameters are defined as

$$D_{layer,COV} = \frac{\text{standard deviation}(S_1, S_2, ..., S_i)}{\text{packing density of the image}} \qquad C.8$$

and

$$D_{line,COV} = \frac{\text{standard deviation}(T_1, T_2, ..., T_i)}{\text{packing density of the image}}. \qquad C.9$$

As before, the COV based parameter is a better comparative tool than the standard deviation based parameter, since it takes into account the overall packing density of the sample.

As in the case of the packing density measurement technique, the use of multiple images from the same sample will increase the area being analyzed and improve the overall

defect measurement accuracy. The two differences in procedure when using multiple images are that the lists of scan parameters $S_1, S_2, ..., S_i$ and T1, $T_2, ..., T_i$ now contain information from all the images, before the calculation of the defect parameters, and the average packing density of all the images is now used in the denominator of expressions C.8 and C.9.

Finally, it should be noted that during the development of these packing defect analysis procedures, the images which were analyzed all had a magnification of 50x. The intent early on was to use a lower magnification than was used in the packing density measurements (100x) in order to scrutinize more part cross-sectional area with fewer images. In retrospect, the collected data would have been more consistent and comparable if the images analyzed for layer and line defects were also 100x magnification. However, a significant number of samples had already been analyzed for layer and line defects at 50x magnification by the time this was realized. The 50x magnification was therefore used for all analysis of layer and line defects in this research.

C.6 Measuring Local Composition in Bimodal Parts

In order to successfully use bimodal powders to attain a high green density part, the composition of the bimodal mixture must be the same throughout the part. If one region of a part has a greater percentage of fines than another, detrimental effects will occur. First, the packing density throughout the part is likely to vary, because the maximum packing density of a bimodal mixture is heavily influenced by the bimodal composition. This will likely lead to irregular part properties, since one region of the part may contain more steel than another. Second, dimensional change throughout the part during post-processing operations is likely to be anisotropic. During sintering, those regions of the part which contain a greater percentage of fine particles will sinter and shrink to a greater extent, causing warpage and distortion across the part.

Variations in the internal bimodal composition of a printed part originate from segregation of the large and small powder components. This segregation can occur during handling of the bimodal mixture, such as when a pile of powder is dispensed and spread into the next powder layer. Identification of the presence or absence of bimodal segregation on a micro-scale level is therefore critical to successful development of a bimodal powder printing process.

The development of computer algorithms to measure composition on the micro-scale level is the subject of this section. The goal of this development effort was to be able to determine the composition of a region within a bimodal part by analyzing an image of a 2D cross-section. In order to determine the bimodal composition of this image, the large and small particles within the image needed to be identified by the computer.

The organization of this section is as follows. First, two distinct numerical approaches for the measurement of composition from a 2D image are presented. Simplified cases, in which the images contain perfectly circular particles with no size variation, are discussed first . Later, more complex cases in which the images being considered more closely resemble actual microstructures are considered. The limitations of the two approaches are examined. Finally, a modified approach is developed which overcomes most of the limitations of the earlier methods. The operation of this modified approach is explained and critiqued.

C.6.1 Numerical Approaches for Composition Measurement

Earlier in this appendix, a description was given of how local packing density could be obtained from a digitized micrograph of a printed part. In this case, the numerical procedure simply involved counting all the white pixels in the image, and dividing that quantity by the total number of pixels in the image. The specific *operation* which was used was a pixel count. In fact, most operations performed using digital photographic analysis involve some form of pixel counting. For measurement of bimodal composition, however, no variation of pixel counting seemed to be a workable approach. The first step in developing an algorithm to measure the bimodal composition of a digitized micrograph, therefore, was to consider what other possible *operations* could be performed on the image in order to obtain the necessary information. These operations would proceed from the same starting point as a pixel count in the packing density measurement - a black and white image in which the white pixels represented metal regions, and the black pixels represented void regions. The numerical operations of *intersection* and *erosion* are presented here as two distinct methods for measuring composition. The overall concepts behind each operation are first presented. Later, the mathematics which can be applied to each operation to measure composition are developed.

C.6.2 The Intersection and Erosion Operations

The first numerical operation to be considered is called *intersection*. The intersection operation is conceptually very similar to the scanning line analysis procedure presented in section C.5.1 for the measurement of packing inhomogeneities. Referring again to figure C.15, the intersection operation involves horizontally scanning each pixel row of the digitized image. The intersection operation differs from the scanning line procedure in that as each pixel row is scanned, the number of transitions from black to white or from white to black is counted. For example, as the scanning line passes through the center of a circular particle, two transitions are counted. One when the scanning line first enters the particle, and the second when the scanning line exits the particle. The process is repeated for every row in the image, and a single grand total of all intersection transitions made during the procedure is created by summing the intersection counts from all the rows.

The intersection operation can be viewed as an operation which acts upon particle *perimeters*. Conceptually, the number of intersections generated for a given image is tied to the amount of particle perimeter in that image. If two black and white images have the same total number of white pixels, but one image has all the white pixels clustered into a single solid area, and the other image has the white pixels divided up into many smaller areas, then the later image would produce a larger total intersection count. This is because the later image has more particle perimeter for the intersection operation to act upon. The use of the intersection procedure to measure image composition will be developed below, after the second image operation concept is discussed.

The second numerical operation to be considered is called *erosion*. The erosion process involves the selective, sequential removal of white pixels from the microstructural image. The erosion procedure takes place during repeated erosion passes. During each erosion pass, a single layer of white pixels is removed from the perimeter of the powder particles. In effect, the powder particles are "eaten away" during the erosion process, with the larger particles "surviving" for more erosion passes that the small particles. The erosion concept was not new to this research, and was already utilized in commercial photographic analysis packages, but not with the intent of measuring bimodal composition. Instead, the erosion procedure as used in commercially available packages is intended to "clean up" a dirty image, which, due to problems during image acquisition or because of surface contamination issues, has small speckles which must be removed. In this case, one

or two erosion passes is all that is required to clean up the image, without (hopefully) significantly altering those features of the image which were of interest.

The erosion process has the unique characteristic that the larger particles in the image survive more erosion passes than the smaller particles. It is this characteristic which gives the erosion process potential as a means for measuring local composition. Illustrations of how the erosion process proceeds on a bimodal microstructural image are given below. In figure C.20 a bimodal microstructure is shown, along with the same image after 2, 4 and 6 erosion passes. In this case, the image is a 50x magnification of a bimodal mixture made from 71 and 9μm powders. Note that after only six erosion passes, nearly all of the small particles have been eroded. Image magnification plays a key part in how quickly the particles in an image disappear. If a portion of the same microstructure had been captures at a higher magnification, a greater number of erosion passes would have been required to completely erode the small particles, since the individual particles would be represented by more pixels in the image.

Close-up images of a digitized microstructure prior to erosion are shown in figure C.21. The left-hand image is approximately 200x, while the right-hand image is approximately 800x. Note that both of these images were obtained by zooming in on a portion of an image which had been initially acquired at an SEM magnification setting of 50x. This is why the individual pixels are identifiable in the right-hand image. If the same portion of the microstructure shown in the right-hand image had been initially captured using an SEM setting of 400x, then the particle boundaries would be much more accurately defined, and the individual pixels would not be visible. The right-hand image indicates how "pixelation" error - the error that occurs during the digitization process - is incorporated into the delineation of particle boundaries.

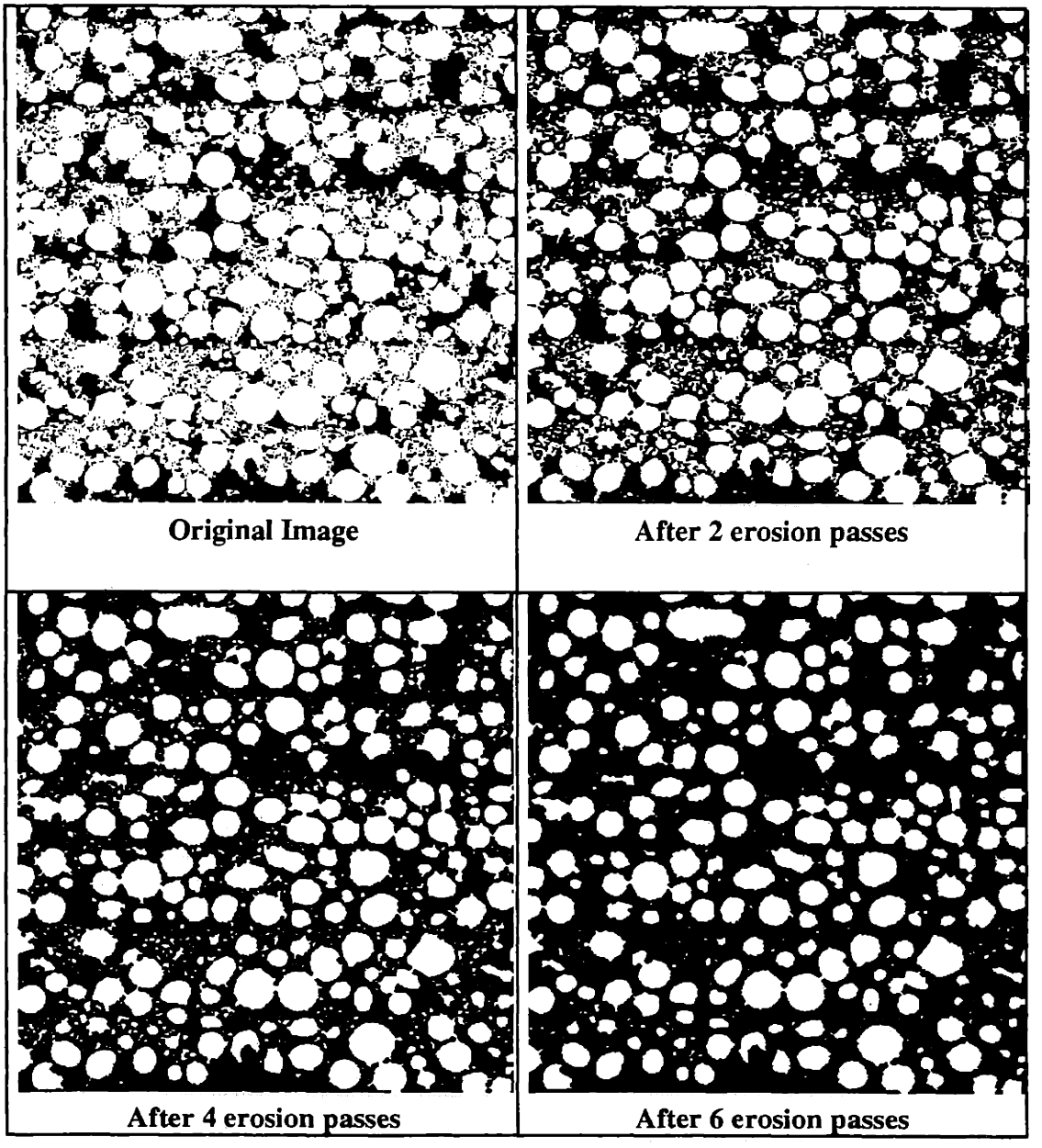

Figure C.20: A demonstration of the erosion concept, showing the effect on powder particles after 2, 4 and 6 erosion passes.

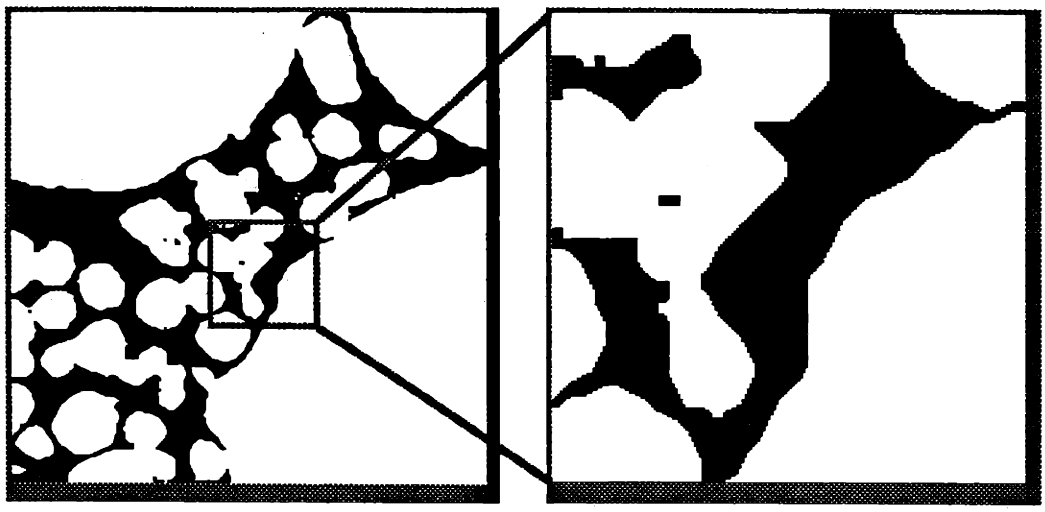

Figure C.21: Enlargements from a digitized 50x magnification image of a bimodal microstructure. The right image shows the pixelation which occurs at powder particle boundaries.

In figure C.22, the erosion process has been graphically enhanced to illustrate the effect of individual erosion passes on the digitized microstructure. This figure initially started out as the right-hand image in figure C.21. The image has been subjected to 12 erosion passes, but instead of the eroded white pixels being changed to black as they would have in the standard process, different shades of gray have been inserted. After 12 passes, only a portion of the large particle in the lower right corner remains. Note that, although erosion might be conceptualized as a continuous process, in actual operation erosion proceeds in discrete steps.

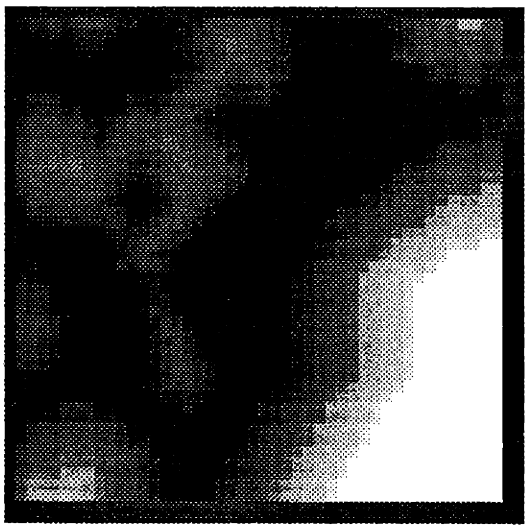

Figure C.22: An illustration of how the erosion process proceeds. To obtain this image, twelve erosion passes were performed on the right-hand image in figure C.21.

A final issue related to the conceptual description of the erosion process is concerned with the erosion "criterion". Any numerical algorithm which is used to perform erosion passes on an image must be equipped with a specific set of criterion for determining when it is appropriate to erode a given pixel. Three different criterion are discussed here. These are the, "8-way", "4-way" and "minimum number" criterion. Figure C.23 is an illustrative aid for describing these different criterion.

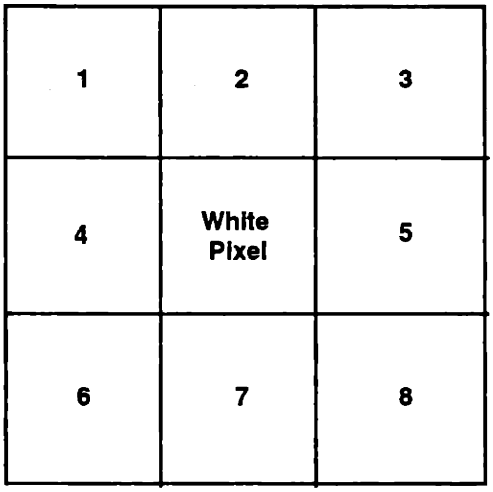

Figure C.23: Identification of the pixels which neighbor any given white pixel in a digitized image.

Figure C.23 is an illustration of 9 pixels - a center white pixel and the eight pixels which surround it. (White pixels along the outside edge of the image are a special case.) In determining whether or not the white pixel should be eroded, the erosion algorithm looks at the neighboring eight pixels and applies the erosion criterion. The 8-way criterion is the most straightforward. It says that if any of the eight neighboring pixels is black at the start of the current erosion pass, the center white pixel will be changed to black during that erosion pass. This criterion results in the fastest erosion of particles in the image, since there are the most opportunities for white pixel elimination in a given erosion pass. The 4-way criterion is less aggressive. It states that the center white pixel will be eroded only if any of pixels 2, 4, 5 or 7 is black at the start of the erosion pass. These pixels share an entire edge with the middle pixel, whereas pixels 1, 3, 6 and 8 only touch the center pixel at the very corner. If one were to draw a comparison between pixel erosion and the erosion

of metal particles in an acid bath, then it would make sense that erosion should only occur at the exposed "surfaces" of a particle. The 4-way erosion criterion most closely resembles this erosion condition. The "minimum number" criterion states that the center white pixel will be eroded only if a certain minimum number of surrounding pixels are black at the start of the erosion pass. The lower the minimum number, the more aggressive the erosion process will be.

All three erosion criterion were investigated during the course of this research. For all the discussion which follows, both in this appendix and in the main text, the 4-way erosion criterion was utilized. Its primary advantages were that it eroded particles more slowly and in a manner which was "visually consistent" with an erosion process. By this it is meant that circular particles remained circular during erosion, just as one might expect a spherical metal particle to remain spherical during erosion in an acid bath. In contrast, using different quantities for the minimum number criterion, particles would tend to flatten or elongate during erosion. The 8-way criterion simply eroded particles too fast. A full discussion of the differences in erosion criterion is beyond the scope of this text. Suffice to say, the 4-way criterion works very well in its intended purpose. However, it should be noted that these and other criterion, when used on microstructural images similar to those above, can produce some very fascinating looking pieces of artwork !

Having described the conceptual details behind the intersection and erosion operations, the question which remains is how can we use either or both processes to determine the bimodal composition of a microstructural image. The answer to this question has already been alluded to. In the intersection operation, the total number of intersections in an image has been shown to be affected by the size and number of particles. Similarly, in the erosion process it was shown that small particles have the property that they erode first. Presented next are formal mathematical derivations which show how the intersection and erosion operations can be used to measure image composition, under certain conditions.

C.6.3 Intersection Operational Relationships

Before considering how the intersection and erosion operations would act on actual microstructures such as the one shown in figure C.14, it would be helpful to consider some simplified or idealized cases. In figures C.24-25, two very simple cases are illustrated. The first case (referred to below as case 1) represents a single particle of radius R in an

image with sides which measure x by y. The particle is perfectly circular. It is also assumed that, although the image is constructed of discrete pixels, the single particle has a diameter of several hundred pixels or more, and therefore has a "smooth" perimeter. The second case (referred to below as case 2) is slightly more complex, where in addition to a single large particle of radius R_L, the are four small particles of radius R_S. In this later case, the small particles are assumed to have a diameter of at least several hundred pixels. The first case might be considered to be a highly simplified monomodal powder mixture. (Indeed, it only has one particle!) The second case is representative of a bimodal powder mixture.

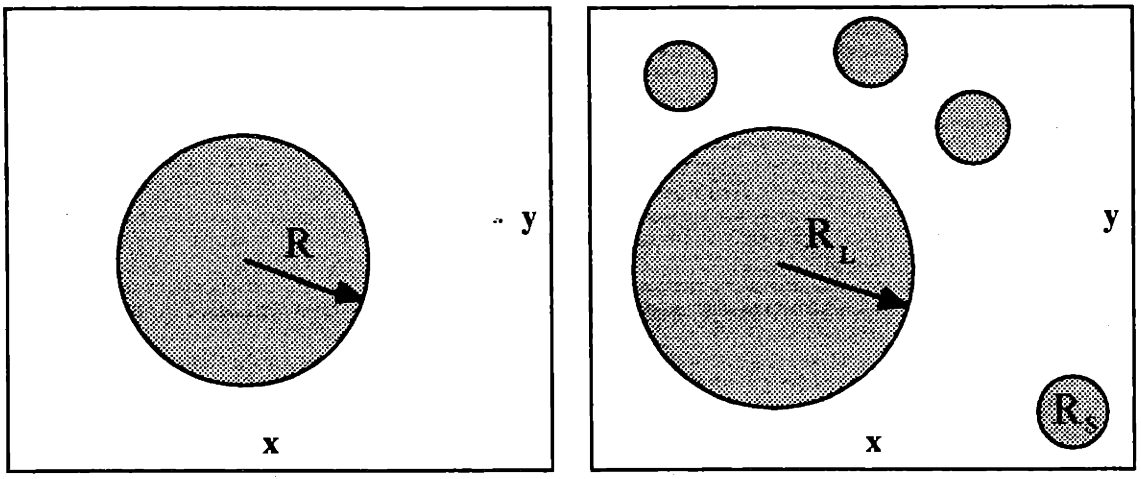

Case 1 **Case 2**

Figures C.24 and C.25: Two highly simplified microstructures.

The analysis which follows will first define some basic quantities to be used throughout this discussion, followed by the application of the intersection operation to the images in figures C.24-25. Finally, the erosion operation will be given a similar treatment.

The packing density Ø in case 1 is simply the ratio of the area of the circle to the image area,

$$\phi = \frac{\pi R^2}{xy}. \qquad \text{C.10}$$

Similarly, the packing density for case 2 is

$$\phi = \frac{\pi R_L^2 + n\pi R_S^2}{xy}. \qquad C.11$$

where n, the particle ratio, is defined as

$$n = \frac{\text{number of small particles}}{\text{number of large particles}}. \qquad C.12$$

In case 2, $n = 4$. The quantity n is chosen to be an integer for the following analysis since it is conceptually easier to talk about a whole number of small particles, however, the analysis is valid for any real value of n. The bimodal composition, C, of the mixture in case 2 is given by

$$C = \frac{\text{area of small particles}}{\text{area of all particles}} = \frac{n\,\pi R_S^2}{\pi R_L^2 + n\,\pi R_S^2}. \qquad C.13$$

Solving for n, we have

$$n = \left(\frac{C}{1-C}\right)\left(\frac{R_L}{R_S}\right)^2, \qquad C.14$$

which can also be expressed as

$$n = \left(\frac{C}{1-C}\right)\left(\frac{D_L}{D_S}\right)^2, \qquad C.15$$

where D_L and D_S are the diameters of the large and small particles, respectively.

With these basic definitions in place, it is now possible to explore the use of the intersection operation. In case 1, the total number of intersection transitions, m, is given by

$$m = \#\text{ of intersections} = 2(2R) = 4R, \qquad C.16$$

where the particle radius R is expressed in pixels. There are two intersection transitions for each of the $2R$ horizontal sweeps which cross the particle. In case 2, m is given by

$$m = 4R_L + n(4R_S). \qquad \text{C.17}$$

A quantity which will be of use below is the ratio of total intersections to image area, which is given as

$$\frac{m}{\text{area of image}} = \frac{4R}{xy}, \qquad \text{C.18}$$

for case 1, and

$$\frac{m}{\text{area of image}} = \frac{4R_L + n(4R_S)}{xy}, \qquad \text{C.19}$$

for case 2. We can now define an intersection parameter, I, which is the ratio of intersections per unit area to packing density. The intersection parameter I is only of interest for case 2, for which it is given by

$$I = \frac{\dfrac{m}{\text{area of image}}}{\phi} = \frac{4R_L + n(4R_S)}{\pi R_L^2 + n\pi R_S^2} = \left(\frac{4}{\pi}\right)\left(\frac{R_L + nR_S}{R_L^2 + nR_S^2}\right). \qquad \text{C.20}$$

Note that the image dimensions x and y cancel during this division. Substituting equation C.14 for n, we have

$$I = \left(\frac{4}{\pi}\right)\left(\frac{R_L + \left(\frac{C}{1-C}\right)\left(\frac{R_L^2}{R_S}\right)}{R_L^2 + \left(\frac{C}{1-C}\right)R_L^2}\right) = \left(\frac{4}{\pi R_L}\right)\left(1 - C - C\left(\frac{R_L}{R_S}\right)\right). \qquad \text{C.21}$$

Which now gives I only as a function of C, R_L and R_S. Simplifying and solving for C, we have

$$C = \frac{\left(\frac{\pi R_L}{4}\right)(I) - 1}{\left(\frac{R_L}{R_S}\right) - 1}. \qquad \text{C.22}$$

Expression C.22 is significant in that the composition of the image is determined using only the intersection parameter *I*, and knowledge of the radii of the two powder components. Information about the total image area *xy*, the particle ratio *n*, or the packing density Ø is not required.

C.6.4 Erosion Operational Relationships

The erosion operation will now be similarly studied to demonstrate how it can be used to provide compositional information. We will first consider case 1. During erosion, the area of the circular particle becomes progressively smaller. Also, the number of erosion passes which are required to completely remove a particle is related to the particle radius. Considering these two factors, an erosion parameter *E* is defined as

$$E = \sum_{r=R}^{0} \frac{\pi r_i^2}{\pi R^2}. \qquad \text{C.23}$$

By this definition, *E* is the summation of the ratios of current particle area to initial particle area. During the erosion process, this ratio becomes progressively smaller, but the summation increases until the particle is completely eroded. Note that *R* is expressed in pixels. If the radius *R* is much greater than the pixel dimensions (which was initially assumed), then the above summation can be rewritten in integral form as

$$E = \int_R^0 \frac{\pi r^2}{\pi R^2}\, dr = \left[\left(\frac{-1}{R^2}\right)\left(\frac{r^3}{3}\right)\right]_R^0 = \frac{R}{3} = \frac{D}{6}. \qquad \text{C.24}$$

A similar expression can be written for the bimodal case 2. Again, an integral expression will be created which continuously sums the ratio of current particle area to initial particle area. In this case, *E* is given as

$$E = \int_0^{R_s} \frac{\pi (R_L - r)^2 + n\pi (R_S - r)^2}{\pi R_L^2 + n\,\pi R_S^2}\,dr + \int_{R_L - R_s}^{0} \frac{\pi r^2}{\pi R_L^2 + n\,\pi R_S^2}\,dr. \qquad \text{C.25}$$

In this later case, E is broken up into two separate integrals to simplify the derivation. The first integral in expression C.25 is a continuous ratio summation taken during the initial stage of the erosion process, in which both the large and small particles still remain. When the integration variable r reaches the integration limit R_S, the small particles have been completely eroded. The second integral in expression C.25 considers the second stage of the erosion process, in which the large particles, which have already been partially eroded, are now completely removed.

Completing the above integration, we obtain

$$E = \left(\frac{1}{R_L^2 + nR_S^2}\right)\left[\frac{-(R_L - r)^3}{3} - \frac{n(R_S - r)^3}{3}\right]_0^{R_s} + \left(\frac{-1}{R_L^2 + nR_S^2}\right)\left[\frac{r^3}{3}\right]_{R_L - R_s}^{0}, \qquad \text{C.26}$$

which further simplifies to

$$E = \left(\frac{1}{3}\right)\left(\frac{R_L^3 + nR_S^3}{R_L^2 + nR_S^2}\right), \qquad \text{C.27}$$

or, in alternate form

$$E = \left(\frac{1}{6}\right)\left(\frac{D_L^3 + nD_S^3}{D_L^2 + nD_S^2}\right). \qquad \text{C.28}$$

Substituting expression C.14 into expression C.27 gives

$$E = \left(\frac{1}{3}\right)\left(\frac{R_L^3 + \left(\frac{C}{1-C}\right)R_L^2 R_S}{R_L^2 + \left(\frac{C}{1-C}\right)R_L^2}\right), \qquad \text{C.29}$$

which simplifies to

$$C = \left(\frac{R_L - 3E}{R_L - R_S} \right). \qquad C.30$$

At this point we have a relationship similar to expression C.22 in that, as before, the composition of the image is determined using only the erosion parameter E, and knowledge of the radii of the two powder components. Again, information about the total image area xy, the particle ratio n, or the packing density $\emptyset$ is not required.

C.6.5 Simulated Bimodal Microstructures

Having established two independent methods for determining bimodal composition of the hypothetical image in case 2, the next step was to evaluate both operations on simulated microstructural images which were slightly more complex than those considered in the above two cases. To this end, a bimodal image generation algorithm was written to create digitized black and white images of arbitrary packing density and composition. The radii of the large and small particles are fixed at a specified number of pixels. As in the above cases, there is no size distribution in the large and small components. The images generated are 1024 x 1024 pixels, similar to those produced by the backscatter SEM process described in section C.3.4. Examples of two simulated microstructures are shown in figures C.26-27 below.

The image generation algorithm works as follows. Data for the pixel radii of the large and small particles is input, in addition to the monomodal packing density of the large particles, and the bimodal packing density for the entire image. (Note - this information is sufficient to completely define the image composition. The mathematical relationships between particle radii, packing density and image composition are developed elsewhere.) The algorithm first generates the large particles. Using a random number generator, an arbitrary location for a large particle is chosen. If the new particle does not overlap any previously placed large particles, then the location is considered acceptable and the large particle is inserted. Particles can be placed partially outside the boundaries of the final image. In this case, the particle is suitably cropped to fit in the final image. A running tally of the large particle packing density is kept by the algorithm. Additional large particles are placed, until the monomodal packing density of the image is equal to or slightly greater than the value which was previously input. At this point, the small particles are randomly placed in a similar fashion. A potential location for a small particle is considered acceptable

if the new small particle will not overlap any previously placed large or small particles. The small particles are added until the bimodal packing density of the image is equal to or slightly greater than the previously specified value. The run time for the image generation algorithm was greatly affected by the packing density values which were initially input. For very high packing densities, the algorithm may need to evaluate thousands of potential particle locations for the last few particles to be placed before it finds positions with no overlap.

There is no physical relationship between how particles are placed in the simulated images, and how actual particles in a bimodal micrograph are arranged. In the later case, the entire history of each particle in the micrograph would need to be known in order to determine how it came to its final position. This type of particle specific information is not available. The only check, therefore, that the simulated images are a reasonable, simplified representation of actual bimodal microstructures is a visual one. For the purposes of verifying the relationships between the intersect and erosion parameters and image composition, the simulated images were deemed acceptable.

C.6.6 Performance of Intersection and Erosion Operations Using Simulated Bimodal Microstructures

Two groups of simulated images were generated. In the first group, the large particles had a 70 pixel radius and the small particles had a 10 pixel radius. In the second group the radii were doubled, with the large particles having a 140 pixel radius and the small particles having a 20 pixel radius. The two different size ranges were chosen to test for errors in the analysis operations. It was expected that the group of images with the smaller radii might cause greater errors in composition measurement, since an earlier assumption was that the smallest particles in the images were several hundred pixels in diameter.

Figures C.26-27 show two simulated images with the 70 / 10 radii and compositions of 9.1% and 27.3% fine particles. Both images have a bimodal packing density of 55%. Sixteen images of differing compositions were generated with the 70 / 10 radii, and eight images of differing compositions were generated with the 140 / 20 radii. All images were analyzed using the intersection and erosion procedures. For each image, the analysis algorithm generated an intersection and erosion parameter. Using these

parameters, and the particle radii, the composition of each image was calculated using expressions C.22 and C.30.

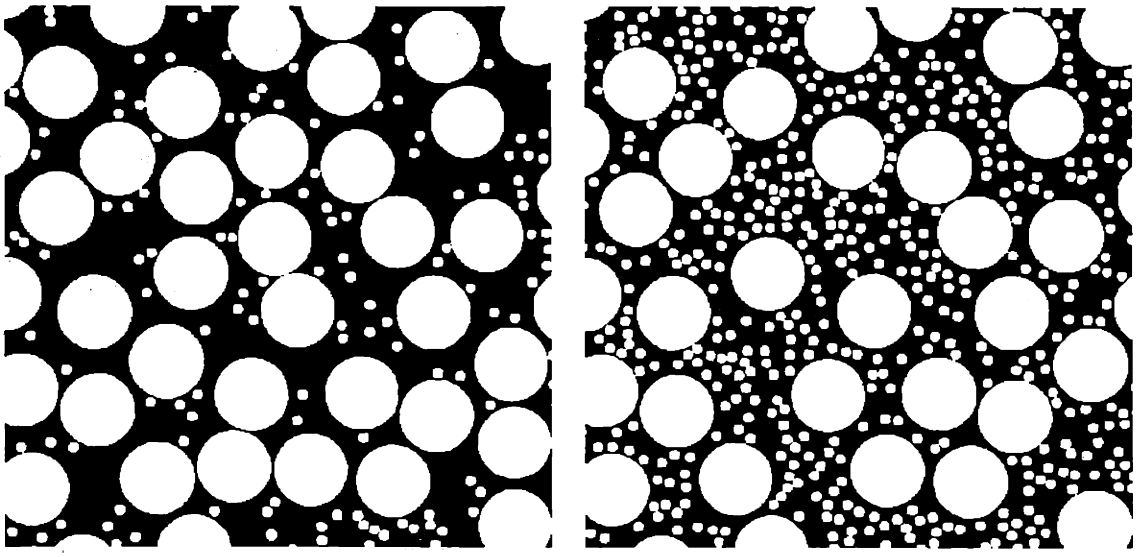

Figures C.26 and C.27: Simulated bimodal microstructures with 9.1% (left) and 27.3% (right) small particles. Both images are 55% packing density. Large particles have a 70 pixel radius, and small particles have a 10 pixel radius.

Figures C.28-29 are plots of composition determined by image analysis vs. actual composition for the two groups of images. A 45° line is drawn in each graph to indicate where the ideal measurements would lie. Both the intersection and erosion operations tracked the image composition very well. The largest errors occurred in the 70 / 10 radii images where the mixture was composed of mostly fine particles. This was expected, since the 10 pixel radius particles deviate the greatest from the continuity assumptions made above. In these cases, the intersection operation consistently underestimated the composition of the image. Note that in the range of compositions which we will be concerned with in this research, which were located around 26.5% fine particles, both operations track composition very well.

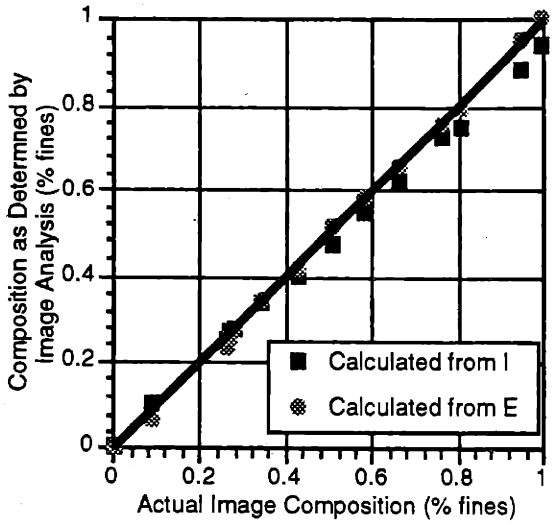

Large Particles = 70 pixel radius
Small Particles = 10 pixel radius

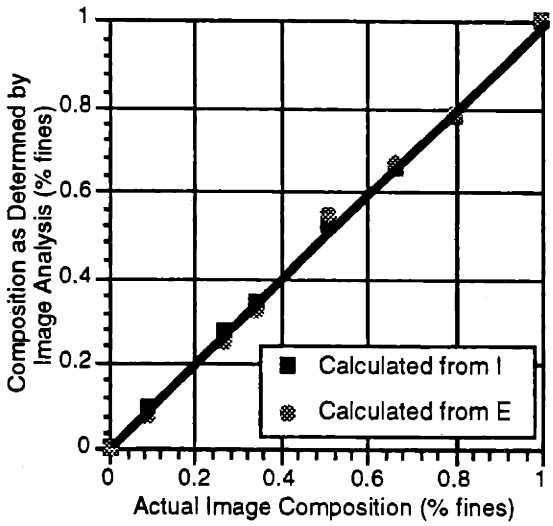

Large Particles = 140 pixel radius
Small Particles = 20 pixel radius

Figures C.28 and C.29: Plots of actual image composition vs. composition calculated from image analysis.

C.6.7 Continuous Particle Size Distributions

In all the above examples, the particles in a bimodal mixture have been represented by one of two discrete radii. In a real microstructural image, the particle radii range over a continuous distribution. (Refer to figure C.14 for a image of a real bimodal microstructure.) The continuous distribution of particles which is seen in a cross-sectional micrograph originates from two sources. First, the process of sectioning the sample in order to view a 2D plane results in a distribution. Consider a hypothetical powdered metal sample made from a spherical monomodal powder in which all the particles were *exactly* the same size. When this metal sample was sectioned, the sectioning plane would not necessarily pass through the centers of all the particles, but would split each particle across some unique plane. In the viewing plane, the particle diameters which could be observed would range from zero to the actual diameter of the 3D particles.

The second source of particle size distribution in a cross-sectional image results from the size distributions in each of the monomodal powders which are blended to create the bimodal mixture. No monomodal powder is truly monomodal - even a tightly cut monomodal sample has an average particle size and some variation about this mean.

We will now consider how the presence of size distributions in the simplified bimodal images would effect the mathematics behind the intersection and erosion operations. By adding size distributions to the hypothetical bimodal case and to the simulated images, the bimodal images will move one step closer to resembling actual powdered metal microstructures.

The expressions for the intersection and erosion parameters as derived above can be readily generalized to bimodal mixtures where each component in the image exhibits a continuous range of particle sizes.

We begin by considering the intersection parameter I for the bimodal case, which was defined above as

$$I = \left(\frac{4}{\pi}\right)\left(\frac{R_L + nR_S}{R_L^2 + nR_S^2}\right). \qquad \text{C.31}$$

We can relate the particle ratio n to two new parameters, n_S and n_L, with the expression

$$n = \frac{\text{number of small particles in the image}}{\text{number of large particles in the image}} = \frac{n_S}{n_L}. \qquad \text{C.32}$$

Also, the parameter N can be defined as

$$N = \text{total number of particles in the image.} \qquad \text{C.33}$$

Multiplying the numerator and denominator of expression C.31 by n_L / N, we obtain

$$I = \left(\frac{4}{\pi}\right)\frac{\left(\frac{n_L}{N}\right)R_L + \left(\frac{n_S}{N}\right)R_S}{\left(\frac{n_L}{N}\right)R_L^2 + \left(\frac{n_S}{N}\right)R_S^2}, \qquad \text{C.34}$$

where the ratios $\left(\frac{n_L}{N}\right)$ and $\left(\frac{n_S}{N}\right)$ are simply the fractions of the total number of particles which have the radii R_L and R_S, respectively.

For an image with i different particle radii, there would be the i corresponding particle fractions $\left(\frac{n_1}{N}\right), \left(\frac{n_2}{N}\right), \left(\frac{n_3}{N}\right) \ldots\ldots \left(\frac{n_i}{N}\right)$, which would be subject to the constraint that

$$\sum_{x=1}^{i} \frac{n_x}{N} = 1. \qquad \text{C.35}$$

In this case, the intersection parameter would be defined as

$$I = \left(\frac{4}{\pi}\right) \frac{\left(\frac{n_1}{N}\right)R_1 + \left(\frac{n_2}{N}\right)R_2 + \left(\frac{n_3}{N}\right)R_3 \ldots + \left(\frac{n_i}{N}\right)R_i}{\left(\frac{n_1}{N}\right)R_1^2 + \left(\frac{n_2}{N}\right)R_2^2 + \left(\frac{n_3}{N}\right)R_3^2 \ldots + \left(\frac{n_i}{N}\right)R_i^2}. \qquad \text{C.36}$$

Now consider an image with a continuous distribution of particle radii. In continuous terms, there exists a distribution function $f(r)$ such that

$$f(r) = \frac{\text{number of particles in image with radius r}}{\text{total number of particles in image}}, \qquad \text{C.37}$$

where correspondingly, if R_{max} is the largest particle in the image, the distribution function is subject to the constraint that

$$\int_0^{R_{max}} f(r)\, dr = 1. \qquad \text{C.38}$$

For this continuous case, the intersection parameter can be rewritten as

$$I = \left(\frac{4}{\pi}\right) \frac{\int_0^{R_{max}} [f(r) \cdot r]\, dr}{\int_0^{R_{max}} \left[f(r) \cdot r^2\right] dr}. \qquad \text{C.39}$$

In an analogous fashion, the erosion parameter E for an image with a continuous distribution of particle radii can be written as

$$E = \left(\frac{1}{3}\right)\frac{\int_0^{R_{max}}\left[f(r)\cdot r^3\right]dr}{\int_0^{R_{max}}\left[f(r)\cdot r^2\right]dr}. \qquad C.40$$

The continuous distribution function $f(r)$ for a given bimodal mixture can, in theory, be determined. Exact information about the particle size distribution for each of the monomodal components would be required. In addition, the effect of sample sectioning, as described above, on the distribution which is actually viewed in the 2D cross-section would need to be taken into account. The added complexity for such a procedure greatly diminishes the utility and practicality of the intersection and erosion operations for the purposes of measuring image composition. All is not lost, however ! In finishing this section, a work-around procedure is considered which avoids the difficulties associated with determining a continuous distribution function for the images to be analyzed.

In order to assist in the development of techniques for measuring composition in images with continuous distributions, the simulated bimodal image generation algorithm described above was modified. Facilities were added for the specification of size distributions in each of the monomodal components. Figures C.30-31 show two examples of the modified simulated bimodal microstructures. The images have compositions of 16.7% and 34.4% fine particles. In both images, the large particles have a radius of 70 pixels with a standard deviation of 5 pixels, and the small particles have a radius of 10 pixels with a standard deviation of 2 pixels.

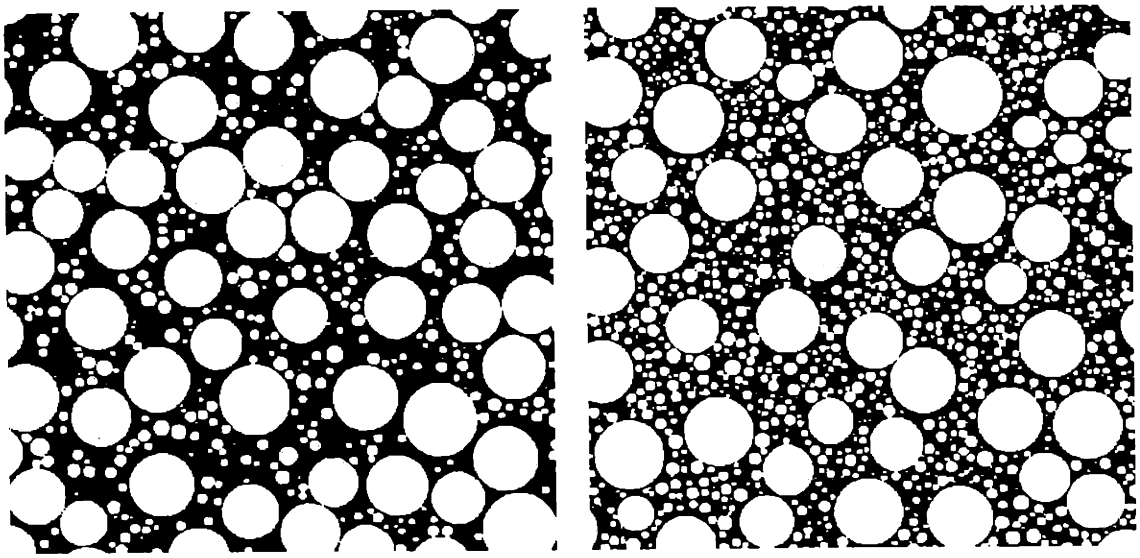

Figures C.30 and C.31: Simulated bimodal microstructures with 16.7% (left) and 34.4% (right) small particles. Both images are 60% packing density.

The work-around procedure involves using monomodal images with continuous distributions as calibration samples for the intersection and erosion operations. Consider the two simulated monomodal distributions in figures C.32-33.

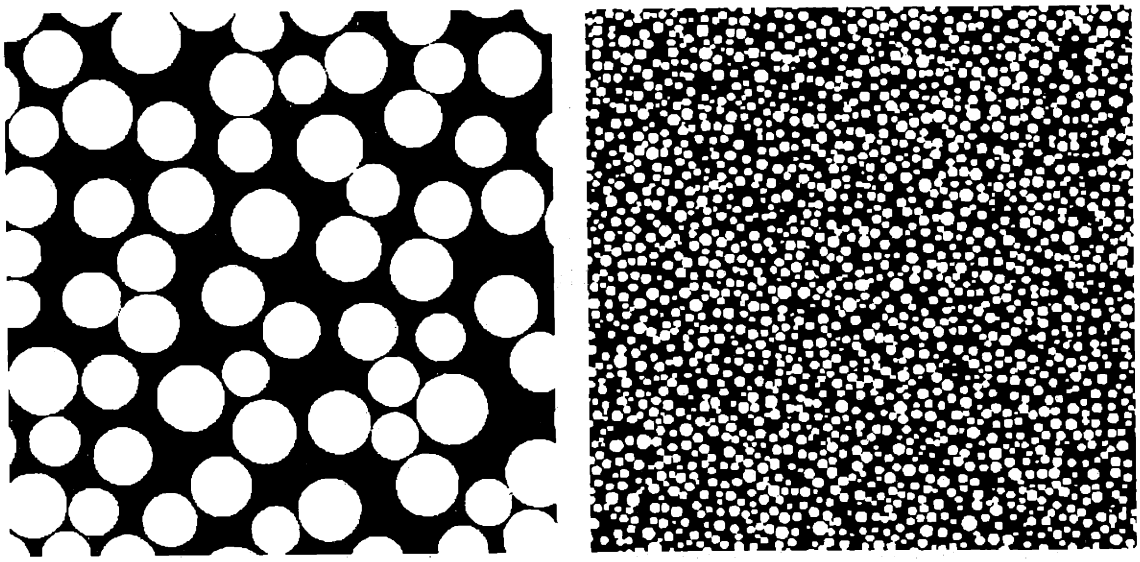

Figures C.32 and C.33: Simulated monomodal microstructures with particle size distributions. The packing densities are 55% (left) and 40% (right).

Even though information about the particle size distributions of the images may not be available, if the intersection and erosion procedures as described above are applied to these images, then a single intersection and erosion parameter would be generated to describe each image. In effect, the numerical operations are "blind" to the fact the images contain continuous distributions. The intersection and erosion parameters for monomodal samples have previously been shown to be

$$I = \frac{4R}{\pi R^2} = \frac{4}{\pi R} \qquad \text{and} \qquad E = \frac{R}{3}. \qquad \text{C.41-42}$$

By solving the above expressions for *R*, and inserting the values for *I* and *E* which were obtained during the analysis of the continuous monomodal distributions, an *effective radius* for the particles in each image can be calculated as

$$R_{effective} = \frac{4}{\pi I}, \qquad \text{C.43}$$

or

$$R_{effective} = 3E. \qquad \text{C.44}$$

If, for example, a monomodal image were generated in which every particle had a radius equivalent to the effective radius of the particles in figure C.32, then the erosion and intersection parameters for this image and the one in figure C.32 would be identical.

Assume that for each powder in figures C.32-33 an effective radius had been calculated using either the intersection or erosion procedures. Now consider the case in which the monomodal powders in figures C.32-33 were blended together in some arbitrary amount to make a bimodal mixture. Although it will not be rigorously demonstrated here, it is the case that the composition of this arbitrary blend can be determined using either the expression

$$C = \frac{\left(\frac{\pi R_{effective,\,L}}{4}\right)(I) - 1}{\left(\frac{R_{effective,\,L}}{R_{effective,\,S}}\right) - 1}, \qquad \text{C.45}$$

or

$$C = \left(\frac{R_{effective,\,L} - 3E}{R_{effective,\,L} - R_{effective,\,S}} \right). \qquad C.46$$

These expressions were obtained by direct substitution in the expressions C.22 and C.30 as defined above.

These final two expressions are extremely powerful. They state that the intersection and erosion operations can be used to determine the composition of *any* bimodal powder mixture which has been blended from monomodal components which have *any size distribution*. All that is required is that the effective radius of each monomodal component be determined a priori. It will also be stated, without proof, the these analysis procedures can be applied to non-spherical particles, within certain constraints. Specifically, the particles need to be equiaxed, with aspect ratios near one.

It may seem that at this point our work in determining local composition via image analysis is done. Unfortunately, this is not the case. Several aspects of real bimodal images can cause the intersection and erosion procedures to produce serious compositional measurement errors. These aspects are examined next.

C.6.8 Practical Limitations to the Numerical Approaches

Although the majority of work in this thesis has centered around the use of spherical, gas atomized stainless steel powders, the individual powder particles are never perfect spheres. In general, the larger the particle size, the more the particle shape can deviate from spherical. Also, the individual particles may have flaws, such as internal porosity, which become apparent during cross-sectioning.

In the development of the intersection and erosion operations above, the simulated bimodal images had many of the characteristics of real bimodal images, such as variations in packing density and composition, interstitial porosity and powder size distributions. Two elements of real images which were not duplicated in the simulated images were particle pinholes and particle contiguity. Examples of these two features are shown in figure C.34. A particle pinhole is an internal defect, such as an enclosed pore, which shows up as a black region within a particle. In regions which exhibit particle contiguity,

neighboring particles are partially bonded together. These contiguous regions are formed for two reasons. First, during the light sintering which occurs during sample preparation, small interparticle necks are formed in order to bond the part together. Although the sintering performed is the minimum amount necessary for sample preparation, regions which contain large portions of small particles can display significant contiguity. Particle contiguity is also effected by the choice of image magnification. Even if two closely positioned particles are not metallurgically bonded, a contiguous region may be present in the digitized image if the magnification is too low. Higher magnifications can help reduce particle contiguity, but with the tradeoff that the image area being analyzed becomes smaller. In doubling image magnification, four times as many images must be analyzed in order to study an equivalent area.

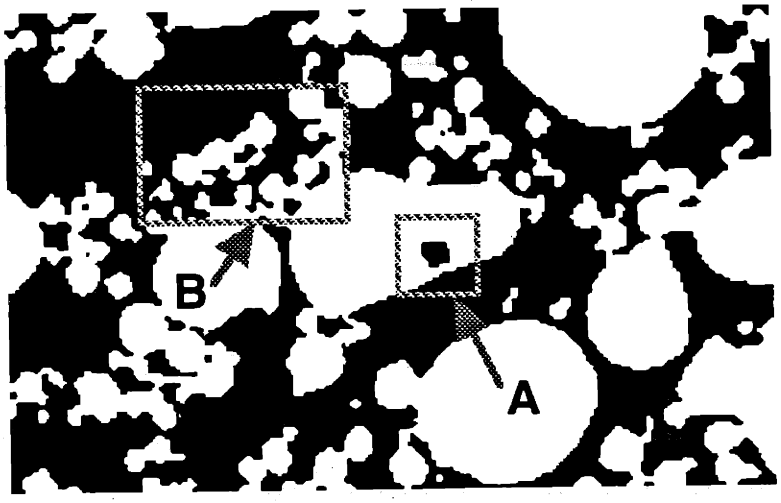

Figure C.34: Examples of particle pinholes (region A) and particle contiguity (region B).

Particle pinholes and contiguity both alter the amount of particle perimeter on which the intersection and erosion procedures operate. In the case of the intersection operation, the presence of pinholes increases the number of intersection transitions in a given image, thereby increasing the predicted amount of fine particles. Conversely, particle contiguity reduces the amount of intersection transitions. In the case of the erosion operation, particle pinholes increase the rate at which large particles are eroded, whereas contiguity reduces the erosion rate, since less perimeter is exposed. The greater the extent of pinholes and contiguity in an image, the greater the error in the composition measurement.

The presence of a particle size distribution in the monomodal components of a bimodal mixture is, in effect, a similar alteration in the amount of perimeter which each monomodal component exposes in a cross-section. We have seen that the monomodal calibration procedure described above eliminates the effect of particle size distributions from the composition measurement. An argument can be made, therefore, that if the monomodal samples used to calibrate the intersection and erosion procedures exhibit the same amount of pinholes and contiguity as the bimodal samples to be analyzed, then any error effects created by the presence of pinholes and contiguity will be similarly eliminated.

A problem which now arises is how to quantitatively define and measure contiguity. Also, a monomodal calibration sample made from fine powder will exhibit a disporportionally higher amount of contiguity than a bimodal sample made with that powder as one component. In the monomodal sample, the sintering potential is much higher, since every small particle is in contact with other small particles. Even if the monomodal and bimodal samples are furnace processed identically, the monomodal sample will show excessive contiguity.

At this point in the compositional measurement development, it became apparent that there were too many unknowns associated with the intersection and erosion operations to use them with confidence. Although the procedures show great promise, it was decided to use a more simplified approach, based on the erosion concept, to measure composition. This modified erosion approach is described in the next section. An additional benefit of this modified approach is that besides determining image composition, the approach also precisely locates the positions of the large and small particles. This additional information can then be used to study bimodal segregation on a microstructural level.

C.6.9 A Modified Erosion Approach

The erosion operation as described above was the starting point for the development of the simple but robust compositional measurement tool described here. The key characteristic of the original erosion process which was leveraged for this development was that, as seen in figure C.20, the small particles are usually completely eroded long before the large particles. The new erosion approach centered around the concept of reconstructing the large particles, back to their original shape, after the small particles had been removed. If this could be done, then the composition of the initial image could be determined from the expression

$$C = 1 - \frac{\text{number of white pixels in the large particles}}{\text{number of white pixels in all particles}}. \qquad \text{C.47}$$

The process of selectively reconstructing only the large particles after the entire image had been partially eroded was given the name *evolution*. The combination of a modified erosion operation followed by an evolution operation would proceed as follows. The modified erosion process would happen in a similar fashion to the original erosion process described above, using a 4-way criterion to remove white pixels from the image. Every erosion pass would, as before, remove another layer of pixels from the particle perimeters. Also as before, the digitized image would be stored in the computer memory as a 1024 x 1024 array of single byte length numbers. White pixels in the initial image were represented with the number 255, and black pixels were represented with the number zero. In the original erosion process, every time a white pixel was eroded, the value in its corresponding memory location was changed from 255 to 0. In the modified erosion process, when a white pixel was eroded, its value was changed from 255 to the number of the erosion pass on which the change occurred. For example, if a white pixel was eroded on the third erosion pass of the image, then its value would be changed from 255 to 3. The erosion process would continue until all the small particles had been removed. At that point, reconstruction of the large particles using the evolution process would begin. Note that all information about the starting image is retained using this modified erosion operation. All pixels with a value greater than zero were white pixels in the initial image.

In a similar fashion to the erosion process, the evolution process happens as a series of evolution passes, in which layers of pixels are added back to the image. The key to the evolution process is the criterion which is used to determine which eroded pixels should be added back to form an image of only the large particles. This criterion is as follows. On any given evolution pass, a previously eroded pixel is added back only if that pixel is adjacent to a white pixel. For example, on the first evolution pass, only those eroded pixels which are adjacent to a white pixel (i.e. a pixel which survived all the erosion passes) would be added back. The 4-way criterion is again used for this process. Conceptually, at the moment when the erosion process is halted, the eroded particles which still remain in the image act as seeds for the evolution process. If a small particle has been completely eroded, then there is no seed from which to grow back the particle.

C.6.10 Evaluation Modified Erosion Approach Using Simulated Images

To evaluate the modified erosion process, it was first tested with the simulated bimodal images and then later tested with actual bimodal images. In the simulated image tests, five bimodal images of differing compositions were generated. In all five images, the large particles had a radius of 70 pixels with a standard deviation of 5 pixels, and the small particles had a radius of 10 pixels with a standard deviation of 2 pixels. Since the particle size distributions could be so completely defined in these simulated images, it was known a priori that 16 erosion passes would be sufficient to remove all the small particles. This is because the largest of the small particles would have a radius of $10+3\sigma$, or 16 pixels. Since each erosion pass would remove one pixel off the radius (or two off the diameter), 16 passes would eliminate all the small particles. Therefore, after 16 erosion passes had been completed, the evolution process would be begun to reconstruct only the large particles.

The results of the simulated evaluation are shown graphically in figure C.35. The modified erosion procedure was extremely accurate in determining the composition of the simulated bimodal images.

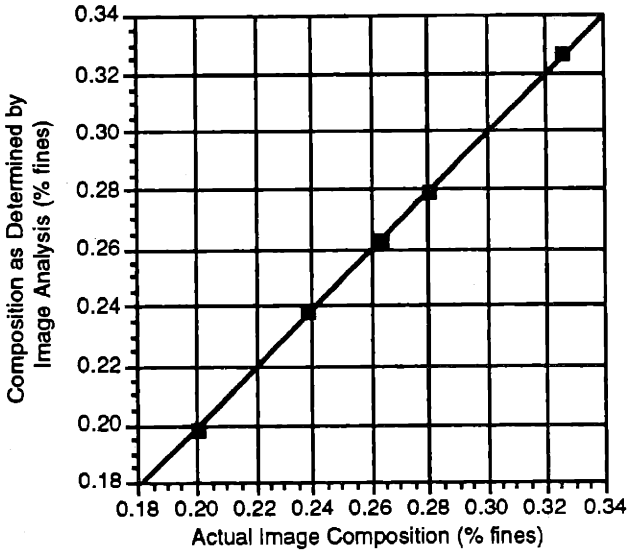

Figure C.35: A plot of analyzed vs. calculated composition.

One of the simulated images from the above series was analyzed to demonstrate how the program is succeeding in identifying the large particles. This is shown in figure

C.36. After the large particles had been reconstructed, the pixels were changed from white to gray, and this image was overlaid onto the initial bimodal image. Note that in addition to correctly determining the composition of the simulated image, the modified erosion process can also determine the positions of the large and small particles within the image.

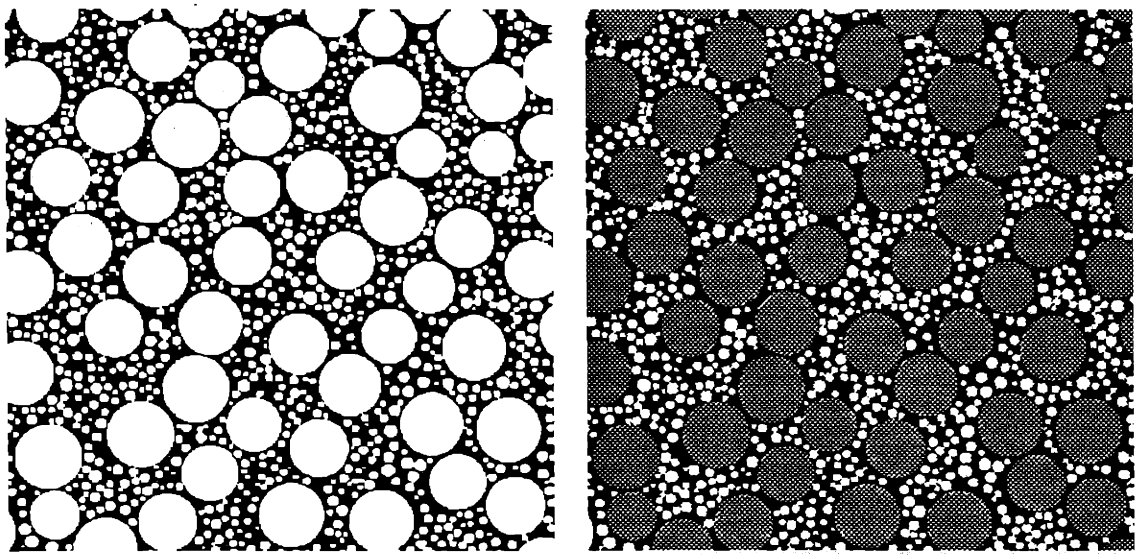

Original image

After identification of the large particles

Figure C.36: Simulated bimodal microstructures before and after identification of the large particles.

The final test in the evaluation of the modified erosion approach was to correctly identify the large particles in a real bimodal image. To successfully accomplish this, the program must first be calibrated using bimodal images of known composition. Calibration is required because, in contrast to the previous simulated test, the appropriate number of erosion passes which must be performed before the evolution process is begun is not known a priori. The calibration procedure requires the introduction of several new mathematical relationships. The first of these is concerned with the average composition of a large area which is to analyzed with multiple micrographs.

C.6.11 Calibration of the Modified Erosion Approach

In the measurement of average packing density $\emptyset_{avg}$ over a given area, we have previously seen that this quantity is simply the algebraic average of the packing densities of all the micrographs which were taken to cover this area. If *i* micrographs were required to

cover a given area, where the packing densities in each micrograph were $Ø_1, Ø_2, ..., Ø_i$, then the average packing density for the entire area is

$$Ø_{avg} = \text{Average}(Ø_1, Ø_2, ..., Ø_i). \qquad \text{C.48}$$

It is not the case, however, that the average composition for the area, C_{avg}, is obtained by averaging the individual compositions. Instead, if $C_1, C_2, ..., C_i$ are the compositions of the individual micrographs, then the average composition for the area is given by

$$C_{avg} = \frac{(C_1\phi_1 + C_2\phi_2 +, ..., +C_i\phi_i)}{\phi_{avg}}. \qquad \text{C.49}$$

In order to obtain the average composition for the entire area, both the packing densities and compositions of the individual micrographs must be known.

This last expression is necessary for calibration because, in general, analysis of multiple images is required to get an accurate measure of composition. The next step in the calibration procedure is to obtain multiple cross-sectional micrographs from a bimodal control sample of known composition. The bimodal control sample is made from the same powder mixture which the parts to be later analyzed are made from. Furnace processing for both the control and actual samples is the same, insuring a similar degree of interparticle contiguity.

After acquisition of the control images, each image is analyzed for packing composition using the modified erosion operation, and an average composition for the set of images is determined. An initial guess has to be made as to how many erosion passes should be performed in order to remove the small particles. If this initial guess is too low, then not all of the fines will be removed from the eroded image, resulting in individual and average composition values which are too low in the percentage of fines. Conversely, if too many erosion passes are performed, some of the large particles will be completely removed and therefore not reconstructed. This would result in individual and average composition values which were too rich in the percentage of fines.

Two control samples, one made from the 120/20μm 316L bimodal mix, and the other made from the 71/9μm bimodal mix, are used below as an example of how to

calibrate the modified erosion procedure. Both control samples had a composition of 26.5% fines. Ten images from each sample were obtained using the backscatter SEM technique. A magnification of 100x was used to obtain the 120/20μm images, and 150x was used for the 71/9μm images. Higher magnification was used on the 71/9μm sample to better capture the finer detail of the particles, as compared to the 120/20μm sample.

Figure C.37 is a plot of average composition vs. number of erosion passes for both control samples. In both cases, as the number of erosion passes increased, the indicated value for the average composition (% fines) also increased.

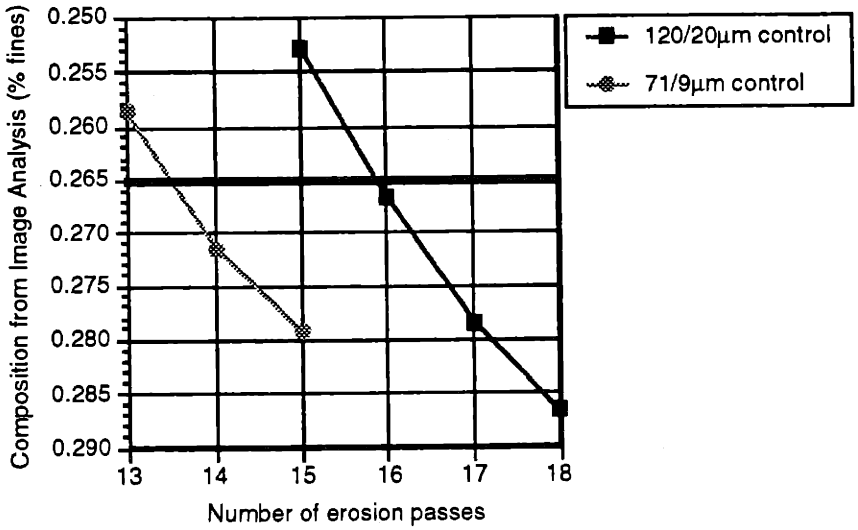

Figure C.37: Calibration plot of average composition vs. number of erosion passes for control samples made from the 120/20μm and 71/9μm 316L bimodal powder mixtures.

As seen from figure C.37, there was no whole number of erosion passes which gave the correct composition value of 26.5% fines for either control sample. An inherent limitation of the erosion process is that the number of erosion passes which are to be taken is restricted to an integer value. The final step in the calibration process is to make a linear interpolation between the erosion pass quantities which bracket the correct average composition value.

For the control samples, the following linear interpolations were determined. These relationships would be used to determine the composition of all future samples made from the same powders.

120/20μm control: Composition = 0.886(16 pass value) + 0.114(15 pass value)

71/9μm control: Composition = 0.504(14 pass value) + 0.496(13 pass value)

Listed below is a summary of the steps required to utilize the modified erosion approach to measure the composition of a given bimodal sample.

1) Create a control sample of known composition, using the same powders that are in the actual sample. Furnace process the control sample identically to the actual sample.

2) Obtain multiple images from the control sample. More images will give a more accurate calibration, an the expense of processing time. Magnification should be selected so that the smallest particles can be resolved. A good starting point is to select a magnification such that the small particles in the image have a radius of twenty pixels.

3) Guess at a number of erosion passes with which to analyze the control images. Using the modified erosion process, obtain an average composition value for the control sample. If this calculated average value is too low compared to the actual value, increase the number of erosion passes. If this calculated value is too high, decrease the number of erosion passes.

4) Repeat the analysis until the correct composition of the control sample is bracketed by two calculated composition values. Determine a linear interpolation between the two calculated values.

5) Obtain multiple images of the actual sample to be analyzed. Note - the magnification used must be the same as that used for the control sample !

6) Perform two individual analyses on the group of sample images, using the numbers of erosion passes which correctly bracketed the control sample. Obtain two different average composition values from the analyses.

7) Using the linear interpolation previously obtained, and the two preliminary composition values from step 6, calculate the correct average composition for the sample.

From figure C.37 it can be seen that, for the 120/20μm control sample, 16 erosion passes almost gives the correct composition even before the use of the linear interpolation approximation. A single image from the 120/20μm control was analyzed for composition using 16 erosion passes. The image, before and after the identification of the large particles, is shown in figures C.38-39. In this visual evaluation, the algorithm does a very good job of identifying the large particles. Pinholes which are present in several of the particles are correctly ignored. Note the one large particle near the center of the image with a very large internal void. Although the particle was correctly identified as being large, the small metal island in the center of the pore was identified as a small particle. This type of defect, however, is extremely rare and should not affect the overall accuracy of the procedure.

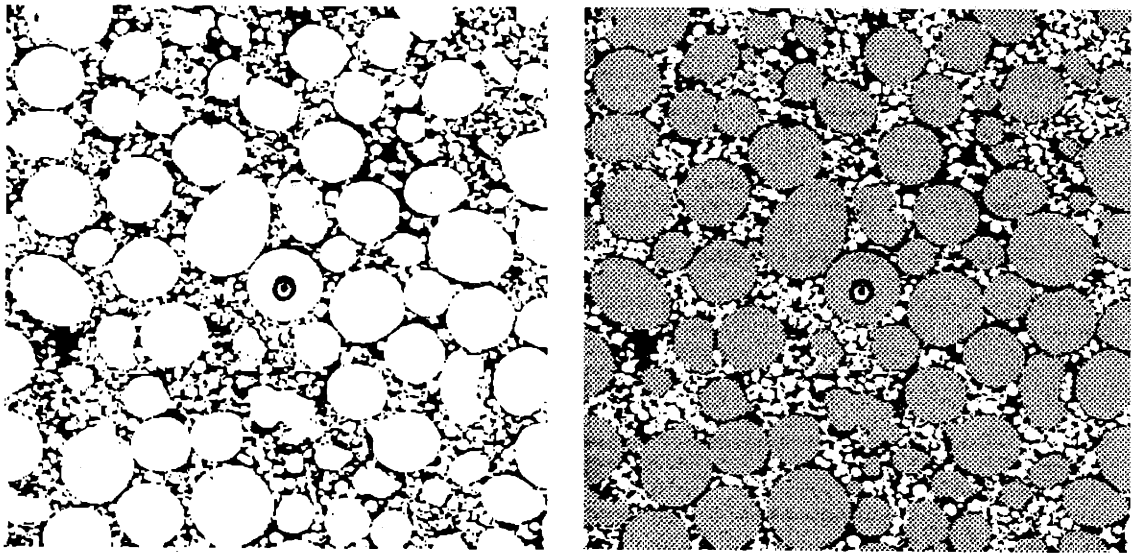

Original image of 120/20μm bimodal control

After identification of the large particles

Figures C.38 and C.39: The gray particles in the right image are those which the composition identification algorithm has determined to be from the large powder component.

At this point, the development work in compositional measurement using image analysis was ended. Although the final approach using the modified erosion operation is not without flaws, it was considered accurate enough for the purposes of this research.

C.7 Using the Analysis Software

This section gives a step by step description of how to use the image analysis software. All software was written for the Apple Macintosh computer. It is highly recommended that a very fast Macintosh, with either a 68040 or PowerPC microprocessor, be used to run this software. Photographic analysis is extremely processor intensive, with a single 1024 x 1024 image requiring in excess of 100 million comparison operations. All code was written in C, and was compiled using Symantec Think C v.7.0 programming software.

Four separate applications were written to perform the analysis process. Two applications were utility programs designed to reduce image file storage requirements. The second two applications were versions of the analysis software which differed only in the type of input file format which they accepted. The use of these four applications is described below.

C.7.1 Program Input

The 1024 x 1024 backscattered images files produced by the Isis software were stored using the TIFF file format. After all images from a given photo session had been acquired, the image files were downloaded to a Macintosh computer for analysis. With each image requiring 1Mbyte of storage space, and with each imaging session typically generating 100 - 200 images, file storage requirements soon became an issue. To reduce the file storage requirements, the gray scale images were thresholded into final black and white form and then stored for later processing. Black and white images can be stored in bitmap form, which requires 1/8 the storage space of the initial gray scale image. The application program **compress** was written to threshold the gray scale images and store them as bitmap files. The program uses a threshold value of 127, as explained earlier. It was occasionally necessary to review an image of a given microstructure after that image had been compressed. Before a compressed image could be viewed using an application such as Adobe Photoshop, the bitmap file had to be converted into a format which was recognized by the Photoshop software. The application program **decompress** was written to convert compressed bitmap images into Photoshop "raw" format so that they could be viewed. Note that the **decompress** application does not recover any of the gray scale

information from the initial image - it simply generates a different format of black and white image which can be viewed in Photoshop.

A unique file naming convention was created to allow the four application programs to correctly locate and process multiple batches of files. All file names were composed of two characters - a base character and a suffix character. If a single batch of files was being analyzed, the base character chosen for the batch was "a". If more than one batch of images was to be analyzed, the base characters chosen were "a", "b", "c", etc.. The suffix characters chosen were ASCII characters which appeared sequentially in the computer's character set. Table C.2 demonstrates the use of the file naming convention for three batches of image files.

Table C.2: Example of the File Naming Convention.

Image Number	Image Batch "a" File Names	Image Batch "b" File Names	Image Batch "c" File Names
1	a;	b;	c;
2	a<	b<	c<
3	a=	b=	c=
4	a>	b>	c>
5	a?	b?	c?
6	a@	b@	c@
7	aa	ba	ca
8	ab	bb	cb
9	ac	bc	cc
*	*	*	*
*	*	*	*
*	*	*	*
34	ax	bx	cx
35	ay	by	cy
36	az	bz	cz
37	a[	b[	c[
38	a\	b\	c\
39	a]	b]	c]
40	a^	b^	c^
41	a_	b_	c_
42	a`	b`	c`

Using this file naming convention, a maximum of 42 images could belong to any one batch. (Note - Capital letters could not be used as suffix characters, since the Macintosh operating system does not discriminate between capital and lower case letters in file names.) A few examples will help to clarify the file naming convention. If a single batch of 10 images was to be analyzed, then the individual files would be named a;, a?, a=,

....., ac, ad. If two batches of 8 images each were to be analyzed, the individual files would be named a;, a<,..., aa, ab for the first batch and b;, b<, ..., ba, bb for the second batch. Although this file naming convention may seem arcane, it greatly simplified the code required for file I/O.

Once the input files had been correctly named and compressed, they were ready to be analyzed with the analysis software. The application **batch compressed photo** performed this task. An input requirement was that all file batches contain the same number of images. In operation, the **batch compressed photo** application file and all the image files to be analyzed were placed in the same folder on the Macintosh desktop. Otherwise, the application would not be able to locate the image files.

An additional application, **batch raw photo**, was also written. This application differs only in that it accepted images in Photoshop raw format for input, instead of the compressed format.

C.7.2 Program Operation

When initially opened, the **batch compressed photo** application queries the user for the necessary operating information. These input queries are explained below.

1) *How many batches are there (integer) ?* - An integer value for the number of image batches to be analyzed is input.

2) *How many images are there in a batch (integer) ?* - An integer value is entered for the number of images in a batch. As mentioned earlier, all batches must have the same number of images.

3) *How many erosion passes to remove the small particles (integer) ?* - An integer value is entered. Determination of the correct value was explained earlier. If a value of zero is entered, then compositional analysis is not performed on any of the images. This greatly speeds up the other analysis operations and significantly reduces total processing time.

4) *What is the scale of the image in microns per pixel (float) ?* - A real value is entered here. For the images used in this research, a value of 1.563 was used

for 50x magnification images, 0.982 for 100x magnification, and 0.645 for 150x magnification.

5) *What is the layer thickness in microns (integer) ?* - This value will determine the width of the layer scanning window. A value of 175 was used for this research. The program will divide this quantity by 2 in calculating the correct window width.

6) *What is the line spacing in microns (integer) ?* - This value will determine the width of the line scanning window. A value of 175 was used for this research. Again, the program will divide this quantity by 2 in calculating the correct window width.

7) *What is the name of the output data file ?* - Enter any desired file name. This name will serve as a base name for the output data, and will be modified for each batch of images which are processed.

Upon answering the final input query, the analysis operations begin. A brief summary of these operations is given below.

1) Image Loading - The algorithm operates on each image individually. An image is loaded into memory. Also, a strip of image 4 pixels wide is trimmed from the four sides of the image. This region often contains artifacts generated during the image acquisition process.

2) Packing Density Measurement - The packing density for the image is determined, and this value is written to a file named **packing data**. A unique packing data file exists for each batch of images.

3) Packing Defects - The image is next scanned for layer and line packing defects. Two separate files, **layer packing data** and **line packing data** are created, which contain the packing density values for each window position. These files are essentially long lists of packing numbers which are stored for later statistical analysis.

4) Compositional Measurement - Next, the modified erosion process is performed on the image. Based on the input number of erosion passes, a composition value for each image is determined, and this information is stored to a **composition data** file. The composition and packing density values for each image are multiplied, and this information is saved to an **avg composition data** file. The data in this later file will be used to calculate the average composition of the entire batch.

5) Statistical Processing - Using the information in the above files, statistical operations are performed to calculate the descriptive parameters for each batch of images.

C.7.3 Output Data

After processing, a summary data file is created for each batch of images. The names of these summary data files are based on the file name which was input during the initial input queries. An example of a summary data file is given in figure C.40.

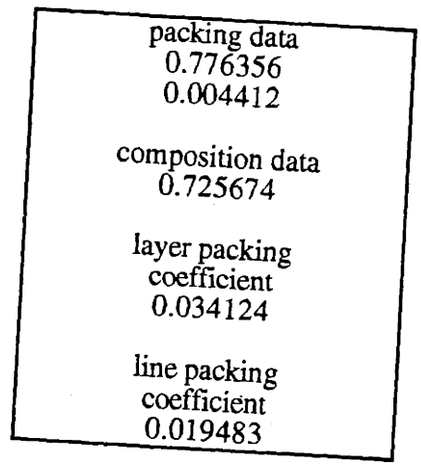

Figure C.40: Example of a summary data file.

The average packing density of the images in the batch is given, along with the standard deviation of the individual image packing density values. The packing variation based on the COV can be obtained from these two values. The average composition is given, followed by the COV parameters for layer and line packing defects.

C.8 Discussion

The photographic analysis procedure described here is a powerful tool for comparing the microstructures of parts printed with different printing parameters. To be used effectively as a comparative tool, all the analysis steps must be applied consistently to each microstructure studied. The algorithms will always generate "numbers", regardless of what quality of images which are input. For these numbers to have value for the purposes of part comparison, they must be obtained while maintaining the highest levels of consistency.

As with any newly developed process, there will invariably be modifications and improvements made over time. The analysis procedures, as described here, certainly have plenty of room to mature. The concepts presented for the investigation of powdered metal microstructures are truly only starting points. Other potential methods for part analysis are limited only by the creativity of the researcher.

Appendix D: Powder Preparation and Recycling Procedures

D.0 Introduction

The procedures for preparing metal powders with boric acid locking agent, and recycling the powder from unprinted regions of the powder bed, are given below.

D.1 Powder Preparation

The following procedure can be used to produce metal powder coated with 0.05g of boric acid per 100g of powder. The procedure can be readily adjusted to produce other coating concentrations.

1. A dilute solution of boric acid in water needs to be prepared first, as this will make precise dispensing of the boric acid easier. Using a balance accurate to +/-0.01g, measure out 10g of boric acid. Combine the boric acid and exactly 1000g of distilled water in a polypropylene storage container. Make sure the boric acid is completely dissolved before proceeding.

2. Weigh out the total amount of powder to be treated and pour it in a rectangular Pyrex baking dish. For every 100g of powder to be treated, add 5g of the boric acid solution. The solution should be dribbled evenly across the powder surface using an eye dropper or large pipette.

3. Next, saturate the powder with additional distilled water and stir the powder slurry around. The goal is to more evenly distribute the boric acid throughout the powder. Enough water should be used to produce standing puddles on the surface of the powder after stirring has stopped.

4. Place the Pyrex dish in an oven and heat to approximately 150°C. Stir the powder every 15 minutes to prevent boric acid from building up on the top surface as the water evaporates. Continue until the powder is completely dry. It is normal for there to be large chunks of locked powder present at this point.

5. Allow the powder to cool, but do not leave it exposed to room humidity for any length of time. The goal is to keep the powder as dry as possible whenever handling it.

6. The Pyrex dish should be scraped clean with a steel blade to ensure the all the boric acid remains with the powder. Place the powder and/or powder chunks in a ball mill jar. It is highly recommended that a dedicated ball mill container be used for powder preparation to prevent cross-contamination with other material systems. A 2000ml polypropylene jar works well for milling. Add stainless steel ball milling media to the container in approximately a 1:1 volume ratio with the powder. The steel balls should be between 1/4" and 1/2" in diameter.

7. Mill the powder for a minimum of one hour. Remove the milling media with a coarse sieve, and immediately transfer the powder to an airtight container.

D.2 Powder Recycling

The following procedure can be used to recycle coated metal powder which has been reclaimed from the unprinted regions of the powder bed after a printing run.

1. Ensure that absolutely no powder contaminated with binder is utilized for recycling. This can sometimes inadvertently happen when printing errors place binder where it wasn't supposed to go, unbeknownst to the operator. Some prefiltering of the powder can be done by forcing the locked powder through a 60 mesh sieve. Use the sieve like a cheese grater to pulverize the locked powder into smaller pieces. Binder contaminated areas usually won't make it through.

2. Place the powder in a Pyrex dish and heat to 150°C for one hour. The goal is to remove any residual moisture which may be present in the powder.

3. Perform steps 5 - 7 of the above powder preparation procedure in order to break all the remaining interparticle salt bonds.

Appendix E: A Preliminary Investigation of Metal Slurry Spreading

E.0 Introduction

During the early portion of this research, a preliminary investigation was performed into the use of metal slurries for layer creation. Metal slurries had several potential advantages over dry metal powder. Finer powders (less than 10μm) could be used in slurry form because the liquid vehicle would act as a lubricant, thereby reducing the otherwise extremely high levels of interparticle friction found in similar dry powders. Safety concerns associated with the dusting of fine, dry powders would also be greatly reduced. In the case of a bimodal slurry, the presence of a liquid vehicle would also assist in more complete mixing of the large and small components, leading to improved homogeneity and packing. [42]

Presented below is a summary of the observations which were made during this investigation. A brief review of how slurries are used in industry is presented first to provide the necessary background information.

E.1 Background Material

The use of slurries for the creation of thin layers was well established in the industrial process of tape casting. [17] In this process, a doctor blade is used to spread the slurry, or "slip", over a non-porous substrate. This substrate is usually a long polymer tape, hence the name tape casting. Typically a single thin layer of slip is spread, although the process can be repeated to build up multiple layer thicknesses. A polymeric binder in the slip holds the layer together after the liquid carrier is removed by evaporation. The layer is then fired in a furnace to remove the binder and sinter the particles together. Tape casting is typically performed with ceramic powders to form thin sheets of solid material.

Another industrial use of slurries is slip casting, in which a ceramic or metal slip is poured into a porous ceramic mold. [26, 57] Particles in the slip build up on the internal mold surfaces as the slip carrier passes through the porous mold walls and is evaporated. Additional slip is added as the liquid carrier is expelled in order to completely fill the mold.

When no more slip can be accepted, the mold is dried, curing the binder. A solid article is formed which can be removed from the mold and again fired to create a fully dense part.

A typical slip will contain a liquid vehicle (often water), the powder, a binder, and wetting agents or surfactants. It may also contain plasticizers, homogenizers and release agents. [17] Often, a single chemical compound is used to perform several of these functions, although slip formulations can become quite complex.

The central parameter which determines the behavior of a slip during processing is the slip viscosity. As the solids loading of a slip is increased, the slip viscosity increases until the point where the slip more closely resembles a thick paste. Slips which flow readily have lower solids content. There is a necessary tradeoff between how much solid material can be attained in the final product and how easy it is to work with a given slip. In the slip casting process, slip viscosities are targeted for between approximately 10,000 and 30,000 centipoise to ensure that the small features of the mold cavity are filled.

For suspensions with high solids concentrations, such as the slurries of interest for 3DP, the viscosity may be expressed in terms of the volume fraction of particles, Ø, in the slurry by the Mooney equation [39]:

$$\mu_r = \frac{\mu}{\mu_0} = \exp\left(\frac{a\,\phi}{1 - \phi/\phi_{tap}}\right) \qquad \text{E.1}$$

where $\emptyset_{tap}$ is the tap density of the powder in the dry condition, and a is the Einstein constant for a shape factor, which has a theoretical value of 2.5 for spherical, non-interacting particles. [30] Also, μ is the viscosity of the slurry, and μ_o is the viscosity of the liquid carrier before the powder was added. The relative viscosity, μ_r, is therefore the factor by which the original viscosity of the liquid carrier was increased by the addition of powder.

Figure E.1 is a plot of relative viscosity μ_r versus powder volume fraction Ø. Several curves are drawn for different values of $\emptyset_{tap}$. (Note: $\emptyset_{tap}$ is labeled as $\emptyset_p$ in the illustration.)

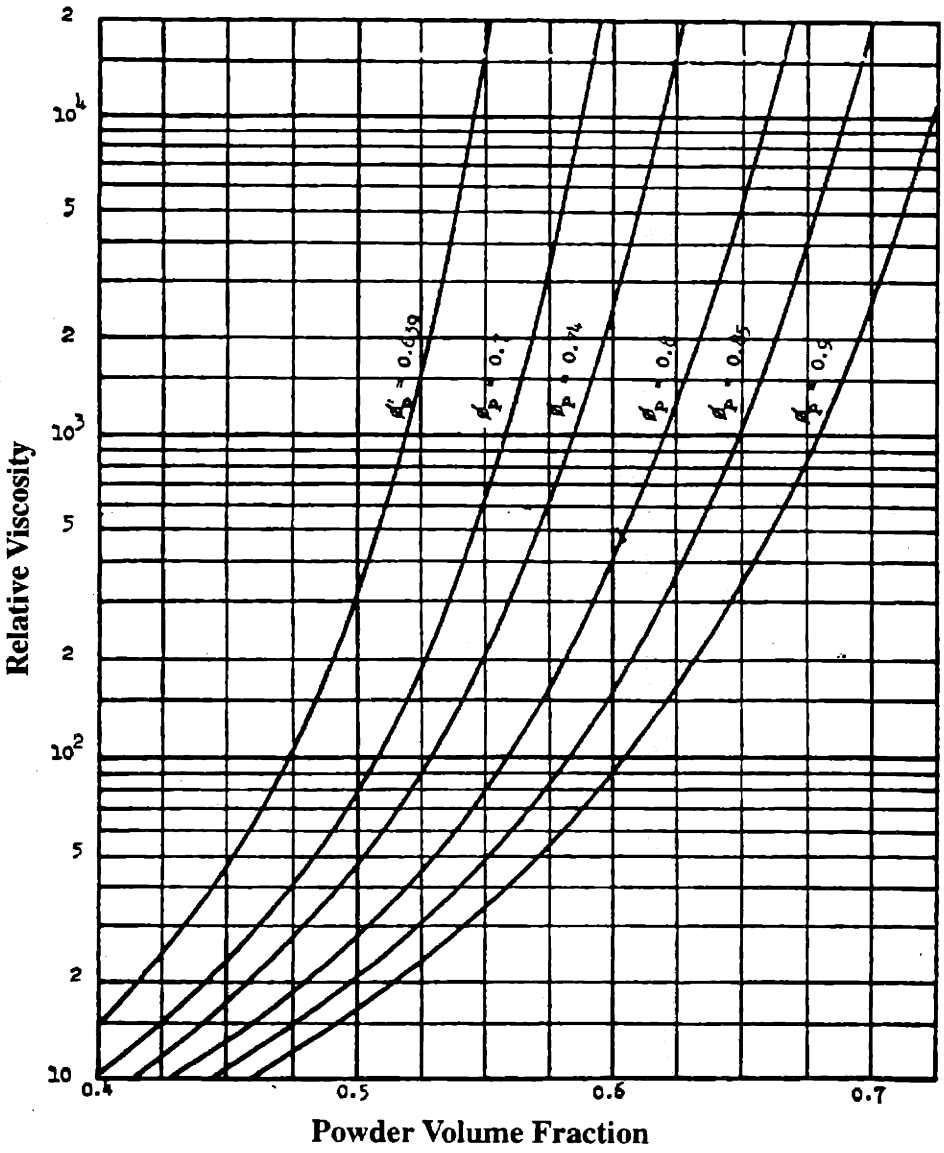

Figure E.1: Relative viscosity μ_r vs. powder volume fraction Ø for different values of $Ø_{tap}$. [30]

Viscosity increases exponentially with the amount of powder which is present in the slurry. When a slurry is loaded to 80% of a powder's tap density, the viscosity is already 3,000 times that of the carrier fluid. At 85%, the viscosity is 43,000 times higher. Once a slurry becomes highly load, very small changes in the volume fraction of powder can produce significant changes in the slurry viscosity. Note that it is impossible to produce a free-flowing slurry at the tap density of a powder.

E.2 Experimental Procedure

For these tests, slurries were formulated from mixtures of powder, water, and various water-soluble polymers. The polymer acted as a thickening agent, allowing the slurry to be relatively stable for short periods of time after mixing. The polymer additive was necessary since the metal powders used would have settled too fast in just pure water. The polymers also acted as surfactants.

Slurries were made with either polyvinyl alcohol, sodium alginate or methyl cellulose as the polymer additive. Enough polymer was dissolved in the water to produce a mixture with a viscosity of approximately 200 centipoise. This typically required 1 - 2% polymer by weight.

Monomodal and bimodal powders were used to make the high solids loading slurries. Powder was added to each of the above water / polymer mixtures and blended by hand. Various volume fractions were tried.

Slurry spreading in the powder piston was performed using a 4" putty knife as a doctor blade. A quantity of slurry was manually dispensed at the front of the piston, and the putty knife was used to strike the layer. The first layer of slurry was spread on an alumina substrate attached to the bottom of the piston. Figure E.2 is an illustration of the layer generation process.

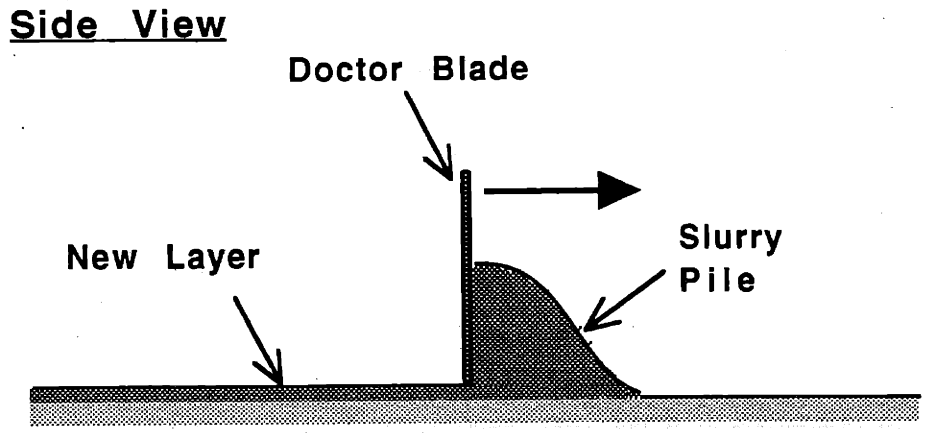

Figure E.2: Illustration of how a doctor blare was used to strike each new layer.

Once the slurry layer was spread, the residual moisture from the slurry needed to be removed prior to printing, so that the liquid binder dispensed from the printhead would have open porosity to flow into. A hot air gun was used for this purpose. After drying, the polymer carrier in the slurry acted as a form of locking agent, providing cohesive strength to the layer surface.

Multiple layer bars were printed for each of the slurries tested.

E.3 Results and Conclusions

An unexpected difficulty associated with the viscosity of the slurry became apparent at the start of the printing trials, for which a solution was never found. Specifically, for any of the slurries tested, the *second and subsequent* slurry layers could not be spread smoothly. For these layers, the surface upon which they were being spread was the porous upper surface of the previous layer. During the course of the spread, moisture from within the slurry pile would wick down into the previous layer. This had the effect of increasing the solids loading within the pile. Because the slurries were already highly loaded, pile viscosity increased dramatically during the first moments of layer spreading. Layer surfaces would begin smooth, but would begin to roughen and tear during the later portion of the layer spread. This effect is illustrated in figure E.3.

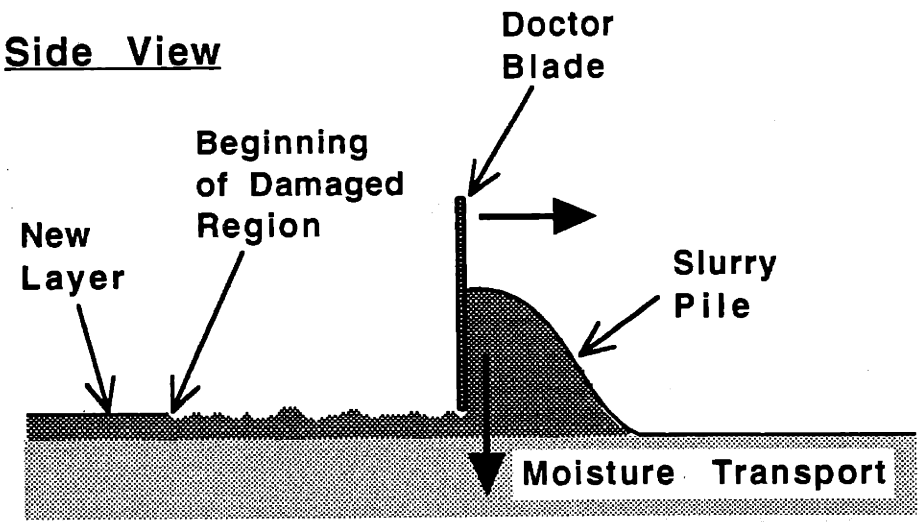

Figure E.3: Illustration of moisture transport from the slurry pile to the powder bed, with the resulting degradation in spread layer quality.

Variations in the initial solids loading of the slurries and the speed with which the layer was spread were tried, but only with marginal success. No condition was found which could consistently create multiple smooth layers.

Spreading did improve slightly over those regions of the previous powder layer which had been printed into, although these regions still experienced some layer tearing. Presumably, the additional polymer binder present in these regions reduced the amount of open porosity, and locally decreased the rate of moisture transport.

A final difficulty with the slurry approach was in removing the printed bars from the powder bed after printing. The bars were already weakened from internal voids caused by the non-uniform layer spreading. The surrounding unprinted regions had appreciable strength due to the presence of the polymer thickener in the slurry, and could only be removed by washing with water. During this washing process, the printed bars were either partially or completely destroyed.

No immediate solutions for the problems described above could be found. Due to the initial difficulties of printing with metal slurries, no further work was performed.

Bibliography

1. Amaya, H.E., "Size and Distortion Control in MIM Processing," Advances in Powder Metallurgy - 1991, Powder Injection Molding, 1991, vol. 2, pp. 285-296.
2. Andrade, E.N. da C., and Fox, J.W., "The Mechanism of Dilatancy", *Proceedings of the Physics Society*, vol. 62, 1949, pp.483 - 500.
3. Ayer, J.E., and Soppet, F.E., "Vibratory Compaction: I, Compaction of Spherical Shapes", *J. Amer. Ceramic Soc.*, Vol. 48, No. 4, 1965, pp. 180 - 183.
4. Baumann, G., Janosi, I.M., and Wolf, D.E., "Particle Trajectories and Segregation in a Two-Dimensional Rotating Drum", *Europyysics Letters*, **27** (3) pp. 203 - 208, (1994).
5. Bell, W.C., Dillender, R.D., Lominac, H.R. and Manning, E.G., "Vibratory Compacting of Metal and Ceramic Powders", *J. Amer. Ceramic Soc.*, Vol. 38, No. 11, 1955, pp. 396 - 404.
6. Billiet, R., "The Challenge of Tolerance in P/M Injection Molding," 1985 Annual Powder Metallurgy Conference Proceedings, Progress in Powder Metallurgy, 1985, vol. 41, pp. 723-741.
7. Bindell, J.B., "Elements of Scanning Electron Microscopy", *Advanced Materials and Processes*, March 1993, pp. 20 - 27.
8. Bredt, J.F., "Binder Stability and Powder \ Binder Interaction in Three Dimensional Printing", 1995, Ph.D. Thesis, MIT, Cambridge, MA.
9. Brown, R.L. and Richards, J.C., *Principles of Powder Mechanics - Essays on the Packing and Flow of Powders and Bulk Solids*, Pergamon Press, 1970.
10. Cook, N.H., *Mechanics and Materials for Design*, McGraw-Hill, New York, 1984, pp. 451 - 453.
11. D'Appolonia, E.P., "Dynamic Loading", *Journal of Soil Mechanics and Foundations Division*, ASCE, 96 (SM1), 1970.
12. Das, B.M., *Fundamentals of Soil Dynamics*, Elsevier Science Publishing Co., Inc., New York, New York, 1983, pp. 328 - 352.
13. Davies, T.G., "Machine Foundations", *Cyclic Loading of Soils: From Theory to Design*", Ch. 8, edited by M.P. O'Reilly and S.F. Brown, Van Nostrand Reinhold, New York, NY, 1991, pp. 367 - 410.
14. Dobry, R., and Whitman, R.V., "Densification of Sand by Vertical Vibrations in 'Standard' Molds", Research Report R70-05, Soils Publication 251, Dept. of Civil Engineering, M.I.T., 1969.

15. Dobry, R., and Whitman, R.V., "Compaction of Sand on a Vertically Vibrating Table", Research Report R72-23, Soils Publication 302, Dept. of Civil Engineering, M.I.T., 1972.
16. Drucker, D.C., Gibson, R.E. and Henkel, D.J., *Trans. Am. Soc. Civ. Engrs.*, **122**, (338) 1975.
17. Fiori, C. and De Portu, G., "Tape Casting: A Technique for Preparing and Studying New Materials", *Novel Ceramic Fabrication Processes and Applications*, Davidge, R.W., Ed., British Ceramics Proceedings, No. 38, December, 1986, pp.213 - 225.
18. Furnas, C.C., "Grading Aggregates I - Mathematical Relations for Beds of Broken Solids of Maximum Density", *Industrial and Engineering Chemistry*, 1931, vol. 23, pp. 1052 - 1058.
19. Galla, M.P., "Process Development for Three Dimensional Printing of Metal Loaded Binders", 1994, M.S. Thesis, MIT, Cambridge, MA.
20. German, R.M., *Powder Metallurgy Science*, 2nd Edition, Metal Powder Industries Federation, Princeton, NJ, 1994.
21. German, R.M., *Powder Injection Molding*, Metal Powder Industries Federation, Princeton, NJ, 1990.
22. Goetzel, C.G., "Infiltration," *Metals Handbook Ninth Edition*, Powder Metallurgy, vol. 7, American Society for Metals, Metals Park, OH, 1984.
23. Gray, W.A., *The Packing of Solid Particles*, Chapman and Hall Ltd., London, 1968.
24. Grey, R.O. and Beddow, J.K., "On the Hausner Ratio and its Relationship to Some Properties of Metal Powders", *Powder Technology*, 2 (1968 / 69) pp.323 - 326.
25. Hausner, H.H., Foward to *Perspectives in Powder Metallurgy*, vol.2, *Vibratory Compacting - Principles and Methods*, Plenum Press, New York, 1967.
26. Hausner, H.H., "Slip Casting of Metal Powders", *Perspectives in Powder Metallurgy - Fundamentals, Methods and Applications, Vol.1, New Methods for the Consolidation of Metal Powders*, Plenum Press, New York, 1967, pp.221 - 238.
27. Jenike, A.W., *Bull. Univ. Utah*, **53** (26), p.1, 1964.
28. Khanuja, S., "Ink Jet Printing of Concentrated Ceramic Suspensions", 1994, Internal Document, MIT, Cambridge, MA.
29. Lambe, T.W. and Whitman, R.V., *Soil Mechanics, SI Version*, John Wiley and Sons, New York, 1979.
30. Lee, D.I., "Packing of Spheres and its Effect on the Viscosity of Suspensions", *Journal of Paint Technology*, Vol. 42, No. 550, November 1970, pgs. 579-587.

31. Marcus, H.L. and Bourell, D.L., "Solid Freeform Fabrication Finds New Applications", *Advanced Materials & Processes*, September 1993, pp.28 - 35.
32. McClintok, F.A. and Argon, A.S., *Mechanical Behavior of Materials*, Addison-Wesley, Inc., 1965.
33. McGeary, R.K., "Mechanical Packing of Spherical Particles", *J. Amer. Ceramic Soc.*, Vol. 44, No. 10, 1961, pp. 513 - 522.
34. Meakin, P., and Skjeltorp, A.T., "Application of Experimental and Numerical Models to the Physics of Multiparticle Systems", *Advances in Physics*, Vol. 42, No. 1, 1993, pp. 61 - 64.
35. Messing, G.L. and Onoda, G.Y., "Inhomogeneity-Packing Density Relations in Binary Powders," *J. Amer. Cer. Soc.*, 1978, vol. 61, p.1.
36. Michaels, S.P.,"Production of Metal Parts Using the Three Dimensional Printing Process," 1993, M.S. Thesis, MIT, Cambridge, MA.
37. Michaels, S.P.,"The Adaptation of the 3D Printing Process to the Production of Metal Parts," 1995, Internal Document, MIT, Cambridge, MA.
38. Mistler, R.E., Shanefield, D.J. and Runk, R.B., "Tape Casting of Ceramics", *Ceramic Processing Before Firing*, Onoda, G.Y. and Hench, L.L., ed., John Wiley and Sons, New York, 1978, pp.411 - 448.
39. Mooney, M., *Journal of Colloidal Science, 6*, 130 (1953).
40. Morris, E.B., "Industrial Hydrocolloids", *The Structure, Dynamics and Equilibrium Properties of Colloidal Systems*, Bloor, D.M. and Wyn-Jones, E., Eds., Kluwer Academic Publishers, Boston, 1990, pp.449 - 469.
41. Norman-Gregory, G.M. and Selig, E.T., "Volume Change Behavior of Granular Soil Columns During Vibration", *Soil Dynamics and Liquefaction*, A.S. Cakmak, Ed., Elsevier, New York, 1987, pp.255 - 267.
42. O'Connor, J.W., Rhee, B.O. and Chung, C.I., "Solution Mixing vs. Mechanical Mixing for Metal Powders with a Solid Polymer Solution Binder", *Advances in Powder Metallurgy - 1991, Vol.2, Powder Injection Molding*, Metal Powders Industry Federation, Princeton, New Jersey, 1991, pp.85 - 93.
43. Onoda, G.Y. and Messing, G.L., "Packing and Sintering Relations for Binary Powders," *Processing of Crystalline Ceramics*, H. Palmour, R.F. Davis and T.M. Hare (eds.), Plenum Press, New York, NY, 1978, p. 99.
44. Onoda, G.Y., Liniger, E.G. and Janney, M.A., "Dilatancy and Plasticity in Ceramic Particulate Bodies", source unknown.

45. O'Reilly, M.P., and Brown, S.F., "Cyclic Loading in Geotechnical Engineering", *Cyclic Loading of Soils: From Theory to Design*", Ch. 1, edited by M.P. O'Reilly and S.F. Brown, Van Nostrand Reinhold, New York, NY, 1991, pp. 1 - 18.
46. O'Riordan, N.J., "Effects of Cyclic Loading on the Long Term Settlements of Structures", *Cyclic Loading of Soils: From Theory to Design*", Ch. 9, edited by M.P. O'Reilly and S.F. Brown, Van Nostrand Reinhold, New York, NY, 1991, pp. 411 - 415.
47. Ranade, M.B., Aerosol Science Technology, Vol. 7, No. 161, 1987.
48. Ristow, G.H., "Particle Mass Segregation in a Two-Dimensional Rotating Drum", *Europhysics Letters*, **28** (2), pp. 97 - 101, (1994).
49. Rosato, A., Prinz, F., Standburg, K.J., and Swendsen, R., "Monte Carlo Simulation of Particulate Matter Segregation", *Powder Technology*, 49 (1986), pp.59 - 69.
50. Roscoe, K.H., Schofield, A.N., and Wroth, C.P., "On the Yielding of Soils", *Geotechnique*, **8**, 1958, pp.22-53.
51. Rumpf, H., *Particle Technology*, Chapman and Hall, New York, 1975.
52. Rumpf, H. and Schubert, H., "Adhesion Forces in Agglomeration Processes", *Ceramic Processing Before Firing*", Ch. 27, G.Y. Onoda and L.L. Hench (eds.), John Wiley and Sons, New York, 1978, pp. 357-376.
53. Sachs, E., Cima, M.J.,Williams, P.,Brancazio, D., and Cornie, J., "Three Dimensional Printing: Rapid Tooling and Prototypes Directly From a CAD Model", *Journal of Engineering for Industry*, vol. 114, no. 4, pp.481-488, (Nov. 1992).
54. Shatalova, I.G., Gorbunov, N.S., and Likhtman V.I., "Physiochemical Principles of Vibratory Compacting", *Perspectives in Powder Metallurgy*, vol.2, *Vibratory Compacting - Principles and Methods*, Hausner, H.H., Ed., Plenum Press, New York, 1967, pp.1 - 197.
55. Stanley-Wood, N.G., "Compact Characterization", source unknown.
56. Suh, N.P., *Int. J. Powder Met.*, **5** (69), 1969.
57. Sulinski, H.V. and Lipson, S., "Slip-Casting of Copper Powder", *Modern Developments in Powder Metallurgy, Vol.1, Fundamentals and Methods*, Plenum Press, New York, 1966, pp.266 - 277.
58. Szechy, K. and Varga, L., *Foundation Engineering - Soil Exploration and Spread Foundations*, Akademiai Kiado, Budapest, 1978.
59. Takahashi, M., and Suzuki, S., "Numerical Analysis of Tapping Behavior of Ceramic Powders", *Ceramic Bulletin*, Vol. 65, No. 12, pp. 1587 - 1590.
60. Westergaard, H.M., *Theory of Elasticity and Plasticity*, Dover Publications, New York, 1964.

61. Williams, J.C., "The Segregation of Particulate Materials", *Powder Technology*, 1975, vol. 15, p.245.
62. Wylonis, E.M. III,"Production of Injection Molding Tooling with Conformal Cooling Channels Using the Three Dimensional Printing Process," 1995, M.S. Thesis, MIT, Cambridge, MA.
63. Yen, K.Z.Y., and Chaki, T.K., "A Dynamic Simulation of Particle Rearrangement in Powder Packings with Realistic Interactions", *J. Appl. Phys.*, Vol. 71, No. 7, 1992, pp.3164 - 3173.